Standalone DC Microgrids Improvements Towards Smarter Grids

by

Hassan Mahmoud Zaytoon

A thesis
presented to the University of Waterloo
in fulfillment of the
thesis requirement for the degree of
Doctor of Philosophy
in
Electrical and Computer Engineering

Waterloo, Ontario, Canada, 2024

Examining Committee Membership

The following served on the Examining Committee for this thesis. The decision of the Examining Committee is by majority vote.

External Examiner:	Bala Venkatesh Professor, Department of Electrical, Computer, and Biomedical Engineering, Toronto Metropolitan University
Supervisor(s):	Magdy Salama Professor, ECE Department, University of Waterloo Ayman Eltantawy Adjunct Assistant Professor, ECE Department, University of Waterloo
Internal Member:	Sheshakamal Jayaram Professor, ECE Department, University of Waterloo Ramadan El Shatshat Lecturer and Director, ECE Department, University of Waterloo
Internal-External Member:	Mehrdad Pirnia Lecturer, ECE Department, University of Waterloo

Author's Declaration

I hereby declare that I am the sole author of this thesis. This is a true copy of the thesis, including any required final revisions, as accepted by my examiners.

I understand that my thesis may be made electronically available to the public.

Abstract

Traditional distribution power systems are facing tremendous challenges in ensuring reliable and secure operation of the energy systems because of the new trend of using small-scale power generation and the proliferation of new types of loads such as electric vehicles. Microgrids have emerged as a promising solution to address the challenges posed by the growing demand for clean and reliable energy. Microgrids are self-sustaining, small-scale power networks, independent of centralized power plants. They offer numerous advantages including enhanced reliability, resiliency, cleaner energy, and economic development. Microgrids are designed to collaborate with Distributed Generation (DG) sources such as Photovoltaic (PV) panels, wind turbines, Energy Storage System (ESS), and small-scale generators. These energy sources are more environmentally friendly than traditional units.

Microgrids can be either AC or DC grid systems. DC microgrids have gained significant attention as they offer remarkable benefits compared to their traditional AC counterparts. DC microgrids offer higher efficiency, improved integration of renewable Distributed Generations (DGs), precise power control, and reduced infrastructure costs compared to AC microgrids. It is clearly obvious that the majority of renewable DGs and ESS produce DC energy which is converted back to AC in order to be connected to the traditional AC grids. Likewise, a considerable portion of modern loads utilize DC power like Variable Frequency Drives (VFD), Electric vehicles (EVs), and electronic-based loads. Despite the considerable interest in DC microgrids, there remain several control and protection challenges that must be addressed to ensure their safe and reliable operation for widespread deployment. Preserving load-generation balance is comprehensively challenging because of the existence of a large number of integrated DGs, ESS, and loads with various technologies. The intermittent power profiles and different capacities of DGs add an extra dimension of complexity to these challenges. Remote and Islanded DC microgrid control is more challenging due to the lack of support from the main grid. As a result, it requires sophisticated control algorithms to ensure the system's stability. Moreover, due to the nature of DC power flow, DC microgrids are facing extremely high fault currents with no zero crossing. In order to address this fault current issue, it is essential to have an effective high-speed protection system to handle these current and interrupting faulted sections rapidly and safely.

Smart grid concept seems as perfect solution for the growing problem of complex microgrid operation. Smart grid entails sophisticated digital automation and intelligent management, which are well suited to solve microgrid operational problems. The current proliferation of DGs and ESS has made modern microgrids more interactive than their predecessors. However, the advent of information technology, and modern communication systems have provided opportunities for automated energy management. By integrating sensors and electronic converters into the energy sources and connecting them to a cloud-based repository of real-time data, a smart system can optimize price, reliability, and the utilization of clean energy based on the available parameters. However, communication networks in smart grids bring increased connectivity at the cost of increased security vulnerabilities. A smart grid can be a prime target for cyber threats due to its critical nature and structure.

Driven by the aforementioned challenges, the broad goal of this thesis is to address the DC microgrids challenges for the sake of the implementation of safe and reliable DC-based smart grids. Firstly, a multi-layer hierarchical control system is proposed. An improved convergence speed Improved Adaptive Model Predictive Controller (IAMPC) is proposed as a primary controller that aims at ensuring optimum, reliable, and extended lifetime operation of the integrated DGs, ESS, and loads. Moreover, an investigation is conducted to assess the robustness of the proposed IAMPC under parameter variations and system degradation. Secondly, a cooperative distributed consensus-based secondary control strategy is proposed ensuring a global voltage regulation and optimum load sharing among the distributed DGs and/or clusters. To address protection challenges in DC microgrids, thirdly, a novel relay protection system is proposed for detecting, identifying, locating, and isolating various faults. The proposed system ensures optimum sensitivity for a wide range of bolted faults and high-resistance faults taking into account the microgrid dynamics during the fault period, the grounding configuration, grounding resistance, and fault resistance. The proposed protection system is capable of clearing faults in less than one resonant cycle while redistributing the load sharing among the updated available generating units.

Acknowledgements

First, I praise and thank Allah Almighty for providing me with the ideas and patience necessary for the successful completion of this thesis.

Secondly, I would like to express my sincere gratitude to my supervisors: Prof. Magdy Salama, and Dr. Ayman Eltantawy, for their invaluable guidance, patience, and counsel in the past years. I feel privileged that Prof. Sheshakamal Jayaram, Dr. Ramadan El Shatshat, Prof. Mehrdad Pirnia, and Prof. Bala Venkatesh have examined this dissertation. Their time and insights are greatly appreciated and respected. Last but not least, I would like to thank my family: my wife, who gives me moral and emotional support in my life.

Dedication

To my cherished wife and kindred spirit, in acknowledgment of your boundless patience, affection, backing, and motivation.

Table of Contents

List of Figures

List of Tables

List of Abbreviations

AC Alternating Current 10

ADC Analog to Digital Converter 138, 139, 141, 142, 159

AIE Active Impedance Estimation 45

AMPC Adaptive Model Predictive Controller 59, 60, 72, 74

BESS Battery Energy Storage System 31, 61, 64, 72, 73, 80

BJT Bipolar Junction Transistor 144

CCS-MPC Continuous Control Set Model Predictive Controller 4, 6, 57, 58, 175

CERTS Consortium for Electric Reliability Technology Solutions 1

DBS DC Bus Signaling 30

DC Direct Current 8, 10

DG Distributed Generation iv, 1, 3, 9, 13, 23, 25, 30, 33–36, 38, 44, 50, 163, 164, 166

DGs Distributed Generations iv, v, 1, 4, 6, 9, 10, 12, 21, 30, 31, 33, 35, 36, 43, 49, 50, 174, 175

DI Droop Index 26, 27

DoD Depth of Discharge 68, 69

DoS Denial of Service 34, 35, 101

EMC Electromagnetic Compatibility 38

EMPC Explicit Model Predictive Controller 60

ESS Energy Storage System iv, v, 1, 2, 4, 6, 10–13, 21, 29, 30, 33, 35, 36, 38, 43, 44, 49, 50, 174–176

ESU Energy Storage Unit 21, 29, 30, 33, 36

ET-MPC Event Triggered Model Predictive Controller 58

EVs Electric vehicles iv, 2, 11, 14

FC Fuel Cell 11

FCS-MPC Finite Control Set Model Predictive Controller 6, 56

FDI False Data Injection 35, 101

GSMPC Gain-Scheduled Model Predictive Controller 59

HESS Hybrid Energy Storage System 69, 77

HVDC High Voltage DC 47, 48

IAMPC Improved Adaptive Model Predictive Controller v, 4, 6, 50, 60, 72, 74, 83, 175

Li-Ion Lithium-Ion 70, 71

MHE Moving Horizon Estimation 5, 6, 86, 102, 104, 105, 107–109, 117, 120, 121, 123, 130, 175, 176

MPC Model Predictive Control 4, 6, 50–53, 56, 108

MPP Maximum Power Point 23, 33, 64

MPPT Maximum Power Point Tracking 13

OP-AMP Operational Amplifier 47, 138, 139, 141, 159, 160

OSS-MPC Optimum Switching Sequence Model Predictive Controller 57

OSV-MPC Optimum Switching Vector Model Predictive Controller 57

PCB Printed Circuit Board 160, 161

PCC Point of Common Coupling 6, 10, 90, 115, 116, 131

PE Protective Earth 38, 39

PG Pole-to-Ground 36, 37, 134–136, 146–150, 152–155, 157, 158

PLS Power Line Signaling 31

PP Pole-to-Pole 37, 134, 135, 137, 152–159, 164, 165

PV Photovoltaic iv, 11, 13, 23, 30, 31

PWM Pulse Width Modulation 58

SC Super Capacitor 11

SCC Signal Conditioning Circuit 7, 133, 134, 138, 139, 141, 143, 159–161, 164, 173

SoC State of Charge 3, 4, 29, 30, 33, 68, 69, 80, 175, 176

SPC Signal Peak Capture 7, 133, 134, 138, 139, 141–144, 155, 161–165, 170, 173

SSCB Solid-State Circuit Breaker 161

SVM Space Vector Modulation 58

VFD Variable Frequency Drives iv

VSC Voltage Source Converter 11, 14, 42

WT Wavelet Transformation 46

Chapter 1

Introduction

In recent decades, as the global population has grown, there has been an unprecedented surge in energy consumption. Unfortunately, this surge has taken a toll on conventional resources such as coal, crude oil, and natural gas, depleting them rapidly [1]. The environmental repercussions of exploiting these resources are dire, primarily due to the escalation of greenhouse gas emissions [2]. Policy frameworks addressing climate and energy challenges are aligned with the ambitious commitment to decrease greenhouse gas emissions, ultimately striving to establish a carbon-neutral energy system within the forthcoming decades. To realize this vision from the standpoint of the power grid, the achievement of such a target demands the formulation of economical strategies that effectively address the challenges of affordability, competitiveness, security of supply, and the sustainability of electric power systems entirely reliant on renewable energy sources [3].

The proliferation of Distributed Generations (DGs) within the power system has brought about fundamental shifts in control and operational paradigms. This transformation has led to the expansion and evolution of microgrids, which are now regarded as pivotal components for future smart grids. The concept of microgrids, introduced by the Consortium for Electric Reliability Technology Solutions (CERTS), aims to enhance the reliability, sustainability, and efficiency of modern power systems. These microgrids encompass a combination of DG units, distributed ESS, both sensitive and nonsensitive loads, and centralized/decentralized control systems [4]. Operating as controllable subsystems, they have

the capacity to function in either grid-connected or islanded modes.

As these innovative systems have emerged, the traditional power system is well-known issues have required a reassessment. The key issues for effective operation, control, and protection of these systems encompass integration technologies, hierarchical control methodologies, and optimization approaches that should be carefully updated [5]. The landscape now comprises AC, DC, and hybrid microgrids. Recently, DC microgrids have gained significant attention as they offer remarkable benefits compared to their traditional AC counterpart in terms of system efficiency, cost-effectiveness, and size. DC microgrids have an advantage due to their diminished dependency on power electronic converters, leading to an overall enhancement in efficiency. Moreover, the absence of a transformer requirement for AC/DC converters significantly reduces the physical footprint of DC microgrids [6]. Furthermore, the majority of available ESS inherently operate on a DC basis, while the increasing adoption of EVs represents a demanding challenge in DC power [7]. Similar to the AC microgrid, an energy management system is required with the DC microgrid as well. However, there is only a need for voltage stabilization. Compared to an AC microgrid, support for frequency stabilization is not required in the case of a DC microgrid. Consequently, strong arguments indicate that implementing DC microgrids is simpler, more reliable, and more efficient.

1.1 Motivation and Challenges

Despite the conceptual simplicity of DC microgrids compared to AC microgrids, they are often perceived as a forward-looking concept requiring advancements across various technical domains. While theoretical advantages of DC microgrids have been substantiated through calculations, analysis, and simulations, the subsequent imperative involves the execution of practical DC microgrid demonstration projects to validate these concepts under real-world conditions.

The advancement toward larger and more comprehensive demonstration endeavors is now being propelled by governmental support, predominantly in Europe and North America. However, developers undertaking the construction of DC microgrid demonstrations

encounter a series of challenges, including:

- Necessity for custom-made Industrial power electronics equipment integrating controls and communication features specific to DC microgrids, demanding extensive research and development efforts, thereby escalating costs and project timelines.
- The need to develop robust hierarchical control structures that can link all the integrated agents that are suitable for various network configurations in the presence of increasing trends of the installed intermittent energy sources, ensuring economic, secure supply, reliable, and expandable operation of the microgrid network.
- The need for secure communication infrastructure for data exchange through the network nodes as well as microgrid clusters, providing resiliency against various cyber threats and communication failures, which ensure reliable and stable operation of the network, while facilitating plug and play operation of DG units and the implementation of smart grids.
- A kind of smart management system is required for handling the local integrated storage devices, intermittent renewable sources, and transient loads, while maintaining a global voltage balancing and proportional load sharing among all the network buses, ensuring stable operation of the network while maximizing the lifetime of the integrated storage devices through the real-time monitoring of the State of Charge (SoC) and charging/discharging cycles.
- Uncertainties regarding requisite protections for DC systems and the lack of protection devices specifically designed for DC setups. Due to the DC power nature, the protection system has to ensure effective, selective, and safe operation during normal and fault conditions considering various grounding schemes of the microgrid.
- A wide spectrum of ratings and specifications, compounded by uncoordinated efforts instead of collaborative endeavors, could expedite practical DC microgrid implementations. This stems from the independent conception and design of DC microgrids by disparate academic and industrial groups, characterized by minimal cooperation among them.

- Resistance from local authorities to approve DC installations due to limited familiarity with this project type and the absence of established safety code references.

1.2 Objectives

This research work aims to improve DC microgrids in terms of operation and protection basis towards the implementation of smart microgrids by addressing the aforementioned challenges. The research objectives can be listed as follows:

- Developing a primary control layer that can handle the local transient loading and the high intermittent power profiles of the renewable DGs while ensuring safe and extended life operation of the integrated ESS through real-time monitoring of the rate of charging/discharging and the SoC levels. For the sake of developing the literature Model Predictive Control (MPC) based control systems as a primary controller, An IAMPC is proposed as a primary controller in a hierarchical multi-layer smart control structure. Unlike conventional Continuous Control Set Model Predictive Controller (CCS-MPC), an improved convergence speed IAMPC is proposed that can handle non-linear systems effectively in real time especially for relatively long prediction horizons, while considering dynamic equality and inequality constraints. Moreover, IAMPC has a high level of robustness against parameters variation and system degradation. The controller performance is investigated with the help of the CasADi online optimization platform.

- Developing a secondary control layer that can be used for any network configuration and incorporates the capability of exchanging nodes data through communication infrastructure while ensuring a global voltage regulation of all network clusters and proportional power sharing for all generating units. A cooperative distributed consensus-based secondary control strategy is proposed as a second control layer in the hierarchical control system structure. Unlike conventional consensus-based controllers initially developed in 2014 [8], the proposed controller has the ability to work under limited communication infrastructures with limited available data.

Moreover, the proposed controller is equipped with a state estimation layer based on Moving Horizon Estimation (MHE) algorithm that improves the control system resiliency against various cyber threats and transducer uncertainties. Furthermore, the knowledge of the network line parameters is not required, which facilitates the plug-and-play operation. The proposed system also has a bounded operation of voltage balancing through dynamic objective relaxation. A robustness and resiliency assessment of the proposed controller is carried out through different operational scenarios including power line outage, communication line failure, presence of measurement uncertainties or cyber threats, and plug-in of generating units.

- Introducing a novel protection system for DC microgrids for detecting, identifying, locating, and isolating various faults. The proposed system incorporates multi-protection coordinated circuits ensuring optimum sensitivity and selectivity for a wide range of bolted faults and high-resistance faults. Unlike the majority of the literature on DC microgrid protection systems, the proposed protection system takes into account the effects of the fault resistance, DC link capacitor dynamics, grounding configuration, and grounding resistance. Moreover, the proposed system has the ability to detect both faults under high-frequency variable oscillation, especially for bolted faults, and damped currents of high resistance faults within a time frame of microseconds.

1.3 Outline of the Thesis

The remainder of this thesis is organized as follows:

Chapter 2 presents a thorough literature review of the concept of microgrids and their types. Then a comparison between DC and AC microgrids is carried out in terms of the system architectures and challenges facing both configurations. Then, the literature control systems for DC microgrids are investigated including centralized, decentralized, and distributed schemes. Additionally, the cyber security challenges in microgrids have been highlighted. Finally, the protection challenges in DC microgrids are illustrated and the literature protection schemes are investigated. The

grounding configurations are also discussed and their effects on various network faults are described.

Chapter 3 provides firstly, a detailed review of MPC based controllers including Finite Control Set Model Predictive Controller (FCS-MPC) and CCS-MPC that are used for DC microgrid applications. Then a high-speed convergence, continuous control set MPC-based controller called Improved Adaptive Model Predictive Controller (IAMPC) is proposed. This control system ensures a coordinated operation of the ESS and DGs connected locally. IAMPC provides an extended lifetime, safe operation, and effective protection of the connected ESS. Due to the short convergence time, the proposed IAMPC has a fast dynamic operation that can handle highly intermittent generation profiles while meeting the reference trajectory from the secondary control layer. The proposed IAMPC has a high level of robustness against model parameters' wide variations, and hence accurate system parameters setting is not necessary and long-term degradation effects of the system parameters have no effect on system performance.

Chapter 4 reviews distributed controllers for DC microgrids. Then a cooperative distributed consensus-based strategy is proposed which is used for proportional load sharing and global voltage balancing objectives in DC microgrids. This control strategy operates at reduced communication requirements which can effectively reduce the risk of cyber threats while facilitating the integration of DGs to the microgrid. Moreover, the strategy incorporates a state estimation layer that utilizes MHE algorithm for mitigation of cyber threats and system uncertainties, which effectively improves the distributed control resiliency. The proposed control strategy only relies on measurements of generated currents, without the need for knowledge of the Point of Common Coupling (PCC) voltages or the microgrid parameters. The effectiveness of the controller is demonstrated in that the microgrid objectives can converge to the desired steady state values regardless of the initial conditions of the physical system or the controller state. Five case studies are carried out to investigate the robustness and resiliency of the proposed control strategy against various contingency conditions and cyber threats.

Chapter 5 proposes a novel protection relay system that can detect, identify, locate, and isolate various fault conditions in DC microgrids. It consists of two elements: directional and distance elements for optimum identification and locating faults. Both elements are achieved by integrating a sensing inductor at both positive and negative poles of the power line connecting the network DC buses. By effectively capturing three local measurements: relay inductor voltage, relay terminal voltage, and the relay inductor current, the fault location is accurately determined. The design and consideration of the relay inductor are deeply described, while the effect of the fault types, fault resistance, grounding configuration, and grounding resistance are investigated. The proposed protection system incorporates SCC and SPC units for accurately capturing the relay measurements at the fault instance for both bolted faults and resistance faults. The proposed protection system has the ability to clear faults in the time frame of microseconds.

Chapter 6 provides the conclusion of the thesis. It also articulates the platform for future research work.

Chapter 2

Background and Literature Review

2.1 Introduction

With the rapid growth of the world economy due to the industrial revolution, the increasing consumption of fossil fuels caused severe environmental negative impacts [9, 10]. On the other hand, the worldwide response to COVID-19 and associated lockdowns inadvertently led to a reduction in economic activity, which unintentionally helped achieve goals for limiting climate change [11] with negative growth rates of all fossil fuels for the first recession in history and global oil demand dropping by nearly 10%. However, unless policymakers take swift action, this progress will be reversed back again. The use of renewable energy sources as a share of electricity generation also rapidly increased [12]. Renewable energy sources are becoming integrated into power networks to meet the fast-growing energy demand and address environmental concerns caused by conventional energy sources. However, this integration can result in new challenges, such as security of supply, baseload energy capacity, and seasonal effects, particularly in aging electrical grids [13]. Recent advancements in microgrid technology, utilizing renewable energy sources and smart grids, have proven to offer higher reliability and efficiency in a cost-effective manner [14]. Additionally, utilizing Direct Current (DC) distribution in microgrid systems can further improve the reliability and efficiency of electrical grids. DC microgrid technology is attractive due to its natural interface with renewable energy sources, electric loads, and energy storage systems. With

the increase in research work in this area, the practical implementation of DC microgrid technology is becoming more feasible [6].

2.2 Microgrid definition and capabilities

Power generation is undergoing significant changes due to regulations and technological advancements. These changes, along with economic and environmental incentives, have created new possibilities for generating electricity on-site [15, 16]. Smaller-scale power systems, such as microturbines, solar panels, and wind turbines, have become viable options for electricity users. This kind of DG offers a promising solution to meet the growing demand for electric and thermal energy [17, 18]. Their focus is on ensuring reliability and maintaining high power quality standards. A microgrid is a fundamental component of the evolving smart grid infrastructure. It refers to a network comprising low voltage power generation units, energy storage devices, and loads [19, 20]. Unlike traditional grids, which are centralized systems managed by a utility company, a microgrid can operate in a decentralized fashion and can function autonomously [21–23]. It integrates various DGs with different technologies and capacities to generate and distribute electricity within its boundaries. Microgrid implementations are expected to enhance power quality, lower emissions, alleviate network congestion, reduce power losses, improve energy efficiency, and potentially enhance the economic viability of the system. Additionally, microgrids have the potential to eliminate the need for additional investments in generation and transmission infrastructure to cater to remote loads. Furthermore, the ability of microgrids to operate autonomously during faults or disturbances in the main grid can significantly enhance both the reliability and resilience of the grid for both the utility and customers [5, 24–26].

2.3 DC microgrids vs AC microgrids

2.3.1 System Architecture

DC microgrids utilize DC current for the distribution of electricity through the microgrid network. DC-DC converters are used to integrate different DC DGs, DC ESS, and DC loads to the microgrid buses, while DC-AC converters are used to feed the AC loads, and AC-DC converters are used to integrate AC DGs or linking the network to the utility grid. The general architecture of a DC microgrid is illustrated in Fig. 2.1. The utility grid can be connected to the network through a DC-AC converter and a transformer at the PCC which depends on the DC network operating voltage level [27–29].

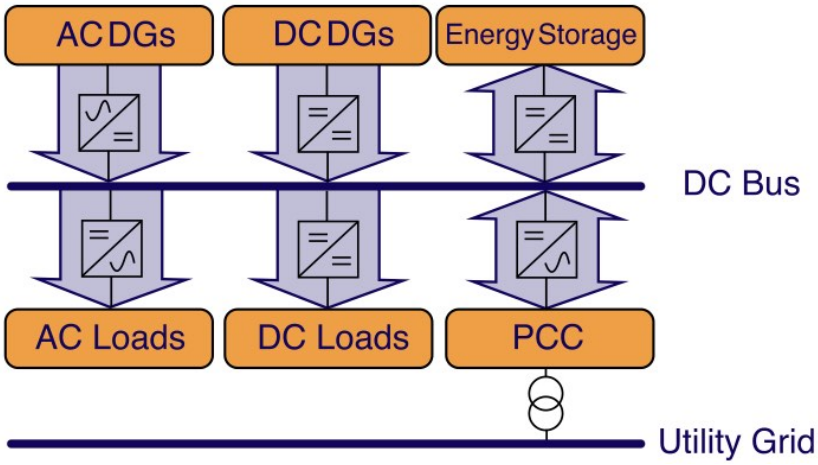

Figure 2.1: DC Microgrid general architecture

On the other hand, Alternating Current (AC) microgrids operate on AC current which follow the standards of conventional AC distribution systems [30, 31]. AC loads, DGs, and ESS are directly connected to the AC buses or through transformers, while the DC loads are fed through rectification converters and DC DGs and ESS are connected to the network through DC-AC converters. Fig. 2.2 represents the general architecture of an AC microgrid.

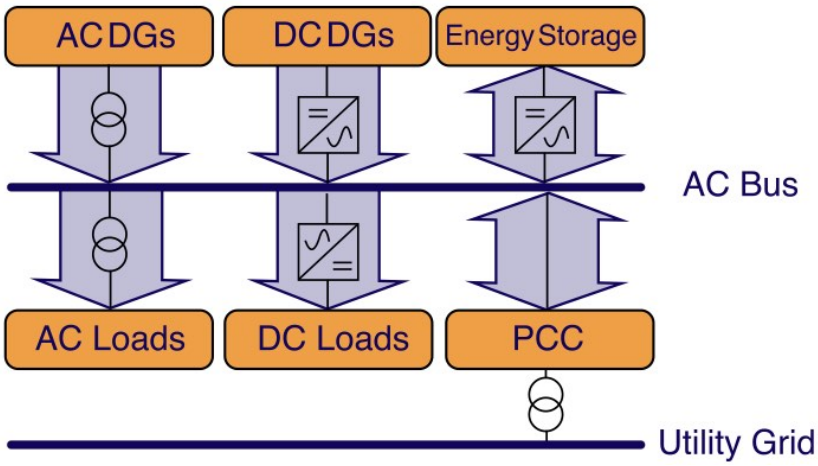

Figure 2.2: AC Microgrid general architecture

2.3.2 Integration of Renewable Energy Sources and Energy Storage Devices

Due to the increasing utilization of DC renewable energy sources such as solar PV panels and Fuel Cell (FC)s, DC ESS as batteries and Super Capacitor (SC), and DC loads like EVs, DC microgrids have been gaining more importance as these sources inherently generate DC power. DC microgrids can directly connect and utilize the output of these sources without the need for additional power conversion stages. However, for AC microgrid counterparts, the integration typically requires additional power conditioning converters like Voltage Source Converter (VSC) for converting the generated DC power to AC for compatibility with the AC network [32].

2.3.3 Control Systems

DC systems offer enhanced controllability and stability due to their simpler control schemes and reduced complexity as compared to AC microgrids. Unlike conventional AC grids, DC microgrids do not have inherent issues such as generating unit synchronization, harmonics, reactive power control, and frequency control [33, 34]. One important feature for DC

microgrids is that the system power balance condition is indicated by the DC bus voltages [35]. It should also noted that adequate operation of DC microgrid is still challenging, especially in the presence of DGs with intermittent nature power profile [36,37]. Moreover, ensuring a kind equal load sharing between all connected DGs and stable voltage regulation is important to ensure optimum and reliable operation of DC microgrids [38,39]

2.3.4 Power Conversion Efficiency

DC microgrid systems generally exhibit higher power conversion efficiency compared to AC systems. They have lower conversion losses since there is no need for AC-DC and DC-AC conversions for the purpose of integrating most modern DGs, ESS, and loads. Taking the loads as an example, DC power is pervasive in numerous electronic load devices commonly utilized in various work environments, including smartphones, computers, printers, and overhead lighting [40]. Beyond these applications, DC power plays a crucial role in data centers, where it supports information technology systems [41], and in variable-speed motor drives, which facilitate heating and air conditioning systems. Notably, solar panels produce native DC power, which is subsequently converted to AC power for distribution within buildings. Unfortunately, this conversion from DC to AC and back to DC for specific device use, like lighting, incurs significant energy losses, amounting to approximately 15% or more of the solar energy generated [42].

2.4 DC microgrid configurations

2.4.1 Single Bus Topology

In this basic setup, all the power supplies including DGs and ESS as well as the loads are connected to a single bus. Single bus topology is widely used for limited-size DC microgrids [43–45]. Fig. 2.3 shows the basic construction of this topology. It can be seen that DC DGs (PV Arrays) are connected to the common DC bus through a unidirectional DC-DC converter like Buck or Boost. These power-electronic converters can be controlled

to extract the maximum power from the DG like the common Maximum Power Point Tracking (MPPT) operation of PV systems.

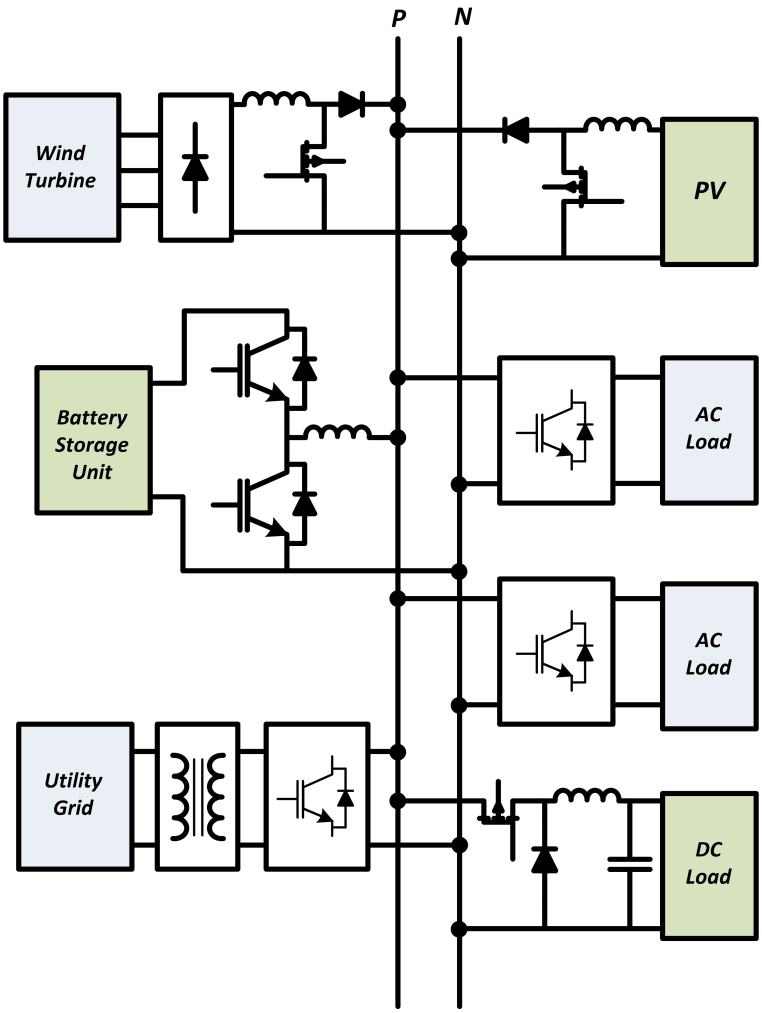

Figure 2.3: Single Bus DC microgrid configuration

For a wind turbine as an AC DG, a rectification unit is used to rectify the variable frequency, and variable voltage output of the wind generator. Then, a DC-DC converter is connected to the rectification unit output to provide a voltage regulation to integrate the DG to the DC microgrid [46]. On the other hand, the DC ESS, like battery packs, are connected to the common DC bus through a bidirectional DC-DC converter allowing dual

power flow during charging and discharging. The DC loads can be directly connected to the common bus, or through a DC-DC converter. The type of connection depends on the load-rated voltage level and/or if the load is controlled which is the case of modern dynamic load management in EVs charging application in which an optimum power distribution is maintained for all EVs that are charged simultaneously [47, 48]. The AC loads are connected to the common DC bus through a VSC which is responsible for providing a stable voltage and frequency to the AC load. Single bus configuration of DC microgrid is simple and cost-effective for small-scale applications, but it lacks redundancy and may have limitations in terms of system reliability and fault tolerance [49, 50].

2.4.2 Dual bus and bus selector

In this configuration, two redundant buses are connected to a critical load through auctioneering diodes [51]. The diode operation ensures that the bus with the higher voltage level will be switched on being forward biased to feed the critical load. Moreover, the reverse current and back feeding for the two buses are prevented. However, the current sharing between both buses is uncontrollable as the feeding currents depend only on the instantaneous voltage level of the two buses. The voltage level at each bus depends on the instantaneous operating point of the system as well as the impedance of the electronic converter typologies at each bus. To solve this issue, many literature studies were introduced. The diodes, acting as passive switches, can be replaced with an active switch like controller thyristors or DC-DC converters [49, 51]. The operation of the active switches ensures controlled load sharing among the DC buses. The load sharing for each bus can also be controlled to achieve a specific operational objective or a multi-objective operation [52]. The configuration of the dual bus and auctioneering diodes bus selector is illustrated in Fig. 2.4, while Fig. 2.5 shows the controlled bus selection through DC-DC converters.

2.4.3 Multi cluster configuration

In a multi-bus DC microgrid system, each bus is capable of exchanging energy with its neighbor group of buses known as microgrid clusters. These multi-bus configurations can

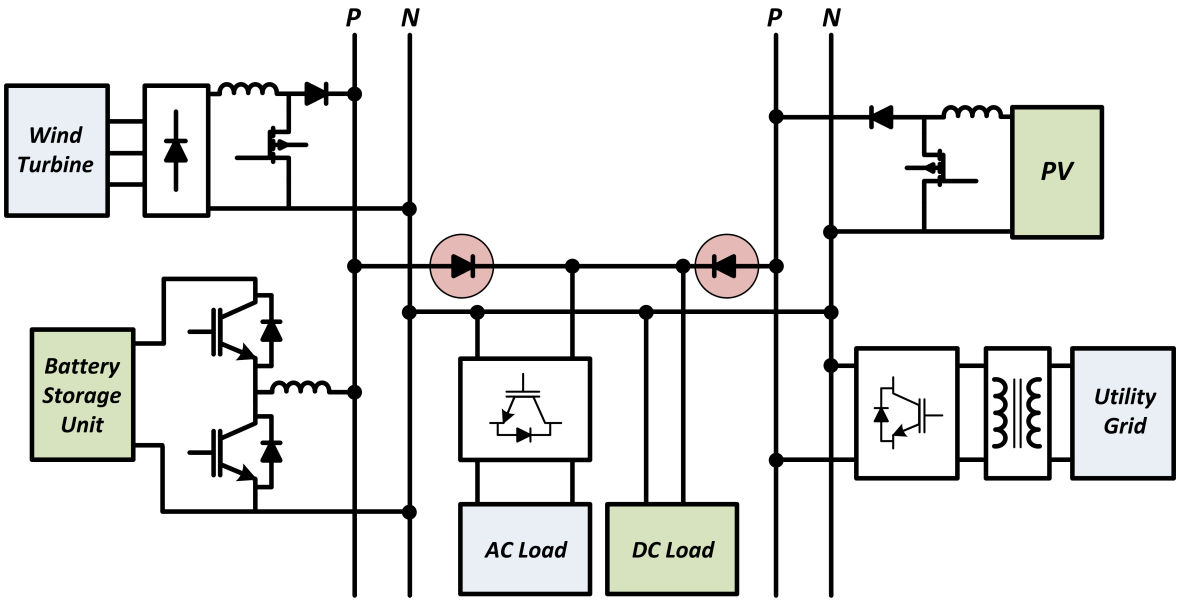

Figure 2.4: Dual Bus Diode Bus Selector Configuration

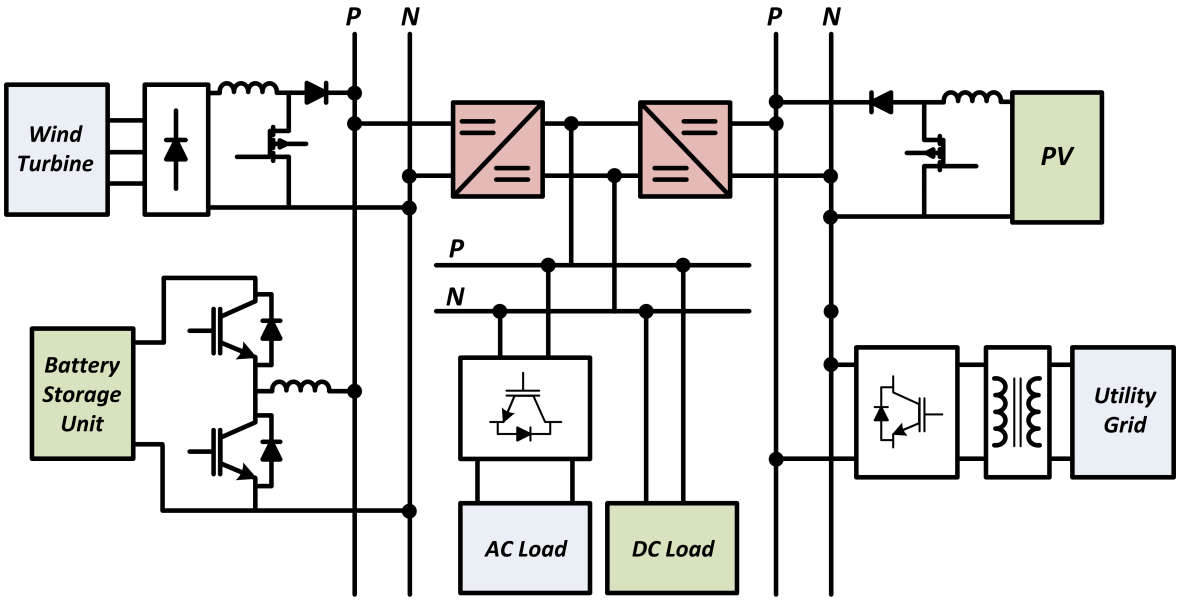

Figure 2.5: Dual Bus-DC-DC Converter Bus Selector Configuration

be organized in series [50] or parallel arrangements [53] as shown in Fig. 2.6 and 2.7 respectively. These configurations can be considered as an expanded version of radial system topology which provides a higher reliability level [54]. Moreover, these configurations have an inherent feature for isolating the faulty sections and/or buses [55, 56].

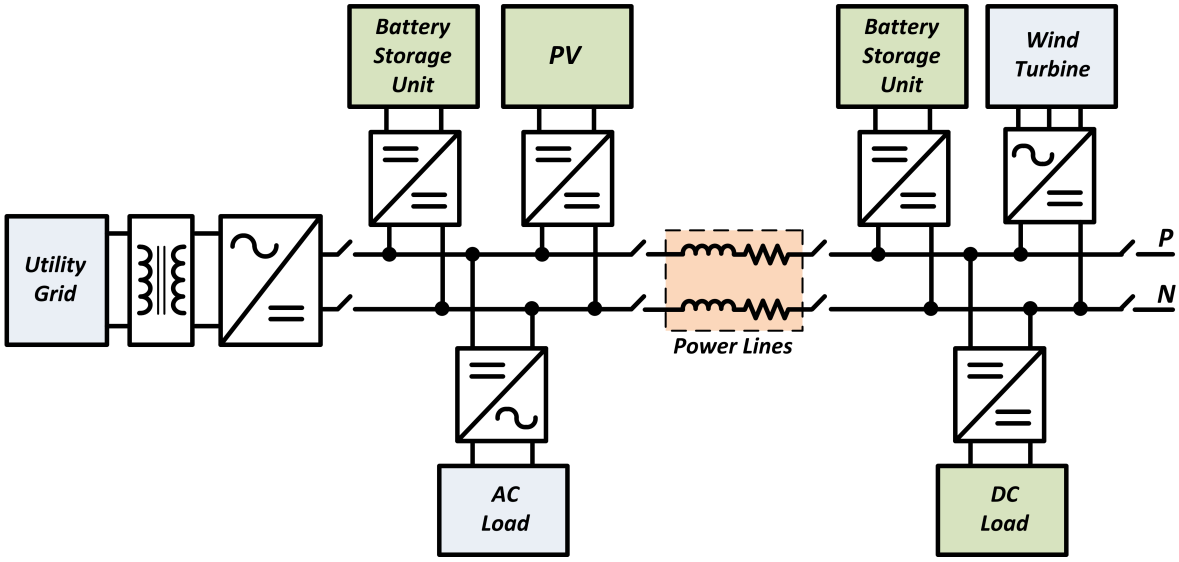

Figure 2.6: Series Multi Bus Configuration

2.4.4 Ring configuration

To enhance flexibility and improve fault management beyond the limitations of a radial bus topology, a loop or ring-type distribution system can be implemented. The fundamental concept of the ring-type topology is illustrated in Fig. 2.8. This approach involves the interconnecting generation, storage, and load units along a single ring, and protection switches are strategically placed before and after each bus on the ring for safety purposes. As a result, each component within the system has two possible ways to connect or disconnect from the ring, providing redundancy along the line on each bus side. This configuration performance can even improved if there is a communication infrastructure that facilitates communication channels between the ring buses and a centralized controller [57]. This can ensure prompt detection of faults, isolation of the faulty bus, and establishing

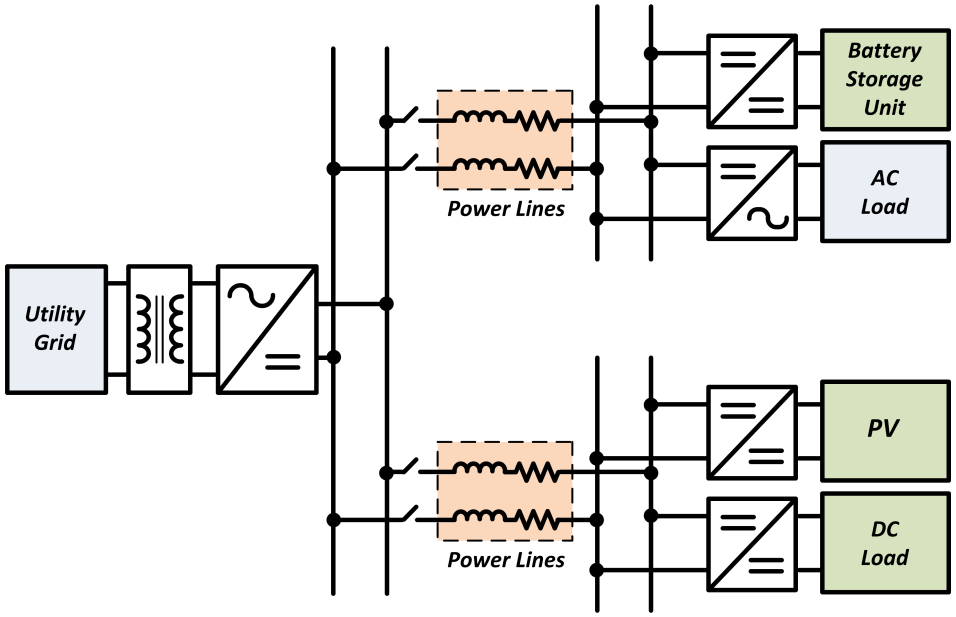

Figure 2.7: Parallel Multi Bus Configuration

an alternative route for supplying power to consumers. This type of supply system has been effectively deployed in cities and industrial settings. Compared to the radial topology, the ring topology offers higher dependability and flexibility. In the event of a fault, the corresponding switches isolate the faulty section, allowing all other units to continue functioning normally. The ring topology's inherent flexibility provides the DC microgrid with remarkable resiliency, reliability, and redundant operation [58].

2.4.5 Ladder configuration

The ladder bus structure is based on the concept of a ring bus structure. Distributed generation sources' output is connected to the rings of this laddered DC structure. Subsequently, these rings are linked to two buses, each capable of supplying DC power to other rings of the ladder. This design significantly enhances system redundancy. Fig. 2.9 illustrates a typical ladder structure. Compared to other systems, the ladder bus DCMG exhibits the highest level of redundancy, enabling it to effectively eliminate single points

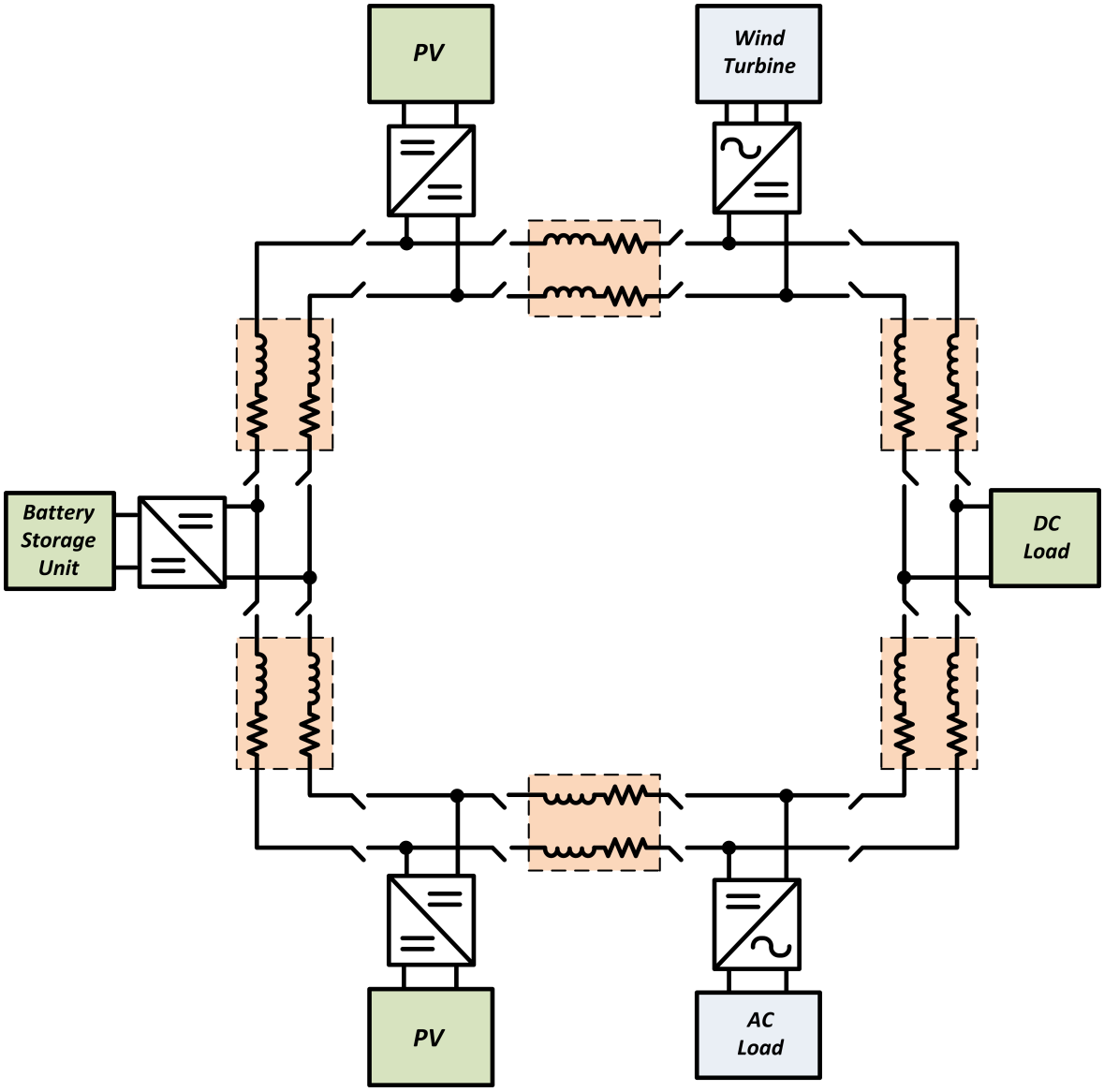

Figure 2.8: Ring Configuration

of failure and open circuit faults, leading to exceptional system availability [59]. Moreover, its scalability is excellent, allowing for the seamless addition of distributed sources without affecting other parts of the system [60]. Due to its numerous advantages such as high availability, scalability, and reliability, along with being free from open circuit faults,

the ladder configuration is increasingly becoming the preferred choice for modern systems, including electric ships, data centers, and telecom appliances [53].

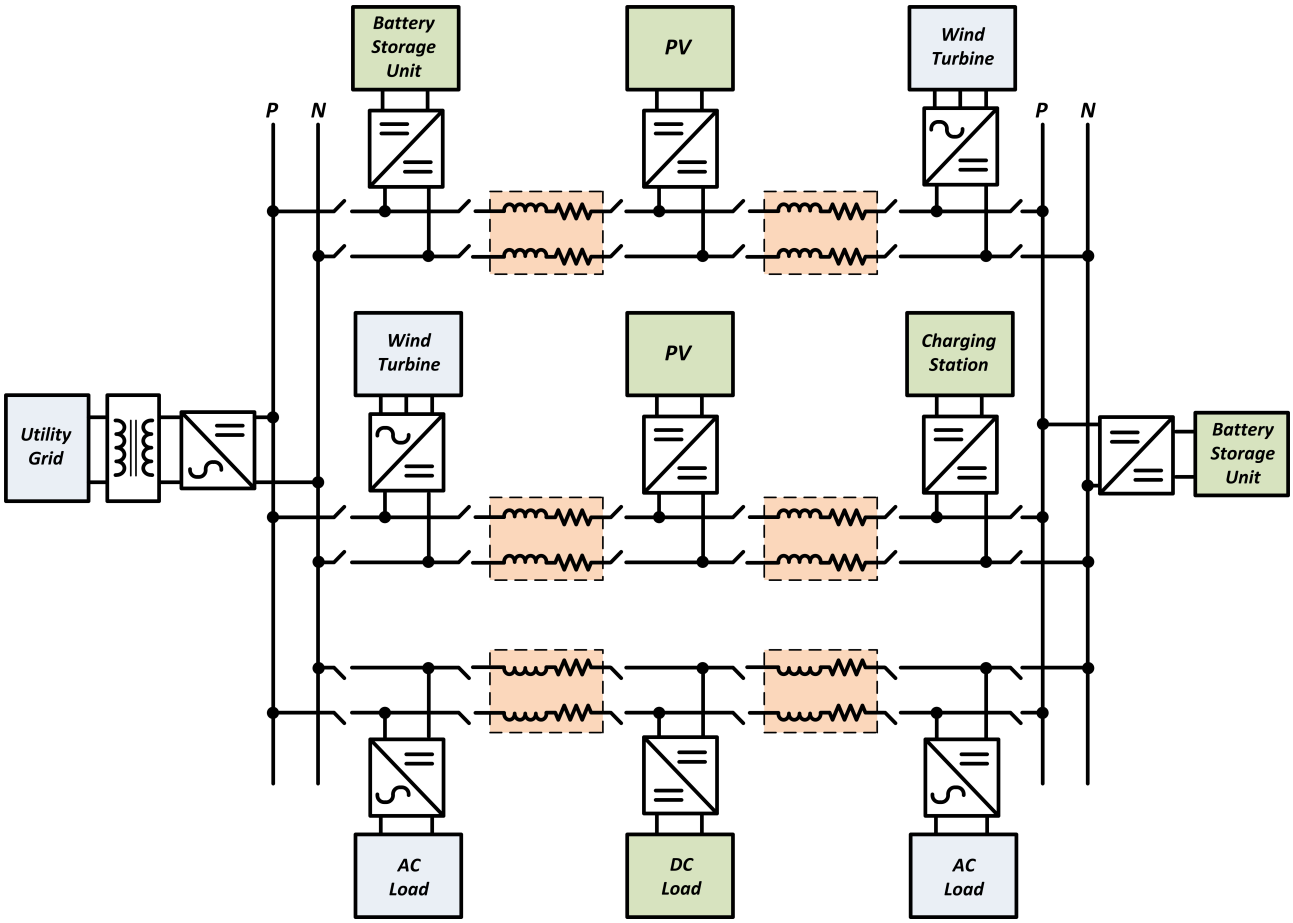

Figure 2.9: Ladder Configuration

2.5 DC Microgrid Supply Polarity

2.5.1 Unipolar configuration

In a unipolar configuration of DC microgrids, the power distribution system operates with a single polarity, either positive or negative. In this setup, all the power sources, energy

storage devices, and loads are connected in parallel, sharing the same polarity. This configuration simplifies the system design and reduces the complexity of power electronics converters and control algorithms [61]. One of the key advantages of the unipolar configuration is its ease of implementation. The absence of a neutral line simplifies the overall system architecture and reduces the number of components required for power conversion and control. This leads to cost savings and potentially higher overall system efficiency. However, the unipolar configuration also poses some challenges. Since all power sources and loads share the same polarity, careful management of voltage levels and current balancing is necessary to prevent any voltage or current imbalances within the system [62]. Special attention should be given to monitoring and control mechanisms to ensure proper voltage regulation and equal distribution of power among the sources and loads.

2.5.2 Bipolar configuration

In a bipolar configuration of DC microgrids, the power distribution system employs both positive and negative polarities. This setup allows for a more flexible power flow and accommodates a wider range of power sources and loads. In this configuration, the power sources and loads are connected in series with a neutral line or center-tapped bus, forming a bipolar distribution system [63]. The bipolar configuration offers several advantages. Firstly, it enables the integration of both unipolar and bipolar devices and facilitates the connection of different types of power sources and loads, including those designed for unipolar systems. Secondly, the use of a neutral line allows for better voltage balancing and improved control of the system, resulting in enhanced power quality and efficiency. Additionally, the bipolar configuration provides increased fault tolerance as it allows for fault isolation in one polarity without affecting the other. On the downside, the bipolar configuration introduces additional complexity compared to the unipolar configuration [64]. The presence of a neutral line requires additional components, such as center-tapped transformers or additional power converters, increasing the system's cost and complexity. The management of voltage levels and control algorithms becomes more intricate due to the need to balance power flows in both polarities.

2.6 DC Microgrid Control Systems and Challenges

To ensure the well-organized operation and stability of a DC microgrid system, a robust control strategy is essential, especially in the presence of various DGs, and ESS with different technologies and capacities. The power-electronic converters are controlled such that the optimum overall operation is achieved for the entire microgrid. This optimum operation includes proper load sharing and harmonized interconnections among various units within the DC microgrid. Moreover, for microgrids with complicated interconnection architecture, it is crucial to achieve flexible voltage regulation, precise current control, and effective power sharing between all connected DGs and storage devices [65]. The control structures have grown significantly due to the increased utilization of non-linear generation sources and loads [66]. The main basic objectives of DC microgrid control can be summarized as follows [59, 67, 68]:

- Effective current control for optimum load sharing among all connected generating/ storage units.
- Bus Voltage regulation for the network buses ensuring a global voltage balancing.
- Management of the integrated DGs and the Energy Storage Unit (ESU) with different capacities and technologies, ensuring optimum and safe operation.
- For control systems that involve communication channels, resiliency against communication link failure and cyber threats has to be maintained.

By accomplishing these objectives through control strategies, optimizing the performance and overall efficiency of the DC microgrid system, enabling it to effectively handle varying generation and load conditions can be achieved. The control system schemes can be divided into three main categories which are described in the following subsections.

2.6.1 Centralized Control

In a centralized control, each source is controlled through a single-point central controller and a communication link. The control structure can be easily implemented as the central

controller is aware of the status of each node (bus) of the DC microgrid [69].

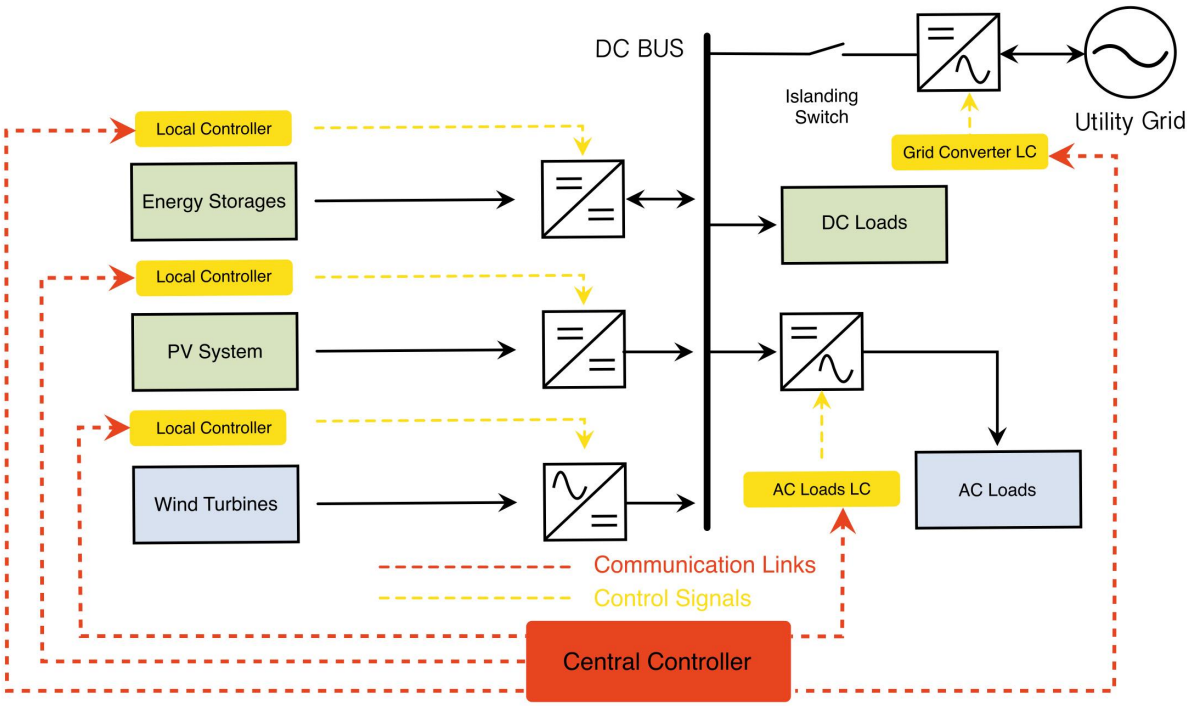

Figure 2.10: Centralized Control Operation

However, the reliability of the system is degraded as the control system depends on the communication link and the central controller for optimum operation. In other words, if the communication link fails, the centralized control approach may not properly operate during the failure period of the communication link [50]. In the centralized control approach, data from distributed units are collected by the centralized aggregator, and then processed, and feedback commands are sent back to the distributed units through communication links [70].

2.6.1.1 Master-Slave Control

One of the most common centralized controllers is the master-slave control [71–73]. In this control strategy, there is one master node in which the integrated power converter

is commonly responsible for maintaining the microgrid voltage level, while other slave converters operate as power or current regulators [74]. For example, a PV base DG is usually operating at Maximum Power Point (MPP).

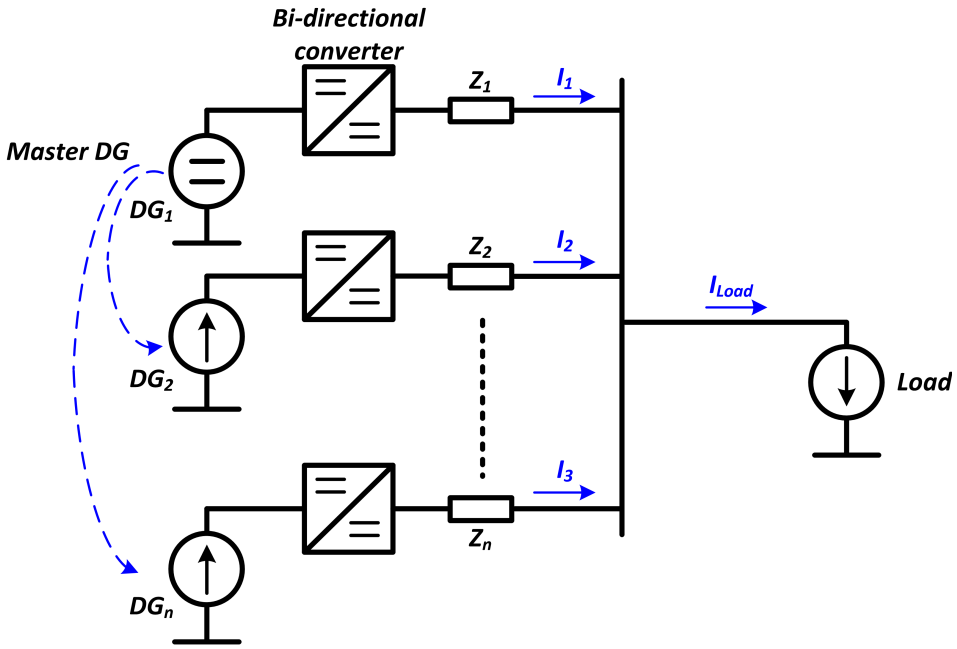

Figure 2.11: Master-Slave Control Configuration

The master DG usually has the highest power capacity as compared to the other slave DGs, and it should be equipped with a bi-directional converter to enable delivering and absorbing power for maintaining a stable bus voltage. The basic configuration of the master-slave control strategy is illustrated in Fig. 2.11. One downside of master-slave control is that the master converter has to be active all over the time. If there is a fault or maintenance for the master converter, the microgrid has to be shut down entirely, or the microgrid operation can switch to another master DG, but that needs more communication infrastructure. On the other hand, the communication channels should have high bandwidth and be securely protected. Any communication delays or cyber-threats may lead to a full shutdown of the microgrid [67].

2.6.2 Decentralized Control

In decentralized control, each source operates independently using terminal measured quantities and hence the inherent reliability in the structure of a microgrid is maintained [75–77]. However, implementing a control law to operate the system in an optimal fashion is impossible, as each node doesn't have any kind of knowledge of the other nodes in the system [78]. This is because there are no communication links between the microgrid nodes, and power lines are only the channel of indirect communication. In the following subsections, the common decentralized controllers are illustrated.

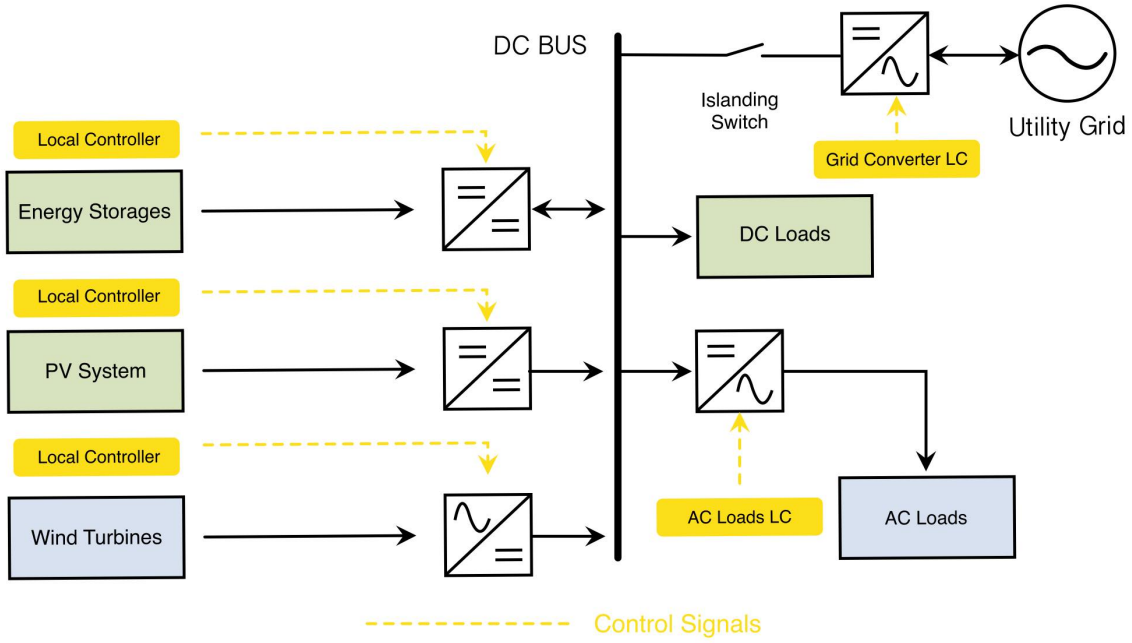

Figure 2.12: Decentralized Control Operation

2.6.2.1 Droop Control

For DC microgrids, the conventional droop control has a different concept than the AC networks. The DC microgrid drop controller sets a direct relationship between a DC

bus reference voltage and the total generated current at this bus [79, 80]. The equation governing the conventional droop control in a DC microgrid can be represented as:

$$v_{DCn} = v^*_{DC} - i_{DCn} R_{DCn} \tag{2.1}$$

where v_{DCn} is the output voltage for each converter, v^*_{DC} is the reference DC bus voltage, i_{DCn} is the generated current, and R_{DCn} is the droop coefficient.

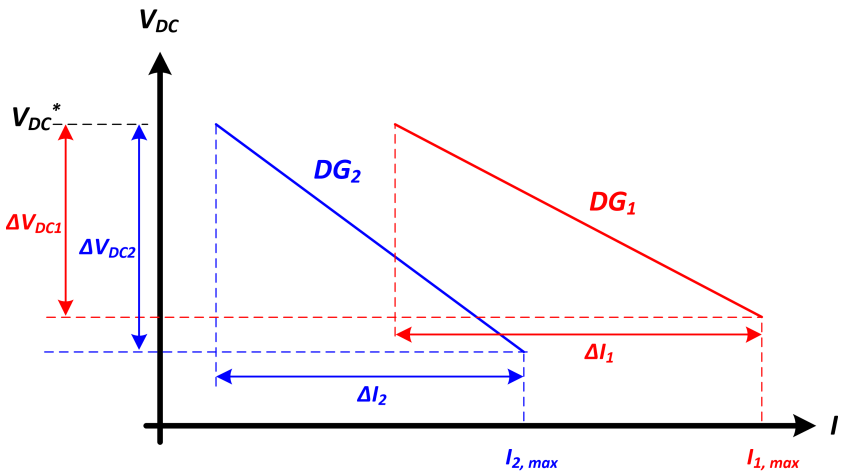

Figure 2.13: Conventional Droop Control

The major drawback of the droop controller is that the droop slop is different for each DG, and hence the voltage regulation for each DG has different performance [81]. Similarly, the load sharing depends on the slop of the droop, and the performance of each DG may be different. In other words, the conventional drop control degrades current sharing and voltage regulation accuracy due to unequal voltage drop across line resistances [82]. Fig. 2.13 illustrates a droop control for two generating units. It can be seen that, based on the droop slops of the generating units, DG1 has a better bus voltage regulation while DG2 has better load sharing. Having a good voltage regulation will experience poor load sharing and vice versa. Small droop characteristics give less voltage deviation between multiple converters but lead to large differences in current sharing. In contrast, large droop characteristics give improved load sharing but lead to large voltage deviations.

2.6.2.2 Virtual Resistance-based Droop Control

By generating a P amount of power at a specific node, when it reaches the other node it will be deducted due to the power loss in the lines, while the current flowing in each line is usually unknown. This issue affects the load-sharing process dramatically. In the virtual resistance-based technique, better power sharing can be achieved by including the effect of power line resistances [83]. To overcome the effect of power line resistance, a virtual resistance is considered in the feedback path [84] and hence, the droop voltage equation can be represented as:

$$v_{DCn} = v^* + \delta v_o - i_o R_v \tag{2.2}$$

where δv_o is the compensator correction factor required for restoring the microgrid voltage, which is usually implemented in the secondary control layer, i_o is the converter output current, R_v is the virtual droop resistance, and v^* is the output reference voltage.

2.6.2.3 Adaptive Droop Control

In this control technique, the droop coefficient is corrected [85, 86] or determined [87] in real time to achieve the optimum slop of the droop controller corresponding to the required objectives. The general construction of this technique can be expressed as follows:

$$v_{DCn} = v^* - i_o R_{droop}(v, i_o, P_{Loss}, SoC, ..etc) \pm \Delta v \tag{2.3}$$

where Δv is a shifting factor that is usually used to improve the voltage regulation performance [88, 89], R_{droop} is the adaptive droop coefficient, and v_{DCn} is the updated droop voltage reference set point. The graphical representation of this control technique is illustrated in Fig. 2.14. In [87], a performance metric called Droop Index (DI) is introduced to determine the optimum droop coefficient for two objectives, minimizing the circulating current and power loss for two parallel connected converters. This performance metric is a function of the difference in normalized current sharing and power loss. For two parallel converters' operation, the DI can be expressed as [87]:

$$DI = min[\frac{1}{2}[|I_1 - I_2|_{N_i} + (P_{Loss})_{N_P}]] \tag{2.4}$$

where I_1 and I_2 are the converters' currents, P_{Loss} is the output power loss of the converter, N_i stands for normalization of the difference in current sharing to the rated load current, and N_p is normalization of the output power loss to the maximum allowable losses based on the converter rated power. The values of the droop resistances are calculated

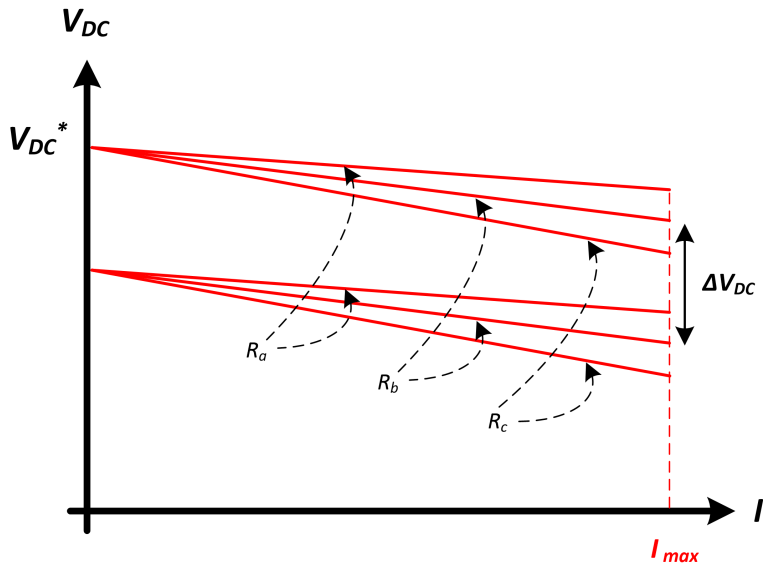

Figure 2.14: Adaptive Droop Control

to achieve the minimum value of the DI. This requires the full knowledge of bus voltages, generated currents, and power line resistance. Moreover, the ratio of droop coefficients for the generating units is assumed to be proportional to the resistances of cables connecting the converters to the common load. As a result, this method is not feasible for mesh DC microgrid configuration in which different length power lines may exist. In [89], the current sharing of the same network configuration is determined based on the local droop coefficient and the connected cable resistances to the load bus, while the effective local droop resistance is adaptively adjusted using an additional adaptive factor. This correction factor is determined based on the voltage deviation between the parallel connected converters.

This can be expressed for two parallel converters' operation as:

$$\begin{aligned}
&\text{if } V_{dc1} > V_{dc2} \begin{cases} R'_{d1} = R_{d1} + \Delta R \\ R'_{d2} = R_{d2} - \Delta R \end{cases} \\
&\text{if } V_{dc1} < V_{dc2} \begin{cases} R'_{d1} = R_{d1} - \Delta R \\ R'_{d2} = R_{d2} + \Delta R \end{cases} \\
&\text{if } V_{dc1} = V_{dc2} \begin{cases} R'_{d1} = R_{d1} \\ R'_{d2} = R_{d2} \end{cases}
\end{aligned} \tag{2.5}$$

where V_{dc1} and V_{dc2} are the converter output voltages, R_{d1} and R_{d2} are the initial droop coefficients, R'_{d1} and R'_{d2} are the adjusted droop coefficients, and ΔR is the adaptive droop factor. The adaptive droop coefficient is determined as the average of the initial droop coefficients which can be represented as [89]:

$$\Delta R = \frac{R_{d1} + R_{d2}}{2}, \qquad R_{di}^{max} = \frac{\Delta V_{dc}^{max}}{I_{o,i}^{max}} \quad \forall i = \{1, 2\} \tag{2.6}$$

where V_{dc}^{max} is the maximum allowable deviation range, which is assumed to be $\pm 10\%$ of the load bus voltage [90], while $I_{o,i}^{max}$ is the maximum current capacity of the i_{th} converter. A second outer control loop is established to maintain the remote load bus voltage within an acceptable range. Hence, a voltage shifting correction factor is added to the droop voltage reference. This voltage shifting correction output can be expressed as an output of PI controller as [88]:

$$\Delta V_{shift} = K_{P,i}(V^{ref} - V_{Bus}) + K_{I,i} \int (V^{ref} - V_{Bus}) \quad \forall i = \{1, 2\} \tag{2.7}$$

The same network configuration is used in [81], however, the drop coefficient has two additive values as follows:

$$R_{droop,i} = R_{di0} + R_{Vi} + R_{Ii} \tag{2.8}$$

where R_{di0} is the initial droop coefficient value, R_{Vi} is the adaptive droop component for bus voltage restoration, and R_{Ii} is the adaptive droop component for current sharing control. The values of R_{Ii} and R_{Vi} are determined in a secondary control layer that has the information of the other agent generating current.

For integrating multiple ESU, other constraints should be taken into account such as the SoC and rate of charging/discharging [91–94]. For multiple distributed storage, a SoC balancing for all connected ESU to avoid overcharging/discharging of single ESU [95].

2.6.2.4 Intelligent Technique-based Droop Control

In this technique, the virtual resistance for each generating unit is changed using the intelligent method to achieve the system objectives, while maintaining minimum voltage deviation. The general structure of this technique is illustrated in Fig. 2.15. The error voltage signal is fed to the controller as well as other local system measurements corresponding to the required objective, while the output parameter is the optimum droop coefficient. In [96], a fuzzy logic-based control strategy is used to change the virtual resistance depending on the SoC of the connected ESS. The adjustment of the fuzzy logic into

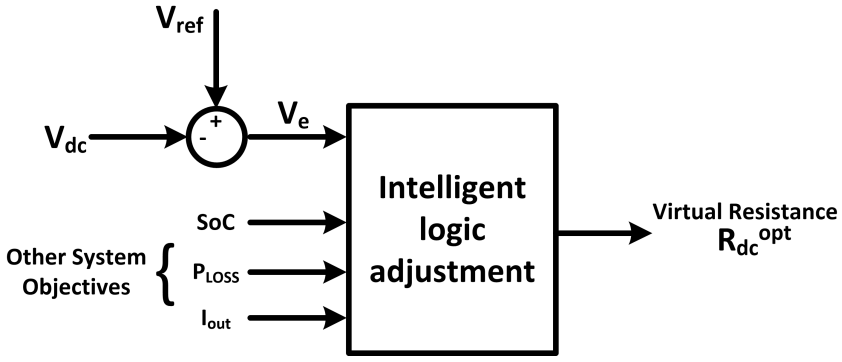

Figure 2.15: Intelligent Technique-based Droop Control

the droop coefficient reduces voltage deviations in the DC bus and ensures a balance of the stored energy in multiple storage units. The SoC of generating units as well as the voltage errors are the input to the fuzzy controller, while the output is the corresponding virtual resistance. Although this technique maintains low voltage deviations, while balancing the SoC of connected generating units, the power-sharing is not optimally guaranteed. Moreover, generating unit converters are assumed to be connected in a single bus, disregarding the power line parameters in mesh DC grid configuration.

2.6.2.5 Mode Adaptive Droop Control

In this method, the droop line is divided into multi-segments with different droop coefficients [35]. This strategy is optimum for coordination between DGs and ESS. This method has been used in literature. However, it has some limitations. Having full control of the load sharing while maintaining a stable bus voltage is challenging. In [35] there is no direct load sharing control, only bus regulations. Moreover, the power line parameters for each connected generating unit are assumed to be identical resulting in identical slops of all distributed droop controllers. Having different different lengths of power lines results in a different performance for each droop controller. In [97], cable resistance for each connected generating unit (Energy storage unit or Renewable generation unit), the microgrid structure is assumed to be a single bus in which all units are participating to regulate the voltage of this single bus according to the SoC level of the storage units in an islanded dc microgrid.

2.6.2.6 DC Bus Signalling

The DC Bus Signaling (DBS) method is widely used for decentralized coordination in DC microgrids, enabling coordinated operation among various DG technologies. This is accomplished by detecting changes in the common DC bus voltage [98]. Fig. 2.16 illustrates the DBS principle, which comprises three operating modes. Each mode involves different combinations of PV, ESU, and ac grid interfacing converters. The figure shows that the units are either current sources/sinks or represented by Thevenin equivalent circuits, depending on their internal mode of operation [99]. The Thevenin circuit is used to indicate when a unit is in droop control mode. The voltage source serves as a reference voltage, while the series impedance functions as a virtual impedance. The shifts between modes are initiated by preset DC bus voltage values.

2.6.2.7 Power Line Signalling

A carrier communication signals of a specific frequency are injected into the DC bus, allowing each device to send and receive information on its status, performance, history, or

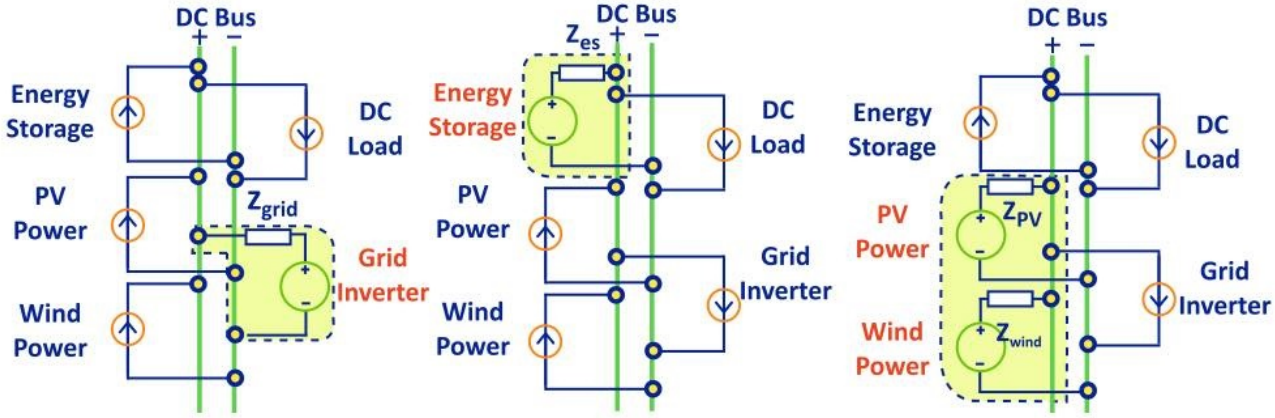

Figure 2.16: DC Bus Signaling operation

internal operational mode. Although Power Line Signaling (PLS) relies on digital communication, it is categorized as decentralized since the power network is the only communication medium [100]. The carrier communication signal is generated as a variable frequency sinusoidal signal or pulse width modulation [101]. PLS is more complex as compared to other decentralized methods. PLS is commonly used only for changing operating modes or shutting corrupted DGs of the system, and it is not suitable for power-sharing as the communication bandwidth is limited and communication signals may interfere with the measurements uncertainties.

2.6.3 Distributed Control

In a distributed control approach, although communication links exist, they are applied only between the units, and coordinated control strategies are implemented for optimum operation. With distributed control, the control process is distributed throughout the network. This approach improves the reliability of the control system as compared to the centralized control, as the system can operate even in case of node failure. [85] proposes a cooperative adaptive droop controller for islanded DC microgrid with multiple BESS and PV in which a communication channel is established between all generating units, while [8] introduces the concept of consensus-based distributed control in DC microgrids. A detailed

explanation of the consensus-based controllers, formulation, Advantages, and limitations are introduced in Chapter 4, hence, a novel cooperative distributed secondary controller is proposed.

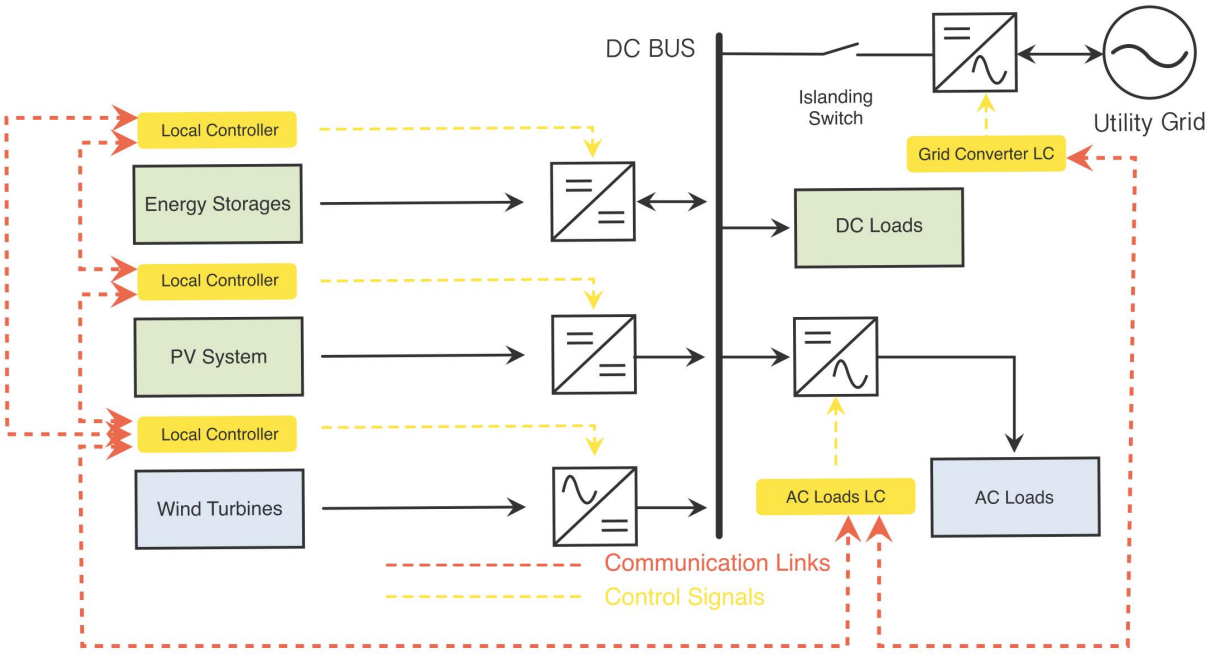

Figure 2.17: Distributed Control Operation

2.7 DC Microgrids Operation Modes

2.7.1 Grid-Connected Operation

The DC microgrid is connected to the utility through a bidirectional converter and the bidirectional power flow happens according to the microgrid objectives.

Table 2.1: Comparison for different Decentralized controllers

	Conventional Droop Control	VR-based Droop Control	Adaptive Droop Control	Mode Adaptive Droop Control	DC Bus Signalling	Power Line Signalling
Simplicity	✓	✓	✗	✗	✓	✗
DGs/ESS Coordination	✗	✗	✓	✓	✓	✓
Suitability of multi-microgrid clusters	✗	✗	✗	✗	✗	✓
Communication Requirements	✗	✗	✗	✗	✗	✓
Improved Load Sharing	✗	✗	✓	✓	✓	✓
Immunization against communication failure or delay	✓	✓	✓	✓	✓	✗

2.7.2 Islanded Operation

In this mode, the DC microgrid is either disconnected from the utility or is located far away from the reach of the conventional grid. The power management in the DC microgrid is performed such that the DC bus voltage is always regulated [102].

2.7.2.1 Single Islanded Microgrid

In this mode, the DC microgrid continues to generate, distribute, and consume electricity using its local energy resources and ESS without relying on external power sources. A single microgrid can be controlled through decentralized, centralized, or distributed controllers. Decentralized control is usually used due to its cost-effectiveness and reliability. For a microgrid consisting of an ESU, renewable DG, and loads, the integrated renewable DGs is operating in MPP or off MPP based on the SoC of the connected ESU [98].

2.7.2.2 Multiple Islanded Microgrids

For a single microgrid with high penetration of renewable DGs, it may fail to support the bus voltage in case of excessive generated power. By connecting different microgrids forming a cluster, the system performance can be effectively improved. This is because the maximum utilization of renewable DGs can be achieved, while the overall system reliability is improved [103]. Moreover, the maintenance cost is reduced and the lifespan of the network can be extended. If the inertia of the interconnected microgrids is relatively high, the overall system stability is improved. To achieve a high-quality service of global voltage regulation and power flow control, a communication control layer should be applied to the system.

2.8 Cyber security in microgrids

Modern microgrids harness the capabilities of information technology to intelligently manage energy delivery through bi-directional communication and efficiently incorporate green technologies to meet environmental demands. However, the vulnerability of communication technology has made the system susceptible to various security threats [104]. In modern microgrids, the cyber system plays a crucial role in collecting, transmitting, and processing data to manage the physical system's operations. For effective control, the cyber system's data flow must be efficient, reliable, and timely. However, cyber-attacks targeting the data flow can disrupt the system control channels, potentially resulting in a complete shutdown of the entire system [105]. In the following subsections, two common cyber attacks are described which have severe effects on the microgrid operation.

2.8.1 Denial of Service (DoS)

Potential intruders attempt to disrupt data availability by making communication networks inaccessible [106]. They can perform Denial of Service (DoS) attacks in two main ways: flooding services and crashing services. In flood attacks, attackers send an overwhelming amount of traffic to the server, aiming to slow down and eventually halt the services.

Alternatively, jamming signals may be used to block communication channels, preventing data from reaching its intended destination, and causing a disruption in the services [107, 108].

2.8.2 False Data Injection (FDI)

The objective of attackers for False Data Injection (FDI) attack model is to compromise data integrity by manipulating the states of a system through the injection of false data into sensors [109]. This attack can be executed through various means, including sensor spoofing, intrusion of communication links, magnetic field injection attacks, GPS spoofing, and more. In systems with unstable modes, dynamic FDI attacks aim to alter system measurements to render some of the unstable system modes unobservable. Similar to DoS attacks, FDI attacks can also be targeted at both actuator and sensor channels [108].

2.9 Protection Challenges in DC Microgrids

- Due to the integration of renewable DGs as well as ESS which are usually distributed through the microgrid network, the power flow in the network becomes bidirectional. As a result, certain accurate protection schemes have to be developed to maintain a reliable and stable operation.

- Most of the DGs and ESS are integrated into the DC microgrid network through DC-DC converters, which are connected to the DC buses through DC capacitors. Once a fault occurs, a rapidly rising capacitor discharging currents are feeding the faulted point. The rate of change of this fault current is also limited by the line inductance and depends on how far the fault point is from the DC buses. Once the adjacent DC capacitors are fully discharged, the stored energy in the line inductances is free-wheeled back to the buses through the converter's freewheeling diodes which may damage them causing a full operation shutdown at those buses, hence a propagated cascaded failures may occur. So, the protection system should be able to isolate the faulted lines as fast as possible to avoid fault current freewheeling.

- Unlike AC current faults, due to the DC fault currents nature, there is no zero-crossing point making it more challenging to interrupt the current during the fault period. Interrupting DC current generates a significant arcing. As a result, specialized circuit breakers and current interruption devices have to be developed to handle such DC fault currents.

- The fault current levels are not constants for each specific location in the network. For example, if a bolted fault at mid midpoint of a specific distribution line occurs twice a day, the fault current level may be not the same for both fault times. This is because the fault current level depends also on the status of the integrated DGs/ESS at the fault instant. Moreover, the microgrid configuration has a dominant effect on the fault current level. In other words, if the DC network is connected to the utility grid the fault current will be higher than if it operates in islanded mode, even if the fault occurs at the same exact location with the same fault resistance. As a result, relying on the over-current concept for detecting the faults is not sufficient.

- Fault currents through resistance are challenging to detect, and most conventional protection systems have poor selectivity to such faults, especially for high resistance faults. The protection system has to differentiate between the power line faults and the load switching or the plug-in of a DG/ESU. Moreover, it has to identify the fault type, and hence isolate the faulted line only. The types of faults are classified in the following subsections.

2.9.1 Types of Faults

2.9.1.1 Pole-to-Ground (PG) Faults

A line-to-ground or PG fault occurs when one conductor (pole) of a power line is shorted to the ground. The faulted line may be shorted to the ground directly, which is called bolted fault, or through an equivalent resistance. PG faults are the most frequent faults that occur in the networks. Fig. 2.18a shows a simplified illustration of PG faults. The level of the short circuit current depends on many factors that should be considered for

correct fault analysis. These factors include the fault location, the fault resistance, the grounding resistance, and the network grounding configurations. The common network grounding configurations will be described in the following subsections.

(a) PG fault (b) PP fault

Figure 2.18: DC microgrid faults

2.9.1.2 Pole-to-Pole (PP) Faults

A line-to-line or PP fault occurs when two conductors (poles) of a power line come into contact with each other, resulting in a short circuit. This type of fault can be caused by accidental contact between two conductors, insulation failure, or improper installation. The consequences of a line-to-line fault are generally more severe as it can cause a higher current to flow due to a typical low-impedance fault, which can lead to more severe damage and a higher risk of fire or other hazards. Fig. 2.18b shows a simplified illustration of PP faults. Unlike PG faults, PP fault current is not directly affected by the network grounding configuration.

2.9.2 Grounding in DC Microgrids

It should be noted that the grounding configuration of the network has a dominant effect on the fault current levels. In the next subsections, different grounding configurations are described, and then a brief comparison is carried out showing remarks for each configuration.

2.9.2.1 TT Grounding

The TT grounding system involves a direct connection of the supply DG/ESS or transformer (for grid-connected mode) to the earth, while the conductive parts of the equipment are linked to a Protective Earth (PE) provided by a separate local earth electrode. This PE is electrically isolated from the supply earthing point [61]. Fig. 2.19a shows the grounding connections for the supply as well as the connected appliances at a common bus. The TT grounding arrangement is highly efficient in enhancing the Electromagnetic Compatibility (EMC) performance of the system [110]. It minimizes the conductive path for interference generated by other equipment in the installation, contributing to improved overall system performance.

2.9.2.2 TN Grounding

The TN earthing system involves directly connecting the supply source to the earth, while all exposed conductive parts of the installation are linked to the neutral conductor. This arrangement ensures the safety of personnel but may offer less protection for property (such as fire or damage to electrical equipment) [111]. The TN earthing system comprises three sub-systems, each with distinct key characteristics, as described below.

2.9.2.3 TN-S Grounding

The TN-S earthing system has separate neutral and PE conductors throughout the system [112]. The supply source is directly connected to the earth, while all exposed conductive parts of an installation are connected to a PE via the main earthing line of the installation [111, 113]. Fig. 2.19a shows the TN-S grounding configuration.

2.9.2.4 TN-C Grounding

In the TN-C earthing system, Neutral and PE are combined in a single conductor throughout the system like TT systems. However, all exposed conductive parts of appliances are

connected to this combined neutral/PE conductor only, without a separate local appliance earthing [50, 61]. Fig. 2.19c shows the TN-C grounding configuration.

2.9.2.5 TN-C-S Grounding

TN-C-S can be considered as a combination of TN-S and TN-C grounding systems. Neutral and PE are combined in a single conductor at the supply side like a TN-C system. However, on the appliance side, the exposed conductive parts are grounded through a separate PE line like TN-S systems [112, 113]. In other words, this configuration uses a TN-S downstream circuit from an upstream TN-C circuit. The PE and neutral lines are solidly connected at the supply side. Fig. 2.19d shows the TN-C-S grounding configuration.

2.9.2.6 IT Grounding

In this system, although all exposed conductive parts of connected appliances are connected to an earth electrode constructing a PE point, the supply source is isolated from the earth as shown in Fig. 2.19e [114]. Unlike the previous source grounded configurations, the IT system does not provide a low impedance path for the fault current loop through the supply neutral [115]. As a result, the fault current remains very low, and the system operation resumes without tripping. However, a second ground fault may produce a large transient voltage as the faulted circuit becomes closed, which can lead to significant safety concerns for the system [110].

2.9.3 DC Microgrids Fault Phases

The fault period can be divided into two phases: the DC link capacitor discharging phase and the DC-DC converter freewheeling phase [116, 117]. Each phase has its own dynamic behavior and its impact on the network performance during the fault period.

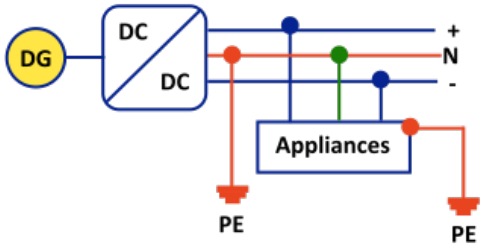

(a) TT Grounding

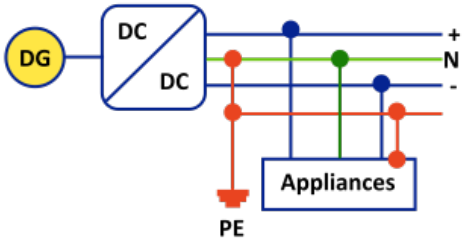

(b) TN-S Grounding

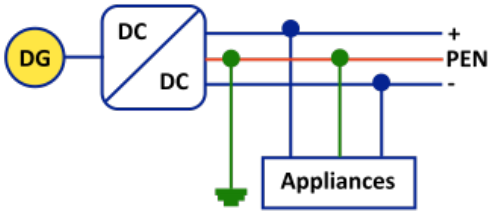

(c) TN-C Grounding

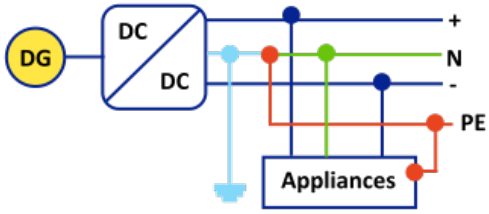

(d) TN-C-S Grounding

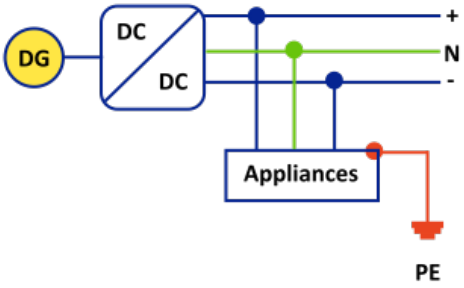

(e) IT Grounding

Figure 2.19: Grounding Configurations in DC Microgrids

2.9.3.1 Capacitor Discharge Phase

In the DC link capacitor discharge period, the capacitors that are connected across the network buses are discharging toward the fault location. The magnitude of this discharge current depends on the fault location, the fault type, and the network grounding [117].

Table 2.2: Grounding Configuration in Microgrids

	Connection Details	Remarks
TT	Neutral line is connected to the earth and exposed metallic parts of the appliance are also directly connected to the earth	• Simple and easy to install • Fault does not propagate to other parts of the grid
TN-S	Neutral is connected to earth, and the exposed metallic parts of the appliances are connected to neutral. Separate wires for protective earth (PE) and neutral (N) conductors are used	• Has highest electromagnetic compatibility • Higher safety than TN-C • Suitable for telecommunication networks
TN-C	PE and N conductors are combined to form a PEN conductor	• Cost-effective • Poor safety
TN-C-S	It is a combination of TN-S and TN-C grounding system	• Combines the benefits of both TN-S and TN-C • Identification of fault becomes difficult in case if neutral is disconnected
IT	Neutral point is not grounded and the exposed metallic parts of the appliance are separately grounded	• Small line to ground current • Difficult to predict the fault current path through DGs in case a second LG fault occurs simultaneously

Fig. 2.20a illustrates a simplified capacitor discharging through the fault location considering the line impedance and the fault resistance. Once the DC link capacitors are fully

discharged, the freewheeling phase starts.

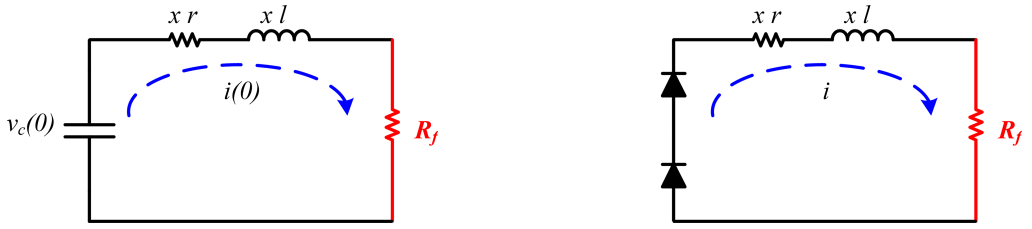

(a) Capacitor discharge phase (b) Diode freewheeling phase

Figure 2.20: DC microgrid fault phases

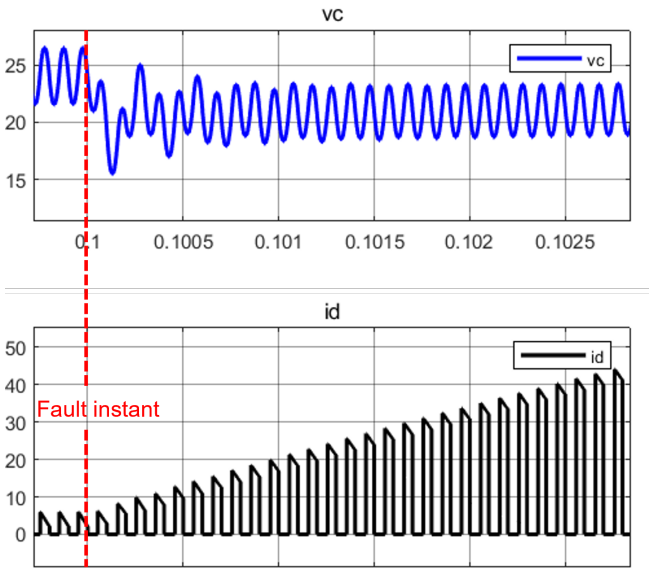

Figure 2.21: Fault phases illustration in DC microgrids

2.9.3.2 Diode Freewheeling Phase

Most of the VSC and DC-DC converters have freewheeling diodes at the output stage which are used to create a safe path for the converter inductor current during the converter switch-off period to protect the switch from the transient induced voltage across the inductor

[118, 119]. During the fault condition in the DC microgrid and the capacitor discharging phase, the fault can be detected and the converter active switch can be deactivated by simply disabling its gate signal. However, the converter diode is an uncontrolled device and cannot be fully deactivated. As a result, the stored energy in the power line inductance can be released through the diode, and hence the diode may be damaged. So, the protection scheme should be extremely fast and able to isolate the faulted power line within the first phase. The diode freewheeling phase is illustrated in Fig. 2.20b. If the converter switches are not forced to turn off during the fault condition, the converter will try to regulate the DC bus voltage and feed the fault with rapidly increased current as shown in Fig. 2.21. In this case, both the converter switches and the freewheeling diodes are subjected to excessive current and may be damaged.

2.9.4 Design Framework of DC Microgrid Protection Systems

2.9.4.1 Unit protection VS Non-unit protection

Unit protection refers to the zonal-based protection system that focuses on safeguarding specific zones of the DC microgrid. This zone may include a power line or common DC bus with integrated converters, DGs, ESS, and Loads. All components in the protected zone are exchanging information. It employs schemes like differential protection and restricted earth-fault protection to protect all components in this specific zone [116, 120]. On the other hand, non-unit protection also safeguards DC microgrid components but is not zone-specific [121, 122]. It involves locally measuring a designated system parameter, and fault detection occurs when the measured value exceeds a predetermined threshold. Non-unit schemes typically serve as backup protection in DC microgrids and include methods like overcurrent protection, under/overvoltage protection, and current derivative/voltage derivatives protections.

2.9.4.2 Single-ended VS Double-ended protection

Single-ended protection schemes use local measurements of voltage and/or current to detect faults, such as overcurrent and current derivative-based relaying. In contrast, double-

ended protection schemes, like differential protection, utilize sensors at both ends of the transmission line or feeder to measure the system parameter for comparison-based fault detection [123].

2.9.5 Protection Strategies for DC microgrids

2.9.5.1 Overcurrent protection

As clearly stated in the DC microgrid protection challenges, a DC microgrid exhibits certain characteristics, including low resistance and varying fault current levels and directions. Consequently, traditional overcurrent protection methods which are based only on threshold current comparison encounter several challenges. These issues include difficulties in relay coordination, delayed or non-operation of relays, and false tripping [124]. Notably, fault loop impedance significantly affects the natural frequency and transient fault current oscillation. As the conventional overcurrent protection approach does not consider fault impedance in its formulation, it faces serious limitations in various DC microgrid configurations, which is not the case in AC microgrids [125].

2.9.5.2 Under/over voltage protection

A comparison is made between the change in system voltage during a fault event and a predefined "threshold voltage value" to generate a trip signal. This method allows for reasonably fast fault detection but lacks the ability to differentiate between temporary and permanent faults. In other words, a transient load change or plugging in a DG / ESS may cause false tripping, which restricts its usefulness in DC microgrid systems. An alternative approach that is proposed in the literature is based on voltage prediction, where the relay's threshold value is determined using specific mathematical models [126]. Fault detection and isolation are achieved by activating the relay when the measured system voltage significantly deviates from the predicted voltage value. However, the method falls short in accurately locating faults for short-distance faults, especially in low-voltage DC microgrids.

2.9.5.3 Voltage and current rate of change protection

As mentioned in the fault phases section, When a fault occurs in the DC microgrid, a fault occurs, the power converter's output capacitors discharge, contributing to the transient fault current. To prevent excessive currents, protection mechanisms based on current derivatives aim to interrupt the fault before the DC link capacitor currents reach their peak [127]. A current rate of change-based protection scheme is suggested for a divided DC system comprising interconnected zones controlled by the central unit. The highest di/dt value measured in each zone is utilized for fault detection and localization [128]. However, designing an appropriate di/dt-based protection scheme is challenging as the current rate of change is highly influenced by fault impedance as well as the grounding impedance. For fault location and relay coordination, the initial response of the DC link capacitances to low or high impedance faults is taken into consideration [129].

2.9.5.4 Distance/Impedance protection

The operation of this protection system is to estimate the distance of the fault location from the point of detection by directly measuring the voltage and current to calculate the fault loop impedance. This method is widely used and effective in AC systems. However, in DC systems, applying a passive impedance estimation protection for DC microgrids faces significant challenges due to the small system impedance and the lack of a well-defined fundamental frequency for rapidly rising transients [125]. A passive impedance estimation scheme is proposed in [130]. This approach involves measuring voltage, current, and current derivatives at different time instances. The collected data is then processed online using a moving window least-square method to determine the equivalent inductance, which provides information about the distance between the fault and the detection point. Another emerging technique in distance protection schemes is the Active Impedance Estimation (AIE) method [131]. This approach involves injecting predefined voltage and current signal spectra into the system using a current injection circuit combined with a signal processing algorithm to determine the impedance between the fault and the point of detection. However, the accuracy of AIE protection schemes can be affected by systems with high resistance loads [132]. Moreover, the deployment of additional equipment, such

as current injection units, high bandwidth measurement devices, and computational units, increases the cost of the protection system.

2.9.5.5 Differential protection

The fault response of a DC network is greatly influenced by fault impedance. Many non-unit protection techniques deployed in such networks have overlooked this crucial factor, leading to suboptimal fault discrimination, especially in complex network configurations. To improve fault discrimination, unit protection like differential protection is recommended within the network, as it ensures higher selectivity and faster fault clearing [133]. Although current differential protection is a viable solution for complex DC microgrids, its implementation poses challenges due to the added cost of communication infrastructure. In comparison to AC systems, measuring DC fault current requires only the magnitude comparison, resulting in faster response times [127]. However, under high di/dt conditions, synchronizing current measurements and generating trip signals within a specific time frame is challenging. To ensure cost-effective communication in a limited coverage area, Ethernet cables with communication delays less than the DC cable's propagation velocity and sampling time are employed [134]. However, to synchronize relay operations through communication, GPS transducers with optimal accuracy are required. Additionally, a GPS signal failure detector becomes necessary to mitigate the risk of severe communication outages [135].

2.9.5.6 Travelling wave-based protection

In this method, the fault is detected through the transient waves of current and voltage caused by the fault which propagate through the power line until the circuit is interrupted [136, 137]. To enhance the traveling wave-based technique, communication channels are incorporated to ensure precise time synchronization, and Wavelet Transformation (WT) is effectively utilized as a tool for detecting rapid signal changes [138]. Traveling wave-based protection is explicitly applied in bipolar HVDC systems [139], where symmetrical components from the initial traveling wave characteristics enable rapid fault detection,

classification, and identification of the faulty pole. The accuracy of traveling wave-based schemes greatly depends on precise detection time calculations and the performance of the data acquisition tools used. Ensuring accurate detection and efficient data acquisition is essential for achieving optimal accuracy in traveling wave-based protection techniques.

Table 2.3: Comparison of various protection schemes for DC microgrid

Scheme	Sensitivity	Reliability	Simplicity	Cost	Speed	Remarks
Overcurrent Protection	Low	High	Simple	Medium	Medium	• Accurate and fast detection of current direction is vital • Vulnerable to noise and other disturbances • Fails to detect high resistance faults
Under/Over Voltage Protection	Low	High	Simple	Medium	High	• Difficult to discriminate internal and external faults. • Cannot detect high resistance ground faults.
Current Derivative Protection	Low	High	Medium	Medium	Medium	• Very effective in detecting bolted faults. • Difficult to detect high-resistance ground faults.
Distance/ Impedance Protection	Medium	Medium	Medium	Medium	High	• Limited accuracy in short lines. • Sensitive to fault resistances.
Limiting reactor-based Protection	High	High	Medium	Medium	High	• Suitable for High Voltage DC (HVDC) applications. • Requires high bandwidth measuring devices.
Differential Protection	High	High	High	High	High	• Need a reliable high-bandwidth communication channel. • Difficult to synchronize currents under high di/dt conditions.
Traveling Wave Protection	High	High	High	High	High	• Impacted by physical reasons, such as cable junctions and terminals. • Not suitable for compact low or medium-voltage microgrids.

2.9.5.7 Limiting reactor-based protection

In this protection scheme, the fault is detected by collecting local measurements for an integrated reactor at each power line end for each bus in multi-terminal networks. This concept has been used in literature in HVDC networks [140–142]. A method based on measuring the ratio between the transient voltage across an integrated inductor and the bus capacitor is proposed in [143] to distinguish between local and external faults. However, this method assumes that a capacitor is always connected at each bus of the system, which may not hold for DC microgrids. In [144], a pilot protection scheme is suggested, comparing transient voltages of the inductors at both ends of each line. Nonetheless, the reliance on communications makes this approach unsuitable for microgrid applications. Moreover, protection schemes designed for HVDC systems are often based on assumptions that might not apply to medium voltage and low voltage DC microgrids. For instance, HVDC systems are assumed to have a large inductor at the end of each line, and it is assumed that high-resistance faults draw high fault currents, making their detection easier. These assumptions render HVDC protection approaches unsuitable for direct adoption in DC microgrids. In [145], the concept of limiting-reactor-based protection is applied to DC microgrids by integrating a reactor at both ends of each power line. A differential Operational Amplifier (OP-AMP) circuit is used to catch local measurements precisely. However, the dynamic interaction of the integrated reactor with the line resistance and bus capacitance is neglected. Moreover, the effects of the grounding resistance, fault type, fault resistance, and the network grounding configuration on the protection system performance are not investigated. A Novel protection system is proposed in Chapter 5 to fill these gaps. The proposed protection system can detect various types of faults in a time zone of microseconds taking into account all the aforementioned system parameters.

Chapter 3

Improved Adaptive Model Predictive Controller of DC Microgrids Resources Considering System Nonlinearities, Constraints and Convergence Time

3.1 Introduction

The recent trend of integrating a large number of Distributed Generations (DGs) in active distribution systems faces several challenges. These challenges hinder the stable and reliable operation of the distribution system. Energy Storage System (ESS) is seen as a practical solution to overcome some of the obstacles that prevent the reliable integration of renewable DGs [146, 147]. Several technologies are used for the manufacturing of ESS. These ESS have a large range of capabilities and operating conditions. However, managing these different types of ESS and ensuring their optimal operation in supporting the distribution system has to be studied thoroughly [148, 149].

On the other hand, active distribution systems are moving towards the distributed configuration [150, 151]. This configuration offers high reliability, better stability, and flexible expandability [35, 152, 153]. This configuration is manifested in the microgrid architecture. Microgrids are a popular form of small-scale active distribution systems in which electricity consumption, generation, and storage cooperate [154–156]. Also, due to the DC nature of many renewable DGs (like PV) as well as ESS (such as batteries and supercapacitors), DC microgrids become an optimum configuration that avoids conversion stages redundancy [157]. Based on the DC microgrid architecture, numerous drawbacks associated with AC counterparts can be mitigated, such as issues with reactive power flow, synchronization of generating units, and the occurrence of transformer inrush currents. [158].

A decentralized cooperative control between all system elements of the DC microgrid will ensure reliable, stable, and expandable operation. This thesis proposes a novel distributed cooperative predictive control system. This system consists of two control layers, primary and secondary layers. These control layers are used each DG and/or ESS in the DC microgrid as shown in Fig. 3.1.

An Improved Adaptive Model Predictive Controller (IAMPC) is proposed as a primary control layer to optimize the coordination between the integrated DGs and ESS at each node (bus). The proposed IAMPC considers the system nonlinearities, and dynamic constraints while ensuring extended lifetime operation of the integrated ESS. This primary control layer is discussed in detail in this chapter (Chapter 3), while the proposed secondary controller and its integrated sublayers are illustrated in the next chapter (Chapter 4). The rest of this chapter is organized as follows: In section 3.2, the generalized Model Predictive Control (MPC) optimization approach is described including all tuning parameters and settings selection criteria, while section 3.3 illustrates the common MPC strategies used for Power converter applications. In section 3.4, the proposed IAMPC is introduced and the corresponding mathematical formulation is illustrated. Hence, the proposed IAMPC is applied to a PV-ESS system connected at a microgrid node through DC-DC converters. The state-space modeling and desecratization for the ESS-connected converter are described in detail. This model is then fed through the IAMPC algorithm. Finally, the system verification and simulation results are described in section 3.5.

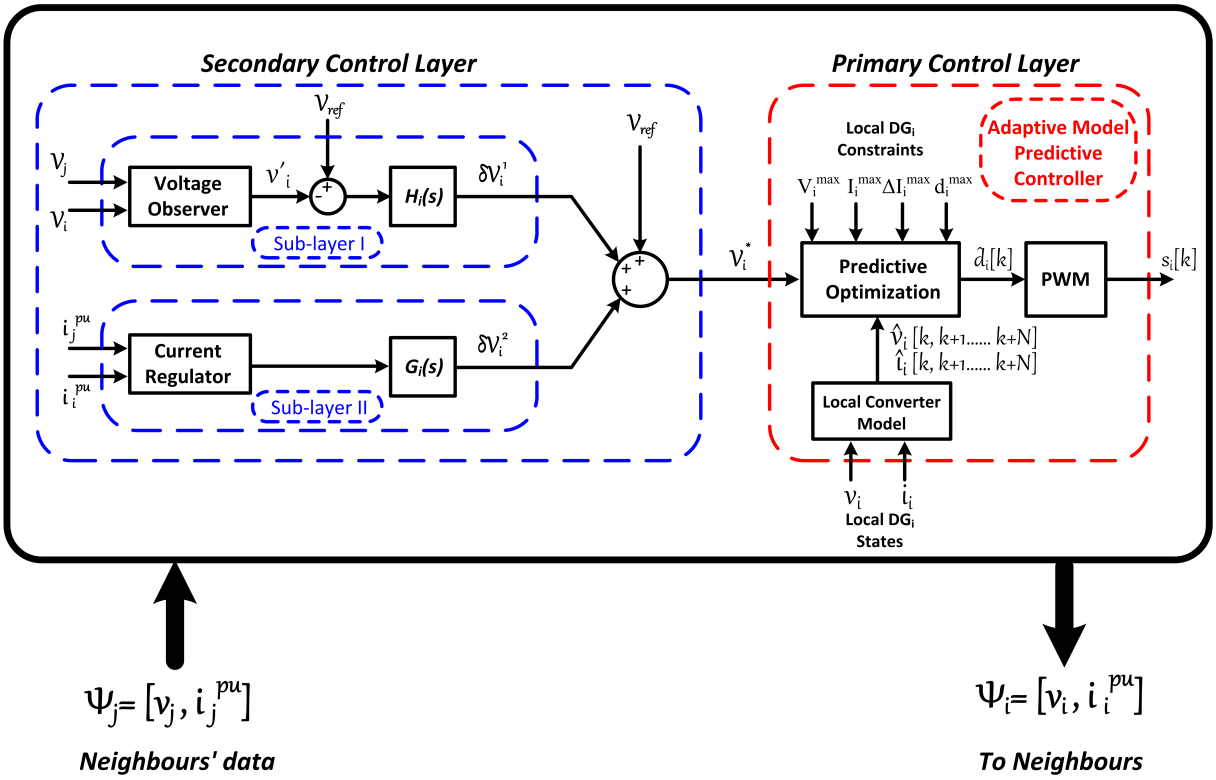

Figure 3.1: Proposed primary predictive controller in the hierarchical control system

3.2 Generalized Model Predictive Control Optimization Approach

MPC is an optimization-based controller that is capable of optimizing processes in multi-input multi-output systems [159]. MPC can control systems with multi-variable coupled dynamics [160]. Moreover, it can easily handle constraints on the system states or even the control input commands. Furthermore, non-linearity in the system model can be handled with such a controller in a natural way [161]. MPC consists mainly of two parts; an optimizer and the discrete model of the plant under control as shown in Fig. 3.2. MPC controller uses the model of the plant as well as the system measurement model to make predictions of the future plant output behavior [162]. The measurement model determines

the relation between the plant-measured output(s) under control and the internal system states. Moreover, the MPC optimizer is responsible for ensuring that the predicted future output of the plant tracks the desired reference dynamic trajectory [163] taking into account all the dynamic constraints of the plant. By solving the optimization problem, the MPC controller tries to minimize the error between the reference and the predicted trajectory through control commands. The inputs to the controller are the plant states after propagation through the measurement model, while its outputs are the optimized decision variables which are also called the manipulated variables that are applied to the actual physical system plant.

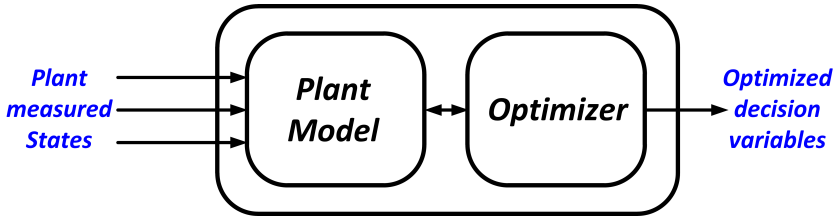

Figure 3.2: MPC basic construction

The plant model dynamics can generally be represented as:

$$\begin{aligned} x[k+1] &= f(x[k]\ ,\ u[k]) \\ y[k] &= h(x[k]\ ,\ u[k]) \\ x\ &\in\ \mathbb{R}^n \quad \textit{is the state vector} \\ u\ &\in\ \mathbb{R}^m \quad \textit{is the vector of manipulated variables} \end{aligned} \tag{3.1}$$

where $f(x[k]\ ,\ u[k])$ represents the system dynamics, while $h(x[k]\ ,\ u[k])$ is the measurement model. As seen from the previous equations, the system model has to be discrete so that the MPC controller can predict the future states and decision variables (manipulated variables). MPC operation sequence is illustrated in Fig. 3.3. $x(.)$ is one of the system states that is controlled to follow a reference value x^r, while $u(.)$ is one of the optimal decision variables. $u^*(k)$ represents the optimum control input that is applied to the system for the period k *to* $k+1$. MPC operation sequence can be listed as:

- At instant k, the system states are measured $(x[k])$

- Based on the measured value $x[k]$, the state vector is propagated through the system model over a specific number of time steps N called prediction horizon. Then, the future state vectors $x[k+1]$ to $x[k+N]$ are determined as a function of the unknown system inputs $u[k]$ to $u[k+N-1]$. The optimal sequence of input controls $u^*(x[k])$ (manipulated variables) are computed by running the optimization problem over the prediction horizon N to achieve a specific objective(s). These control input sequences can be represented as:

$$\begin{aligned} u^*(x[k]) =& (u^*[k], u^*[k+1], ..., u^*[k+N-1]) \\ & where\ u[k+i]\ \in\ \mathbb{R}^m \end{aligned} \tag{3.2}$$

- The first control input $u^*[k]$ vector is applied to the physical system on the sampling period $[k, k+1]$, while the remaining computed control vector is used as the initial condition vector for the next optimization instant.

- At instant k+1, the sequence is repeated.

For the simple example shown in Fig. 3.3, the objective was that the state variable $x(.)$ to follow a specific constant reference x^r through minimizing a single-objective cost function containing the error signal over the prediction horizon. Generally, MPC has the ability to solve multi-objective optimization problems in real-time while considering the dynamic system constraints even for the output manipulated variables [164], but some tuning parameters should be considered for the effective optimization process, which is described in the following subsections.

3.2.1 Prediction and Control Horizons

Prediction and control horizons are key design parameters of the MPC optimization problem. Prediction horizon N is the number of future decision instants which MPC controller must evaluate at instant k by running the optimization problem. On the other hand, the control horizon M is the number of predicted decision variables u at decision instant k that are being used as initial conditions for the next optimization instant [165]. The control

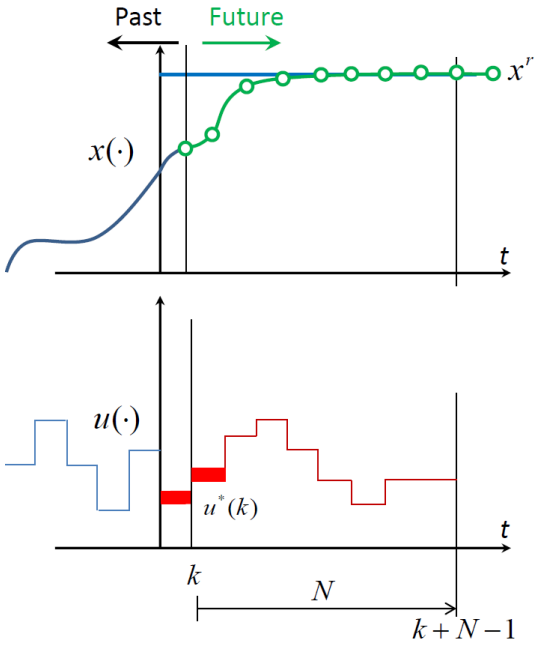

Figure 3.3: MPC operation sequence

horizon value is in the range between 1 and the prediction horizon value N [166]. For $M = 1$, the optimizer is going to determine only one manipulated variable vector $u[k]$, while for $M = N$, the optimizer is going to determine $N - 1$ manipulated variable vector $u[k]$ to $u[k + N - 1]$. It should be noted that for both cases, the initial conditions for $u[k]$ to $u[k + N - 1]$ should be fed to the optimizer at each optimization step. For $M = N$, all these initial condition data are available from the previous optimization instant. However, for $M = 1$, there is one initial condition for $u[k]$ only, which has to be copied to all initial condition vectors, which can affect the optimization process performance. Fig. 3.3 shows that the control horizon is equal to the prediction horizon as the number of the predicted decision variables at instant k is equal to the prediction horizon N. In many applications, the control horizon M is selected to be smaller than the prediction horizon to reduce the computation burden, but this can affect the control dynamics. Fig. 3.4 shows the MPC operation with unequal prediction and control horizons. It can be seen that, at the k instant, the predicted system states $\hat{y}$ are determined for $k+1$ up to $k+N$ (whole prediction horizon period), while the control actions are determined for k (which is applied to the

physical system during [k] to [k+1]) up to $k + M - 1$ only (control horizon period). The control actions for$k + M$ up to $k + N$ are simply set to be equal to $u[k + M - 1]$ [167].

The sampling time Δt, prediction horizon N, and control horizon M should be tuned for better controller performance [168]. The sampling time should fit within 0.05 to 0.1 of the rise time of the open loop system response. The prediction horizon should be 20 to 30 covering the open loop transient system response. The control horizon shouldn't be less than 10% of the prediction horizon.

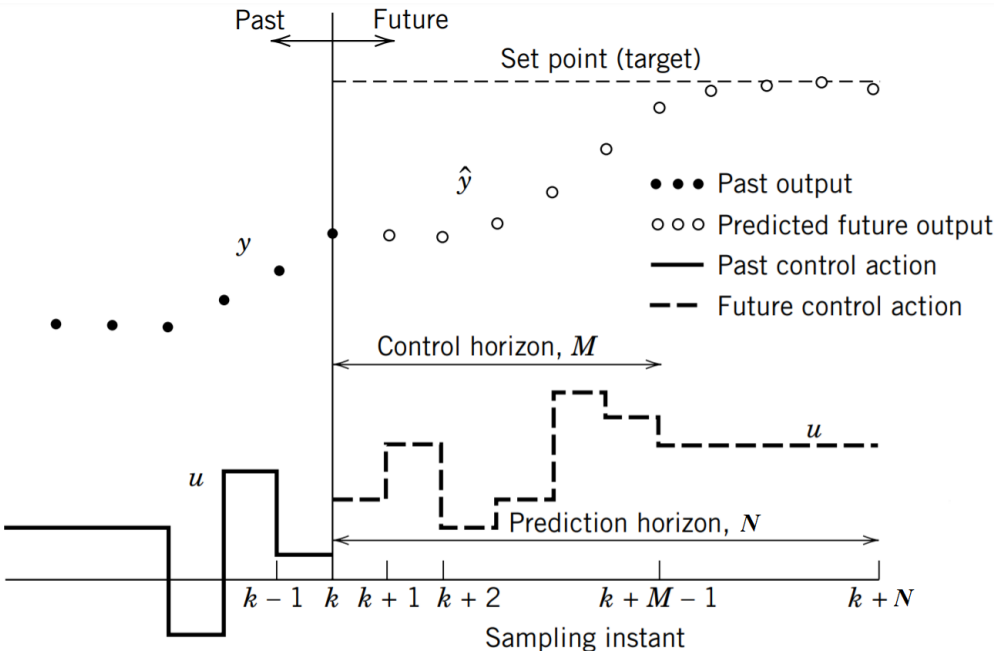

Figure 3.4: MPC operation for unequal prediction and control horizons

3.2.2 Running Stages and Cost Function

The MPC optimization problem is carried out to minimize a single or multi-objective function which is called the cost function. The cost function is the summation of the running stages over the prediction horizon N, while the running stage is the error quantity between the reference trajectory and measured system signal at a specific sample instant.

This can be applied to the system states and/or decision variables. The running stage can mathematically be represented in quadratic form as:

$$\ell(x,u) = \parallel x_u - x^r \parallel_Q^2 + \parallel u - u^r \parallel_R^2 \tag{3.3}$$

where Q and R are the weighting factors for the system state and decision variable errors respectively, which are responsible for determining and tuning the dominant objective in multi-objective optimization problems. The cost function is the evaluation of the running stages over the whole prediction horizon N. It can be represented in terms of the running stage as:

$$J_N(x,u) = \sum_{k=0}^{N-1} \ell(x_u[k], u[k]) \tag{3.4}$$

3.3 Model Predictive Controller Strategies for Power Electronic Converter Applications in DC Micro-grdis

MPC have been used in various fields for the sake of achieving optimum operation of the system. For microgrid systems in which various DGs and ESS with different technologies and capacities are integrated through power electronic converters, modeling of such converters has the greatest impact on the MPC formulation, dynamic performance, and complexity level. Cost function formulation as well as the integrated system constraints have also reasonable effects as they are parts of the MPC problem formulation. In the following subsections, various MPC-based control strategies used in microgrid applications are listed. Then a comparison is carried out between them based on the formulation, limitation, complexity,..etc.

3.3.1 Finite Control Set Model Predictive Controllers (FCS-MPC)

Finite Control Set Model Predictive Controller (FCS-MPC) takes advantage of the discrete nature of power electronic converters to formulate the optimization problem simply

and intuitively [169]. So, for these types of controllers, no need to integrate any kind of modulator as the output decision variables have a Boolean value that corresponds to the converter switches states [170]. In other words, the control problems and modulation are formulated and solved in one computational stage [171]. However, FCS-MPC suffers from their limited prediction horizons which limits their control performance as compared to the CCS-MPC. Moreover, FSC-MPC techniques can be considered as an enumerated search algorithm rather than an optimization problem [172], as the best-fit switching vector is selected for the minimum cost function. Furthermore, some types of FSC-MPC suffer from variable switching frequencies applied to the converter switches which makes it difficult to design the converter filter and also generates a high level of harmonic contents in the system states [173]. The following subsections illustrate different types of FCS-MPC algorithms.

3.3.1.1 Optimum Switching Vector Model Predictive Controller (OSV-MPC)

For the recent literature, Optimum Switching Vector Model Predictive Controller (OSV-MPC) was the most popular FCS-MPC technique for power converter control applications. The basic principle for OSV-MPC is as follows: 1) Based on the current state measurements (converter current and/or voltage) the predicted states are calculated using the discretized system model. 2) The predicted objective quantities are determined using the measurement model as a function of the converter switching states. 3) The cost function - which generally is the difference between the objective quantity and the given reference- is calculated for each possible switching combination (switching vector). 4) The switching combination corresponds to the lowest cost function applied to the converter switches for the complete switching cycle [174]. This straightforward strategy makes OSV-MPC very intuitive and easy to implement. However, it still suffers from the variable switching frequency as well as the limited prediction horizon. Moreover, OCV-MPC produces a non-zero average steady-state error [175].

3.3.1.2 Optimum Switching Sequence Model Predictive Controller (OSS-MPC)

Optimum Switching Sequence Model Predictive Controller (OSS-MPC) is introduced as a solution for most of the OSV-MPC disadvantages. Instead of applying the optimum

switching vector during the whole switching cycle, a set of optimum switching sequences are applied to the converter switches during each single switching cycle [176]. In this way, OSS-MPC involves the time in the optimization problem and can simulate the modulator effect for achieving equivalent constant switching frequency [177]. Similar to OSV-MPC, the optimal switching sequence has to be previously selected by the optimization algorithm from the possible sets. As a result, OSS-MPC has a fixed equivalent switching frequency and better steady-state performance as compared to OSV-MPC.

3.3.1.3 Event Triggered Model Predictive Controller (ET-MPC)

In order to reduce the computational burden of MPC algorithms, Event Triggered Model Predictive Controller (ET-MPC) is introduced. It is well known that MPC-based controllers have better dynamic performance than most of traditional techniques. The basic principle of ET-MPC is to deactivate the FCS-MPC used for controlling the power converter during normal conditions, and a conventional controller is used instead [178]. In this way, the computational burden can be effectively reduced during normal operation. However, if the state of the target system is evolved to trigger a preset condition, the FSC-MPC is set to the online mode to achieve better dynamic performance during critical events [179].

3.3.2 Continuous Control Set Model Predictive Controllers (CCS-MPC)

Unlike FSC-MPC techniques, Continuous Control Set Model Predictive Controller (CCS-MPC) formulation is based on computing continuous decision variable vectors and then uses an external modulator to generate the optimum switching signals of the power converter. For DC microgrid applications, a Pulse Width Modulation (PWM) based modulator is commonly used [180], while for AC microgrids Space Vector Modulation (SVM) is common. This approach is quite similar to vector control as both concepts have a modulator and operate at a fixed constant frequency [181]. The main advantages of CCS-MPC over FCS-MPC include faster dynamics, minimum overshoots and harmonics, steady-state error

elimination, less sampling time, and a higher degree of robustness [182–184]. Moreover, it can use longer prediction horizons which improves its dynamic performance [185]. However, the formulation of CCS-MPC has a high level of complexity compared to FSC-MPC counterparts as it requires proper modeling of the power converter under control. Moreover, as CCS-MPC involves a true full optimization problem (unlike FSC-MPC), and for nonlinear system models, it may take a quite long time to get the optimum control action. Furthermore, for non-quadratic cost function, and nonlinear system constraints, the optimization problem becomes non-convex, which means the the global optimum control action is not guaranteed [186]. The main types of CCS-MPC are illustrated in the coming subsection, and the corresponding solutions of traditional CSS-MPC are pointed out.

3.3.2.1 Adaptive Model Predictive Controller (AMPC)

Adaptive Model Predictive Controller (AMPC) is suitable for controlling linear and nonlinear system models as it can ensure global optimum control action solution (convex optimization problem) [187]. However, the cost function should be in the form of a quadratic function, and the system constraint should be linear [188], which is generally the case for power converter control applications. For nonlinear system models, AMPC uses Euler or Runge-Kutta to discrete the system model through all the operating conditions [189]. It should be noted that for AMPC, the optimization problem is solved online. As a result, it should be ensured that the optimum control action is obtained before the next optimization instant. Practically, this may be not the case, especially for nonlinear system models and long prediction horizons, and hence a sub-optimum solution is used instead, which is the control action in the last iteration in the optimization cycle [190, 191]. Although this solution is not the global optimum, it still maintains all the system constraints.

3.3.2.2 Gain-Scheduled Model Predictive Controller (GSMPC)

In the case of different constraint settings and system states based on the current operating point, Gain-Scheduled Model Predictive Controller (GSMPC) is the best-fit algorithm as it formulates the problem as separate different MPC controllers [192]. Each controller has

its system constraints and states. Individual controllers are selected online based on the current operating condition through a switching algorithm [193].

3.3.2.3 Explicit Model Predictive Controller (EMPC)

Unlike AMPC and GSMPC, Explicit Model Predictive Controller (EMPC) computes and stores the optimal problem solution offline for all system states in a given preset range. As a result, the online computations are limited to a search algorithm to find the required zone corresponding to the measured states [194]. This method is suitable for very high-level dynamic systems in which the sampling time has to be minimum [195]. However, EMPC requires high storage capacity to store all optimum solutions for different possible state combinations. Moreover, for a large number of optimization zones, the searching algorithm becomes effective in catching the optimum control action during the cycle time [196]. To overcome this problem, some zone merging techniques are introduced to reduce the number of searching zones. However, this can affect the EMPC dynamic performance.

3.4 Improved Adaptive Model Predictive Controller for DC microgrid with high penetration of PV DGs and Energy Storage System

As stated in the previous section AMPC is one of the most effective continuous control set MPC techniques that is suitable for microgrid power converters and it ensures a convex solution. As the optimization problem is solved online at each time step, the main challenge for AMPC is the convergence speed. For fast dynamic systems, the prediction time step has to be reduced as stated in section 3.2.1. Hence, the global optimum solution is not guaranteed.

This section proposes an Improved Adaptive Model Predictive Controller (IAMPC) that offers a faster convergence speed, and hence, the global optimum control actions are determined in a shorter time frame as compared to the optimization cycle. In this way,

the dynamic performance of conventional AMPC controllers can be improved effectively. Moreover, thanks to the natural way of integrating equality and inequality constraints, the proposed IAMPC has the ability for effective coordination between different DGs or DG-ESS connected at the same microgrid node. The main salient contributions for this section can be listed as:

- An improved convergence speed IAMPC is proposed for optimum dynamic performance of DC microgrid power converters.
- An optimized interactive coordination between renewable DG and BESS is achieved by the proposed IAMPC and the dynamic constraint settings. This interactive coordination is described through four different case studies with the help of MATLAB Simulink and the integration of the CasAdi optimization platform.
- A robustness assessment of the proposed IAMPC against parameters variation and system degradation is investigated.

For the rest of this section, the mathematical formulation of the proposed IAMPC is illustrated. The proposed IAMPC is then applied to a PV-ESS system connected to a DC microgrid. The interactive coordinated operation is investigated through four case studies. Finally, a robustness assessment of the proposed IAMPC is carried out.

3.4.1 Mathematical formulation of the Proposed Control Algorithm

As stated in section 3.2, the general plant model can generally be represented in discrete domain as:

$$\begin{aligned} x[k+1] &= f(x[k]\ ,\ u[k]) \\ y[k] &= h(x[k]\ ,\ u[k]) \\ x\ &\in\ \mathbb{R}^n \quad \textit{is the state vector} \\ u\ &\in\ \mathbb{R}^m \quad \textit{is the vector of manipulated variables} \end{aligned} \tag{3.5}$$

where $f(x[k]\ ,\ u[k])$ represents the system dynamics, while $h(x[k]\ ,\ u[k])$ is the measurement model. On the other hand, the predictive optimization is carried out through a cost function minimization. This cost function is evaluated through the summation of the running stages over the prediction horizon N. The running stage at each optimization time step can be expressed as:

$$\ell(x,u) = \parallel x_u - x^r \parallel_Q^2 + \parallel u - u^r \parallel_R^2 \tag{3.6}$$

where Q and R are the weighting factors for the system state and the decision variable errors, respectively. It should be stated that for most power converter controllers, the second part of the running stage is eliminated. In other words, the weighting factor R is set to zero. The second term is essential only if it is required that the control action (output manipulated variable) tends to a specific value at a steady state.

The cost function is then represented as: :

$$J_N(x,u) = \sum_{k=0}^{N-1} \parallel x_u[k] - x^r \parallel_Q^2 + \parallel u[k] - u^r \parallel_R^2 \tag{3.7}$$

To sum up, the optimum control problem is to find the future control sequence that ensures the minimum value of the cost function. It is formulated as:

$$\begin{aligned} minimize\ J_N(x,u) = & \sum_{k=0}^{N-1} \ell(x_u[k], u[k]) \\ subject\ to: x_u[k+1] = & f(x_u[k]\ ,\ u[k]) \\ u[k] \in & \ \mathbb{R}^m, \quad \forall k \in [0, N-1] \\ x_u[k] \in & \ \mathbb{R}^n, \quad \forall k \in [0, N] \end{aligned} \tag{3.8}$$

On the other hand, the standard problem formulation in numerical optimization has the general form of:

$$\begin{aligned} & minimize\ \Phi(\omega) \\ subject\ to: g_1(\omega) & \leq 0, \quad Inequality\ constraints \\ g_2(\omega) & = 0 \quad Equality\ constraints \end{aligned} \tag{3.9}$$

where ω is the decision variable vector. There are many techniques in the literature to convert the optimal control problem into a standard nonlinear programming problem [197]. The most straightforward method is the single shooting technique which is used in many dynamic systems. In the single shooting method, the system measurements are used to determine the system states through the measurement model. Then the current system states are propagated through the discrete system model to determine the predicted system states as a function of the unknown predicted control actions - which are the outputs of the optimization problem - and the previous system states. If the system has linear dynamics, the propagated predicted states will have linear functions to the unknown predicted control actions and system states. However, for nonlinear systems, the non-linearity will be propagated exponentially through the predicted system states, especially for long prediction horizon intervals. As a result, the computation time to achieve the global optimum control actions is extended dramatically. So, the single shooting method is not suitable for nonlinear and/or unstable systems [197–199]. It should be noted that for single shooting the variables (optimization problem outputs) are only the control actions $u[k]$ to $u[k+N-1]$.

In contrast, the proposed IAMPC uses multiple shooting techniques in which the system dynamic model is considered as equality constraints (g_2) and hence the system predicted states are included in the decision variables besides the predicted control actions [200], [197]. Although the number of decision variables (optimization problem output) is increased as it contains both the predicted system states, as well as the predicted control actions, the system's non-linearity is not propagated through the system, states like the case of single shooting. Hence, the overall computational optimization time is effectively reduced [199, 201] Additionally, the system may have many operational limits which can easily be included in the IAMPC optimization problem as inequality constraints (g_1) [198].

So, to sum up, the optimization problem can be expressed as:

$$
\begin{aligned}
&minimize\ \Phi(\omega), \qquad \omega\ =\ [u_0, u_1, ..., u_{N-1}, x_0, x_1, ..., x_N] \\
&subject\ to: \\
&g_1 = \begin{bmatrix} g_1(x_0, u_0) \\ \vdots \\ g_1(x_{N-1}, u_{N-1}) \\ g_1(x_N) \end{bmatrix} \leq 0, \quad g_2 = \begin{bmatrix} \bar{x}_0 - x_0 \\ f(x_0, u_0) - x_1 \\ \vdots \\ f(x_{N-1}, u_{N-1}) - x_N \end{bmatrix} = 0
\end{aligned} \tag{3.10}
$$

where g_2 includes the system dynamics equations as well as any equality constraints corresponding to the power converter references and/or the integrated DGs-ESS equality constraints. g_1 includes all inequality constraints which usually refer to the power converter capability limitations and/or the integrated DGs-ESS Inequality constraints.

3.4.2 IAMPC for PV-ESS System Application

3.4.2.1 System Modelling and Modes of Control

There are two quantities to be regulated for the DGs integrated into the DC microgrids node. These quantities are the local DC bus voltage and the DG load sharing into the microgrid. As stated in Section 3.1, load sharing is achieved in the secondary control layer in which all neighbor DGs are communicated through a cooperative framework. Hence a correction factor is loaded to each local voltage reference at each node as shown in Fig. 3.1. For this study, the main objective is to ensure effective regulation of the local dc link at each node in the dc microgrid. For the node under study, a Lithium-ion BESS is integrated into the same node to ensure a dispatchable power-sharing of the combined PV-ESS connected bus and also to regulate the local dc voltage through charging/discharging of the BESS to compensate for the intermittent output behavior of the PV and the transient local dc demands. Under normal operation, the proposed IAMPC is applied to the ESS-connected dc-dc converter, while the PV is operating at MPP through a boost converter. In critical conditions, cooperative coordination between PV-ESS is carried out through the proposed IAMPC, so that the PV-connected converter becomes driven by the IAMPC rather than operating at MPP.

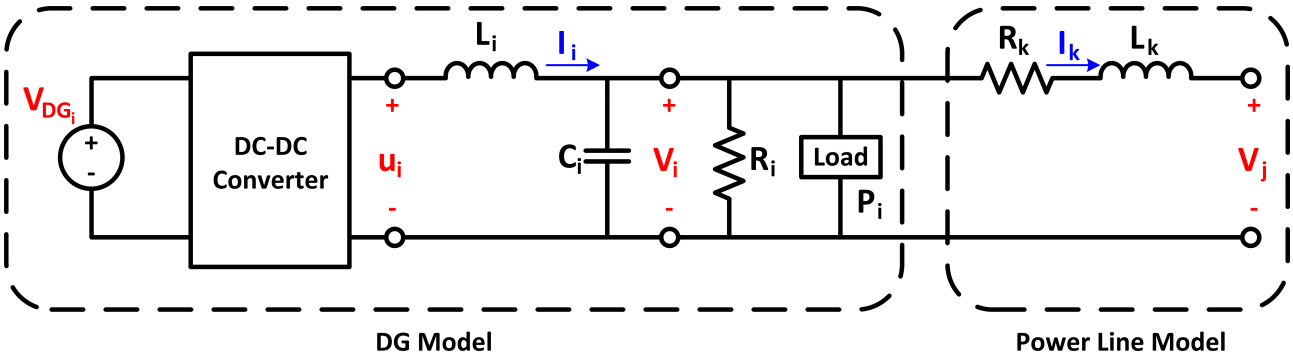

Figure 3.5: DG/ESS integration model in DC microgrids

The general representation of DG or ESS integration into DC microgrids is shown in Fig. 3.5. L_i and C_i are the DG/ESS connected power converter filter components, R_i is output resistance, and P_i is the locally connected DC load. On the other hand, this microgrid bus is connected to neighbor buses j through power lines with R_k and L_k parameters. As stated earlier, the Lithium-ion battery is controlled through a DC-DC converter through the proposed IAMPC, while the PV-connected converter has a coordinated operation with the IAMPC during critical events as shown in Fig. 3.6. Fig. 3.7 shows the BESS integration configuration, where a bidirectional dc-dc converter is used to interface the low voltage level of the battery to the system dc-link high voltage level. The bidirectional converter has two modes of operation, buck mode in which the battery absorbs power from the system dc-link, and boost mode in which the battery is discharged. The converter switches are driven in a complementary order, and hence the converter model can be easily achieved as in equation (3.11).

$$\begin{aligned} S_1 = 0, S_2 = 1 : & \frac{di_L}{dt} = \frac{1}{L} V_B \\ & \frac{dv_C}{dt} = -\frac{1}{C_{dc}} I_{oESS} \\ S_1 = 1, S_2 = 0 : & \frac{di_L}{dt} = \frac{1}{L} (V_B - v_C) \\ & \frac{dv_C}{dt} = \frac{1}{C_{dc}} (i_L - I_{oESS}) \end{aligned} \tag{3.11}$$

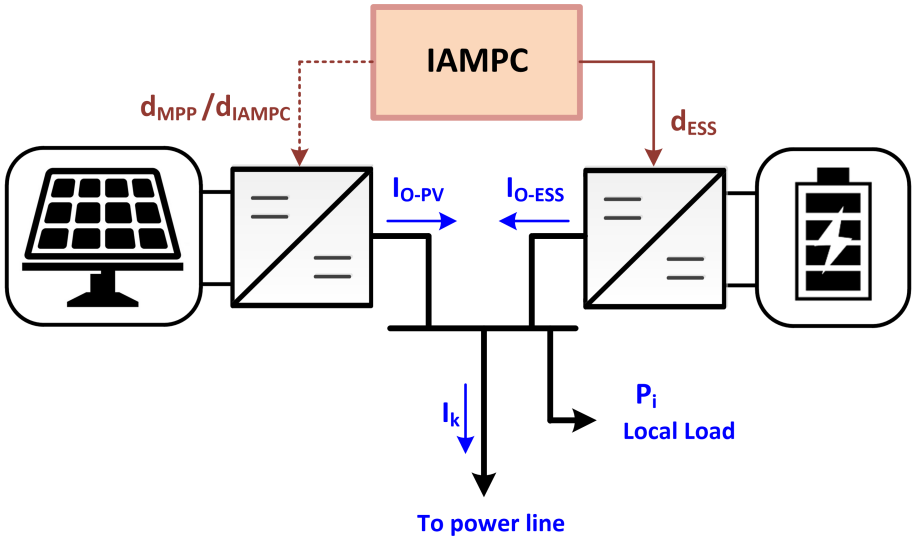

Figure 3.6: DG-BESS System under IAMPC control

Note that the default current flow direction is considered to be the boost mode of operation as shown in Fig. 3.7. For modeling the converter, the state-space model has to be determined first and an averaging technique can be used to get the system model or to derive a small-signal model to study the converter stability. The general form of the system state-space equation is given as:

$$\dot{x} = Ax + Bu \tag{3.12}$$

where x is the state vector and u is the input vector, and they are given as:

$$x = \begin{bmatrix} i_L \\ v_C \end{bmatrix}, \quad u = \begin{bmatrix} V_B \\ I_{oESS} \end{bmatrix} \tag{3.13}$$

From equation (3.11), it can be seen that there are two circuit configurations according to the switch's status. As a result, there are two state space equations corresponding to these two states. These equations can be expressed as:

$$\begin{aligned} S_1 = 0, S_2 = 1 : A_1 &= \begin{bmatrix} 0 & 0 \\ 0 & 0 \end{bmatrix}, B_1 = \begin{bmatrix} \frac{1}{L} \\ -\frac{1}{C_{dc}} \end{bmatrix} \\ S_1 = 1, S_2 = 0 : A_2 &= \begin{bmatrix} 0 & -\frac{1}{L} \\ \frac{1}{C_{dc}} & 0 \end{bmatrix}, B_2 = \begin{bmatrix} \frac{1}{L} \\ -\frac{1}{C_{dc}} \end{bmatrix} \end{aligned} \tag{3.14}$$

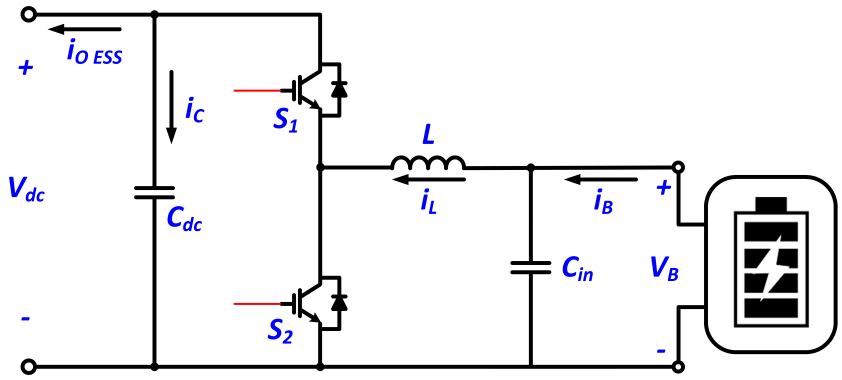

Figure 3.7: Battery/ Bidirectional buck-boost converter

The average state-space representation of equation (3.14) is shown in equation (3.15), where the time of the first and second states are dT_s and $(1-d)T_s$ respectively.

$$\dot{x} = (A_1 * d + A_2 * (1-d))x + (B_1 * d + B_2 * (1-d))u \tag{3.15}$$

So, the mathematical model of the battery dc-dc converter can be expressed as:

$$\begin{aligned} \frac{di_L}{dt} &= \frac{1}{L}\left(V_B - (1-d)v_C\right) \\ \frac{dv_C}{dt} &= \frac{1}{C}\left((1-d)i_L - I_{oESS}\right) \end{aligned} \tag{3.16}$$

For this model, the system states are i_L and v_C, which means that the system measurement model is unity coefficient as the system states are directly measured. On the other hand, the control action (manipulated variable) is the duty ratio (d). From the model equations (3.16), it can be easily seen that the converter model is nonlinear. The proposed IAMPC controller can handle this non-linearity efficiently with a reduced computational burden as described earlier.

It should be noted that the local DC bus reference is assumed to be given by the secondary control layer, which takes into account the main two objectives: 1) the global voltage regulation for the entire DC microgrid, and 2) the proportional load sharing for all connected DGs. The compensated variable trajectory voltage reference given by the secondary controller is then fed to the proposed IAMPC. So, the optimization problem can

be considered as a single objective problem with the following cost function:

$$J_N = \sum_{k=0}^{N-1} (V_i^*[k+1] - V_i[k+1])^2 \tag{3.17}$$

where V_i^* is the local voltage reference given by the secondary controller, while V_i is the measured bus voltage which is also one of the BESS-converter states.

It should be noted that there are some operational constraints from the system including ESS and the power converter that should be considered for economic and safe operation. These constraints are described in the following sub-section.

3.4.2.2 System Constraints and Applied Limitations

Power Converter Constraints: These constraints are generally related to the maximum power capability of the converter switches, i.e. the DC bus voltage and the switch current. Moreover, a maximum and minimum duty ratio has to be set at less than one and above zero to maintain the switching frequency constant. This constraint can be listed as follows:

$$\begin{aligned} d_{min} &\leq d[k] \leq d_{max} \\ i_{SW,min} &\leq i_{SW}[k] \leq i_{SW,max} \\ v_{dc,min} &\leq v_{dc}[k] \leq v_{dc,max} \end{aligned} \tag{3.18}$$

BESS Constraints: For better performance and extended lifetime operation of Lithium-ion BESS, it is recommended to add limitation constraints for the BESS that should be considered in the IAMPC optimization problem.

- **SoC and Depth of Discharge (DoD) [202]:** The state of Charge represents the level of charge inside the cell. It depends on the average concentration of the lithium inside the cell electrodes. The average concentration of lithium isn't affected by changing temperature [203]. So, temperature variations will affect the cell voltage while it does not affect the SoC [203]. SoC changes only according to the current flow due to cell charging or discharging or even due to self-discharge inside the cell

itself. Therefore, cell voltage is useful as an indirect indicator of the SoC but not as a measurement of the SoC. The SoC relation with the cell current can be expressed as the following equation:

$$z(t) = z(0) - \frac{1}{Q}\int_0^t \eta_c \, i(\tau) \, d\tau \tag{3.19}$$

where $z(0)$ is the initial SoC, Q is the cell total capacity in ampere. sec or coulombs, and η_c is the coulombic efficiency. Equation (3.19) is usually used for SoC estimation, and this method is called coulomb counting. Coulombic efficiency is defined as the ratio between the charge delivered by the cell during the discharge period and the charge stored in the cell during the previous charging [204].

On the other hand. the DoD can be considered as the inverse of the SoC. It represents the removed capacity of the fully charged battery it can be calculated from SoC as

$$\begin{aligned} DoD &= 1 - SoC \qquad (expressed\ as\ fraction) \\ &= Q(1 - SoC) \qquad (expressed\ in\ Ah) \end{aligned} \tag{3.20}$$

It is important to note that Lithium-ion cells should avoid being fully discharged (Soc=0) and charged (SoC=100%), as that affects their lifetime dramatically. The smaller the discharge (lower DoD), the longer the battery will last and the more cycles it will be able to do [205]. As a result, a minimum and maximum level of SoC should be maintained during the system operation which can be represented as:

$$SoC_{min} \leq z[k] \leq SoC_{max} \tag{3.21}$$

- **Discharging rate [206]:** Lithium-ion cell rate of discharge is a very important parameter to be considered especially when dealing with transient loads. rate of discharge has a negative impact on the battery's internal resistance and the effective cell capacity [207]. As a result, a rate of discharge constraint can be added to the optimization problem as follows:

$$\Delta I_{B,min} \leq I_B[k] \leq \Delta I_{B,max} \tag{3.22}$$

It should be noted that by limiting the rate of discharge, the dynamic performance of the BESS to transient loads is negatively impacted. In the case of multi-ESS systems,

like Hybrid Energy Storage System (HESS), and with coordination between different ESS, the dynamic performance of the overall system can be improved.

Combining all the discussed constraints and the system model, the formulation of the optimization problem can be represented as:

$$
\begin{aligned}
minimize\ J_N &= \sum_{k=0}^{N-1} (V_i^*[k+1] - V_i[k+1])^2 \\
subject\ to: \ \frac{di_L}{dt} &= \frac{1}{L}\left(V_B - (1-d)v_C\right) \\
\frac{dv_C}{dt} &= \frac{1}{C}\left((1-d)i_L - I_{oESS}\right) \\
d_{min} \ &\leq d[k] \ \leq \ d_{max} \\
i_{SW,min} \ &\leq i_{SW}[k] \ \leq \ i_{SW,max} \\
v_{dc,min} \ &\leq v_{dc}[k] \ \leq \ v_{dc,max} \\
SoC_{min} \ &\leq z[k] \ \leq \ SoC_{max} \\
\Delta I_{B,min} \ &\leq I_B[k] \ \leq \ \Delta I_{B,max}
\end{aligned}
\tag{3.23}
$$

The optimal predicted duty ratio vector $d[k]$ to $d[k+N-1]$ is determined by running the optimization problem described in (3.23). The first duty ratio $d[k]$ in the vector is applied to the converter switches through a PWM modulator up to the next optimization instant, while the rest of the predicted duty ratio elements are shifted back to the optimizer to be used as initial conditions for the next optimization process. The optimum duty ratio ensures a stable local DC-link voltage level. In the next section, the simulation results are introduced for many case studies, hence a robustness assessment is carried out to prove the proposed IAMPC's ability to meet the objective for unstable system parameters or degradation.

3.5 Numerical Simulation Results

The battery storage device is a battery pack connected as series and parallel combinations of Li-Ion cells. The system battery pack has a 240V voltage rating and 100Ah capacity. The battery pack consists of ANR26650M1 Nanophosphate Li-Ion cells [208]. According to the cell datasheet, 73 cells are connected in series, while 44 cells are connected in parallel to achieve the required pack ratings. The technical parameters of the Lithium ANR26650M1 cell are listed in Table 3.1, while the power converter parameters are listed in Table 3.2. The PV system technical parameters are listed in Table 3.3

Table 3.1: Li-Ion cell (ANR26650M1) technical data

Parameter	Value
Nominal Voltage	3.22V
Cell Nominal Capacity	2.3Ah
Fully charged voltage	3.7V
Internal impedance	6mΩ
Operating Temperature	-30°C to 50°C
Maximum Continuous Discharge	50A
Maximum Pulse Discharge (10 seconds)	120A

3.5.1 Convergence time assessment

In this study, a comparison is carried out between the proposed IAMPC and the conventional AMPC based on the average convergence time per optimization step of the MPC algorithm. To establish this comparison effectively, the power converter connected to the BESS is controlled to follow a specific reference for its both states, which are the DC link capacitor voltage and the inductor current. A zero initial state is assumed to effectively test the performance of both techniques by increasing the deviation between the initial and the reference states. The reference values are assumed to be 480V for the DC link

Table 3.2: BESS Power converter parameters

Parameter	Value
Input capacitor	$10\mu F$
Equivalent series resistance of input capacitor	0.074Ω
Inductor	$5mH$
Output capacitor	$15\mu F$
Equivalent series resistance of output capacitor	0.005Ω
Switching frequency	$2kHz$
Sampling time	$10\mu s$
Switch on-state resistance	$1m\Omega$
Switch snubber resistance	$100k\Omega$

Table 3.3: PV system technical parameters

Parameter	Value
Parallel Strings	70
Series-connected modules per string	9
Maximum power for one module	214W
Module open circuit voltage	36.3V
Module short circuit current	7.84A
Module voltage at maximum power point	29V
Module current at maximum power point	7.35A

voltage and 120A for the inductor current. The simulation starts at the initial state values and ends only if the system states reach the reference values with a specific tolerance. Hence, the average time per an optimization step is determined. Fig. 3.8 shows the state trajectory for the converter states at three different time shots from the initial zero states up to reaching the reference ones. It should be noted that the point inside the circle is the

current system state at the time shot, while the points indicated by stars are the predicted system states. The solid red line is the past actual states of the system. Once the states reach the required reference, the predicted states are coincident with the reference states. Fig. 3.9 shows the actual system states during the simulation time.

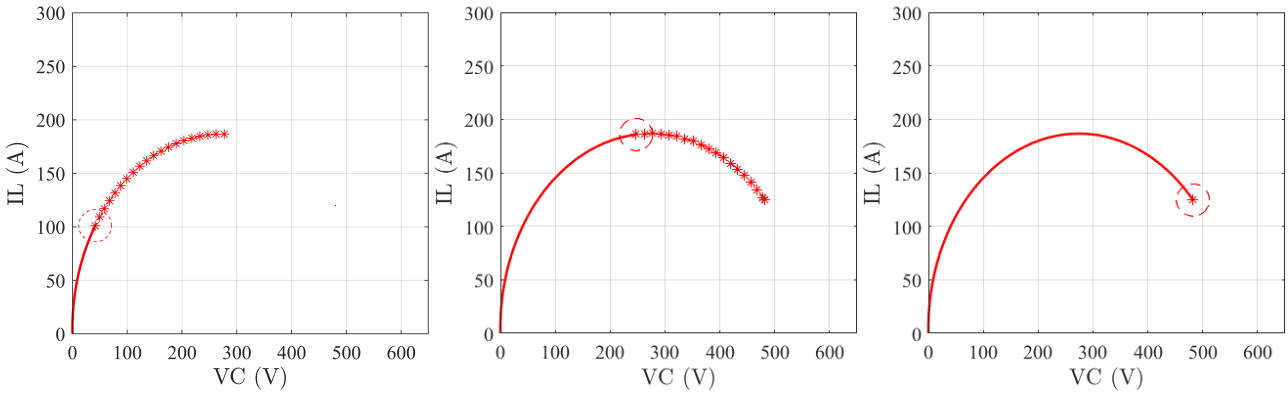

(a) t=t1 (b) t=t2 (c) t=t3

Figure 3.8: Predicted states trajectory for BESS power converter

Now, the effect of longer prediction horizons on the optimization performance is investigated. The prediction horizon is increased and both IAMPC and the conventional AMPCare tested while determining the average convergence time per optimization step for each algorithm. Fig. 3.10 illustrates the effect of increasing the prediction horizon to the convergence time for both techniques. It is obvious that the convergence time of proposed IAMPC has almost no effect on the high prediction horizon frame, however, the convergence time of the conventional AMPC is exponentially increased due to the propagation of system non-linearity through the predicted system states. Each predicted state is a function of both the predicted system at the previous time step as well as the control action (duty ratio). This function is the system dynamics itself. However, for the proposed IAMPC, all the predicted states are considered as optimization variables as well as the control actions. Although IAMPC technique has more optimization variables compared to the conventional AMPC, the system non-linearity is not propagated through the predicted system states, and hence it has extremely shorter convergence time, especially for higher

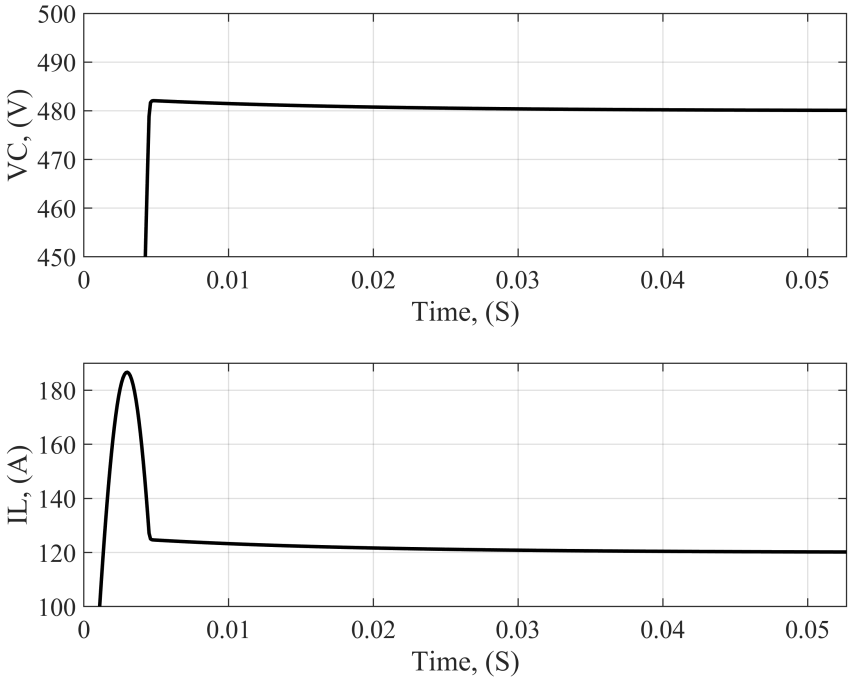

Figure 3.9: States of the BESS power converter

prediction horizons.

3.5.2 Battery SoC Limits Protection

This study focuses on battery protection and lifetime improvement. This can be ensured by ensuring the battery charging/discharging is within its safe SoC levels. The worst case occurs when the battery reaches its maximum SoC, while there is excess output energy from the PV after covering the local load demands and meeting the required dispatched current sharing of the microgrid. For this case, the proposed control system has the ability to force the PV not to operate at MPP and to change the operating point by controlling the PV-boost converter according to the SoC level of the battery. For a better demonstration of this study, the solar irradiation is considered as a constant, while the PV operates at the MPP and the battery is in charging status. When the battery reaches its maximum

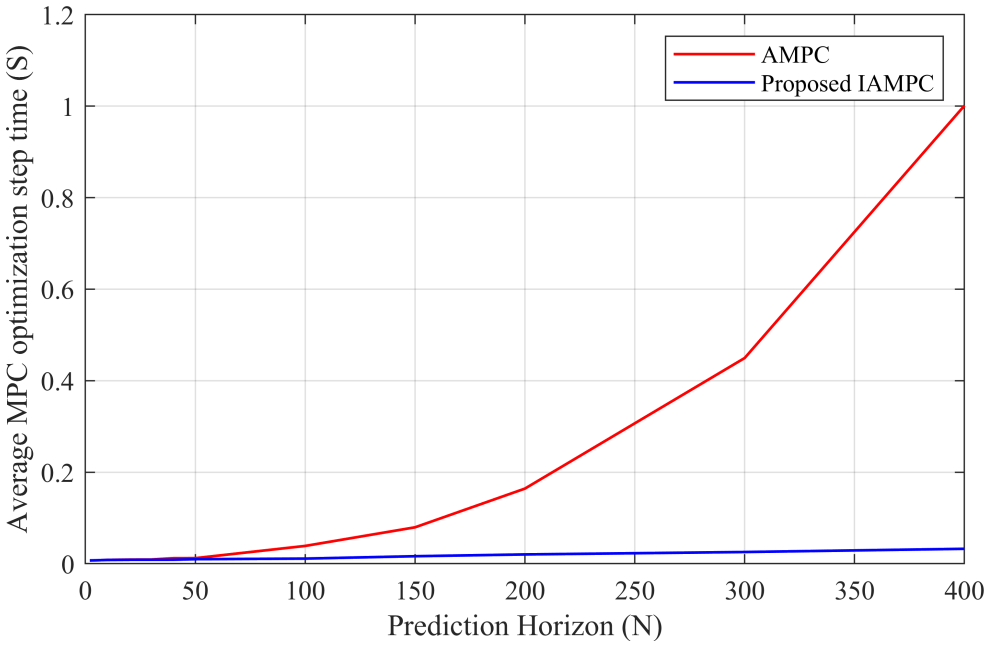

Figure 3.10: Average convergence time per an optimization step

SoC, the PV will be forced to operate at a lower operating point so that, the battery SoC remains at its limit until an increase in the load demand occurs or the load sharing level is increased. Fig. 3.11 shows the simulation results for this case study. The solar irradiation is considered to be constant at 300 W/m^2, while the battery SoC is shown in Fig 3.11b. At time $t = 2.9s$, the battery reaches its maximum SoC limit of 80%, and the controller is triggered to force the PV boost controller to change the operating point as shown in Fig. 3.11c to ensure that the maximum SoC is not exceeded. The dc-link voltage is illustrated in Fig. 3.11a where the maximum dc ripple value is 1.67%.

3.5.3 PV Fluctuated Generation Support

In this case study, a real profile of solar irradiation profile is tested to simulate the worst-case scenario of the daily PV output. Fig 3.12c shows the irradiation solar profile. It can be seen that the proposed IAMPC ensures a stable DC-link voltage level even with

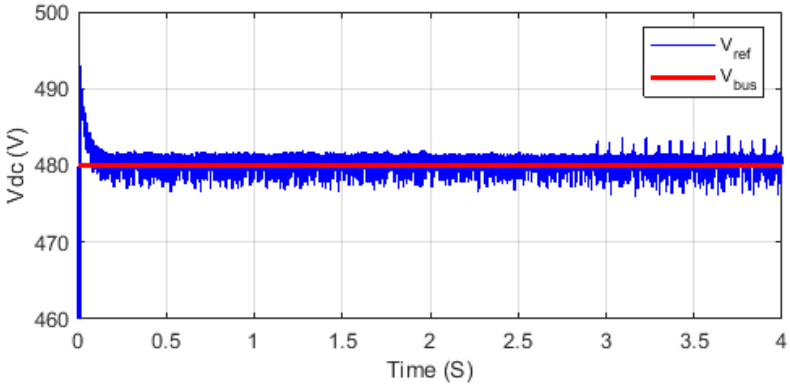

(a) Dc-link Voltage

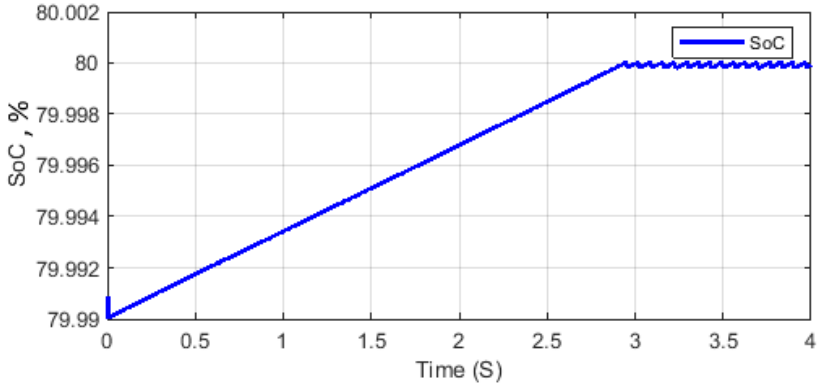

(b) Battery SoC

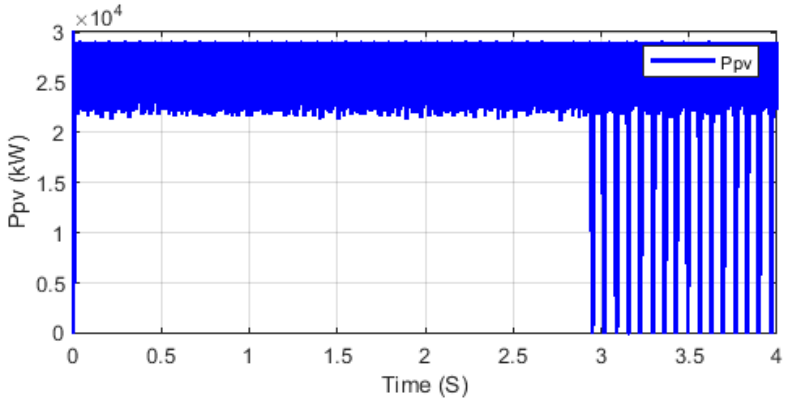

(c) Solar output power

Figure 3.11: Battery SoC Limits Protection

such a high level of fluctuation. The proposed IAMPC controls the ESS so that it absorbs or delivers power generation to support the fluctuated solar output while marinating a stable DC-link voltage and supplying the internally connected DC loads. Fig. 3.12b shows the battery bank SoC. It can be seen that the SoC profile has a downward trend due to supplying the connected constant DC loads. The slope of the SoC changes according to the solar irradiation while the loads are kept constant for this study. It can be seen that the slope is positive at high levels of Irradiation at $t = 0.7s$ and $t = 1.8s$. The dc-link voltage is illustrated in Fig. 3.11a where the maximum dc ripple value is 0.83%.

3.5.4 Variable Load Demand

In this case study, the load demand is set to be doubled momentarily at four instants to prove the proposed IAMPC control rigidness for such a high rate of change in load demands. For better demonstration, the solar irradiations are kept constant at 300 W/m^2 producing a total power of 10kW. Hence the required part of the load demand will be covered by the BESS if necessary. Fig. 3.13 illustrates the proposed IAMPC performance under transient load variations. The default load was 19.2 kW at the beginning of the simulation, which is covered jointly by the PV under MPPT control and the BESS under the proposed IAMPC. When the load is doubled at $t = 0.8S$, the battery terminal voltage gets a small drop due to the high transient of the load variation as shown in 3.13c, however, due to the fast dynamic response of IAMPC, the dc-link voltage is kept within its stable range with a maximum ripple voltage of 1.2% as shown in Fig. 3.13a. As a result of this step change in the load demand, the battery back SoC is decreasing in a higher slope as shown in Fig. 3.13d. Similarly, at $t = 1.6S$ the load demand is tripled with a total of 57.6kW, and the SoC slope is negatively increased. at $t = 2.4S$ and $t = 3.2S$, the demand is decreased to 38.4kW and 19.2kW respectively, while the dc-link voltage is effectively kept constant at its reference 480V level with a maximum ripple voltage of 1.2%.

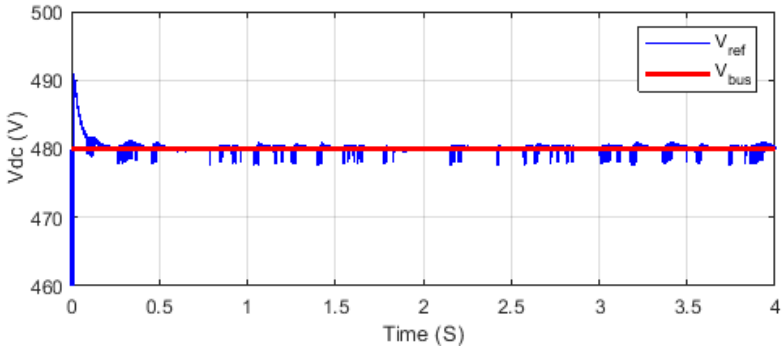

(a) Dc-link Voltage

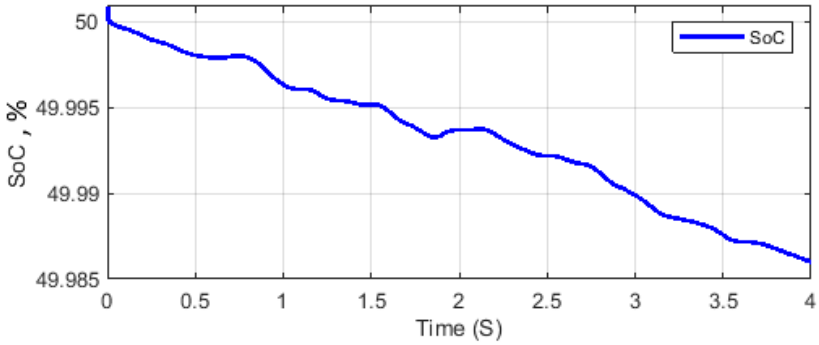

(b) Battery SoC

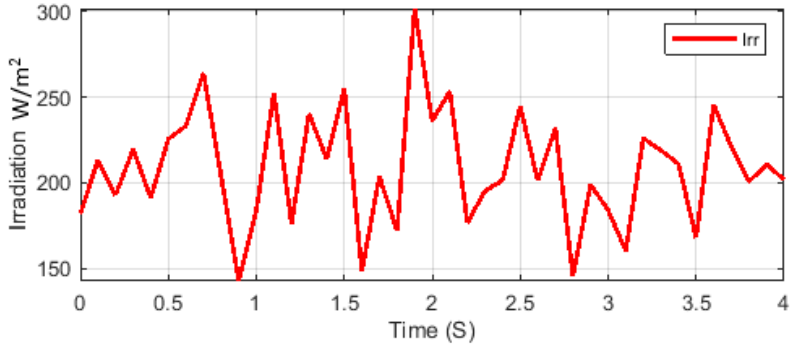

(c) Solar Irradiation

Figure 3.12: PV Fluctuated Generation Support

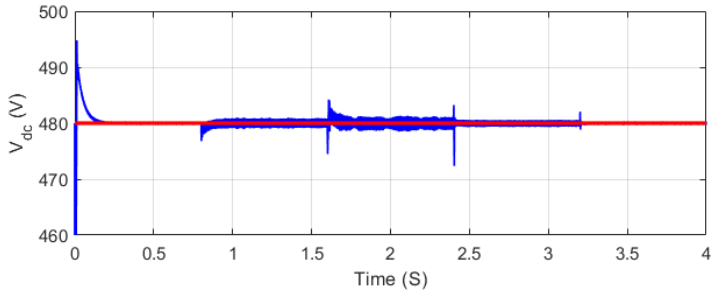

(a) Dc-link Voltage

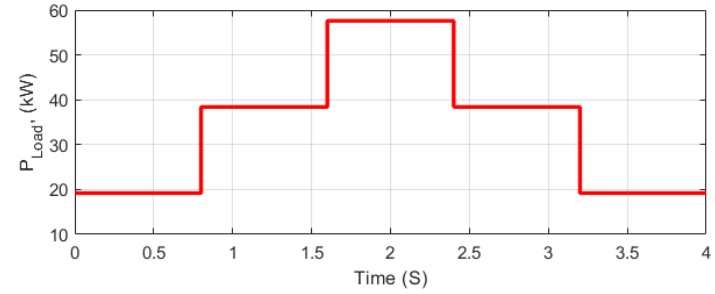

(b) Load Demand

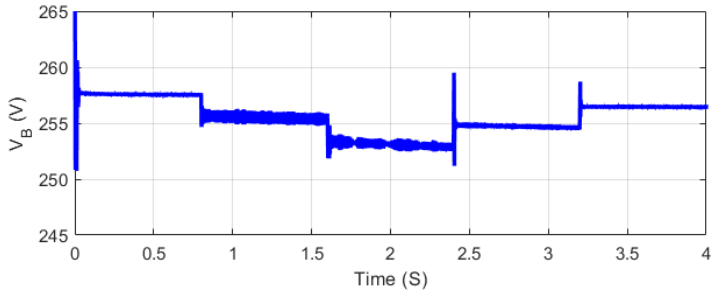

(c) Battery Pack Terminal Voltage

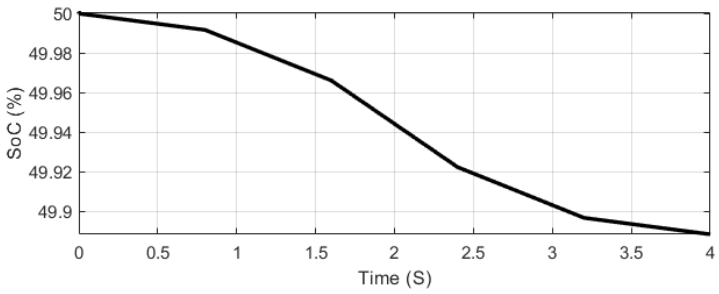

(d) Battery Pack SoC

Figure 3.13: Variable Load Demand Study

3.5.5 Battery Generation Rate of Change Control

This study provides additional improvement of the battery storage lifetime by controlling the rate of change of the battery supply current. Note that for this study, maintaining the DC link voltage is not guaranteed, as the BESS supply current cannot follow any step change in the load demand while the solar energy has a fluctuated profile. This control is optimally suitable for HESS in which there are multiple ESS with a coordinated operation.

When the load transient step occurs, the proposed IAMPC forces the BESS to slowly follow the load variations with a damped online power trajectory. Solar irradiation is considered a constant for better demonstration of the battery generation rate of change control. The trajectories are set as exponential functions with time constant τ_B which determines the response at which the BESS will handle the new value of the load demand. This time constant can be changed online according to the SoC levels. The initial load demand is 5kW and two successive step-increases to 30kW and 70kW occur at times of 0.2s and 1.2s, respectively. Fig. 3.14a shows the load current step-change and the corresponding response of the BESS current which is exponentially delayed as compared to the load current sudden change. It can be noted that the steady-state value of the BESS current is two times the value of the load current due to the converter input/output current ratio. The battery voltage and discharge current are 240V and 21A, respectively, while the DC link voltage and the converter output current are approximately 480V and 10.5A, respectively. Fig. 3.14b shows the duty ratio D of the converter switches which is approximately 0.5. There is some deviation from the nominal value due to the change in the battery terminal voltage which varies during the discharge process. It can be noted that the duty ratio increases at the load step instants to compensate for the drop in the battery terminal voltage due to the discharge current. This voltage drop can be seen in Fig. 3.14c, while the corresponding SoC is shown in Fig. 3.14d. The initial SoC is assumed to be 50% and its slope is negatively increased when load demand is step-increased.

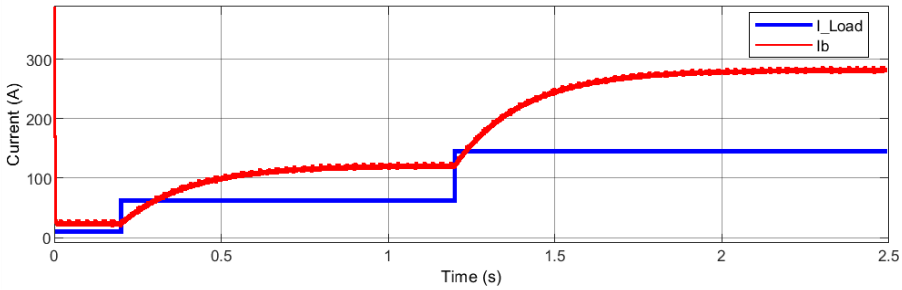

(a) Load current vs battery discharge current

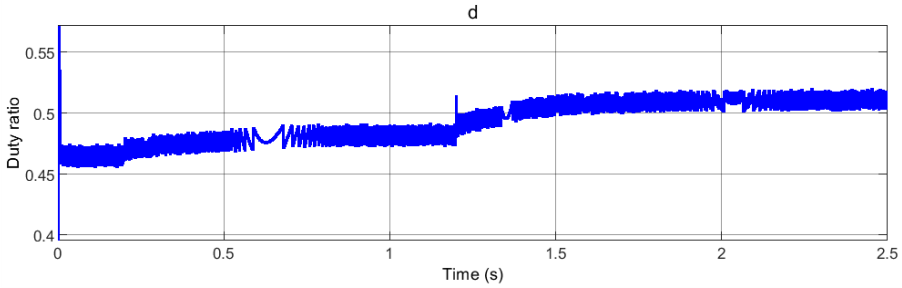

(b) bi-directional buck-boost converter duty ratio

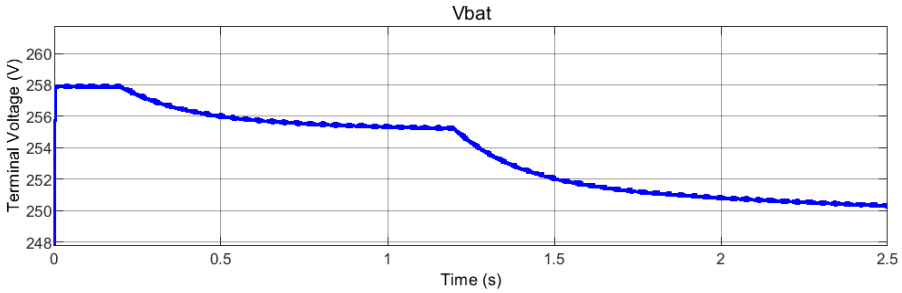

(c) Battery-pack terminal voltage

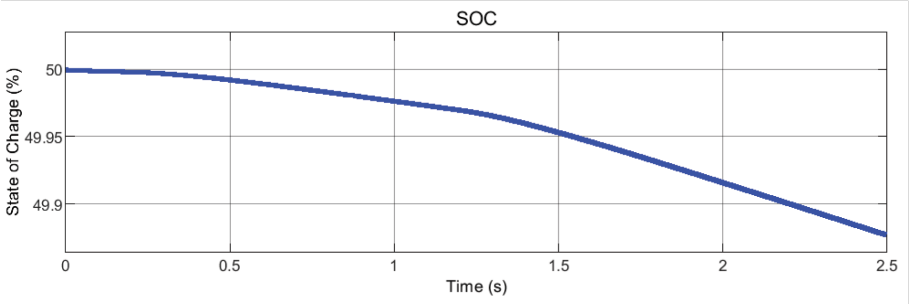

(d) Battery-pack State of Charge

Figure 3.14: Battery Generation Rate of Change Control

3.5.6 Robustness of the proposed IAMPC Control

In this study, the robustness of the proposed IAMPC will be investigated. The power converter model parameters will be changed gradually in both positive and negative ways influencing the controlled plant dynamics and then, the system is tested ensuring to what extent the control objective is achieved. For the ESS-connected dc-dc converter, the dynamic model mainly depends on the input filter inductance and the dc-link capacitor as can be noted from equation (3.16), while the duty ratio is the optimization manipulated variable. The model parameter stored in the proposed IAMPC controller is kept unchanged as stated in Table 3.2, while the physical values of both the filter inductor and the DC-link capacitor will be changed gradually. Then, the percentage ripple voltage of the DC-link will be evaluated to measure the proposed IAMPC system robustness. Firstly, the dc-link capacitor is kept constant at its design value of $15mF$, while the filter inductor value will be changed from $0.05mH$ to $8mH$. Note that the design value of the filter inductor is $1mH$, which means that the test is performed in the range of 0.05 to 8 times the design value. These test results are shown in Fig. 3.15. The design value of the filter inductor of $1mH$ is indicated by the red column with a ripple level of 0.12%. It can be shown that from the range of 0.4mH to 2mH, the ripple voltage is almost zero, while the standard level of dc-link ripples of 5% is guaranteed for the range of 0.1mH (one tenth) to 5mH (5 times).

Similarly, in the next test, the ESS-converter filter inductor is kept constant at its design value of $1mH$, while the dc-link capacitor value is changed from $1mF$ to $70mF$. The design value of the DC-link capacitor is $15mF$, which means that the test is performed in the range of 0.07 to 5 times the design value. The second test results are shown in Fig. 3.16. The design value of the dc-link capacitor of $15mF$ is indicated by the yellow column with a ripple level of 0.08%. It can be shown that from the range of 11mF to 70mF, the ripple voltage is almost zero, while the standard level of dc-link ripples of 5% is guaranteed for the range of 5mF (one third) to 70mF (5 times). These two tests prove the high stability and robustness of the proposed IAMPC against model parameter-wide variations. Note that for both tests more than 42 simulations are carried out to get the results. For all simulation cases, there wasn't any deviation of the controlled DC-link voltage regarding its reference

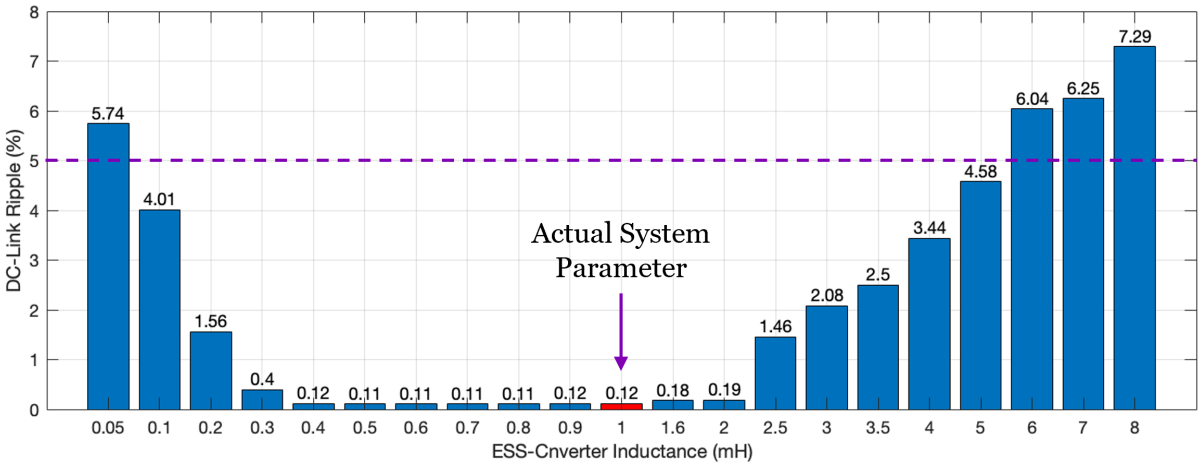

Figure 3.15: ESS-Converter filter Inductor parameter change

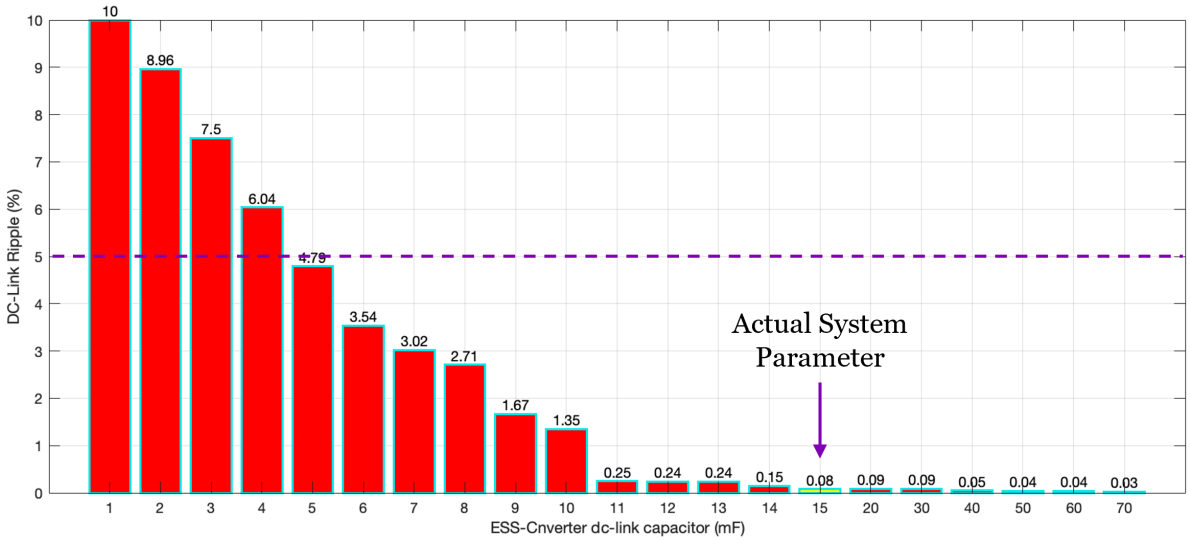

Figure 3.16: ESS-Converter dc-link capacitor parameter change

of 480V, which indicates the system's high level of stability. As a result, accurate system parameters setting is not necessary for the proposed IAMPC. Moreover, the degradation effects of the system parameters do not affect system performance.

3.6 Conclusion

This chapter presents a novel, high-speed convergence, continuous control set MPC-based controller called Improved Adaptive Model Predictive Controller (IAMPC) for DC microgrid applications. This control system ensures a coordinated operation of the ESS and DGs connected at the same microgrid node. IAMPC provides an extended lifetime of the integrated energy storage system and safe operation of the distributed generation. It also ensures effective protection of the connected ESS. Due to the short convergence time, the proposed IAMPC has a fast dynamic operation that can handle highly PV intermittent generation profiles while meeting the reference trajectory. Similarly, transient load variations are also handled effectively with the proposed IAMPC with extremely stable DC bus voltage levels. The proposed IAMPC has a high level of robustness against model parameter-wide variations. This feature will alleviate the need for accurate system parameters setting and therefore, the long-term degradation effects of the system parameters will not affect system performance. The proposed IAMPC scheme is validated through four different case studies with the help of the CasADi online optimization platform integrated with MATLAB Simulink.

Chapter 4

A Cooperative Distributed Secondary Control Strategy for DC Microgrids with Integrated Moving Horizon Estimation Layer Considering Limited Communication Burden and Cyber Threats

4.1 Introduction

In modern DC microgrids, a major challenge is designing control schemes to ensure that power is shared fairly among the various sources and that the voltages at the loads are maintained around desired values [209, 210]. Conventionally, hierarchical control schemes are used to achieve these objectives: voltage references at each connected DG converter are determined to achieve appropriate current sharing [211, 212]. However, due to the required scalability of possible control schemes, while providing a fast response to changing

loads, there has been a growing interest in the development of distributed controllers. The adoption of this distributed secondary control system has become prevalent in DC microgrids, replacing the traditional centralized approach. This shift has brought significant benefits including improved scalability, enhanced reliability, and resiliency to a single point of failure [213]. Simultaneously achieving a form of voltage regulation appears to be more challenging and provided solutions often rely on simplifying assumptions [214]. Cooperative and consensus-based distributed control algorithms have emerged as popular options for secondary control in DC microgrids achieving both microgrid objectives (i.e. proportional current sharing and voltage balancing) [215–218]. These approaches rely on peer-to-peer communication and information exchange among neighboring distributed generation units. However, increasing the number of communication channels and exchanged data can negatively impact the reliability and resilience of DC microgrids due to communication delays, packet drop, and vulnerability to cyber-attacks [219].

This chapter proposes a consensus-based strategy that can maintain the DC microgrid objectives (Load sharing and voltage balancing) with reduced communication links between agents. This strategy doesn't require knowledge of the microgrid transmission parameters. This feature of the proposed strategy can effectively reduce the risk of cyber threats while facilitating a plug-and-play operation of microgrid agents. Moreover, the strategy incorporates a state estimation layer that utilizes a MHE technique for detecting and mitigating cyber threats and system uncertainties. The main salient contributions for this section can be listed as follows:

- A limited communication, consensus-based cooperative secondary controller is proposed for optimum DC microgrid operation achieving proportional load sharing and global voltage regulation.
- An integrated state estimation layer based on MHE is proposed to ensure the resiliency of the control system against cyber threats and uncertainties.
- A robustness and resiliency assessment of the proposed controller is carried out through the following case studies:
  - Power lines disconnection.

- Plug-in and Plug-out of DG units (Plug and Play operation).
- Failure of communication links or communication delays.
- Presence of measurement uncertainties or cyber threats.

For the rest of this chapter, the graphical representation of the DC microgrid will be demonstrated in section 4.2, which includes physical and cyber system modeling. Following that, section 4.3 will discuss the fundamental distributed cooperative operation of the DC microgrid, the mathematical formulation of the primary objectives, and communication requirements. Section 4.4 will explain the concept of consensus dynamics and the investigation of constructing conventional consensus-based distributed controllers, addressing the limitations and problem formulation. The proposed control strategy construction, including the state estimation proposed layer, will be introduced in section 4.5. Finally, in section 4.6, various case studies' numerical simulations will be presented, and section 4.7 will conclude the chapter.

4.2 Graphical Modelling of DC microgrid

This section illustrates DC microgrid modeling in physical and cyber layers. Each DG is modeled as a DC source connected to a DC-DC converter considering the filter dynamics. Each DG is connected to other neighbors through power lines as well as communication links. Power lines are represented by their resistive and inductive parameters. There is a local load connected to each DG node. On the other hand, the communication cyber network has also to be modeled to examine the data flow between DGs during the microgrid operation. The DG model is illustrated in Fig. 4.1, while the dynamic equations for i^{th} DG can be represented as follows:

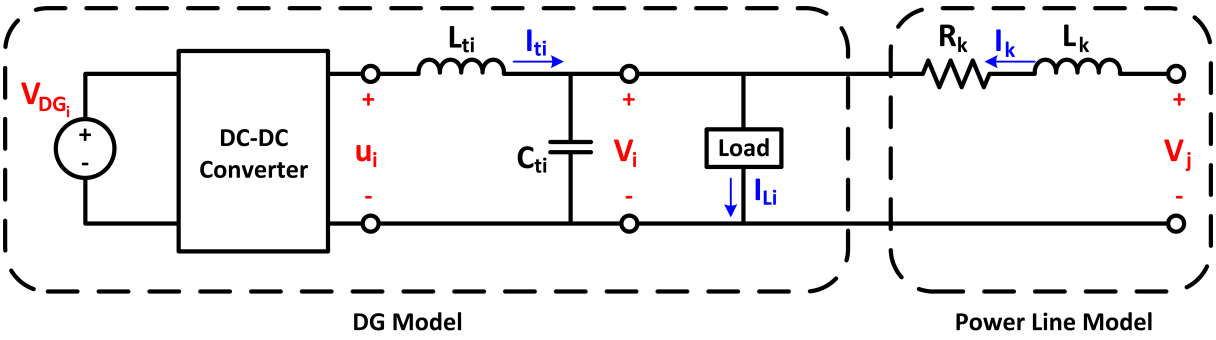

Figure 4.1: DC microgrid DG model

$$
\begin{aligned}
L_{ti}\frac{dI_{ti}}{dt} &= -V_i + u_i \\
C_{ti}\frac{dV_i}{dt} &= I_{ti} - I_{Li} + \sum_{k\in\mathscr{E}_i} I_{k,i} \\
L_k\frac{dI_k}{dt} &= (V_j - V_i) - R_k I_k \quad \forall k \in \mathscr{E}_i
\end{aligned}
\tag{4.1}
$$

where u_i is the converter output voltage, V_i is the i^{th} DG voltage, C_{ti} and L_{ti} are the converter filter parameters, I_{ti} is the converter inductor current, I_{Li} is the current of the load connected at the i_{th} node, and R_k and V_k are the parameters for the power line k. It should be noted that the communication links are not necessary to be consistent with the physical power lines. In other words, the physical and cyber networks have different configurations. Physical and Cyber models are introduced in the following subsections.

4.2.1 Physical DC Microgrid Model

The physical system of a DC microgrid consists of many electrical sources (DGs/ESS) and loads interchanging energy through a power line network. For each bus (node) the DG-Load configuration is illustrated in Fig. 4.1. The overall DC microgrid can be represented

by the following graph function [220]:

$$\begin{aligned} \mathscr{G} &= \{\mathscr{V}, \mathscr{E}\} \\ \mathscr{V} &\text{ is the set of DG nodes} = \{1, 2, ..., n\} \\ \mathscr{E} &\text{ is the set of power lines } = \{1, 2, ..., m\} \end{aligned} \tag{4.2}$$

where n is the number of DG nodes, while m is the number of microgrid power lines. The interconnection between the system DGs and the power line network can be illustrated through an incident matrix $\mathscr{B} \in \mathbb{R}^{nxm}$. Each element in the $\mathscr{B}$ can be expressed as:

$$\mathscr{B}_{ik} = \begin{cases} +1 & \text{if } i \text{ is the negative terminal of line } k \\ -1 & \text{if } i \text{ is the positive terminal of line } k \\ 0 & \text{if } i \text{ is not connected to power line } k \end{cases} \tag{4.3}$$

So, the Boolean nxm incident matrix can be formulated as follows:

$$\mathscr{B} = \begin{bmatrix} \mathscr{B}_{11} & \mathscr{B}_{12} & \dots & \mathscr{B}_{1m} \\ \mathscr{B}_{21} & \mathscr{B}_{22} & \dots & \mathscr{B}_{2m} \\ \vdots & \vdots & \ddots & \vdots \\ \mathscr{B}_{n1} & \mathscr{B}_{n2} & \dots & \mathscr{B}_{nm} \end{bmatrix} \tag{4.4}$$

Based on the previous definition of the incident matrix in equations 4.3 and 4.4, It can be noted that for any network configuration, the summation of all elements in each column in the incident matrix $\mathscr{B}$ equal zero. This result can be expressed as:

$$\mathbb{1}_n^T \mathscr{B} = 0, \quad \mathbb{1}_n \in \mathbb{R}^{n\text{x}1} \tag{4.5}$$

where $\mathbb{1}_n$ is an nx1 vector containing ones. The physical DC microgrid can be represented in matrix form as a function of the incident matrix as follows:

$$\begin{aligned} L_t \dot{I}_t &= -V + u \\ C_t \dot{V} &= I_t + \mathscr{B} I_k - I_L \\ L_k \dot{I}_k &= -\mathscr{B}^T V - R_k I_k \end{aligned} \tag{4.6}$$

where I_t, V, I_L, and u are the vectors of inductor currents, node voltages, load currents, and power converter voltages, respectively. All these vector $\in \mathbb{R}^{n\text{x}1}$. I_L is the load current vector $\in \mathbb{R}^{m\text{x}1}$. L_t and C_t are the power converters' filter inductors and capacitors diagonal matrices $\in \mathbb{R}^{n\text{x}n}$, respectively. L_k and R_k are the power lines' inductors and Resistors diagonal matrices $\in \mathbb{R}^{m\text{x}m}$, respectively. It should be noted that for the DC microgrid model in equation 4.6, the loads are connected to the PCC for each DG node as shown in Fig. 4.1. For DC microgrids with internal non-connected DG nodes, the Kron reduction technique is widely used for obtaining the reduced model of DC microgrid obtained in Fig. 4.1 [221, 222].

4.2.2 Cyber DC Microgrid Model

It should be noted that the cyber network of the DC microgrid is not necessary to be consistent with the physical network [223, 224]. In other words, the cyber network may have a different configuration as compared to the physical microgrid configuration. For example, for a mesh (loop) physical configuration, the cyber network may be connected as a spanning tree in which the communication links have a smaller number than the power lines [225]. Moreover, the direction of data flow should be considered in the cyber model. A bidirectional (undirected) communication graph is considered in this study which represents the data flow between the microgrid nodes (vertices) through the communication links [226]. The communication graph can be modelled using an adjacency matrix $\mathbb{A} \in \mathbb{R}^{n\text{x}n}$ which has the following weight elements:

$$a_{ij} = \begin{cases} > 0 & \text{if } (x_i, x_j) \in E \\ 0 & \text{else} \end{cases} \tag{4.7}$$

where E is the set of communication links, while x_i and x_j are the local and neighbor nodes. It should be noted that for the positive weight of a_{ij} the data direction is from the neighbor node j to the local node i. However, as the communication graph is bidirectional,

we can write:

$$\begin{aligned} a_{ii} &= 0 \quad \forall\, i \in \mathscr{V} \\ a_{ij} &= a_{ji} \quad \forall\, (x_i, x_j) \in E \end{aligned} \tag{4.8}$$

As a result, the adjacency matrix can be formulated based on the communication network weights as follows:

$$\mathbb{A} = \begin{bmatrix} 0 & a_{12} & a_{13} & \dots & a_{1n} \\ a_{12} & 0 & a_{23} & \dots & a_{2n} \\ a_{13} & a_{23} & 0 & \dots & a_{3n} \\ \vdots & \vdots & \ddots & & \vdots \\ a_{1n} & a_{2n} & a_{3n} & \dots & 0 \end{bmatrix} \tag{4.9}$$

On the other hand, an In-degree diagonal matrix D^{in} is defined to indicate the input data flow for each node in the DC microgrid. It can be represented as:

$$\begin{aligned} D^{in} &= diag\{d_i^{in}\} \\ d_i^{in} &= \sum_{j \in N_i} a_{ij} \\ N_i &= \{j \mid (v_j, v_i) \in E\} \end{aligned} \tag{4.10}$$

where N_i is the ith DG neighbor set. In the same way, an Out-degree matrix D^{out} is an indicator of data output flow for each node. If the communication links are bidirectional, then $D^{out} = D^{in}$. Moreover, the communication graph Laplacian matrix becomes balanced. Laplacian matrix can be expressed as follows:

$$\mathfrak{L} = D^{in} - \mathbb{A}, \qquad \mathfrak{L} \in \mathbb{R}^{n \text{x} n} \tag{4.11a}$$

$$\mathbb{1}_n^T\, \mathfrak{L} = 0 \tag{4.11b}$$

where $\mathbb{1}_n \in \mathbb{R}^{n\text{x}1}$ is a vector containing all one elements. The elements in the Laplacian matrix can be expressed as:

$$\mathfrak{L}(i,j) \quad = \quad \begin{cases} -a_{ij} & \text{if } i \neq j \\ \sum_{r \in N_i} a_{ir} & \text{if } i = j \end{cases} \tag{4.12}$$

For easier demonstration Fig. 4.2 illustrates different communication cases as well as communication failure cases, and the corresponding unweighted adjacency and in-degree matrices. It should be noted that equations 4.11b and 4.12 prove that the summation of all elements in each column of the Laplacian matrix equal zero, which indicates that the Laplacian matrix is balanced due to the undirected communication data flow [223, 227].

4.3 Distributed Cooperative Operation of DC Microgrids

Fig. 4.3 shows a layout of a typical DC microgrid including its physical and cyber layers. The physical layer includes the energy sources (DGs/ESS), power lines, and loads. The cyber layer consists of a communication network with a sparse structure that facilitates data exchange across the microgrid. This network contains a communication graph that is designed to remain functional even if some links fail [228] to be at least a spanning tree communication. Each converter transmits a set of data to its neighbors, which includes the converter's estimate of the microgrid's average voltage, the converter's actual local voltage measurement, and the measured current. The control layer is responsible for achieving two objectives: global voltage regulation for all microgrid nodes, and proportional load sharing among all connected DGs based on their different capacities. These two objectives are described in detail in the next subsections. It should be noted that based on equation 4.6, for a given steady state control input vector $\bar{u}$, a steady state solution of the system states (inductor current vector $\bar{I}_t$, node voltage vector $\bar{V}$, and power line current vector) that should satisfy the following equation:

$$\bar{V} = \bar{u} \tag{4.13a}$$

$$-\mathscr{B}\bar{I}_k = \bar{I}_t - \bar{I}_L \tag{4.13b}$$

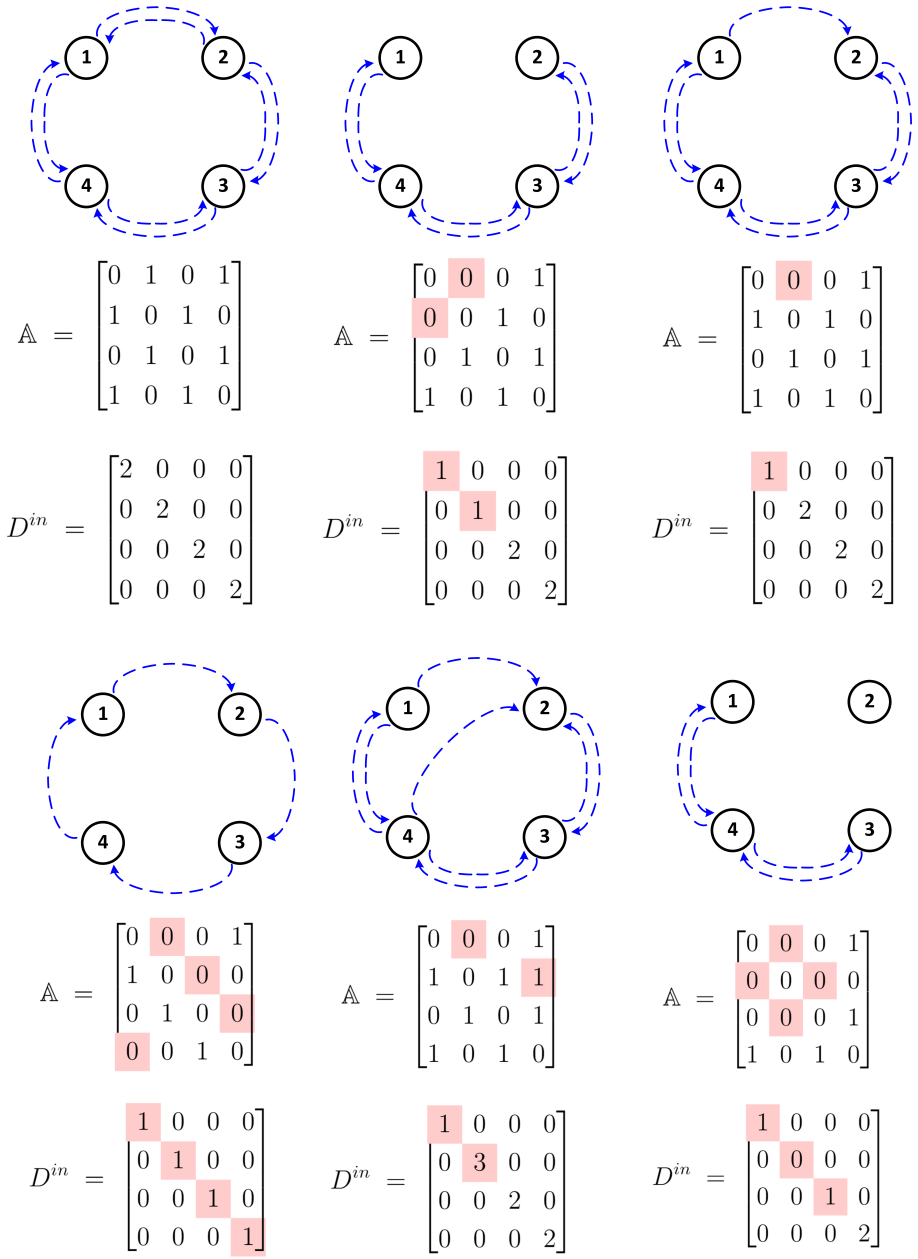

Figure 4.2: Adjacency and In-degree matrices for different communication cases in 4 communication node system

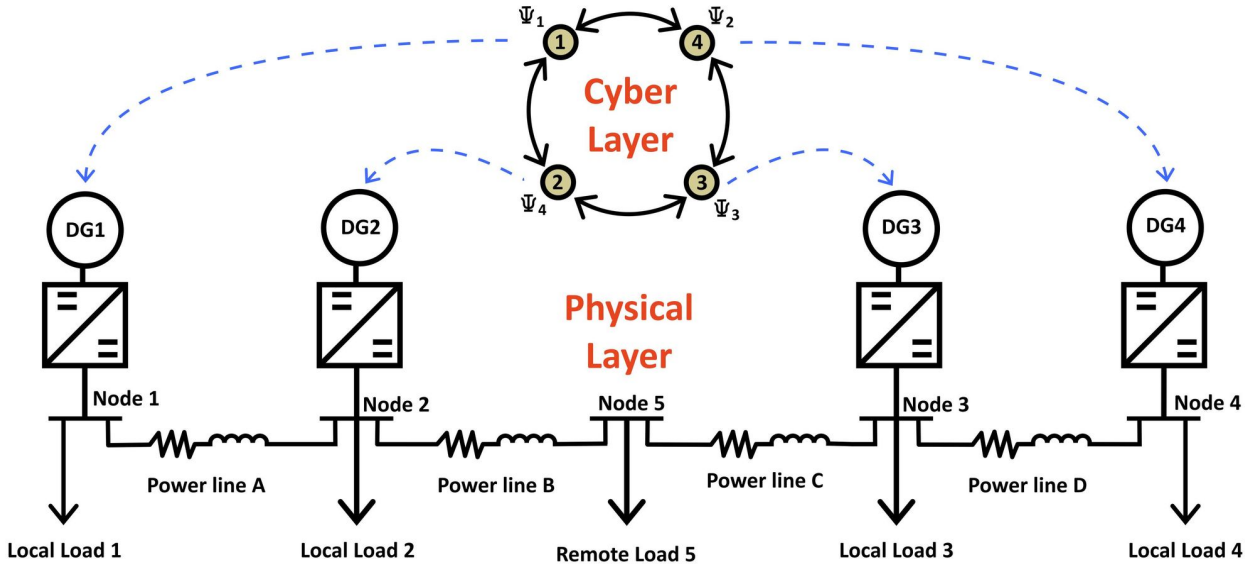

Figure 4.3: Typical layout of DC microgrid physical and cyber layers

$$\bar{I}_k = -R_k^{-1}\mathscr{B}^T\bar{V} \tag{4.13c}$$

It should be noted that equation 4.13b implies the current balance of the network. In other words, it means that the total current generated by DGs equals the total load currents. This point can be explained by multiplying equation 4.13b by $\mathbb{1}_n^T$ and using equation 4.5. The mathematical representation of the point can be expressed as:

$$-\mathbb{1}_n^T\mathscr{B}\bar{I}_k = \mathbb{1}_n^T\bar{I}_t - \mathbb{1}_n^T\bar{I}_L = 0 \tag{4.14}$$

4.3.1 Objectives of Cooperation Operation

4.3.1.1 Proportional Load Sharing

In order to enhance the generation efficiency of the DGs, it is crucial to ensure proportional current sharing among the various DGs based on the generation capacity of their corresponding energy sources [151]. This can be achieved as:

$$\omega_i I_{ti} = \omega_j I_{tj} \qquad \forall i, j \in \mathscr{V} \tag{4.15}$$

where ω_i represents the generation capacity of converter i. Achieving this objective will result in the desired steady-state value of the generated currents I_t, thereby enhancing the overall generation efficiency. Proportional load sharing objective can be expressed mathematically as [229]:

$$\begin{aligned} \lim_{t\to\infty} I_t(t) \;&=\; \bar{I}_t \;=\; W^{-1}\mathbb{1}_n i_t^* \\ i_t^* &= \frac{\mathbb{1}_n^T I_L}{\mathbb{1}_n^T W^{-1}\mathbb{1}_n} \qquad \in \mathbb{R} \\ W = diag\{\omega_1, \omega_2, ..., \omega_n\}, &\quad \omega_i > 0 \quad \forall i \in \mathscr{V} \end{aligned} \tag{4.16}$$

where i_t^* can be defined as the per unit value for all connected DGs, while W is the load current weight matrix for all DGs.

4.3.1.2 Global Voltage Regulation

It should also be noted that based on equation 4.13b and 4.13c, the steady-state voltage is satisfying the following equation [230]:

$$\mathscr{B}R_k^{-1}\mathscr{B}^T\bar{V} = \bar{I}_t - \bar{I}_L = W^{-1}\mathbb{1}_n i_t^* - \bar{I}_L \tag{4.17}$$

where the term $\mathscr{B}^T\bar{V}$ represents the voltage difference between the microgrid-connected nodes which affects the proportional current-sharing process. However, based on the construction of the incident matrix $\mathscr{B}$, the node voltages have the freedom to be shifted with a

constant value while maintaining the proportional load-sharing objective. In other words, it can be stated that:

$$\mathscr{B}^T \bar{V} = \mathscr{B}^T (\bar{V} + a\mathbb{1}_n), \qquad a \in \mathbb{R} \tag{4.18}$$

As a result, the node voltages have to be regulated globally. To define the optimal steady-state node voltages, it is assumed that there is a desired voltage reference at each node PCC V_i^* for all $i \in \mathscr{V}$. The selection of values for V_i^* can be done identically for all microgrid DG nodes.

However, it is generally not possible to achieve $\bar{V} = V^*$ due to the requirement of current sharing, which may cause deviations in voltage from the corresponding reference values. Therefore, an alternative approach is to maintain the weighted average value of the PCC voltages at the steady state to be identical to the weighted average value of the desired reference voltages V^* (known as global voltage balancing) [231]. To achieve this, weights of $1/\omega_i$ can be chosen for all $i \in \mathscr{V}$, so that the DGs with a relatively large generation capacity experience a relatively small voltage deviation. It is common practice for sources with the largest generation capacity to determine the microgrid voltage. As a result, given V^*, a secondary controller has to be designed to meet both load current sharing described in the previous sub-section and the voltage balancing requirement. It should be noted that the node reference voltages V^* are generated by an upper-level control system, which is commonly referred to as the tertiary control [232]. The tertiary controller is responsible for setting the desired value of V^* and sending it to the secondary control layer. In this manner, the value of V^* is made known to the secondary controller, enabling it to regulate the voltage within the microgrid effectively. Global voltage regulation objective and be mathematically represented as:

$$\lim_{t\to\infty} \mathbb{1}_n^T W^{-1} V_t(t) \;=\; \mathbb{1}_n^T W^{-1} \bar{V} \;=\; \mathbb{1}_n^T W^{-1} V^* \tag{4.19}$$

4.3.2 Communication Requirements for Secondary Controller

To meet the previously stated two objectives: proportional load sharing (equation 4.16) and global voltage regulation (equation 4.19), it is necessary for microgrid to have a cooperative distributed control approach for their secondary control layer. This strategy involves each

DG unit sharing its local current $I_{ti}(t)$, local PCC voltage $V_i(t)$, and estimated average voltage value across the microgrid $\hat{V}_i(t)$ with its adjacent DG units. The communication graph utilized in this strategy has been discussed in the cyber-microgrid model section with an adjacency matrix $\mathbb{A} \in \mathbb{R}^{n \times n}$ and a Laplacian matrix $\mathfrak{L} \in \mathbb{R}^{n \times n}$.

4.4 Conventional Consensus-based Distributed Secondary Controller

As mentioned before, a cooperative operation of the DC microgrid secondary control layer is essential to achieve proportional load sharing and global voltage regulation in DC microgrids. In this context, there are many developed strategies presented to achieve these objectives. A detailed survey about different control strategies for DC microgrid is listed in [59, 132, 212, 233–235]. One of the most promising techniques that have been developed in the recent literature is the consensus-based control strategy [44, 236], which is described in detail in the next subsection. The main objective of the consensus algorithm is to update the local controller settings - and hence send the output reference voltage to the primary controller - based on the available data from the neighbor agents [216]. It should be noted that the local reference voltage to be fed to the primary controller at each node is not the same as the global microgrid reference voltage provided by the tertiary control layer [237]. The difference between the global and local reference voltages is the correction factors provided by the secondary control layer [238]. These correction factors are required to achieve the microgrid objectives (the global voltage regulation and the proportional load sharing). The first correction factor is related to the global voltage regulation objective in which a consensus-based voltage observer sublayer is used to update the local reference voltage based on the neighbor voltage data [239]. The proportional load-sharing objective is achieved using a current regulator sublayer which is responsible for updating the second correction factor based on the deviation of the per-unit current of the local and neighbor current measurements [217, 240]. The operation of these two sublayers is described in the next subsections.

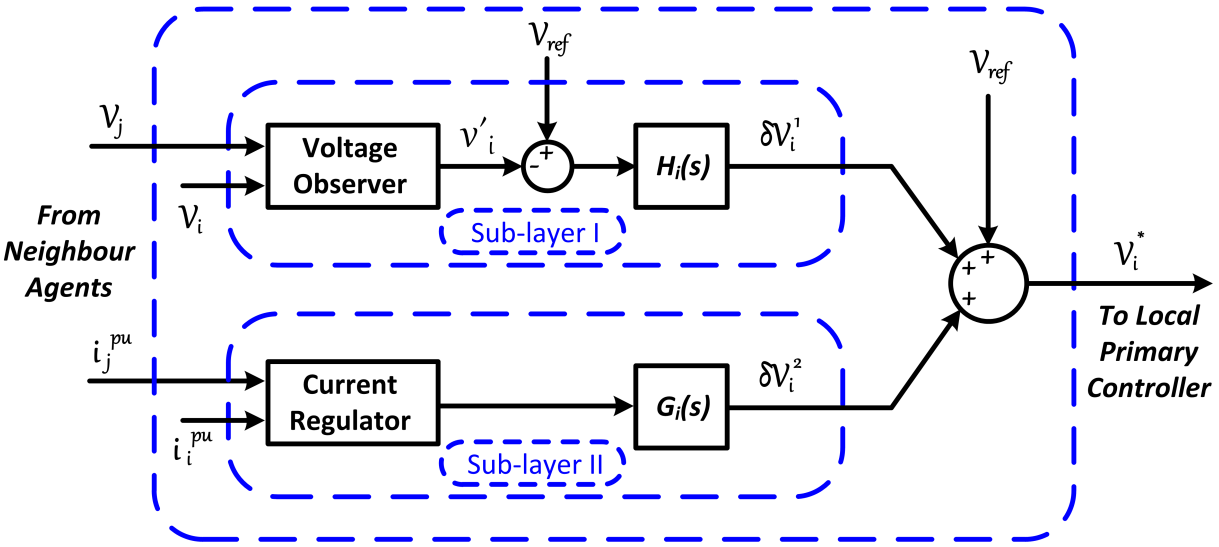

Figure 4.4: Conventional Consensus-based distributed controller

4.4.1 Dynamic Consensus Concept

The basic idea of a consensus-based algorithm is that all the agents in the system (DGs) communicate with each other to reach a consensus on the desired power flow [241]. This consensus is then used to adjust the power output of each agent in the system to ensure that the overall power balance is maintained [242]. The consensus-based algorithm is implemented using a distributed control architecture. This architecture allows each agent in the system to have its controller, which communicates with other controllers to achieve the consensus. The consensus-based algorithm involves three main steps [8]:

- **Information exchange:** Each agent shares its local information, such as output current and voltage, with its neighbors.
- **Consensus formation:** Based on the information received from neighbors, each agent updates its current output to achieve the consensus.
- **Current adjustment:** Once the consensus is reached, each agent adjusts its current output to maintain the desired current flow in the system (proportional load sharing).

4.4.2 Consensus-based Voltage Observer

The consensus-based voltage observer is responsible for estimating the voltage of each node PCC in the microgrid system. In this sublayer, each connected DG in the microgrid estimates its voltage using local measurements and exchanges this information with its neighboring agents. The neighboring nodes then use this information to update their voltage estimates through a correction factor, and the process continues until a consensus is reached among all microgrid nodes. This technique allows for decentralized control of the microgrid, as each DG only needs to communicate with its neighbors, rather than relying on a central controller [243]. The mathematical formulation of the estimated voltage at PCC for each node based on the consensus algorithm is as follows [8, 224]:

$$\hat{V}_i(t) = V_i(t) + \int_0^t \sum_{j \in E} a_{ij}(\hat{V}_j(\tau) - (\hat{V}_i(\tau))d\tau \tag{4.20}$$

where $\hat{V}_i$ and $\hat{V}_j$ are the estimated (predicted) voltage for local and neighbor nodes respectively. V_i is the local voltage measurement, while a_{ij} is the communication weight of the adjacency matrix $\mathbb{A}$. By taking the first derivative and rewriting the equation in matrix form, equation 4.20 can be represented as:

$$\dot{\hat{V}} = \dot{V} - \mathfrak{L}\hat{V} \tag{4.21}$$

where $\hat{V}$ and V are the node estimated and measured vectors respectively, while $\mathfrak{L}$ is the communication Laplacian matrix. To derive the dynamic model of the consensus-based voltage observer, equation 4.21 can be expressed in the frequency domain as [244]:

$$\hat{V} = S(SI_n + \mathfrak{L})^{-1}V = G_{observer}V \tag{4.22}$$

where I_n is the identity matrix $\in \mathbb{R}^{nxn}$ while $G_{observer}$ is the consensus-based voltage observer transfer function. Now, the first correction factor vector can be determined based on the estimated voltage vector and the given microgrid global voltage as [245]:

$$\Delta V^1 = H(V^{ref} - \hat{V}) = H(V^{ref} - G_{observer}V) \tag{4.23}$$

where V^{ref} is the global microgrid reference voltage given by the tertiary control layer, while $H = diag\{H_i\}$ for all $i \in E$ is the voltage controller matrix. It should be noted that in

islanded microgrid mode operation, the microgrid's global reference voltage, V^{ref}, typically equals the rated voltage of the microgrid. However, for grid-connected mode, where the microgrid exchanges power with the main grid, the tertiary control system establishes a new voltage level for the microgrid and communicates the updated reference value to each converter [8].

4.4.3 Cooperative Current Regulator

The main goal of this current regulator is to ensure that each connected DG in the microgrid contributes the appropriate amount of current to the system. In other words, we can say that the current regulator objective is to maintain a constant per-unit output current for all connected DGs. The regulator achieves this by using information about the current output of neighboring agents and generating the second correction factor to the local reference voltage for each DG. The local calculation of the per-unit current mismatch factor at node i can be expressed as:

$$\delta_i = -\sum_{j \in E} c\ a_{ij}\left(\frac{I_{ti}}{I_{ti}^{max}} - \frac{I_{tj}}{I_{tj}^{max}}\right) \tag{4.24}$$

where c is the voltage-current coupling gain, while I_{ti}^{max} and I_{tj}^{max} are the maximum current capacities of local and neighbor converters respectively. Based on equation 4.24, the second correction factor can be expressed in matrix form as:

$$\Delta V^2 = -c\ G\ \mathfrak{L}\ I_t^{pu} = -c\ G\ \mathfrak{L}\ I_{t,rated}^{-1} I_t \tag{4.25}$$

where $G = diag\{G_i\}$ for all $i \in E$ is the current controller matrix, while I_t^{pu} is the per-unit vector of the DG currents. Now, the local reference voltage vector for all DG units can be expressed in matrix form as:

$$\begin{aligned} V^* &= V^{ref} + \Delta V^1 + \Delta V^2 \\ &= (I_n + H)V^{ref} - HG_{observer}V - c\ G\ \mathfrak{L}\ I_{t,rated}^{-1} I_t \end{aligned} \tag{4.26}$$

4.4.4 Limitations and Problem Formulation

It is well known that cooperative distributed control of DC microgrid has several advantages over the centralized control counterpart: flexibility, resiliency, scalability, and reduced infrastructure costs [59, 78]. However, the use of communication in cooperative distributed control also introduces vulnerabilities that can be exploited by malicious data [246] and communication delay problems [217]. System security has a crucial role in ensuring reliable and unbiased coordination among microgrid agents. To maintain security, it is important to guard against potential threats such as cyber-attacks, which can take various forms such as false data injection attacks FDI, DoS, and replay attacks. These attacks have the potential to destabilize the network and the control structures.

The consensus-based distributed control has several advantages over other control methods. It is a distributed control approach, which means that it does not require a centralized controller. This makes the system more resilient to failures and easier to scale [232, 247]. However, maintaining a secure data transmission (agents' PCC voltage and injected current) through the communication network remains a major concern [220, 223].

In the recent literature consensus-based distributed control has been used for global voltage regulation and proportional current-sharing objectives. The stability and resiliency of this distributed control have been discussed in references [217] and [216] respectively.

For the sake of simplifying the controller design, many of the current studies rely on a simplified DC microgrid model though neglecting line inductance [248], assuming identical physical and cyber networks [82], assuming the full knowledge of microgrid parameters [228], or assuming constant local load currents [224]. Additionally, several studies have devised methodologies to address various forms of cyber threats and communication delays [248–250]. However, based on the general construction of the distributed consensus-based controllers, each connected DG has to exchange all of DG PCC voltage, estimated PCC voltage, and locally generated current through the communication network to the neighbor agents to perform the consensus correction factors [251]. This is obvious through equations 4.23 and 4.25 respectively, leading to more complicated controller implementation. Additionally, each of these data may be subjected to an attack, communication delay, or even a loss of communication, which can affect the cooperative controller's reliability.

Moreover, it is required to develop the security layer for each piece of data to ensure communication security. Limiting the communication requirements is a partial solution that can reduce the risk of cyber threats; however, this issue has barely been tackled in the literature. In [214], an averaging controller is introduced to maintain global voltage balancing and load sharing while requiring limited information locally and considering constant load currents. In [252], different types of loads are considered. On the other hand, in [232] another distributed controller is introduced with limited communication requirements based on an unweighted communication graph. Although the aforementioned studies meet the objectives of voltage balancing and current sharing, they didn't consider the presence of cyber threats or measurement uncertainties. Moreover, these controllers are not tested for contingency conditions like power line outages, communication link failures, or Plug-in operations. Furthermore, the voltage balancing operation is unbounded, which could result in over-voltage for high-capacity agents.

4.5 Proposed Distributed Cooperative Secondary Controller

In this section, the proposed cooperative secondary control strategy is introduced. Although this strategy relies on consensus-based operation, it requires minimal communication links between agents. Additionally, it does not necessitate knowledge of microgrid parameters for any plugged-in agent, which enables the plug-and-play operation of microgrid agents. Moreover, it has a bounded operation of voltage balancing to prevent over-voltage at high-capacity DGs. Having limited communication requirements reduces the risk of cyber threats. Additionally, the proposed strategy incorporates a state estimation layer that employs MHE algorithm which improves the control system resiliency against cyber threats and measurement uncertainties.

4.5.1 Mathematical Formulation

The proposed controller can control the coupled dynamics of the agent voltage and the generated current simultaneously. For the sake of simplicity, the distributed controller will be represented at just one node i, then it will be represented in matrix form for all microgrid agents. The controller at node i can be mathematically represented as follows:

$$\beta_i \dot{\chi}_i = \sum_{j \in E} a_{ij}(w_j I_{tj} - w_i I_{ti}) \quad , \chi_i \in \mathbb{R}^{nx1} \tag{4.27a}$$

$$\gamma_i \dot{\upsilon}_i = -\upsilon_i + I_{ti} \quad , \upsilon_i \in \mathbb{R}^{nx1} \tag{4.27b}$$

$$u_i = -k_i(I_{ti} - \upsilon_i) - w_i \sum_{j \in E} a_{ij}(\chi_j - \chi_i) + V_i^{ref} \tag{4.27c}$$

where β_i, γ_i and k_i are the controller tuning parameters. a_{ij} is a part of the adjacency matrix $\mathbb{A}$ represents the weight of the communication link ij. χ_i and υ_i are the controller states, u_i is the converter output,and V_i^{ref} is the tertiary layer reference voltage. It should be noted that the controller equation 4.27a maintains the proportional load sharing operation, equation 4.27b stabilizes the generated DG current, while the coupled dynamic equation 4.27c aims at balancing the PCC voltage. Now, the controller can be expressed in combination with the microgrid mode in 4.6 in matrix form as follows:

$$\dot{X} = -B^{-1}\mathfrak{L}W I_t \quad , B = diag\{\beta_1, \beta_2, ..., \beta_n\} \tag{4.28a}$$

$$\dot{\Upsilon} = \Gamma^{-1}(-\Upsilon + I_t) \quad , \Gamma = diag\{\gamma_1, \gamma_2, ..., \gamma_n\} \tag{4.28b}$$

$$\dot{I}_t = L_t^{-1}(-V - K(I_t - \Upsilon) + W\mathfrak{L}X + V^{ref}) \tag{4.28c}$$

$$\dot{V} = C_t^{-1}(I_t + \mathscr{B}I_k - I_L) \tag{4.28d}$$

$$\dot{I}_k = L_k^{-1}(-\mathscr{B}^T V - R_k I_k) \tag{4.28e}$$

where X and Υ are the controller (nx1) state vectors. It should be noted that the locally generated DG current at each node depends on only one variable data which is the neighbor generated currents as shown in equation 4.28c considering that the controller

state Υ is a function of the neighbor generated currents too as shown in equation 4.28b. On the other hand, the bounded operation of global voltage regulation can be expressed as follows:

$$V_i = V^{ref} \quad \& \quad w_i I_{ti} \neq w_j I_{tj} \quad \forall j \in \mathscr{V} \qquad \text{if } V_i \notin V^{ref} \pm \epsilon \tag{4.29}$$

where ϵ represents the upper and lower tolerance for the local voltage. Based on equation 4.29, the proportional load-sharing objective will be relaxed if the PCC voltage at the agent bus exceeds the limit, and the voltage will be regulated locally at this bus. In other words, the agent's capacity weights are dynamically changed locally if the local voltage exceeds the assigned limits, while it will rest back to the normal assigned value based on the DG capacity if the local voltage is within the limits. This could be the case for higher capacity agents, and the probability of this situation increases if the power lines of the DC microgrid have different length ranges.

4.5.2 Moving Horizon Estimation Layer for improving system resiliency

Moving Horizon Estimation (MHE), also known as recursive or moving window estimation, is a technique used in control engineering to estimate the states of dynamic systems. MHE is a recursive algorithm that updates the estimate of the system's state variables over time by minimizing the difference between the predicted output and the measured output. It uses a moving window of the most recent input and output data to make the estimate [253]. MHE has the advantage of being able to handle nonlinear and time-varying systems and can provide robust state estimation even in the presence of noise and disturbances [254].

4.5.2.1 Mathematical Formulation of Moving Horizon Estimator

MHE is an optimization-based approach that uses data of measurements collected over time that can contain noise and other inaccuracies and provides estimates of parameters and unknown variables that fit the measurements. Unlike deterministic techniques like Kalman filter-based techniques, MHE is based on nonlinear programming solvers to achieve the required solution [255]. MHE is suitable for estimating the states of multi-input multi-output

coupled dynamics systems. It also can handle constraints easily. The basic construction of the MHE is an optimizer and the discrete model of the plant underestimation. MHE algorithm uses the plant model to make better estimates of the system states. A disturbed model of single-input-single-out system model can be represented as:

$$\begin{aligned} x[k+1] &= f(x[k]\ ,\ u[k]) + \mu_x \\ y[k] &= h(x[k]\ ,\ u[k]) + \mu_y \\ x\ &\in\ \mathbb{R}^n \quad \textit{is the state vector} \\ u\ &\in\ \mathbb{R}^m \quad \textit{is the vector of control actions} \end{aligned} \tag{4.30}$$

where μ_x and μ_y are the noise on the system states and the output measurements respectively, while h is the measurement model that determines the relation of the measured quantity to the system states and control input. The MHE operation sequence can be listed as:

- At a certain time step instant k, the past window of system measurements (N_{MHE}) is acquired.
- Based on the past window of measurement, find the optimum state trajectory that best fits the measured values considering the system dynamic model as a constraint.

This process is illustrated in Fig. 4.5, where the doted window of measurements for both the system states as well as the control input are used to perform the estimation process.

The optimum trajectory of the system states can be achieved by minimizing the following cost function:

$$\begin{aligned} J_{N_{MHE}}(x,u) = &\sum_{i=k-N_{MHE}}^{k} ||\tilde{y}[i] - h(x[i])||_V^2 \\ &+ \sum_{i=k-N_{MHE}}^{k-1} ||\tilde{u}[i] - u[i]||_W^2 \end{aligned} \tag{4.31}$$

where $\tilde{y}$ is the measured system states, while $\tilde{u}$ is the measured control actions. $h(x[i])$ is the predicted system states, while $u[i]$ is the predicted control actions. V and W are the

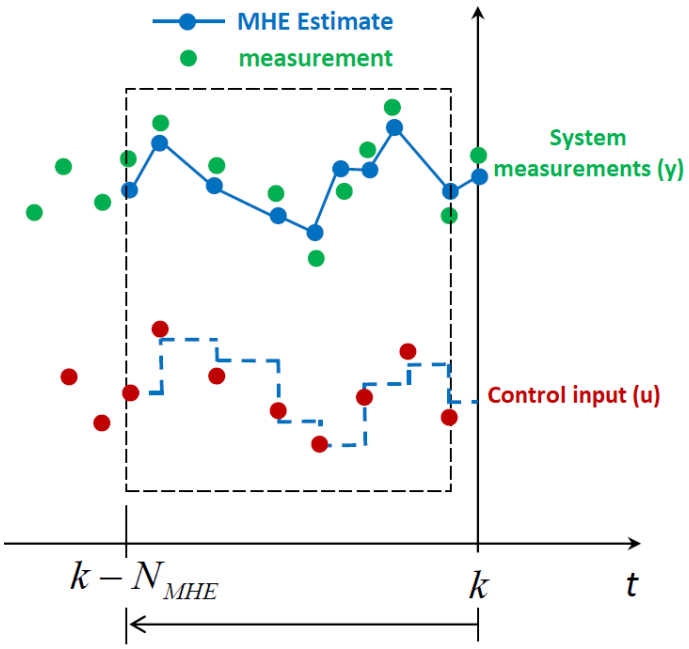

Figure 4.5: Moving Horizon Estimation Concept

weighting matrices for the system states and control action cost function parts, respectively. From equation (4.36) it can be seen that the MHE algorithm not only can estimate the measured system state trajectory but also can estimate the input control actions. This feature is extremely helpful when the applied control actions are subjected to high noise levels. It can be noted that the sum for the output term (states) is one step longer than the sum for the input term. This is because the most recent output (current state) depends on the previous control input, not the current one. The estimation optimization problem can be formulated as:

$$\begin{aligned} &minimize\ J_{N_{MHE}}(x,u) \\ subject\ to:\ &x_u[i+1] = f(x_u[i]\ ,\ u[i]) \\ &u[i] \in\ U, \quad \forall i \in [k - N_{MHE}, k-1] \\ &x_u[i] \in\ X, \quad \forall i \in [k - N_{MHE}, k] \end{aligned} \tag{4.32}$$

It can be seen that the system dynamic model is integrated into the optimization problem

as a constraint. Moreover, if there are physical ranges for the system states and the control action, it can be integrated easily into the optimization problem as inequality constraints to improve the convergence of the optimization problem as shown in equation (4.37) It should be noted that MHE can deal with the exact nonlinear models of systems without linearization. Moreover, unlike Kalman filters, the MHE algorithm considers a window of measurement for the system states and control actions, not just considering the recent state and control action. Furthermore, MHE has the capability to integrate all constraints of the system states and control actions to the optimization problem effectively [256].

For the MHE algorithm, the weighting matrices are determined based on the system model and the noise nature. If the system noise is considered as a Gaussian noise, the weighting matrices can easily be determined based on the standard deviation of the system states as well as control actions as follows:

$$V = \begin{bmatrix} \sigma_{x_1} & 0 & \dots & 0 \\ 0 & \sigma_{x_2} & \dots & 0 \\ \vdots & \ddots & \ddots & 0 \\ 0 & 0 & \dots & \sigma_{x_S} \end{bmatrix}^{-1} \quad W = \begin{bmatrix} \sigma_{u_1} & 0 & \dots & 0 \\ 0 & \sigma_{u_2} & \dots & 0 \\ \vdots & \ddots & \ddots & 0 \\ 0 & 0 & \dots & \sigma_{u_C} \end{bmatrix}^{-1} \tag{4.33}$$

where σ is the standard deviation, while S and C are the number of system states and the control inputs, respectively. It can be noted from equation (4.35) that the measured quantity with a high standard deviation will get a lower weighting factor and hence lower penalization in the cost function. In other words, the higher weights are given to the measured signals that are more certain and vice versa.

MHE is implemented locally at each node in the DC microgrid to estimate the local voltage and generated current based on the local DC-DC converter model. This can mitigate any local measurement uncertainties, making the control system more resilient. Moreover, if the neighbor agent converters are available, the MHE estimator can effectively used to mitigate any cyber threats through the neighbor communication links.

For the DC microgrid under study, a buck converter is used to link the DGs to the DC microgrid. The converter output filter is already modeled in the physical layer modeling section 4.6. The control action equation, which is the duty ratio d has to be added to the

model as follows:

$$\begin{aligned} L_{ti}\frac{dI_{ti}}{dt} &= -V_i + u_i \\ C_{ti}\frac{dV_i}{dt} &= I_{ti} - I_{Li}\sum_{k\in\mathscr{C}_i} I_{k,i} \\ d_i &= \frac{u_i}{V_{DG,i}} \end{aligned} \tag{4.34}$$

The local state vector and the control action can be expressed as:

$$x = \begin{bmatrix} V_c \\ I_l \end{bmatrix} \qquad u = \begin{bmatrix} d \end{bmatrix} \tag{4.35}$$

It should be noted that this model is decentralized using the Euler method to be able to be loaded to the MHE algorithm, like the case of MPC controller described in the previous chapter. Since the system states can be directly measured, the measurement model can be assumed unity. In other words, $y = h(x) = x$, and the cost function can be expressed then as:

$$\begin{aligned} J_{N_{MHE}}(x,u) = &\sum_{i=k-N_{MHE}}^{k} ||\tilde{x}[i] - x[i]||_V^2 \\ &+ \sum_{i=k-N_{MHE}}^{k-1} ||\tilde{u}[i] - u[i]||_W^2 \end{aligned} \tag{4.36}$$

where x is the predicted system states and u is the predicted control action, while $\tilde{x}$ and $\tilde{u}$ are the measured states and control actions respectively. To reduce the computation burden, the system states will only be predicted through the MHE algorithm. There is no need to predict the control actions because it is the output of the local controller which cannot be affected by the communication cyber threats. The MHE Optimization problem can be expressed as:

$$
\begin{aligned}
minimize\ J_{N_{MHE}}(x,u) = & \sum_{i=k-N_{MHE}}^{k} ||\tilde{x}[i]-x[i]||_V^2 \\
subject\ to: L_{ti}\frac{dI_{ti}}{dt} &= -V_i + u_i \\
C_{ti}\frac{dV_i}{dt} &= I_{ti} - I_{Li}\sum_{k\in\mathscr{E}_i} I_{k,i} \\
d_i &= \frac{u_i}{V_{DG,i}} \\
d_{min} < d_i < d_{max}, &\quad \forall i \in [k-N_{MHE}, k-1] \\
x_{min} < x[i] < x_{max}, &\quad \forall i \in [k-N_{MHE}, k]
\end{aligned}
\tag{4.37}
$$

It should also noted that based on MHE algorithm operation, a window of system state measurements with a width of N_{MHE} has to be loaded at each time step to the MHE algorithm in order to estimate the system states. This can be done easily by shifting the previous window of measurement and updating it with the new actual measured system states. On the other hand, at the beginning of the simulation time, the MHE algorithm will be able to estimate the system states only after collecting the first window of measurements.

4.5.3 DC Microgrid Under Study

The DC microgrid under study has four different capacity DGs connected in a mesh configuration through four power lines represented by their resistances and inductances as shown in Fig. 4.6. Each DG is connected to the microgrid through a DC-DC converter and there is a locally connected load at each bus. For the cyber network, the four DGs are connected in a spanning tree configuration with three communication links as shown in Fig. 4.6. The parameters of the DC microgrid are listed in table 4.1, while the power lines parameters are listed in 4.2. Based on the capacity weights, it can be seen that DG1 has the highest capacity, while DG3 has the lowest capacity. Local loads have different distributions. Furthermore, the line parameters are not constant per unit length, which

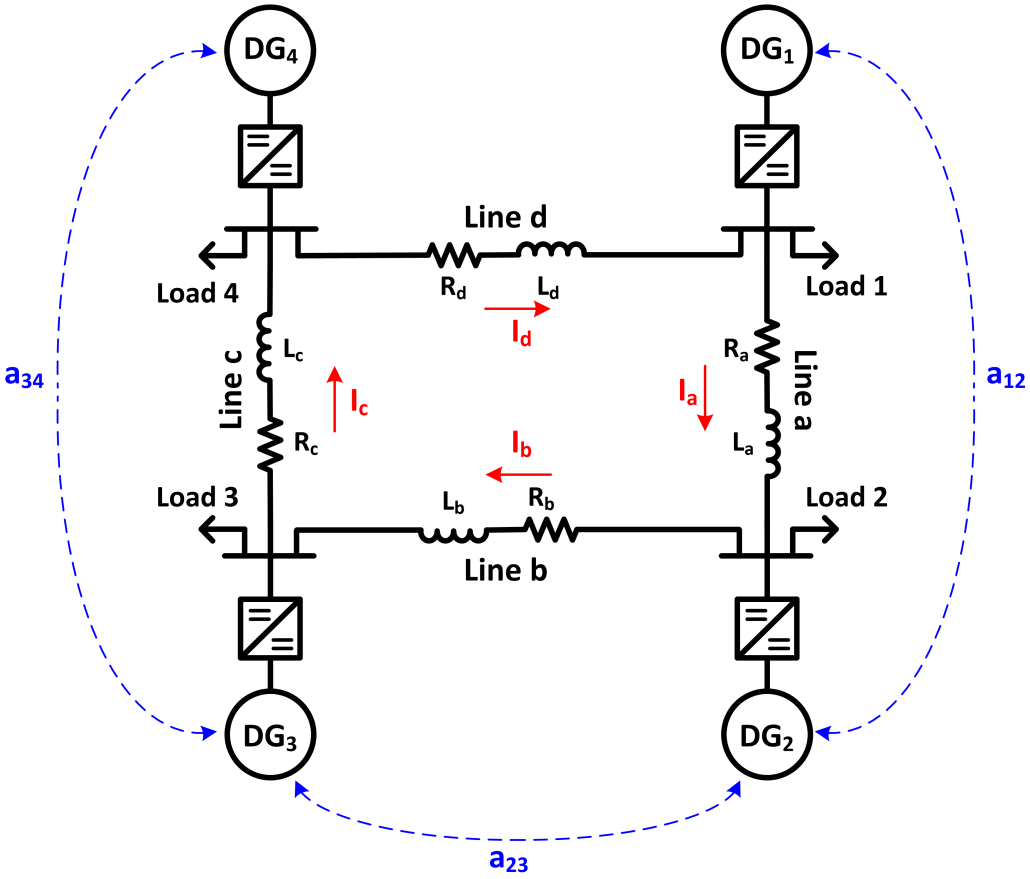

Figure 4.6: DC microgrid under study

means that different AWG and lengths can be used. For the communication links, the weighted adjacency factors are listed in table 4.3. As the communication links are bidirectional, and based on the definitions of adjacency matrix elements in equations 4.7 and 4.8, the adjacency matrix $\mathbb{A}$ can be expressed as:

$$\mathbb{A} = \begin{bmatrix} 0 & 100 & 0 & 0 \\ 100 & 0 & 100 & 0 \\ 0 & 100 & 0 & 100 \\ 0 & 0 & 100 & 0 \end{bmatrix} \tag{4.38}$$

Table 4.1: Parameters of Microgrid under study

Parameter	DG1	DG2	DG3	DG4
Filter Inductor (L_t)	1.8mH	2mH	3mH	2.2mH
Filter Capacitor (C_t)	2.2mF	1.9mF	2.5mF	1.7mF
Capacity weighting factor (w)	1	2	2.67	1.6
Reference Voltage (V^{ref})	480V	480V	480V	480V
Initial Bus Loads (I_L)	20A	8A	40A	21A

On the other hand, the In-degree diagonal matrix can be determined based on equation 4.10 as follows:

$$D^{in} = \begin{bmatrix} 100 & 0 & 0 & 0 \\ 0 & 200 & 0 & 0 \\ 0 & 0 & 200 & 0 \\ 0 & 0 & 0 & 100 \end{bmatrix} \tag{4.39}$$

From equations 4.38 and equation 4.39 the communication Laplacian matrix described in equations 4.11 and 4.12 can be calculated as follows:

$$\mathfrak{L} = D^{in} - \mathbb{A} = \begin{bmatrix} 100 & -100 & 0 & 0 \\ -100 & 200 & -100 & 0 \\ 0 & -100 & 200 & -100 \\ 0 & 0 & -100 & 100 \end{bmatrix} \tag{4.40}$$

Table 4.2: Parameters of the Power lines

Parameter	Line a	Line b	Line c	Line d
Line Resistance (R_k)	70mΩ	50mΩ	80mΩ	60mΩ
Line Inductance (L_k)	2.1μH	2.3μH	2μH	1.8μH

Table 4.3: Parameters of the Communication links

Parameter	a_{12}	a_{23}	a_{34}
Weighted adjacency factor	100	100	100

The current following in the power lines of the DC microgrid is modeled through the incident matrix $\mathscr{B}$ which is defined in equations 4.3, 4.4, and 4.5. It should be noted that the incident matrix $\mathscr{B}$ is an nxm matrix that illustrates the link between the DG units and the microgrid power lines. Based on the power line currents indicted in Fig. 4.6, the incident matrix can be determined as follows:

$$\mathscr{B} = \begin{bmatrix} -1 & 0 & 0 & 1 \\ 1 & -1 & 0 & 0 \\ 0 & 1 & -1 & 0 \\ 0 & 0 & 1 & -1 \end{bmatrix} \tag{4.41}$$

Based on the determined values of the communication Laplacian matrix $\mathfrak{L}$ and the incident matrix $\mathscr{B}$ in equations 4.40 and 4.41 respectively, the dc microgrid model become fully defined.

4.6 Numerical Simulation Results

This section illustrates different case studies to investigate the proposed controller resiliency under various transient and contingency conditions.

4.6.1 Proportional Load Sharing

In this case study, the proposed cooperative controller is tested in the case of transient load change at each bus. The impact of these changes on the microgrid objectives is investigated. The microgrid loads are initially set to the assigned values indicated in table 4.1. At time

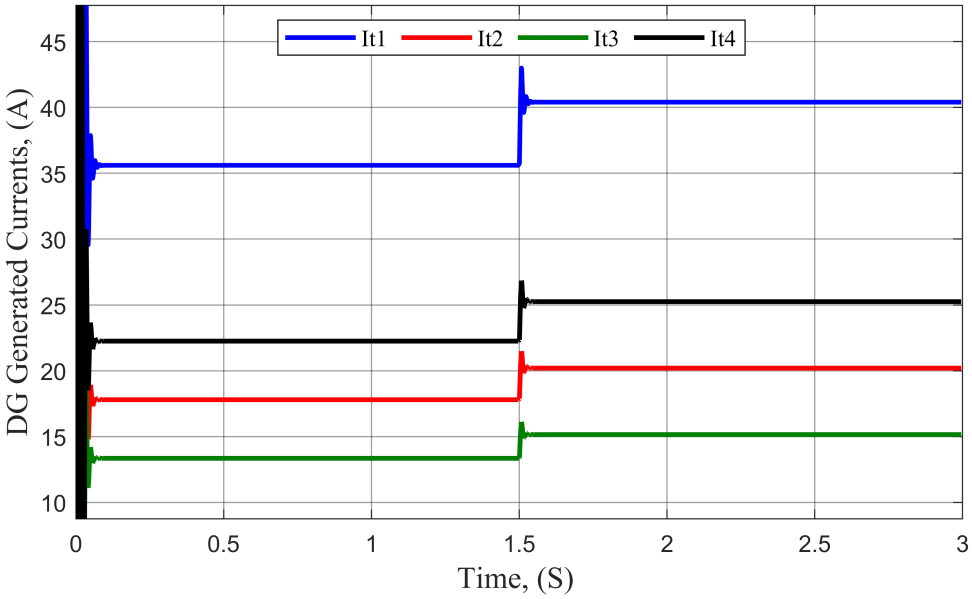

Figure 4.7: Proportional Load Sharing Operation

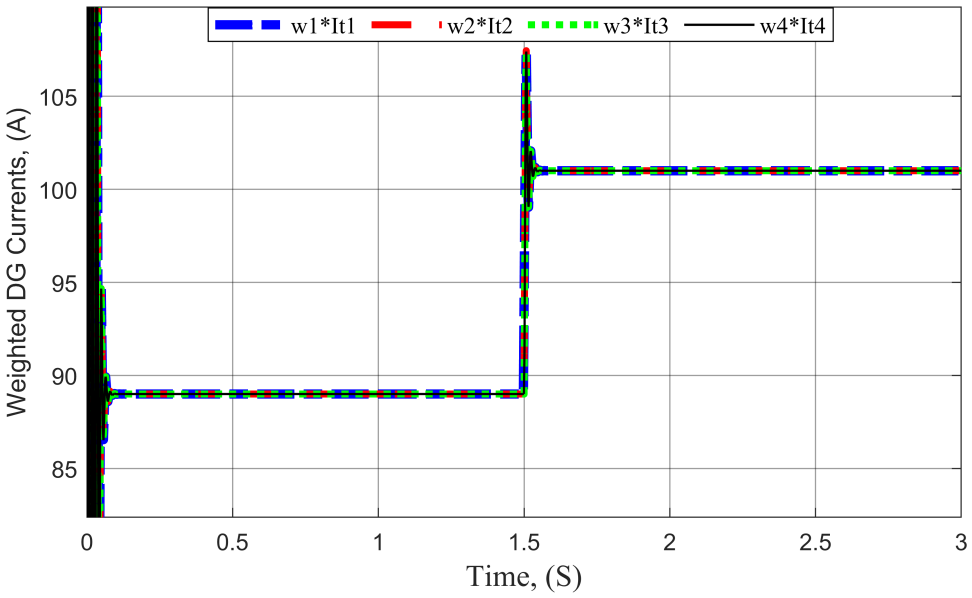

Figure 4.8: Weighted DG Generated Currents

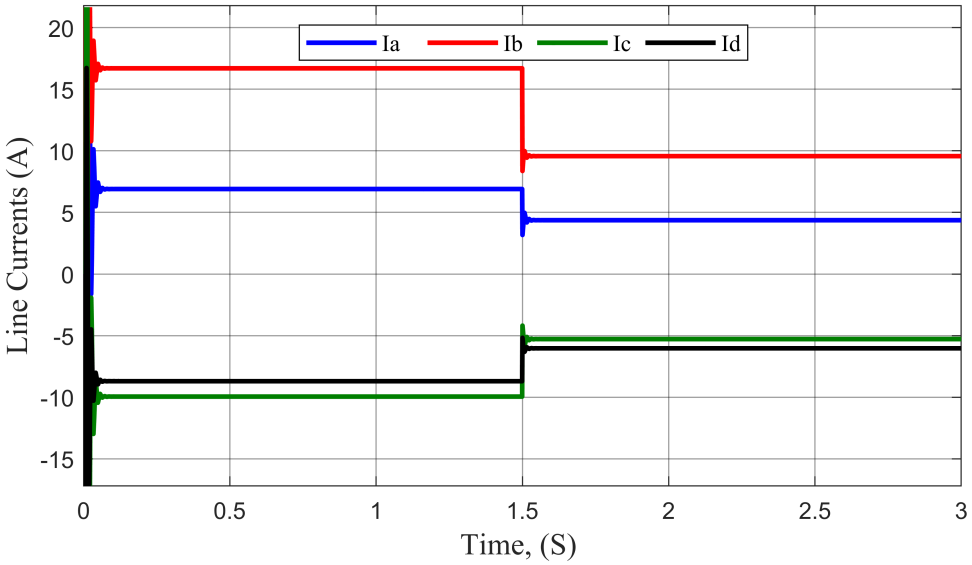

Figure 4.9: Power Line Currents

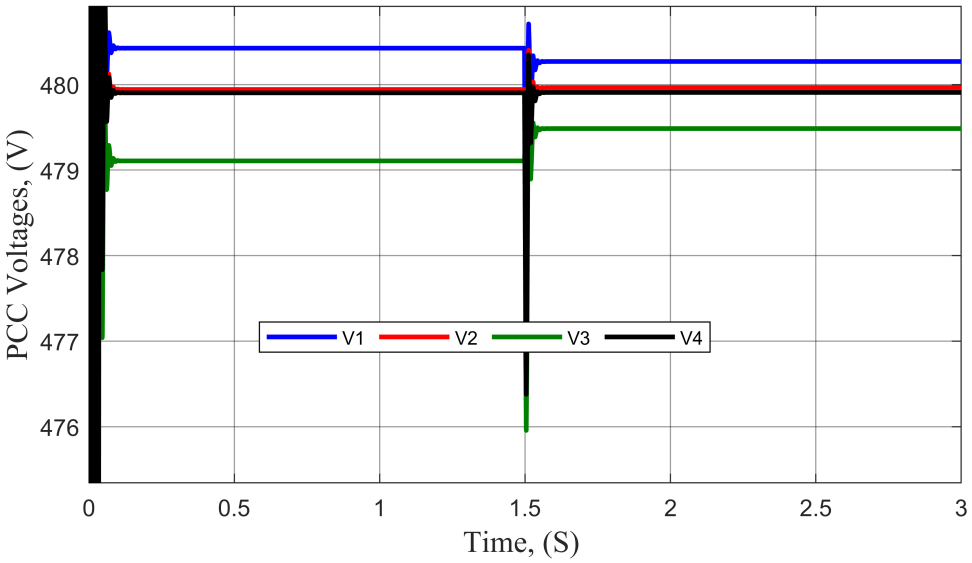

Figure 4.10: Voltage at DGs PCC

$t = 1.5$ the local load for each bus is changed as follows: $I_{L1} = 30A$, $I_{L2} = 15A$, $I_{L3} = 30A$, and $I_{L4} = 26A$. On the other hand, the controller matrices are set as follows: $B = \mathbb{I}_4$,

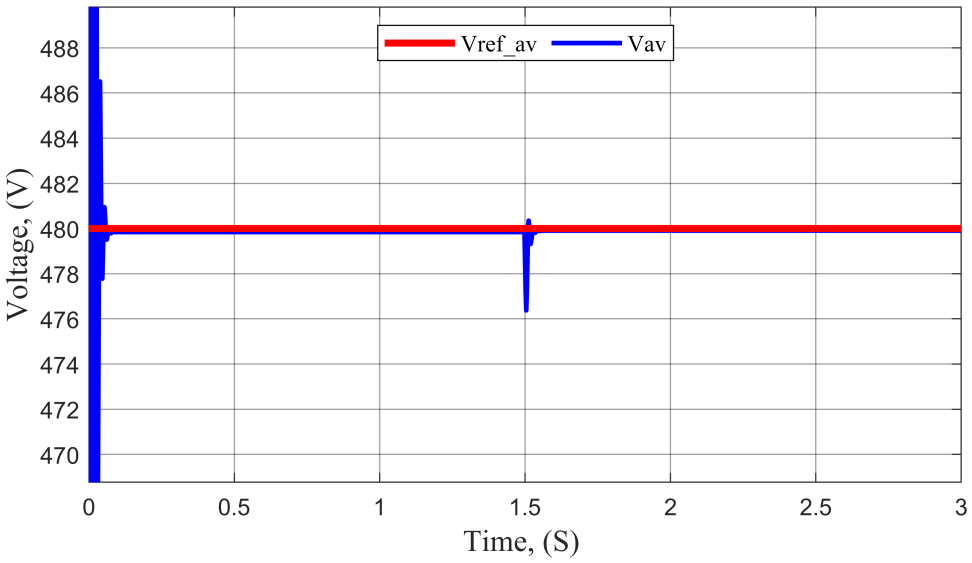

Figure 4.11: Global Voltage Balancing

$\Gamma = 0.01\text{x}\mathbb{I}_4$, and $K = 0.5\text{x}\mathbb{I}_4$. These matrices determine the dynamic response on the controller. The generated currents are illustrated in Fig. 4.7. It can be seen that the generated currents are boosted to meet the transient load demand not only based on the generated capacities but also based on DG unit locations and the power lines' impedance. The proportional current sharing objective for all connected DGs is achieved in Fig. 4.8. It is clearly obvious that the weighted generated currents for all DG units are identical, which means that all DG units are fairly loaded according to their capacity of generation. On the other hand, the power line currents are shown in Fig. 4.9. It should be noted that the power line b and c currents are reduced as the local load at DG3 is decreased, while the capacity of DG3 is not changed. The voltage at PCC for all buses is illustrated in Fig. 4.10, while the global voltage regulation objective is achieved in Fig. 4.11. For a comparison of Fig. 4.8 and Fig. 4.11, it is obvious that the proportional current sharing regulation is more dominant than the global voltage regulation. That is reasonable considering that the proposed controller does not require voltage measurements of neighbors through a communication network, which is not the case for the locally generated currents of DG units. However, the voltage ripple doesn't exceed the tolerance with less than 0.75%

ripples during the transient instant. Based on Fig. 4.11, it can be seen that the average value of the voltage at PCC for all DG units equals the average voltage reference for all DG units. Moreover, the PCC steady-state voltage for all connected DGs is within the normal operating conditions with less than 0.2% tolerance for DG3 unit as shown in Fig. 4.10.

4.6.2 Power Line Outage

In this case study, the performance of the proposed cooperative controller is tested in the case of an outage of a power line. The changes in the generated currents and line currents will be illustrated while investigating the DC microgrid objectives. The load demands were initially at: $I_{L1} = 20A$, $I_{L2} = 8A$, $I_{L3} = 40A$, and $I_{L4} = 11A$. At time instant $t = 1S$, the power line d which interconnects DG1 and DG4 is opened. Hence, the generated DG currents are adjusted to compensate for this change. Hence at time $t = 2$ the local load for each bus is changed as follows: $I_{L1} = 30A$, $I_{L2} = 15A$, $I_{L3} = 30A$, and $I_{L4} = 16A$, while Line d still in outage. The microgrid configuration after the outage of line D is shown in Fig. 4.12, while the power line currents are illustrated in Fig. 4.13. It can be seen that the current of power line d no longer persists after $t = 1S$ and the other line currents are updated based on the new microgrid configuration. Then, the line currents are updated again as the load demand is changed at $t = 2S$. The corresponding DG-generated currents are illustrated in Fig. 4.14. It should be noted that the generated currents have minor effects on the outage of the power line as the proportional load-sharing objective is maintained while there is no change in the load demand during the power line outage. This minor effect is only due to the different line resistances and inductances. The change in the PCC voltages is shown in Fig. 4.15. It is noted that there is a consistency between the bus voltages and the line currents. For example, after the outage of power line d, the line currents a and b are increased, while line current c is decreased as shown in Fig. 4.13. This is due to the increase of PCC voltages for buses 1 and 2 and the decrease of PCC voltages for buses 3 and 4 as shown in Fig. 4.15. The proportional load sharing and the global voltage balancing are maintained during the power line outage and the load change as shown in Fig. 4.16 and Fig. 4.17, respectively

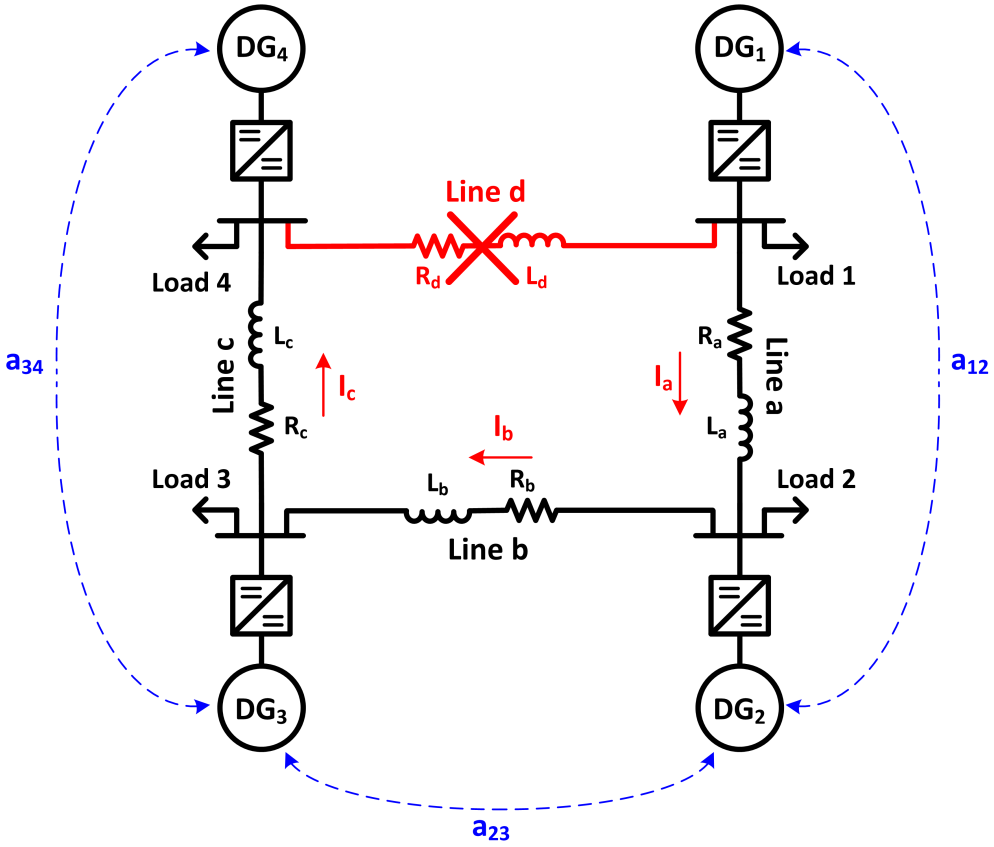

Figure 4.12: Microgrid configuration after Line D outage

.

4.6.3 Measurement Uncertainties and Cyber Threats

In this case study, the performance of the integrated MHE estimator is investigated to improve the control system resiliency against measurement uncertainties and cyber attacks. As mentioned in subsection 4.5.2, MHE estimator uses the most recent rolling window of past measurements to estimate the current state of the system taking into account the system dynamic model. An MHE estimator is attached locally to each bus in the microgrid. Instead of transferring the data directly between neighbor agents, the data is processed by

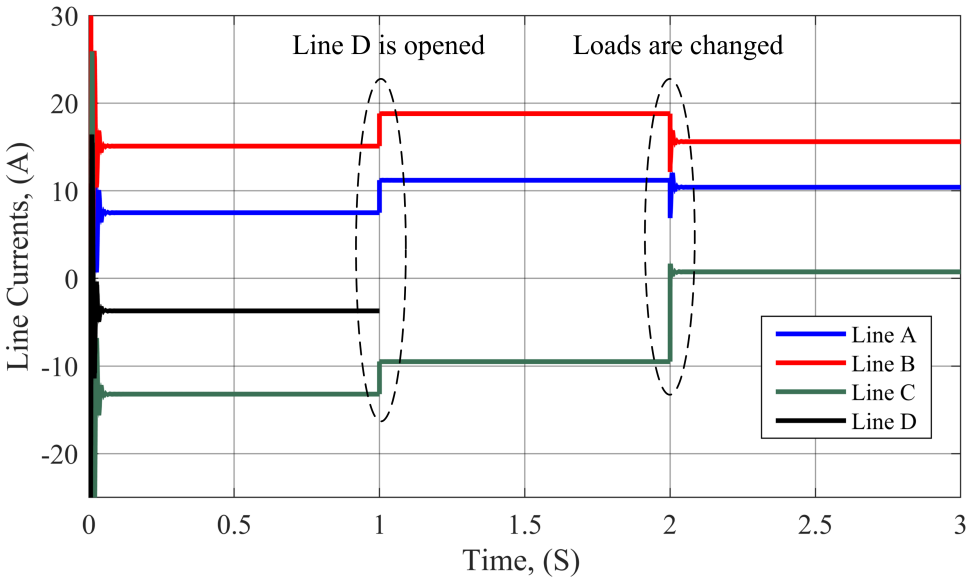

Figure 4.13: Line Currents during Line D outage and consecutive Load change

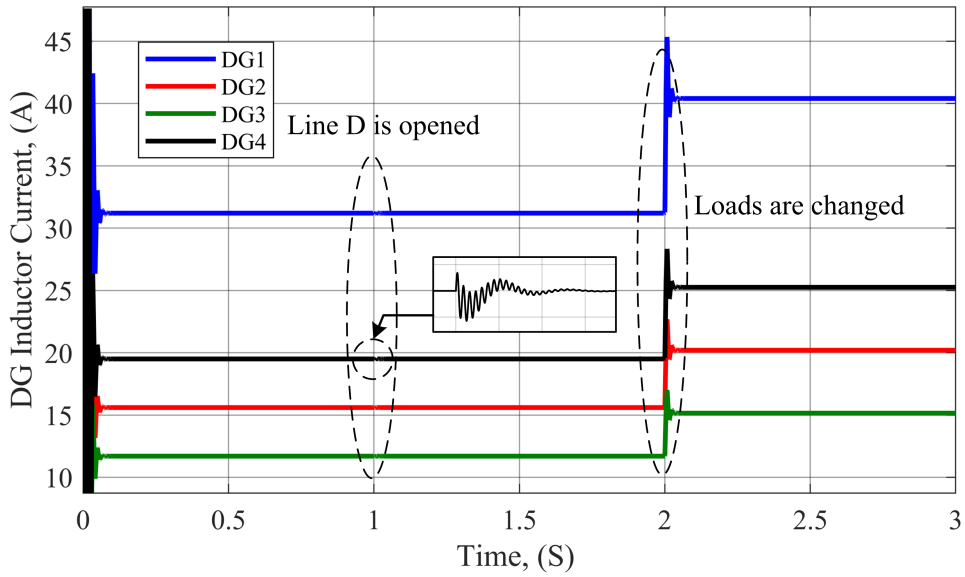

Figure 4.14: DG Generated Currents during Line D outage and consecutive Load change

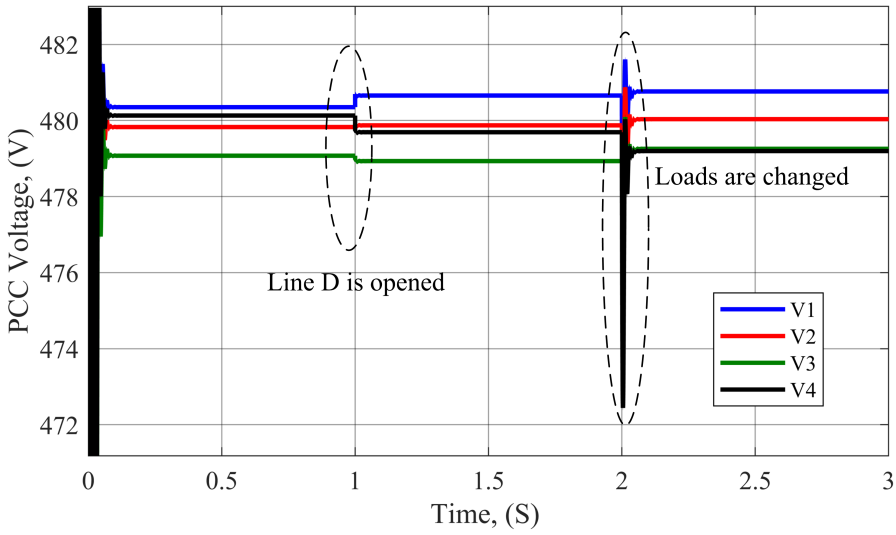

Figure 4.15: PCC DG Voltages during Line D outage and consecutive Load change

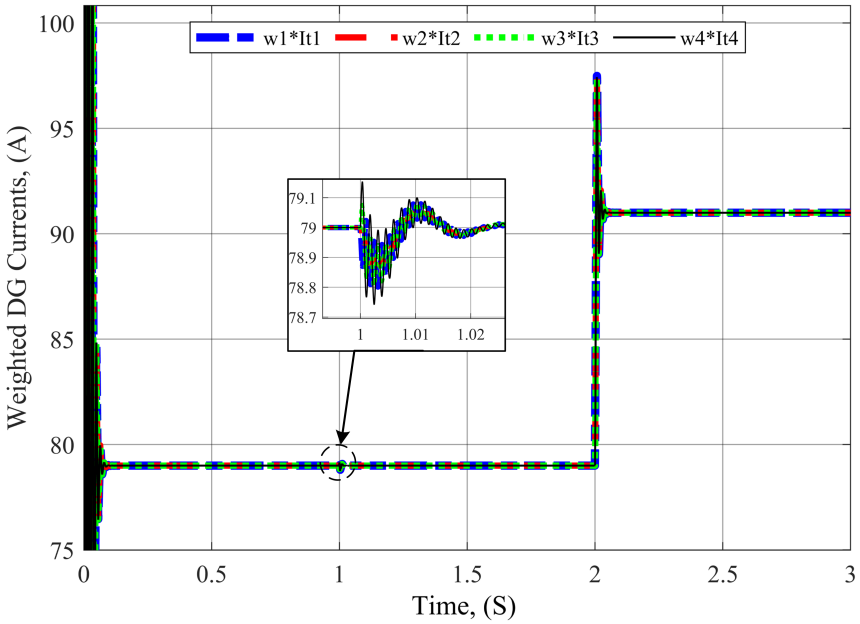

Figure 4.16: Weighted DG Generated Currents

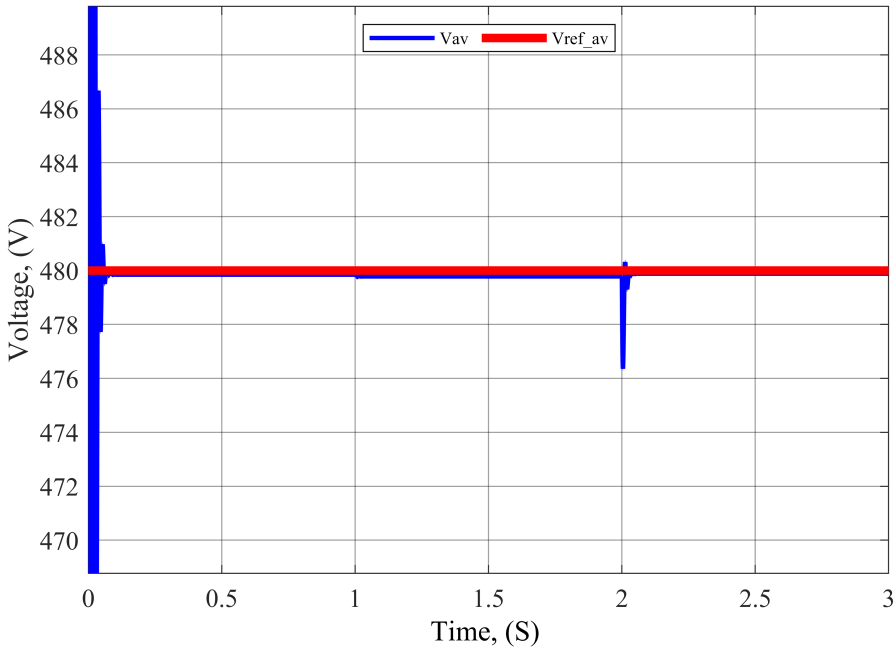

Figure 4.17: Global Voltage Balancing

the MHE estimator and then loaded to the local controller.

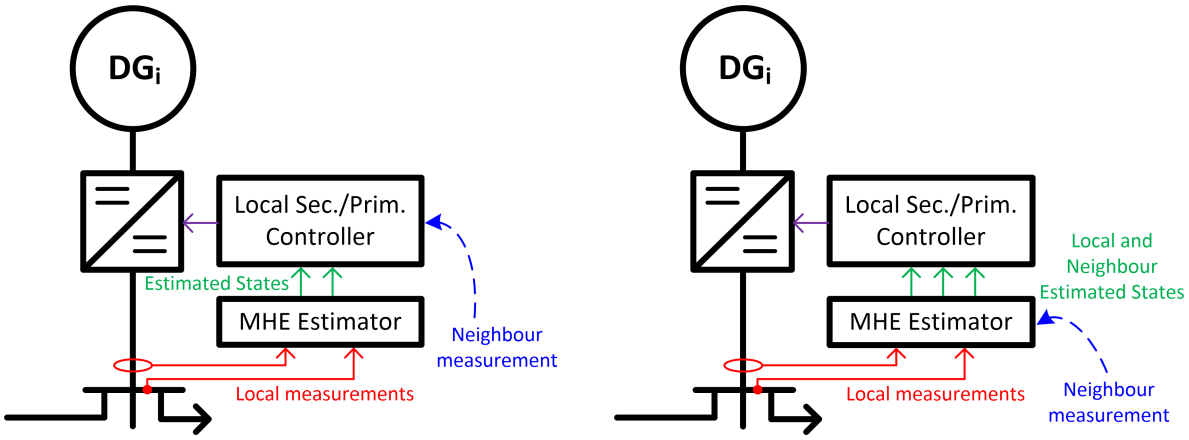

(a) Estimation of local states only

(b) Estimation of local and neighbor states

Figure 4.18: MHE Estimator operation

Attaching a local MHE estimator to each agent can effectively mitigate all local measurement uncertainties. Additionally, MHE estimator can be used to estimate the received data from neighbor agents. However, it necessitates knowledge of the converter models employed by the neighboring agents to effectively estimate the shared generated currents. It should be noted that knowing the neighbor converter model doesn't need any additional communication channels as it is constant (like the weighting factors of generated currents). It should also be noted that even without the knowledge of the neighbor models, the proposed MHE can improve the system resiliency indirectly, as the microgrid objectives depend on two local measurements that are fully protected. The aforementioned two modes of operation are illustrated in Fig. 4.18. In this case study, false measurements are intruded in the DG-generated current signal, while the PCC voltage is not exposed to any threats. The locally generated current of this DG is 100A, and the voltage at PCC is 480V, while the length of the measurement window N_{MHE} is set to be 22. The estimated trajectories of the generated current and the PCC voltage are shown in Fig. 4.19 and 4.20 respectively.

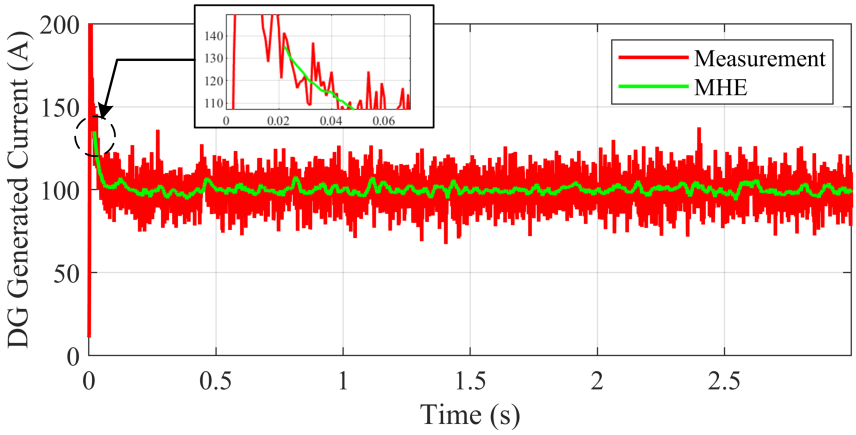

Figure 4.19: Local DG Generated Current Estimation

It can be seen from these results that the MHE estimator effectively mitigate the intruded false measurements from the DG-generated current, while it estimates the same healthy measurements of the PCC voltage. It should be noted that based on the MHE concept of operation, the first estimated state value can be determined after having the

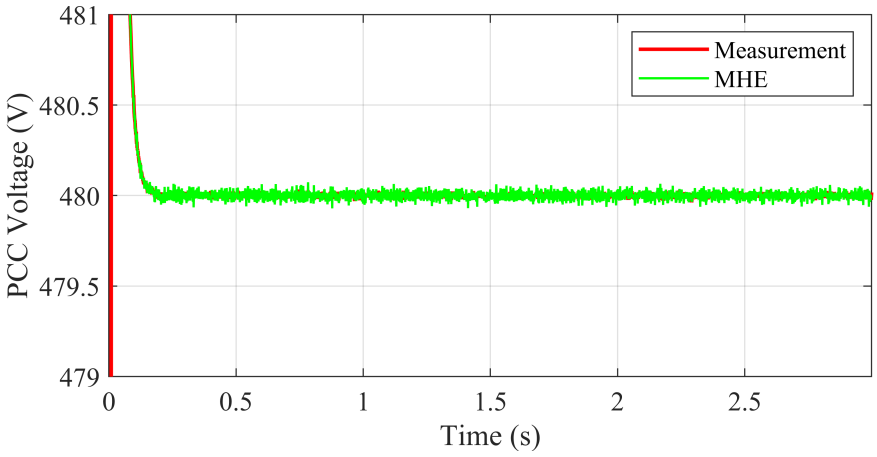

Figure 4.20: Local DG PCC Voltage Estimation

first window of measurements. This observation explains why the estimated state does not start at the beginning of the simulation time as shown in Fig. 4.19.

To investigate the effect of the length of the historical window of measurements that are used for the estimation algorithm, the measurement window N_{MHE} is changed and the results are compared with the previous results. Fig. 4.21 shows the estimated generated current state for different N_{MHE}. It is obvious that increasing the length of the measurement window improves the mitigation of the intruded false data effectively. However, the increase is bounded by the computational burden. Moreover, it should be noted that increasing the length of the measurement window, delays the first estimated system states. Hence, the actual measured state is fed back to the controller during this period which may affect its performance.

4.6.4 Plug-in of DG unit

In this case study, the performance of the proposed cooperative controller is tested in the case of plugging in a new DG to the DC microgrid under study. As shown in Fig. 4.22, a new DG5 with a local load is plugged into the microgrid between DG4 and DG1, while a single bidirectional communication link is established between DG4 and DG5. DG5 is

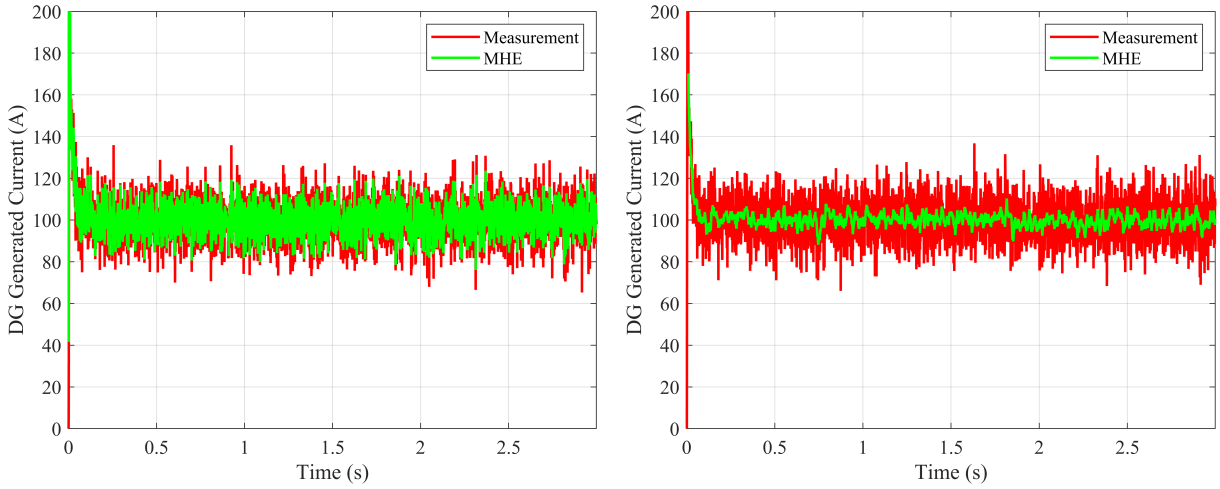

(a) $N_{MHE} = 1$

(b) $N_{MHE} = 10$

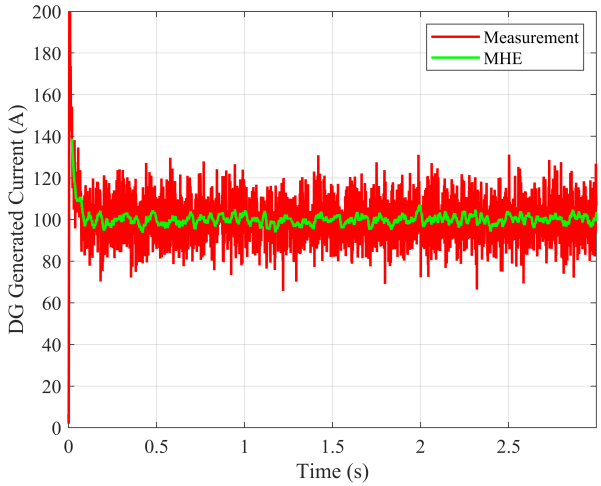

(c) $N_{MHE} = 20$

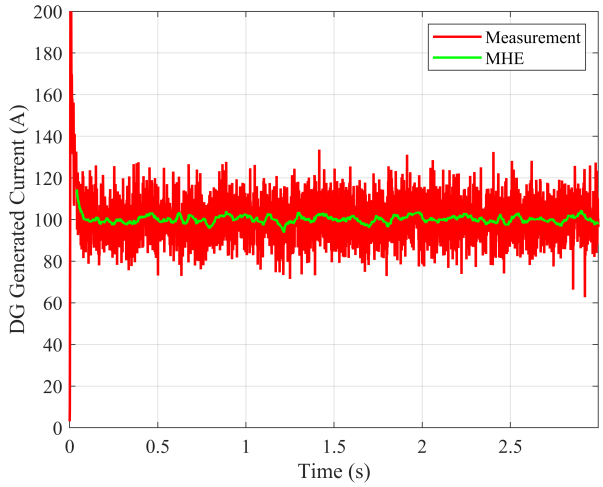

(d) $N_{MHE} = 40$

Figure 4.21: The effect of the length of the moving horizon window of the MHE Estimator

connected to DG4 through line d with the same parameters given in table 4.2, while it is connected to DG1 through a new power feeder line e. The parameters of the new DG5 as well as line e are given in tables 4.4 and 4.5, respectively.

The load demands were initially at: $I_{L1} = 20A$, $I_{L2} = 8A$, $I_{L3} = 40A$, and $I_{L4} = 11A$.

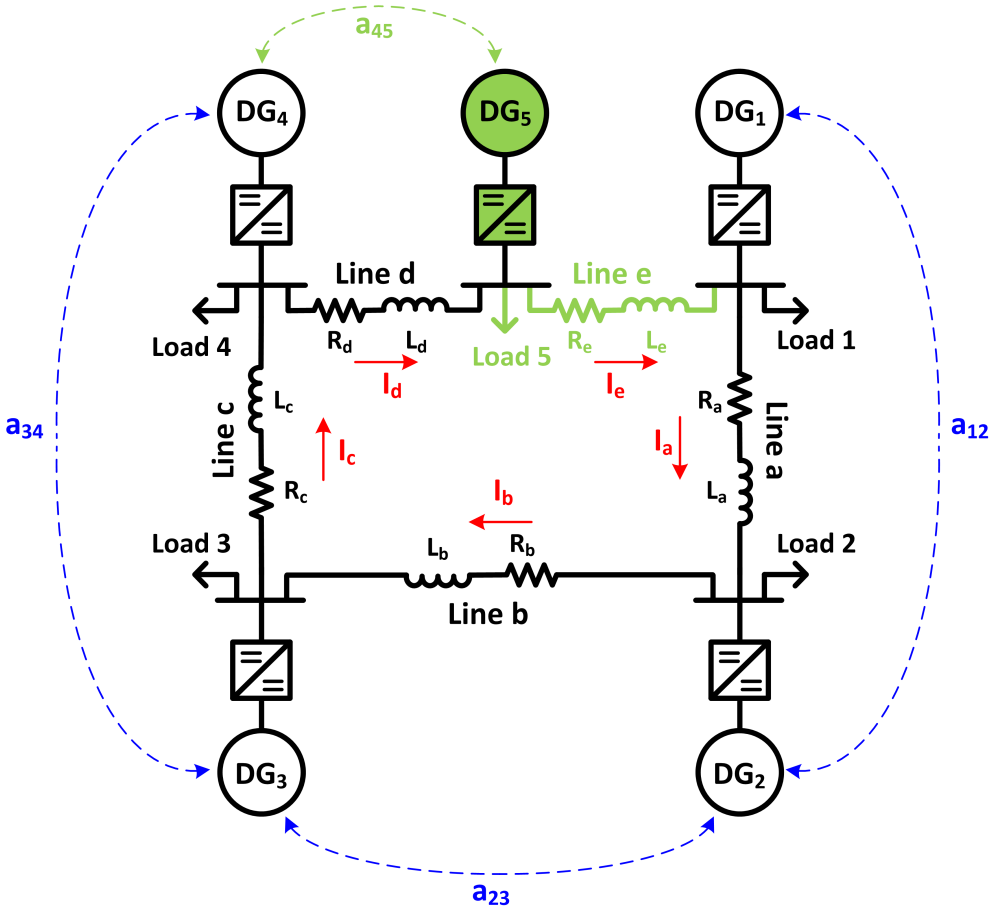

Figure 4.22: Microgrid configuration after DG5 Plug-in

At time instant $t = 1.5S$, the new DG5 with its local load is plugged into the network through power lines d and e and the communication link a_{45}. At this time the network is automatically reconfigured to meet the microgrid objectives. The power line currents are illustrated in Fig. 4.23. It can be seen that the current of power line e starts at $t = 1.5S$ when DG5 is connected to DG1 through this line, while the other line currents are updated based on the new microgrid configuration. The line currents increased due to the new local load connected to the network. The corresponding DG-generated currents are illustrated in Fig. 4.24. Similarly, the generated current of DG5 starts at $t = 1.5S$ when the DG unit is plugged into the system. It is observable that all generated DG currents are reduced

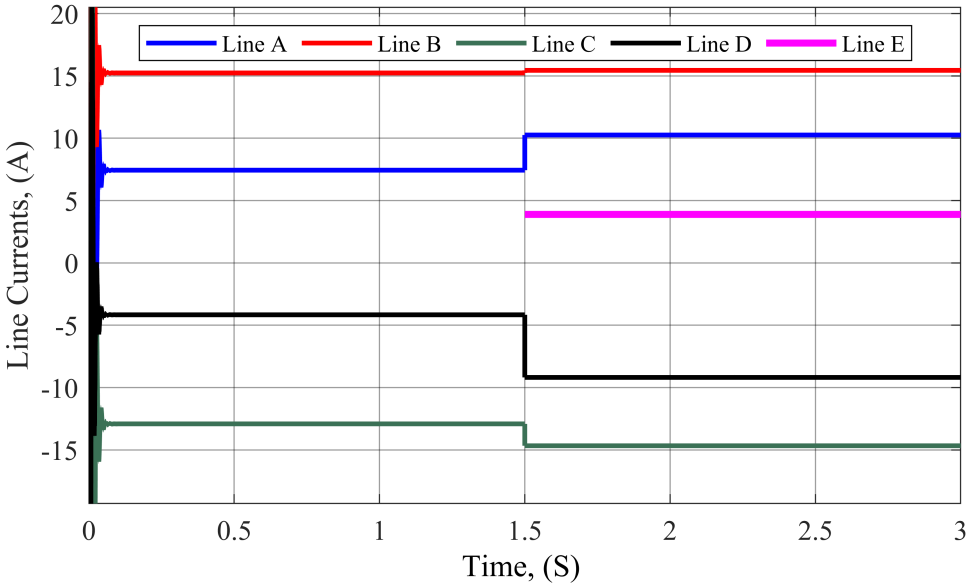

Figure 4.23: Line Currents during Plug-in of DG5

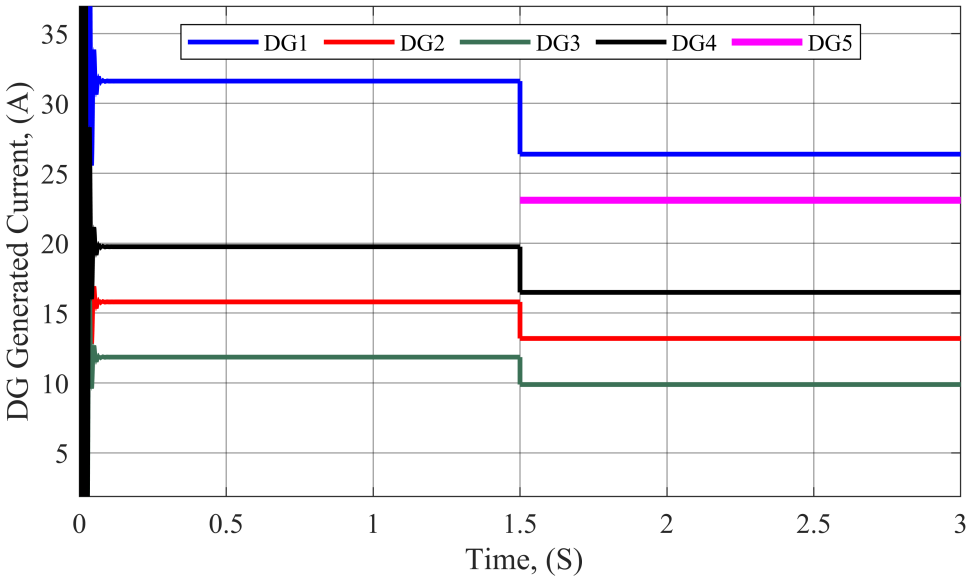

Figure 4.24: DG Generated Currents during Plug-in of DG5

Table 4.4: Parameters of DG5

Parameter	DG5
Filter Inductor (L_t)	2.2mH
Filter Capacitor (C_t)	1.7mF
Capacity weighting factor (w)	1.143
Reference Voltage (V^{ref})	480V
Initial Bus Loads (I_L)	10A
Weighted adjacency factor (a_{45})	100

Table 4.5: Parameters of Power Line e

Parameter	Line e
Line Resistance (R_k)	60mΩ
Line Inductance (L_k)	1.8μH

when DG5 is plugged in, as a new generation capacity is added to the network with a relatively small local load. The change in the PCC voltages is shown in Fig. 4.25. The proportional load sharing and the global voltage balancing are effectively achieved during the plug-in operation as shown in Fig. 4.26 and Fig. 4.27, respectively.

4.6.5 Failure of a communication link and communication delay

In this case study, the performance of the proposed cooperative controller is tested in the case of communication link failure or communication delay. As stated in section 4.5.3, the communication network is configured as a spanning tree in which there are no communication loops as shown in Fig. 4.6. This can limit the risk of intrusion as false data. However, as there are no redundant communication choices, a communication failure can disrupt the entire communication network. The proposed controller capability to deal with a commu-

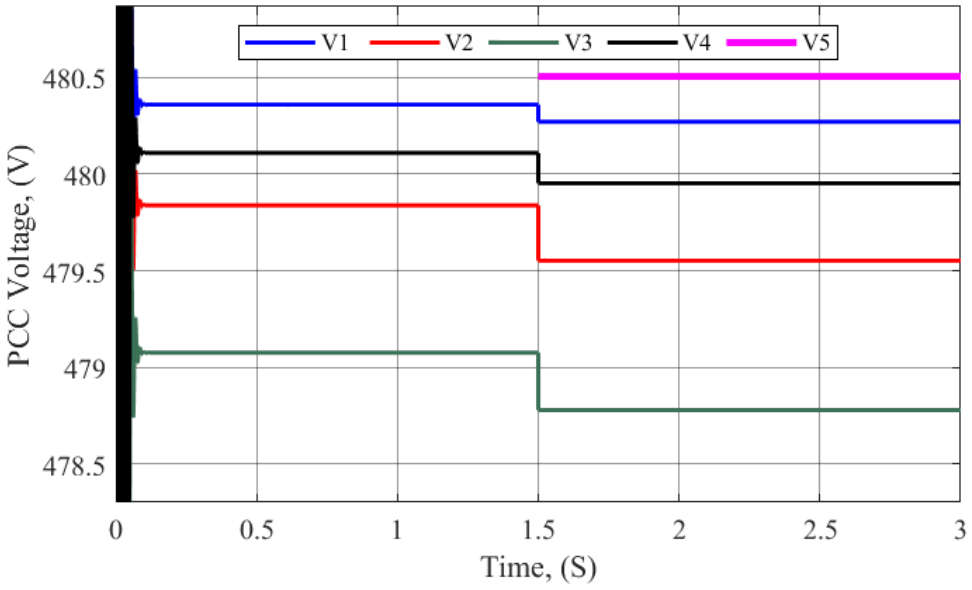

Figure 4.25: PCC DG Voltages during Plug-in of DG5

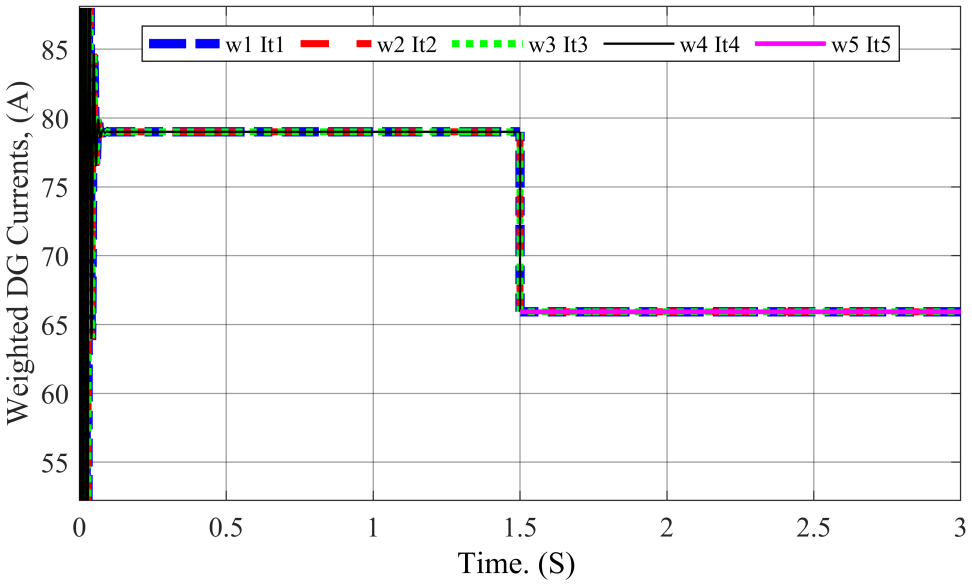

Figure 4.26: Weighted DG Generated Currents during Plug-in of DG5

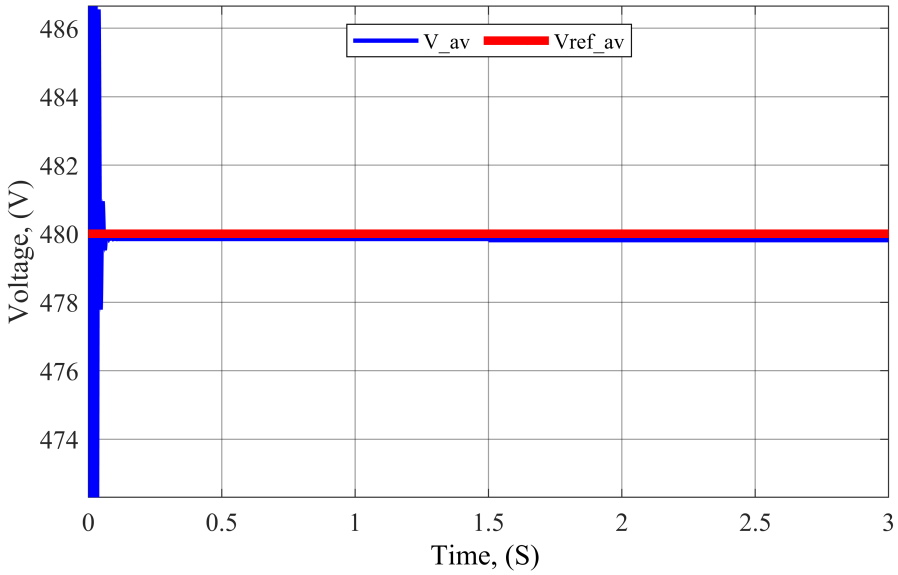

Figure 4.27: Global Voltage Balancing during Plug-in of DG5

nication link failure and a restoration of a communication link (or communication delay) is investigated in this study. The load demands were initially at: $I_{L1} = 20A$, $I_{L2} = 8A$, $I_{L3} = 40A$, and $I_{L4} = 11A$. During steady-state operation, a failure occurs to the communication link between DG3 and DG4 as shown in Fig. 4.28. The event occurs at $t = 1S$. Then at $t = 2S$, the communication link is restored. It should be noted that during the communication failure period, DG4 is not connected to the communication network, while the other DGs are still connected. Based on this situation, the proposed controller assigns DG4 to generate a current such that the local PCC voltage is kept constant at the reference voltage, which improves the global voltage balancing objective, while proportional load sharing is achieved among the other three DGs.

The load demands were initially at: $I_{L1} = 20A$, $I_{L2} = 8A$, $I_{L3} = 40A$, and $I_{L4} = 11A$. Fig. 4.29 shows the generated currents for all DGs. It is clearly obvious that the generated current of DG4 is dropped to meet the local objective of maintaining the local bus voltage at the reference level. On the other hand, all other DGs generated currents are boosted to compensate for the remaining load requirement at bus 4. The corresponding power line currents are illustrated in Fig. 4.30, while Fig. 4.31 shows the voltages at PCC for all

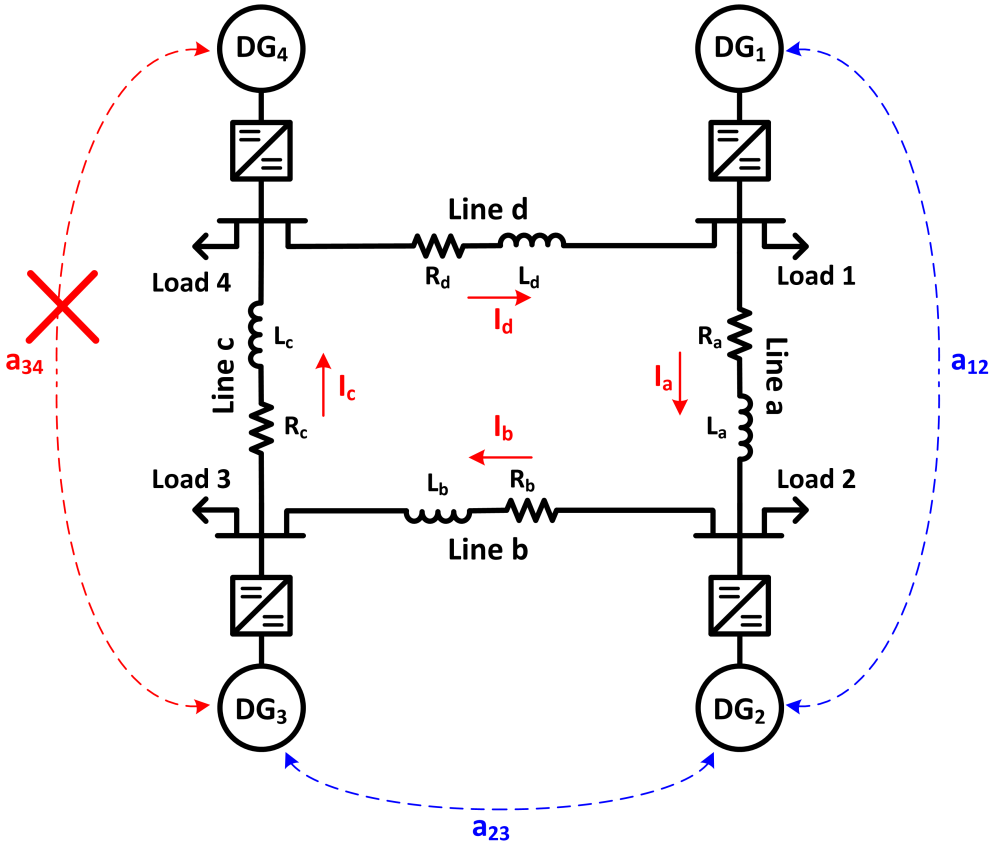

Figure 4.28: Microgrid configuration after communication link failure

DGs. It should be noted that the voltage at PCC for DG4 is kept constant at the reference value of 480V during the communication link failure period as indicated in Fig. 4.31, which improves the global voltage balancing operation as shown in Fig. 4.33. On the other hand, the proportional load sharing is indicated in Fig. 4.32 in which the weighted average of all DGs is plotted. It is obvious that during the communication link failure period, the proportional load sharing objective is achieved for DG1, DG2, and DG3 only, while DG4 is joined with a proportional load share when the communication link is restored at $t = 2S$.

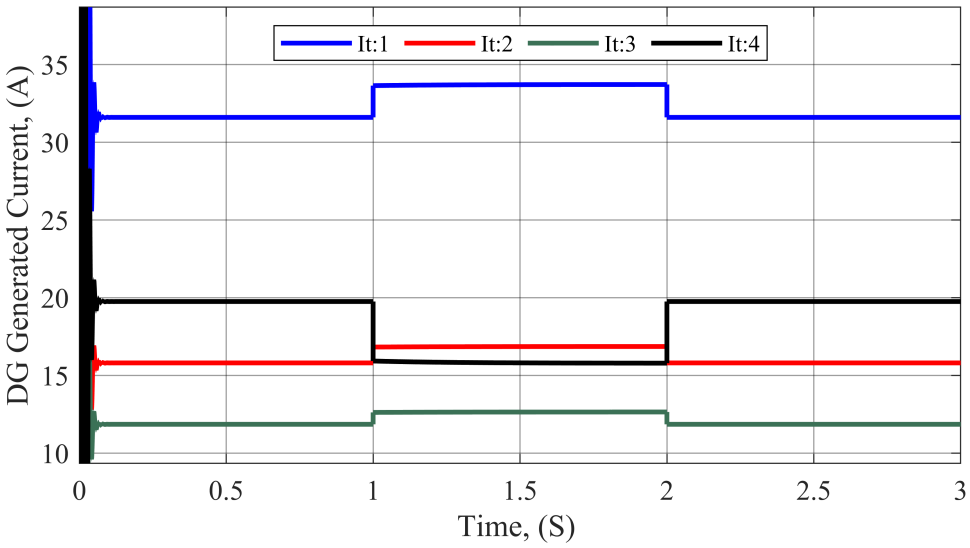

Figure 4.29: DG Generated Currents during communication link failure

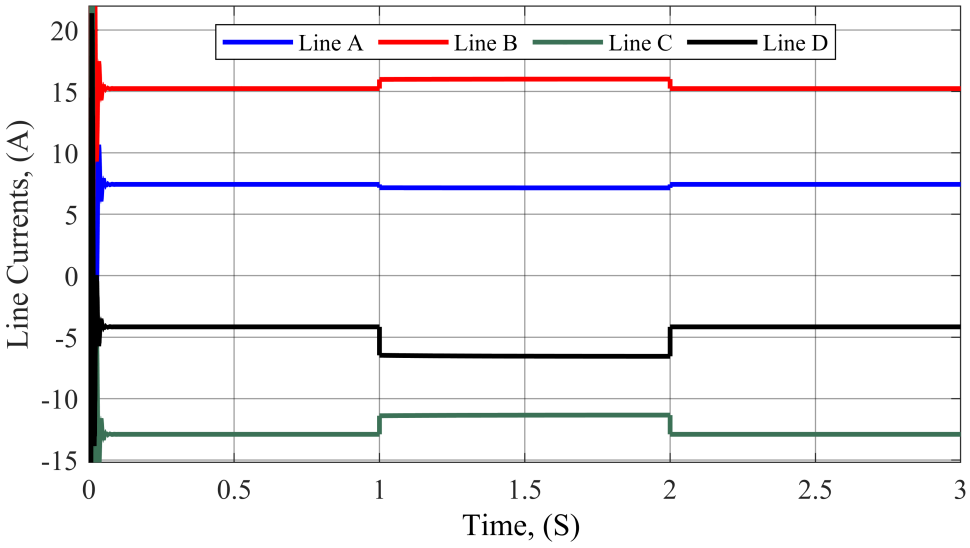

Figure 4.30: Line Currents during communication link failure

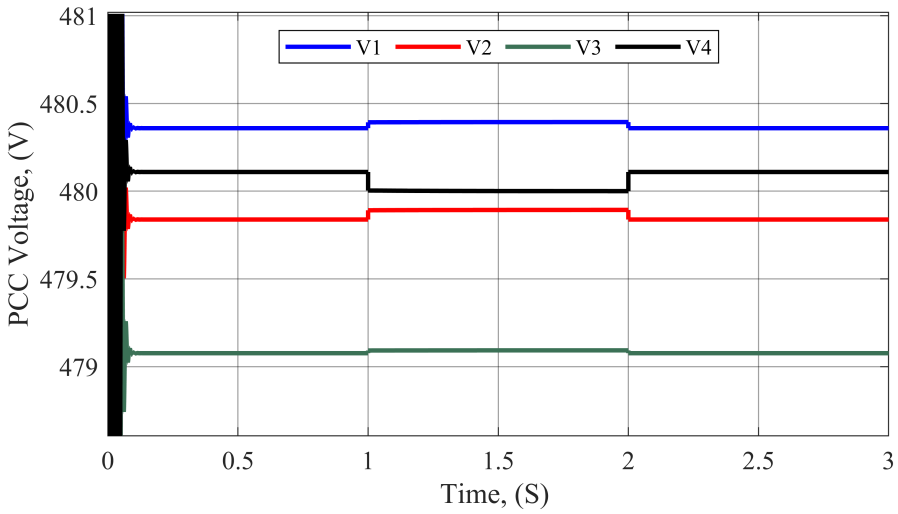

Figure 4.31: PCC DG Voltages during communication link failure

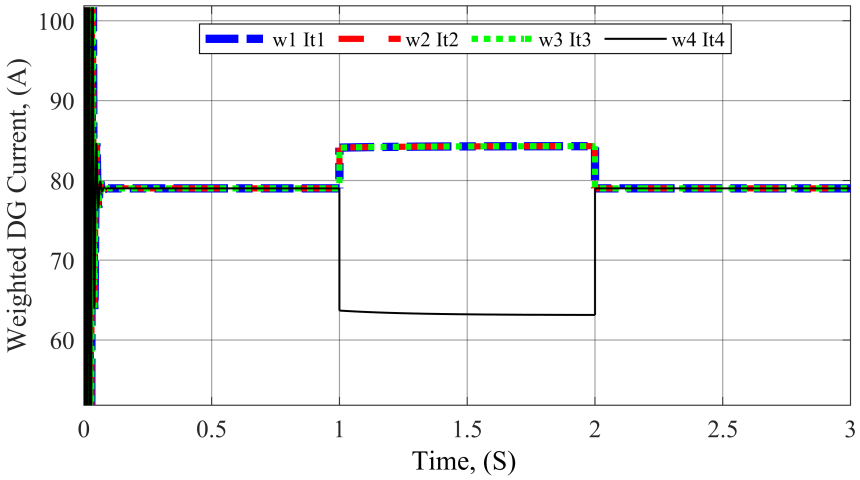

Figure 4.32: Weighted DG Generated Currents during communication link failure

4.7 Conclusion

This chapter proposes a cooperative distributed consensus-based strategy for proportional load sharing and global voltage balancing objectives in DC microgrids. This control strategy operates at reduced communication requirements which can effectively reduce the risk

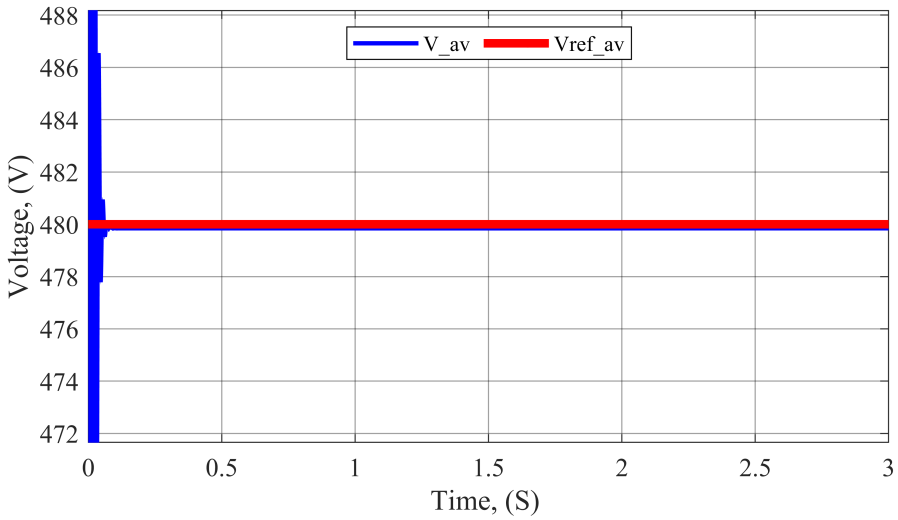

Figure 4.33: Global Voltage Balancing during communication link failure

of cyber threats while facilitating the integration of DGs to the microgrid. Moreover, the strategy incorporates a state estimation layer that utilizes MHE algorithm for the mitigation of cyber threats and system uncertainties, which effectively improves the distributed control resiliency. The proposed control strategy only relies on measurements of generated currents, without the need for the knowledge of the PCC voltages or the microgrid parameters. The effectiveness of the controller is demonstrated in that the microgrid objectives can converge to the desired steady state values regardless of the initial conditions of the physical system or the controller state. Five case studies are carried out to investigate the robustness and resiliency of the proposed control strategy against various contingency conditions and cyber threats.

Chapter 5

Novel DC Protective Relay System for DC Microgrids

5.1 Introduction

The challenge for protection systems in DC microgrids is to quickly detect, identify, locate, and isolate the faults to avoid any voltage collapse in the network as the power electronics-based DC network is very sensitive to faults and disturbances due to their relatively low inertia as compared to their AC counterparts [127, 257, 258] This chapter proposes a novel protection relay system that can detect, identify, locate, and isolate various fault conditions in DC microgrids. It consists of two elements: directional and distance elements for optimum identification and locating faults. Both elements are achieved by integrating a sensing inductor at both positive and negative poles of the power line connecting the network DC buses. By effectively capturing three local measurements: relay inductor voltage, relay terminal voltage, and the relay inductor current, the fault location is accurately determined. The design and consideration of the relay inductor are clearly described, while the effect of the fault types, fault resistance, grounding configuration, and grounding resistance is investigated. The proposed protection system incorporates Signal Conditioning Circuit (SCC) and Signal Peak Capture (SPC) units for accurately capturing the relay measurements at the fault instance for both bolted faults and resistance faults. The pro-

posed protection system has the ability to clear faults in the time frame of microseconds. The proposed relay system is tested and verified using MATLAB Simulink.

The main contribution of the proposed protection system can be summarized as follows:

- A Novel protection system for DC microgrids is proposed for detecting, identifying, locating, and isolating various faults.
- The proposed system incorporates multi-protection coordinated circuits ensuring optimum sensitivity for a wide range of bolted faults and high-resistance faults.
- A detailed design procedure for the relay elements is carried out considering the effects of the fault resistance, DC link capacitor dynamics, grounding configuration, and grounding resistance.
- The proposed system is capable of clearing faults in less than one resonant cycle while maintaining the DC buses in operating states after clearing the fault.

For the rest of this chapter, the principle of operation and relay architecture is demonstrated in section 5.2. Then, section 5.3 discussed a detailed fault analysis for both PG and PP with bolted and resistance faults, considering all the dynamics of the network components. Section 5.4 explains the relay design steps including all associated parameters that should be taken into account. Then the SCC and SPC unit designs are carried out. Finally, in section 5.5, various case studies' numerical simulations are presented, and section 5.6 concludes the chapter.

5.2 Principle of operation and Relay architecture

A sensing and current limiting inductor is integrated at each pole of each power line end, as seen in Fig. 5.2. For the relays placed at bus A on the power line AB, the positive pole relay is denoted by R^{+}_{AB}, while the negative pole relay is denoted by R^{-}_{AB}. For performing the direction and distance calculations, three quantities are measured at each relay which are the line current i_A, the relay inductor voltage v_L, and the relay terminal voltage v_R

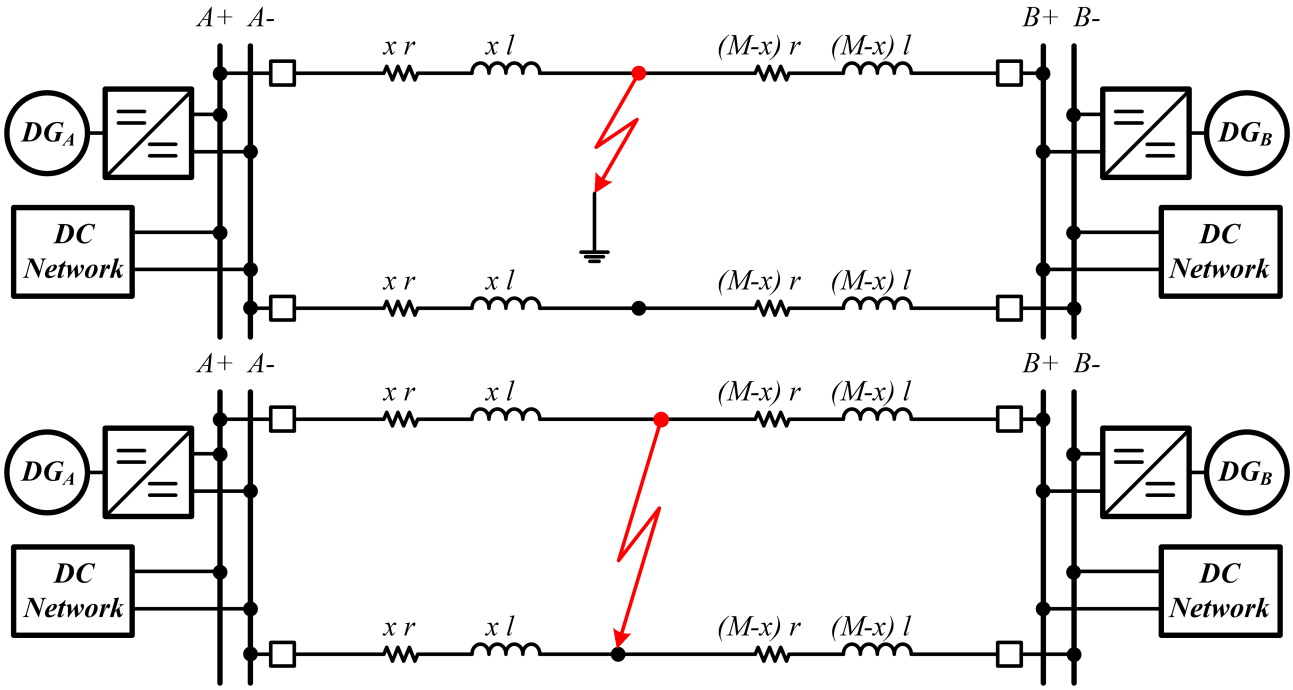

Figure 5.1: Power Line equivalent circuit, (a) PG fault, (b) PP fault

as shown in Fig. 5.2. The detailed calculations for direction and distance elements are described in the upcoming subsections. It is worth mentioning that the local measurements of each relay are not affected only by the fault type, but also by the power line resistance and inductance, DC link capacitors, fault resistance, and grounding resistance. These parameters have major effects on the system dynamics under fault conditions which affect the relay measurements, and hence the detection, identification, and location algorithms.

5.2.1 Power circuit

The power circuit consists of a mesh DC microgrid and relay inductors. These inductors are attached to both of the power feeder poles as shown in Fig. 5.2. The power feeder connecting bus A and Bus B has a length of M, and has a distributed resistance and inductance of r Ω/m and l H/m, respectively as shown in Fig. 5.1. As a general case, a positive PG fault with a resistance R_f takes place at a point with x meters away from bus

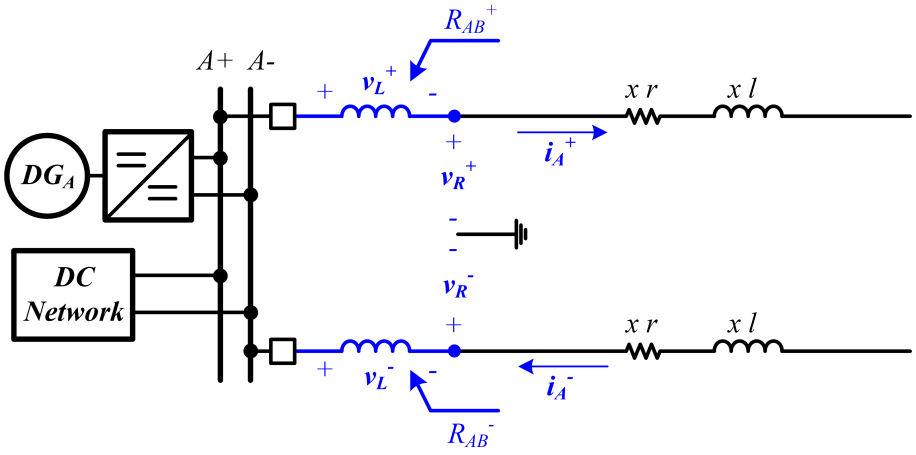

Figure 5.2: Relay placement at bus A for Power Line AB

A as shown in Fig. 5.3. The local measurements of the relay R_{AB}^{+} can be determined as:

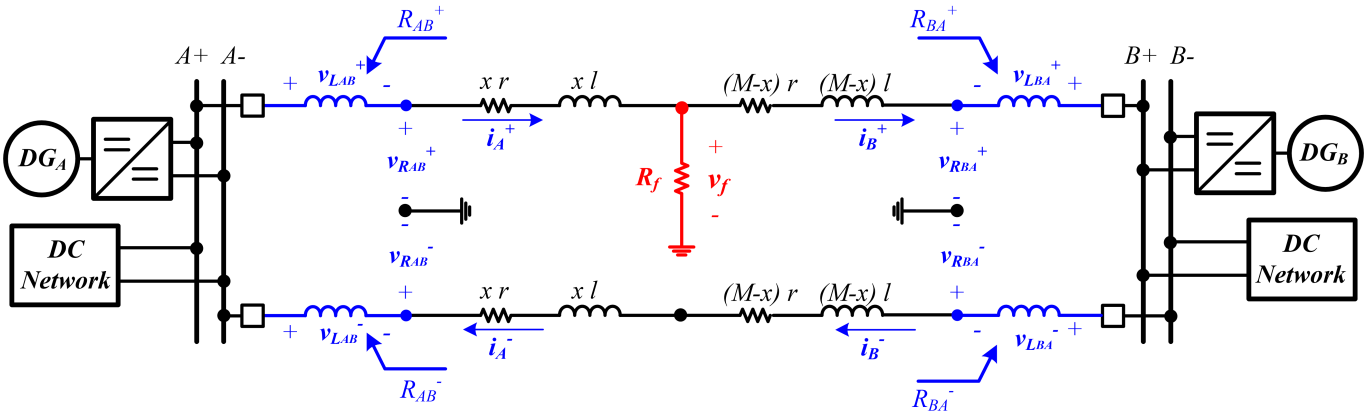

Figure 5.3: Relay Circuits for positive PG fault

$$
\begin{aligned}
v_{R_{AB}}^{+} &= v_f + x\ r\ i_A^{+} + x\ l \frac{di_A^{+}}{dt} \\
v_{L_{AB}}^{+} &= L \frac{di_A}{dt}
\end{aligned}
\tag{5.1}
$$

where $v_{R_{AB}}^{+}$ and $v_{L_{AB}}^{+}$ are the terminal and inductor voltages of the positive pole relay

at bus A, respectively. i_A^+ is the measured power line current at bus A, while x is the distance to the fault location measured at bus A, and v_f is the voltage drop across the fault resistance. Similarly, the local measurements of the relay R_{BA}^+ can be determined as:

$$\begin{aligned} v_{R_{BA}}^+ &= v_f - (M-x)\, r\, i_B^+ - (M-x)\, l \frac{di_B^+}{dt} \\ v_{L_{BA}}^+ &= -L \frac{di_B^+}{dt} \end{aligned} \tag{5.2}$$

where M is the length of power line AB. The fault voltage drop can be determined as:

$$v_f = (i_A^+ - i_B^+) R_f \tag{5.3}$$

where R_f is the fault resistance. Based on equations 5.1 and 5.3, the fault location estimated at bus A can be determined as:

$$x = \frac{v_{R_{AB}}^+(0)}{r\, i_A^+(0) + \frac{l\, v_{L_{AB}}^+(0)}{L}} \tag{5.4}$$

where $v_{R_{AB}}^+(0)$, $v_{L_{AB}}^+(0)$, and $i_A^+(0)$ are the relay R_{AB}^+ terminal voltage, inductor voltage, and current respectively, while x is the fault location measured at bus A. The same analysis can be used for PP faults considering the positive and negative pole symmetry. However, both bus A relays, that is R_{AB}^+ and R_{AB}^- are detecting the faults in the forward direction.

It should be noted that for relay R_{AB}, for example, under normal conditions, the relay inductor voltage $v_{L_{AB}}^+$ is almost zero and has no effect. The relay inductor current i_A^+ equals the assigned line current based on the proportional load sharing and global voltage balancing objectives discussed in Chapter 4. The relay terminal voltage $v_{R_{AB}}^+$ equals half of the DC link voltage at bus A. On the other hand, once a fault occurs, while a line current increases as the DC link capacitors discharge, a positive or negative pulse is induced across the relay inductor indicating a forward or a reverse fault respectively. Based on this principle, the relay directional element is achieved. The relay terminal voltage decreases rapidly during the capacitor's discharging period. Capturing the three local quantities for each relay precisely is mandatory for an accurate estimation of the fault location. However, this may be challenging due to the fast dynamics of the system under fault conditions. For example, for high fault resistance, the voltage measurements of the relay

are damped rapidly. As a result, high bandwidth transducers are required to capture such high transient voltages. The next subsection introduces the relay SCC which is responsible for detecting abnormal conditions and capturing the signals required for estimating the fault location through the SPC unit.

5.2.2 Signal Conditioning Circuit (SCC)

The main function of this unit is to process the instantaneous values of the relay terminal voltage, inductor current, and inductor voltage at the fault instance and make them suitable to be fed to the Analog to Digital Converter (ADC) ports of the processing unit. This can be achieved by attenuating the high-power relay signals while providing a low output impedance to ensure accurate measurements. Moreover, the SCC provides extremely high input impedance for isolating the power and control networks. Furthermore, the SCC can measure high-frequency transients through its high bandwidth capability. This can be achieved by using differential configuration of high bandwidth OP-AMP [259]. Finally, the integrated SPC unit is responsible for maintaining the transient signals until sampled by the processing unit.

5.2.2.1 Relay inductor and terminal voltages

At the fault instant, the transient response of the DC network depends on the dynamic characteristics of the DC link capacitors, the Power line equivalent inductance/resistance, and the integrated relay inductor at each power pole for each bus. Due to the power line and the integrated relay inductance, the fault line's current rate of change is limited. On the other hand, the relay inductor and terminal voltages have high and fast transient profiles due to the inductance differentiation effect. This case becomes worse for through resistance faults, as the measured transient voltages are rapidly damped. As a result, a differential-based OP-AMP conditioning circuit is required to measure such high frequency and damped transients. For the relay R^{+}_{AB}, the relay terminal voltage SCC is illustrated in Fig. 5.4, while the relay inductor voltage SCC is illustrated in Fig. 5.5. It can be seen that the input measured voltages are applied to a voltage divider circuit to step down the voltage

level to be within the operating maximum bias range of the OP-AMP integrated circuits ($\pm 24V$). It should be noted that the relay voltages can be either positive or negative values based on the fault location (Internal or external). Hence the SCC has to be powered with bidirectional bias as shown in Fig. 5.4 and 5.5. The resistors of the SCC are selected to achieve the required attenuation factor to ensure a safe range of the output signals for the processing unit ADC.

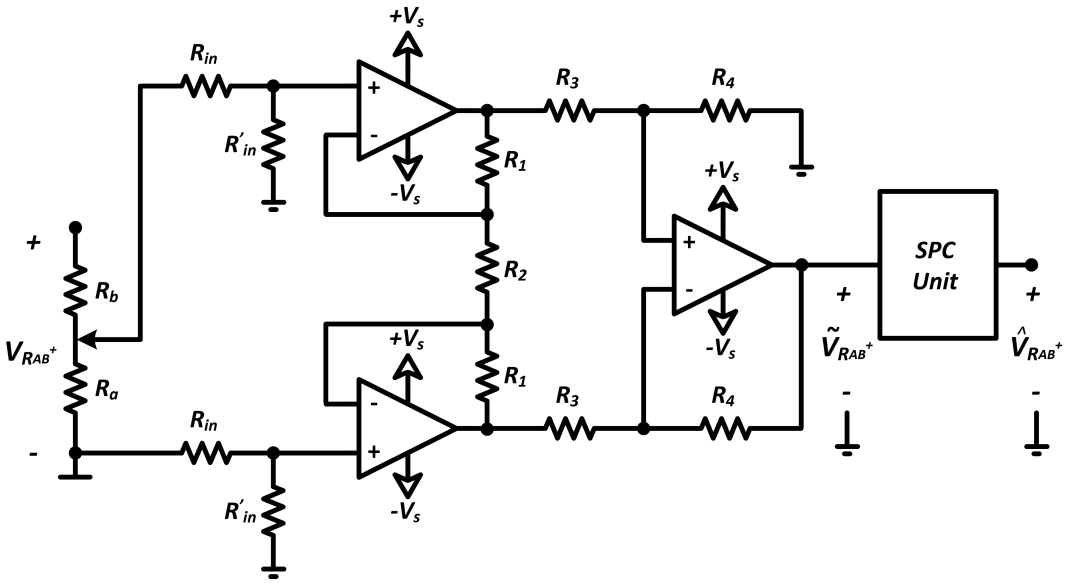

Figure 5.4: Relay terminal voltage signal conditioning circuit

The attenuation factor for the SCC for both relay inductor and terminal voltages can be determined based on the differential circuit configuration as:

$$\begin{aligned} \tilde{v}_{R^+_{AB}} &= G_R * v_{R^+_{AB}} \\ \tilde{v}_{L^+_{AB}} &= G_L * v_{L^+_{AB}} \\ G_R = G_L &= (\frac{R'_{in}}{R_{in} + R'_{in}})(\frac{2R_1 + R_2}{R_2})(\frac{R_4}{R_3}) \end{aligned} \tag{5.5}$$

where R_{in} is the input resistance, while R_1, R_2, R_3, R_4, and R_{in} are responsible to achieve the required attenuation ratio. The output of the OP-AMP network is then fed to the SPC to capture the peak values $\hat{v}_{R^+_{AB}}$ and $\hat{v}_{L^+_{AB}}$ as shown in Fig. 5.4 and 5.5.

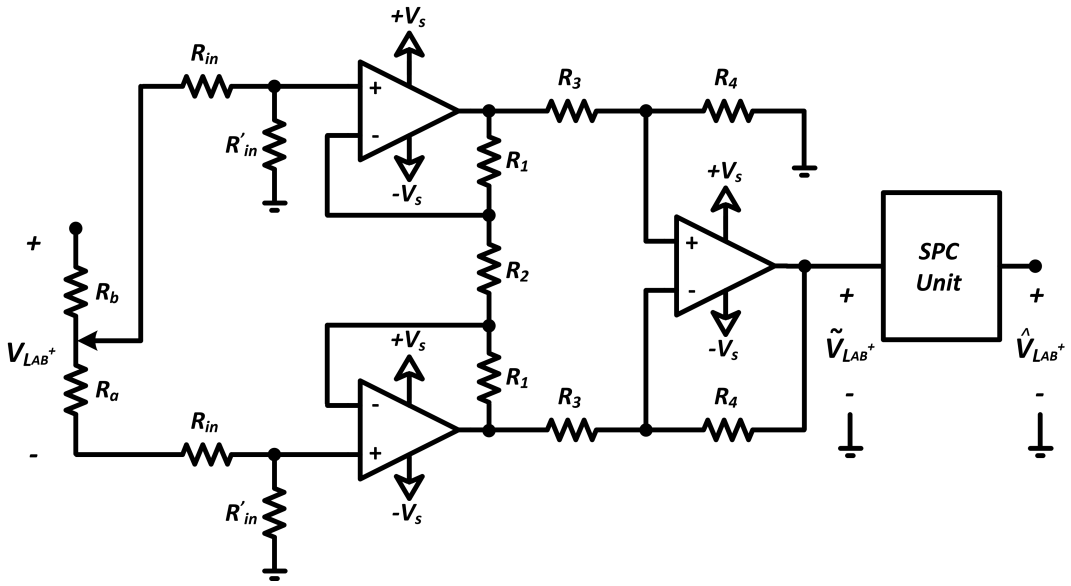

Figure 5.5: Relay inductor voltage signal conditioning unit

5.2.2.2 Relay inductor current

As mentioned in the previous subsection, the fault current rate of change is limited by the power line inductance as well as the integrated relay sensing inductor, which is not the case for the relay voltages. As a result, a lower bandwidth current transducer can be used for current sensing. Industrial hall effect-based current transducers can effectively measure the relay inductor current. In the system under study, the LA55P industrial transducer is used for current measurements [260] as shown in Fig. 5.6. This current transducer has the ability to measure DC, AC, and pulsed power signals with galvanic separation between the power and control circuits. The value of transducer output resistance R_M is selected based on the maximum current capability of the transducer and the processing unit ADC input range as follows [260]:

$$R_M = \frac{V_M}{I_S} = \frac{V_M * 1000}{I_P * N} \tag{5.6}$$

where V_M is the transducer output voltage, I_P and I_S are the maximum primary and secondary currents, N is the number of applied turns across transducer core. On the other hand, resistors R_5 through R_{10} are responsible for tuning the measured signal and inserting

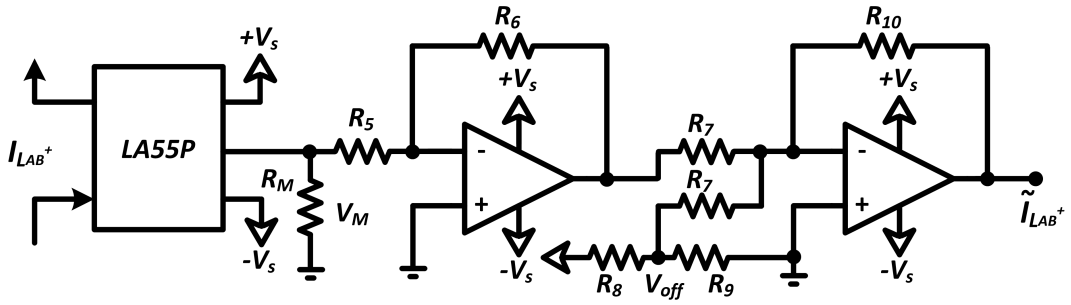

Figure 5.6: Relay inductor current signal conditioning circuit

DC offset to ensure the safe positive range of analog signals to be fed to the ADC unit. The unit output current can be represented by the following equation:

$$\begin{aligned} \tilde{I}_{L^+_{AB}} &= (\frac{R_{10}}{R_7})(\frac{R_6 * R_M * I_P * N}{1000 * R_5} - V_{off}) \\ V_{off} &= (\frac{R_9}{R_8 + R_9})V_S \end{aligned} \tag{5.7}$$

where V_{off} is the DC offset voltage, while V_S is the OP-AMP bias voltage.

5.2.3 Signal Peak Capture (SPC) Unit

The SPC unit is attached to both relay voltage measuring conditioning circuits. SPC has two main functions: to add a DC offset to the output measured signal of the SCC and to capture the peak value of this measured signal and maintain it for the longest sampling time. Adding a DC offset to the SPC measured voltages ensures a safe attenuated positive voltage that can be applied to the ADC unit. It should be noted that adding a DC offset is mandatory as the relay voltages can be positive or negative based on which pole this relay is connected to or whether the fault is internal or external. The SPC consists of a non-inverting OP-AMP with non-inverting positive reference voltage [261] and a Diode-Capacitor peak capture circuit. The construction of the SPC units for the relay inductor voltage and terminal voltage are shown in Fig. 5.7 and 5.8 respectively.

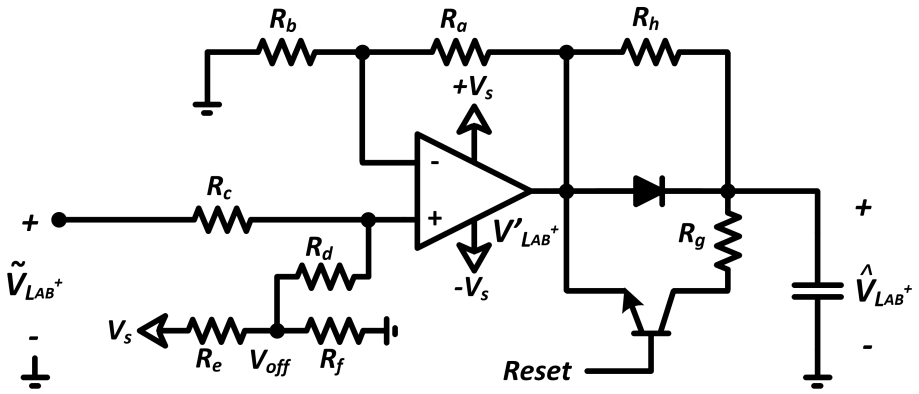

Figure 5.7: Relay inductor voltage SPC unit

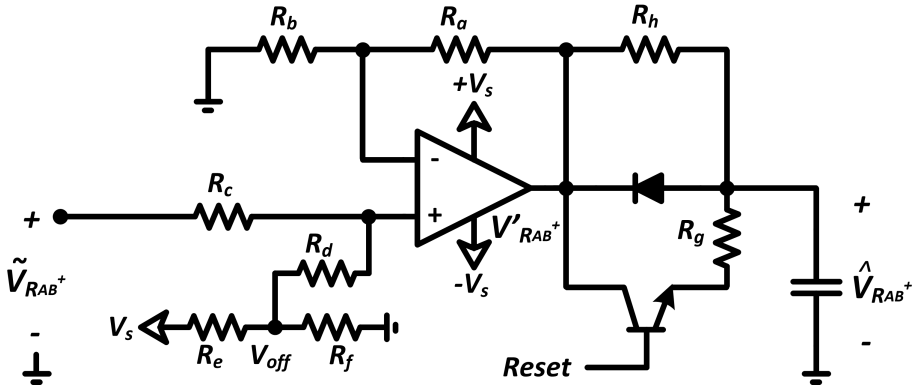

Figure 5.8: Relay terminal voltage SPC unit

The DC offset circuit function is to offset the maximum negative measurements to be almost zero to be sampled safely using the ADC unit, while the maximum positive measurements are to be below the maximum voltage rating of the ADC unit. The output voltage of the offset circuit can be expressed as [261]:

$$
\begin{aligned}
V'_{L^+_{AB}} &= V_{L^+_{AB}} * (\frac{R_d}{R_c + R_d})(\frac{R_a + R_b}{R_b}) + V_{off} * (\frac{R_c}{R_c + R_d})(\frac{R_a + R_b}{R_b}) \\
V'_{R^+_{AB}} &= V_{R^+_{AB}} * (\frac{R_d}{R_c + R_d})(\frac{R_a + R_b}{R_b}) + V_{off} * (\frac{R_c}{R_c + R_d})(\frac{R_a + R_b}{R_b}) \\
V_{off} &= V_S * (\frac{R_f}{R_e + R_f})
\end{aligned}
\tag{5.8}
$$

where $V'_{L^+_{AB}}$ and $V'_{R^+_{AB}}$ are the relay inductor and terminal voltages after attenuation (SCC) and adding the DC offset, while V_S is the bias voltage.

On the other hand, the peak capturing function is achieved using a capacitor-diode circuit as shown in Fig. 5.7 and 5.8. It should be noted that the diode orientation is not the same for the relay terminal and relay inductor channels. For the positive pole relay at bus A towards power line AB, R^+_{AB}, the inductor voltage is normally at zero level, but when a forward fault occurs (internal or external), a positive transient pulse is induced across the relay inductor. Hence, the SPC capacitor is charged through the diode which is connected in a way to capture the maximum positive value as shown in Fig. 5.7. It is worth noting that if a reverse fault occurs a negative pulse is induced across the relay inductor, which means that the voltage across the capacitor remains at its initial zero voltage level which is the maximum voltage level as compared to the negative induced input pulse. In this way, the relay is detecting the forward faults only achieving the directional functionality of the relay. Similarly, the relay terminal voltage normally has a high voltage level (half of the DC link voltage in the case of TNS, TNC grounding schemes with midpoint grounding point). The capacitor is initially charged to the same voltage level during steady-state operation through the charging resistor R_h. When a forward fault occurs (internal or external), a transient voltage drop occurs at the relay terminal voltage due to the induced transient voltage across the relay inductor. Hence, the SPC capacitor is discharged through the diode which is connected in a way to capture the minimum positive value as shown in Fig. 5.8. Similarly, for reverse faults, a positive pulse is induced and accumulated above the operating high voltage level across the relay terminal, which means that the voltage across the capacitor remains at its initial voltage level which is the minimum voltage level as compared to the accumulated induced input pulse. During the normal operation, the

capacitor of the SPC unit is charging from its initial state to the steady state through the charging resistor R_h. This can be formulated as follows:

$$\begin{aligned}
&\hat{v}_{L^+_{AB}}(t) = \hat{v}_{L^+_{AB}}(\infty) + (\hat{v}_{L^+_{AB}}(0) - \hat{v}_{L^+_{AB}}(\infty)) * e^{\frac{-t}{\tau}} \\
&\hat{v}_{R^+_{AB}}(t) = \hat{v}_{R^+_{AB}}(\infty) + (\hat{v}_{R^+_{AB}}(0) - \hat{v}_{R^+_{AB}}(\infty)) * e^{\frac{-t}{\tau}} \\
&\hat{v}_{L^+_{AB}}(\infty) = 0, \quad \hat{v}_{R^+_{AB}}(\infty) = \frac{V^A_{DC}}{2}, \quad \tau = R_h C
\end{aligned} \tag{5.9}$$

where $\hat{v}_{L^+_{AB}}(\infty)$ and $\hat{v}_{R^+_{AB}}(\infty)$ are the steady state values of the inductor and terminal relay voltages, respectively. $\hat{v}_{L^+_{AB}}(0)$ and $\hat{v}_{R^+_{AB}}(0)$ are the initial values of the inductor and terminal relay voltages, respectively. τ is the charging time constant. Once the fault is detected, identified, and then cleared, the SPC unit is reset to be enabled to capture upcoming fault transients. This can be achieved through the resistor-transistor circuit shown in Fig. 5.7 and 5.8. The npn Bipolar Junction Transistor (BJT) is activated after clearing the fault forcing the capacitor to be charged/discharged through the resistor R_g. This charging/discharging process is activated until $\hat{v}_{R^+_{AB}} = v'_{R^+_{AB}}$ and $\hat{v}_{L^+_{AB}} = v'_{L^+_{AB}}$, respectively. The charging/discharging process can be expressed as:

$$\begin{aligned}
&\hat{v}_{L^+_{AB}}(t) = v'_{L^+_{AB}} + (\hat{v}_{L^+_{AB}}(0) - v'_{L^+_{AB}}) * e^{\frac{-t}{\tau_d}} \\
&\hat{v}_{R^+_{AB}}(t) = v'_{R^+_{AB}} + (\hat{v}_{R^+_{AB}}(0) - v'_{R^+_{AB}}) * e^{\frac{-t}{\tau_c}} \\
&\tau_c = \tau_d = R_g C
\end{aligned} \tag{5.10}$$

where τ_c and τ_d are the charging and discharging time constants for the relay inductor and terminal reset circuits respectively.

5.3 Fault analysis

During normal operation without fault conditions, the power line resistance has the dominant effect on the power flow in the DC network [262]. However, when a fault occurs,

many other factors become restrict the power flow. These factors include the power line inductance, the DC link capacitance, the fault resistance, the fault type, the grounding scheme, and the grounding resistance [50, 61, 117, 258]. The dynamic performance of the DC microgrid during the fault condition should be investigated for designing an optimum, fast, and reliable protection system. Hence, all the aforementioned factors should be taken into account during the fault conditions and their effects on the proposed protection system are discussed.

To consider the dynamic behavior of the system under the fault phases, the proposed protection elements have to be considered as they also contribute to the overall system dynamics. For that reason, during the fault condition, the power line of a DC network with the proposed protection system integrated is modeled as shown in Fig. 5.10. It should be noted that the DC buses have a midpoint grounding which is common for unipolar DC microgrids [117]. The grounding point has a dominant effect on the fault current, especially for ground faults [263] as it creates a return path for the fault current as shown in Fig. 5.10. The interaction between the power line inductance/resistance, the DC link capacitors, the integrated relay inductors, the grounding resistance, and the fault resistance formulates the dynamic behavior of the fault current and the protection relay measurements during the fault conditions. This dynamic behavior is studied in the next subsections as follows.

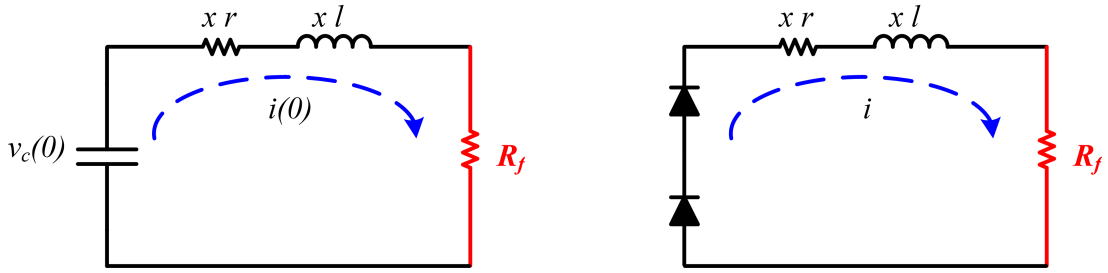

(a) Capacitor Discharge Phase (b) Diode Freewheeling Phase

Figure 5.9: DC Network Fault Phases

The DC network can be considered as a second-order RLC transient circuit with unknown fault resistance and location. The interaction between the circuit inductance, capacitance, and resistance determines the transient response of the network. It should be

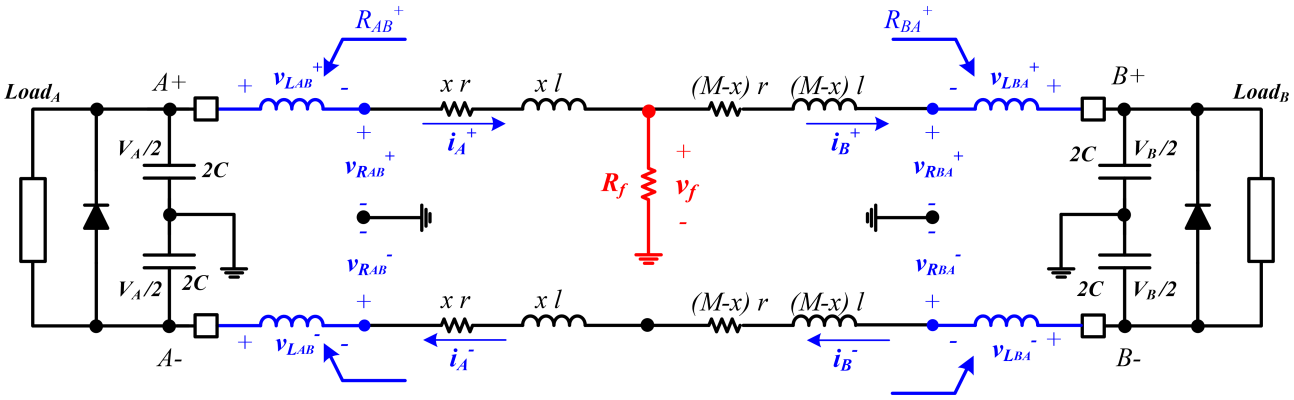

Figure 5.10: System model under fault condition

noted that to detect the fault very fast, the estimated distance should remain steady until the circuit breaker receives the trip signal and opens the faulted power line. This is while the DG converter power switch can be deactivated in a few switching cycles. The estimated distance is affected by the natural response of the RLC combinations of the faulted network after deactivating the DG converter switches. So, the natural response of the fault network should be studied to investigate the operation performance of the protection system.

5.3.1 PG Fault analysis

For the ground faults, the DC microgrid grounding scheme has a dominant effect on the fault current. The fault current that goes through the grounding system and then to the earth is called stray current [50, 110]. The grounding resistance also affects the system's dynamic response during fault conditions. For the TT, TN-S, TN-C, and TN-C-S, the DG's DC-DC converter is grounded, while the appliances connected to the bus have different grounding configurations. For the unipolar DC microgrid network under study, the DC-DC converter of the DG is grounded at the mid-point of the DC link capacitors at each bus as shown in Fig. 5.10. The grounding could be through a resistance to minimize the stray current or solidly to minimize the common mode voltage [125]. For the ungrounded systems, the PG may not be detected, but if a second PG fault occurs, a closed circuit is created producing a high fault current. Even this high fault current may not be detected as

it depends on the fault points locations [264]. For the system under study with 480V DC voltage level, it is recommended to avoid ungrounded systems for safety as the common-mode voltage will be high which presents a danger for personnel [265]. For the grounded system, it is recommended to use the DC bus midpoint as the grounding point to enhance safety and minimize the ground potential [266].

5.3.1.1 Bolted PG Fault

For bolted PG fault, the power line is connected directly to the ground at the fault point. Hence, the DC link capacitors at both buses are going to feed a rapidly increasing current to the fault location. Due to the direct connection of the line at the fault location to the ground, the power line can be considered as two separate sections with separate dynamics. The transient response of each section is determined by the corresponding part of the power line, the bus DC link capacitor, the grounding resistance, and the integrated relay inductors. The dynamic equation that describes the transient response during fault condition at the positive pole relay connected at bus A towards the power line AB can be expressed as:

$$\frac{d^2 i_A}{dt^2} + (\frac{xr + R_g}{xl + L})\frac{di_A}{dt} + (\frac{1}{2(xl + L)C})i_A = 0 \tag{5.11}$$

where $2C$ is the capacitor connected between the faulted pole and the ground, R_g is the grounding resistance, L is the integrated inductor of the relay, x is the fault location concerning bus A towards line AB, and r and l are the power line resistance and inductance per unit length, respectively. The characteristic equation for the above second-order differential equation can be written as:

$$\begin{aligned} S^2 + (\frac{xr + R_g}{xl + L})S + (\frac{1}{2(xl + L)C}) = 0 \\ \text{where } S_1 = -\frac{xr + Rg}{2(xl + L)} + \sqrt{(\frac{xr + Rg}{2(xl + L)})^2 - \frac{1}{2(xl + L)C}} \\ S_2 = -\frac{xr + Rg}{2(xl + L)} - \sqrt{(\frac{xr + Rg}{2(xl + L)})^2 - \frac{1}{2(xl + L)C}} \end{aligned} \tag{5.12}$$

where S_1 and S_2 are the roots of the characteristic equation, which are called the natural frequencies [267]. There are two possible solutions for this second-order equation which express the transient response of the power line current from bus A towards the fault location. These two solutions can be expressed as:

$$\begin{aligned} i_{A1} &= \Gamma_1 e^{-(\frac{xr+Rg}{2(xl+L)} - \sqrt{(\frac{xr+Rg}{2(xl+L)})^2 - \frac{1}{2(xl+L)C}})t} \\ i_{A2} &= \Gamma_2 e^{-(\frac{xr+Rg}{2(xl+L)} + \sqrt{(\frac{xr+Rg}{2(xl+L)})^2 - \frac{1}{2(xl+L)C}})t} \end{aligned} \tag{5.13}$$

where Γ_1 and Γ_2 are constants. A complete solution would therefore require a linear combination of i_{A1} and i_{A2}. Thus, the natural response of the RLC network is $i_A(t) = \Gamma_1 e^{s_1 t} + \Gamma_2 e^{s_2 t}$, where the constants Γ_1 and Γ_2 can be determined from the initial conditions. The dominant terms that determine the transient response of the system are the resonant frequency ω_o and the neper frequency α. These two terms can be expressed as:

$$\begin{aligned} \omega_o &= \frac{1}{\sqrt{2(xl+L)C}} \\ \alpha &= \frac{(xr+R_g)}{2(xl+L)} \end{aligned} \tag{5.14}$$

There are three types of solutions representing the transient response of the power line current during fault conditions. The actual solution depends on the system dynamics, including the power line parameters, the grounding resistance, and the integrated sensing inductor.

If both roots are real values and not equal, the line's current response is overdamped. In this case the $\alpha > \omega_o$. For bolted PG faults, this can occur only if the system is grounded through a relatively high ground resistance as compared to the power line resistance. The higher the grounding resistance, the more damping for the fault current response. The transient response of the power line current from bus A toward the fault location can be determined as follows:

$$i_A(t) = \Gamma_1 e^{-(\frac{xr+Rg}{2(xl+L)} - \sqrt{(\frac{xr+Rg}{2(xl+L)})^2 - \frac{1}{2(xl+L)C}})t} + \Gamma_2 e^{-(\frac{xr+Rg}{2(xl+L)} + \sqrt{(\frac{xr+Rg}{2(xl+L)})^2 - \frac{1}{2(xl+L)C}})t} \tag{5.15}$$

where Γ_1 and Γ_2 can be determined from the initial conditions of the system. If both roots are real values and equal, the line current response is critically damped. In this case

the $\alpha = \omega_o$.The transient response of the power line current from bus A toward the fault location can be determined as follows:

$$i_A(t) = (\Gamma_2 + \Gamma_1 t)e^{-\frac{(xr+R_g}{2(xl+L)}} \tag{5.16}$$

Finally, if both roots are complex values and unequal, the line current response is underdamped with a damped oscillation. In this case the $\alpha < \omega_o$. The frequency of the damped oscillation can be determined as:

$$\omega_d = \sqrt{(\frac{1}{2(xl+L)C}) - (\frac{(xr+R_g)^2}{4(xl+L)^2})} \tag{5.17}$$

where ω_d is the damped oscillation frequency in (rad/s). The transient response of the power line current from bus A toward the fault location can be determined as follows:

$$i_A(t) = e^{\frac{-(xr+R_g)}{2(xl+L)}t}(\Gamma_1 cos(\omega_d t) + \Gamma_2 sin(\omega_d t)) \tag{5.18}$$

Fig. 5.11 shows the different three transient responses for the fault current measured at bus A towards the power line AB.

5.3.1.2 Resistance PG Fault

For the ground faults through a resistance, the fault resistance has a dominant effect on the fault current response. Moreover, the system dynamics are more complex as the power line cannot be separated into two different systems. As a result, the two buses and the total length of the power line affect the transient response of the fault current. The dynamic equation that describes the transient response during fault condition at the positive pole relay connected at bus A towards the power line AB can be expressed as:

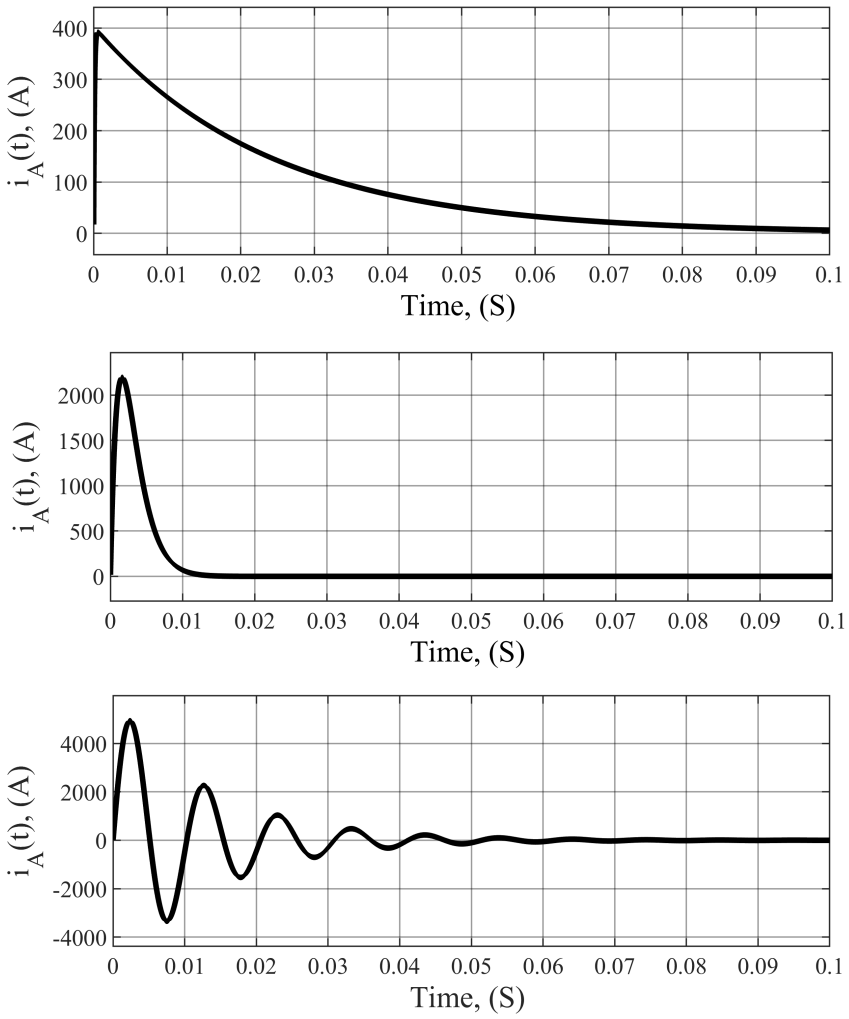

Figure 5.11: Different measured fault current transient responses for PG bolted fault, (a) Overdamped, (b) Critically damped, (c) Underdamped.

$$
\begin{aligned}
&L_A L_B \frac{d^4 i_A}{dt^4} + ((R_f + R_A)L_B + (R_f + R_B)L_A)\frac{d^3 i_A}{dt^3} + \\
&((R_f + R_A)(R_f + R_B) + \frac{L_A - L_B}{2C} - R_f^2)\frac{d^2 i_A}{dt^2} + \\
&(\frac{R_A - R_B}{2C})\frac{di_A}{dt} - \frac{1}{4C^2} i_A = 0 \\
&\qquad R_A = xr + R_g \\
&\qquad R_B = (M - x)r + R_g \\
&\qquad L_A = xl + L \\
&\qquad L_B = (M - x)l + L
\end{aligned}
\tag{5.19}
$$

where R_f is the fault resistance, while R_g is the grounding resistance. It can be seen that the fault current transient response is repressed by a 4th-order differential equation. As this differential equation is homogeneous, it can be solved as a quadratic polynomial. First, the characteristic equation of this differential equation can be expressed as:

$$L_A L_B S^4 + ((R_f + R_A)L_B + (R_f + R_B)L_A)S^3 + ((R_f + R_A)(R_f + R_B) + \frac{L_A - L_B}{2C} - R_f^2)S^2 + (\frac{R_A - R_B}{2C})S - \frac{1}{4C^2} = 0 \tag{5.20}$$

A general form of a 4th-order quadratic polynomial can be expressed as:

$$aS^4 + bS^3 + cS^2 + dS + e = 0 \tag{5.21}$$

The solution of this 4th order quadratic polynomial can be determined as follows [268]:

$$S_{1,2,3,4} = -\frac{b}{4a} + k_{1,2,3,4} \tag{5.22}$$

where the k factor can be expressed as:

$$k_{1,2,3,4} = \frac{-2(\pm\lambda_{1,2}) \pm \sqrt{4(\lambda_{1,2})^2 - 4(\frac{1}{6 \pm \mu + 2y_{1,2,3}})}}{2} \tag{5.23}$$

where the μ factor is determined as a function of λ as:

$$\mu = \frac{-\frac{m}{4}}{\lambda_{1,2}} \tag{5.24}$$

where $m = -\frac{b^3}{16a^2} + \frac{d}{a}$, while $\lambda_{1,2}$ can be expressed as a function of $y_{1,2,3}$ as:

$$\lambda_{1,2} = \pm\sqrt{y_{1,2,3} - \frac{l}{6}} \tag{5.25}$$

where $l = \frac{c}{a}$. The values of the y factor are determined from the following cubic equation:

$$\begin{aligned} & y^3 - [n + 3(\frac{l}{6})^2]y + (\frac{nl}{6} - \frac{m^2}{16} - \frac{l^3}{216}) = 0 \\ & OR \quad y^3 + Ly + M = 0 \end{aligned} \tag{5.26}$$

where $L = -[n+3(\frac{l}{6})^2]$, $M = (\frac{nl}{6} - \frac{m^2}{16} - \frac{l^3}{216})$, and $n = \frac{e}{a} + \frac{23b^4}{256a^4} + \frac{b^2c}{4a^3} + \frac{bc}{2a^2} + \frac{bd}{4a^2} - \frac{3b^2}{16a^3} - \frac{b^4}{64a^3}$. The solution of this cubic equation is expressed as:

$$\begin{aligned} y_1 &= (re^{i\theta})^{\frac{1}{3}} - \frac{3}{(re^{i\theta})^{\frac{1}{3}}} \\ y_2 &= (re^{i(\theta+2\pi)})^{\frac{1}{3}} - \frac{3}{(re^{i(\theta+2\pi)})^{\frac{1}{3}}} \\ y_3 &= (re^{i(\theta+4\pi)})^{\frac{1}{3}} - \frac{3}{(re^{i(\theta+4\pi)})^{\frac{1}{3}}} \end{aligned} \tag{5.27}$$

where $r = r_{1,2}$, for $\omega = \omega_{1,2} = r_{1,2}e^{i\theta}$. $\omega_{1,2}$ can be calculated from the following equation:

$$\omega_{1,2} \frac{-27M \pm \sqrt{729M^2 + 108L^3}}{54} \tag{5.28}$$

The roots of the equation 5.22 determine the transient response of the line current i_A during the fault condition. It should be noted that the lower the fault resistance, the lower the interaction of the rear bus to the near bus during fault conditions. In other words, the transient response can be expressed by the second-order differential equations for low fault resistance faults.

5.3.2 PP Fault Analysis

The PP rarely occurs as compared to PG faults. Although PP faults are very similar to the PG faults in terms of the dynamic response during fault conditions, they are independent of the grounding configuration or the grounding resistance.

5.3.2.1 Bolted PP Fault

For bolted PP faults, as there is no fault resistance, the power line dynamics is divided into two sections like bolted PG faults. However, the freewheeling diodes DC-DC converters, which are connected across each bus pole are involved in the closed fault circuit. So, the protection system must isolate the fault as fast as possible to avoid the fault current

freewheeling that may destroy the diode, which occurs if the fault current has an oscillating response. The faulted circuit includes both the Bus pole's integrated inductors, power line resistance, and inductance, and the series connected DC link capacitors. The dynamic equation that describes the transient response during fault condition at the positive pole relay connected at bus A towards the power line AB can be expressed as:

$$\frac{d^2 i_A}{dt^2} + (\frac{xr}{xl + L})\frac{di_A}{dt} + (\frac{1}{2(xl + L)C})i_A = 0 \tag{5.29}$$

It is clearly seen that the transient response of the PP bolted fault described in equation 5.32 is exactly similar to the transient response of the PG bolted fault described in equation 5.11. The only difference between the two equations is the grounding resistance which has no effect for PP faults. As a result, most of the PP faults have an underdamped fault current response with high peaks, as the faulted circuit has a relatively low resistance of the pole's power lines. The roots and the transient response can be determined from equations 5.12 and 5.18, respectively, with disregarding the grounding resistance R_g. However, as mentioned before, for the underdamped transient response of the fault current, the diode will contribute to the fault circuit. Once the DC link capacitor is fully discharged (at maximum fault current), the stored energy in the power line inductance and the relay inductor will be freewheeled through the diode which shorts the DC link capacitor. This high level of energy is capable of destroying the diode. As a result, the protection system has to isolate the power line during the capacitor discharge period to protect the converters' diodes. During the freewheeling period, the fault circuit contains the relay inductor, the power line parameters, and the converter diode that shorts the DC link capacitor. A comparison between PG and PP underdamped transient fault response for the same system parameters is illustrated in Fig. 5.12.

5.3.2.2 Resistance PP Fault

Similarly, the PP faults through resistance have quite similar dynamics to the PG resistance faults, except for two parameters: the grounding resistance and grounding configuration have no effects, and both positive and negative pole parameters are included in the fault circuit. The dynamic equation that describes the transient response during fault condition

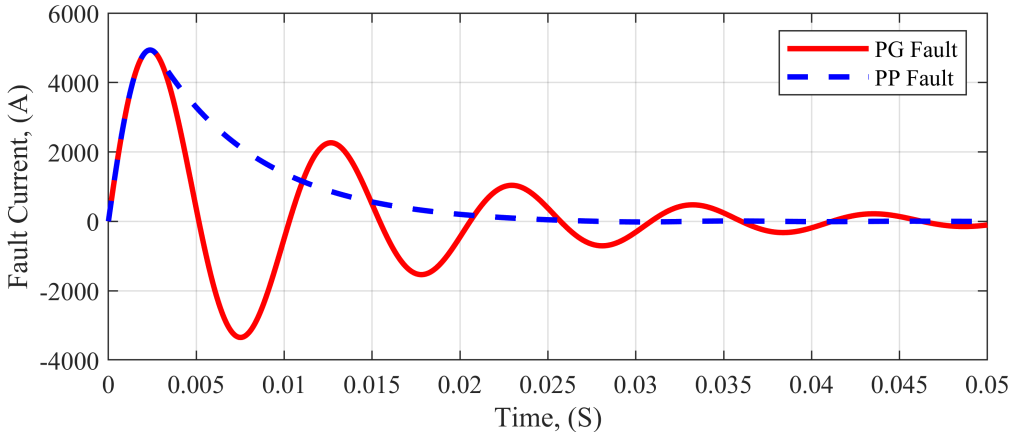

Figure 5.12: PG VS PP faults for underdamped transient fault current

at the positive pole relay connected at bus A towards the power line AB can be expressed as:

$$
\begin{aligned}
&L_A L_B \frac{d^4 i_A}{dt^4} + ((R_f + R_A)L_B + (R_f + R_B)L_A)\frac{d^3 i_A}{dt^3} + \\
&((R_f + R_A)(R_f + R_B) + \frac{L_A - L_B}{C} - R_f^2)\frac{d^2 i_A}{dt^2} + \\
&(\frac{R_A - R_B}{C})\frac{di_A}{dt} - \frac{1}{2C^2} i_A = 0 \\
&R_A = 2xr \\
&R_B = 2(M - x)r \\
&L_A = 2(xl + L) \\
&L_B = 2((M - x)l + L)
\end{aligned}
\tag{5.30}
$$

The roots of this 4^{th} order differential equation can be determined through equations 5.21 to 5.28 while updating the values of R_A, R_B, L_A, and L_B with the values illustrated in equation 5.30. The fault resistance has a dominant effect on the fault current response. The higher the fault resistance, the lower the oscillation probability with high damping. Similarly, with very low fault resistance, the transient response becomes more oscillatory and very similar to the bolted PP faults with the activation of the freewheeling phase.

To sum up, for a particular value of DC link capacitors and power line parameters, increasing the integrated relay inductor, and the ground and/or fault resistances have the opposite effect on the system dynamics during fault conditions.

5.4 System parameters and relay design and tuning

5.4.1 Relay Inductor Design

It can be easily seen from Fig. 5.11 that the underdamped response of the fault current has very high overshoots, which may destroy the power-electronic switches and diodes. The underdamped response is most likely occurring for bolted faults, as the fault circuit resistance is relatively small as compared to the inductance and capacitance. As a result, the worst fault cases are the bolted PG and PP, which are very similar in dynamics. From equations 5.12, 5.13, and 5.14, it is obvious that to maintain a non-oscillatory fault current response, the neper frequency α should be higher than the resonant frequency ω_o. In other words, we can say:

$$\begin{aligned}
&\text{if } \alpha > \omega_o \text{ OR } (xl + L) < 0.5C(xr + R_g)^2, \text{ Overdamped response} \\
&\text{if } \alpha = \omega_o \text{ OR } (xl + L) = 0.5C(xr + R_g)^2, \text{ Critically damped response} \\
&\text{if } \alpha < \omega_o \text{ OR } (xl + L) > 0.5C(xr + R_g)^2, \text{ Underdamped response}
\end{aligned} \tag{5.31}$$

From equation 5.31, it can be concluded that reducing the value of the integrated relay inductance decreases the probability of the overshoot. However, it should be noted, on the other hand, that low values of relay inductance lead to high-rate damping of fault current, which makes it challenging to capture the relay measurements with fast dynamic response. In other words, the integrated relay inductance can be considered a buffer that stores the fault measurements. The lower the relay inductance, the higher the bandwidth requirements of the measuring transducers. Also, SPC unit is used for capturing It is worth noting that underdamped cannot be avoided, especially for solidly grounded systems and for faults near the DC buses. As a result, the relay sensing inductor should be designed to ensure the following objectives:

- Faults must be cleared in less than a quarter resonant cycle from the fault instant to avoid fault freewheeling for PP faults.
- maintains stable captured measurements until clearing the fault.
- ensures that the maximum resonant frequency is lower than a tenth of the bandwidth capability of the measuring transducers.

Fig. 5.13 shows the maximum time before which the fault must be cleared to avoid the freewheeling phase in case of PP faults. Moreover, it shows also the resonant frequency f_r in Hz, which can be determined as a function of the angular resonant frequency ω_o as:

$$f_r = \frac{1}{T_r} = 0.1592 * \omega_o \tag{5.32}$$

where T_r is the resonant periodic time. The minimum value of the relay inductor L_{min} hence can be determined from the oscillating response of the fault current as:

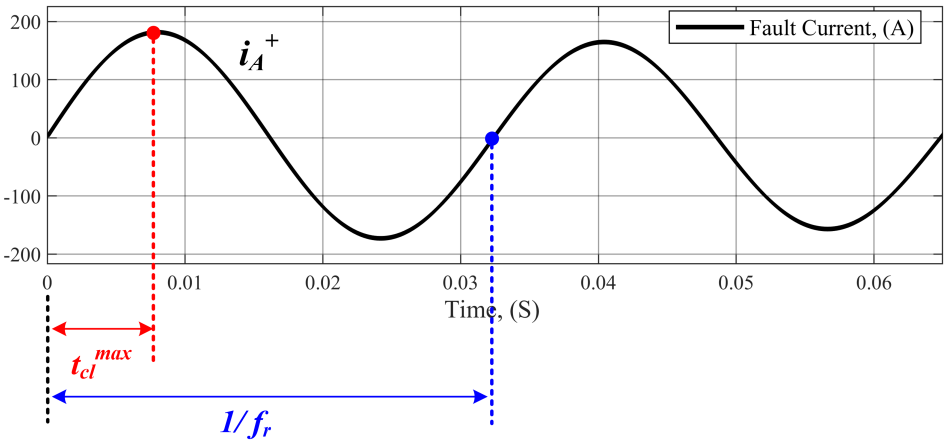

Figure 5.13: Underdamped transient response for relay inductance determination

$$\text{for } L = L_{min} \text{ such that, } \quad i_A(t) = I_{max} = e^{\frac{-(x_{min}r+R_g)}{2(x_{min}l+L_{min})}t}(\Gamma_1 cos(\omega_{d,c}\, t) + \Gamma_2 sin(\omega_{d,c}\, t)) \tag{5.33}$$

where I_{max} is the maximum fault current, Γ_1 and Γ_2 are constants, x_{min} is the starting point in the power line for the relay protection zone, and $\omega_{d,c}$ is the critical damped frequency. The minimum relay inductance can be determined by differentiating equation 5.33 as follows:

$$\frac{di_A(t_c^{max})}{dt} = 0 = (\frac{-(x_{min}r + R_g)}{2(x_{min}l + L_{min})}) e^{\frac{-(x_{min}r+R_g)}{2(x_{min}l+L_{min})} t_c^{max}} (\Gamma_1 cos(\omega_{d,c}\, t_c^{max}) + \Gamma_2 sin(\omega_{d,c}\, t_c^{max})) + e^{\frac{-(x_{min}r+R_g)}{2(x_{min}l+L_{min})} t_c^{max}} (-\Gamma_1 \omega_{d,c} sin(\omega_{d,c}\, t_c^{max}) + \Gamma_2 \omega_{d,c} cos(\omega_{d,c}\, t_c^{max})) \tag{5.34}$$

where $\omega_{d,c}$ is the critical damping frequency, which can be expressed as:

$$\omega_{d,c} = \sqrt{(\frac{1}{2(x_{min}l + L_{min})C}) - (\frac{(x_{min}r + R_g)^2}{4(x_{min}l + L_{min})^2})} \tag{5.35}$$

It should be noted that equations 5.33, 5.34, and 5.35 are valid for both PG and PP bolted faults. However, the critical case for which the relay inductor should be designed is the PP bolted fault or PG bolted fault for the solidly grounded system at which the grounding resistance is not involved in the fault circuit or equal zero, respectively. So, the critical value of the relay sensing inductor can be achieved by substituting R_g equal zero for equations 5.33, 5.34, and 5.35. On the other hand, to avoid the freewheeling phase for PP faults, and protect the DC-DC converter diodes from the stored energy in the power line and relay inductances, the fault should be cleared before the one-quarter cycle of the fault current. So, the critical clearing time can be expressed as:

$$t_c^{max} = 0.25\, \frac{\sqrt{2(x_{min} + L_{min})C}}{0.1592} \tag{5.36}$$

The sensed bolt fault currents for different relay inductance settings are illustrated in Fig. 5.14 and Fig. 5.15. In Fig. 5.14, the relay-measured fault current is presented for fault circuits without including freewheeling diode, which is the case of PG faults, while Fig. 5.15 shows the sensed fault current for faulted circuits that include the freewheeling diode, which is the case for PP faults. Moreover, Fig. 5.16 illustrates the freewheeling diode fault current during the energy discharge of the fault circuit inductances.

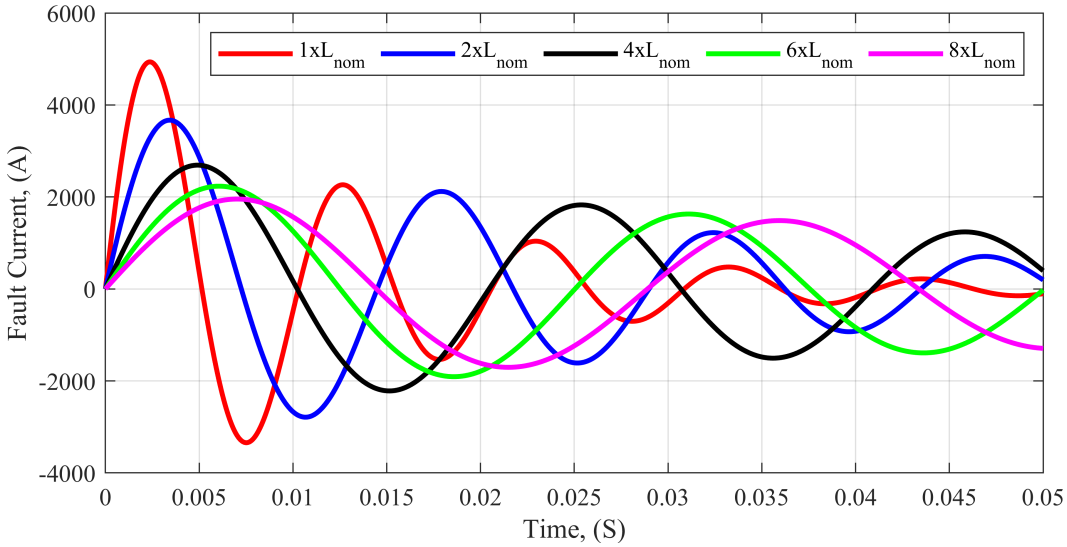

Figure 5.14: Relay Inductor effect on PG bolted faults (No freewheeling diodes)

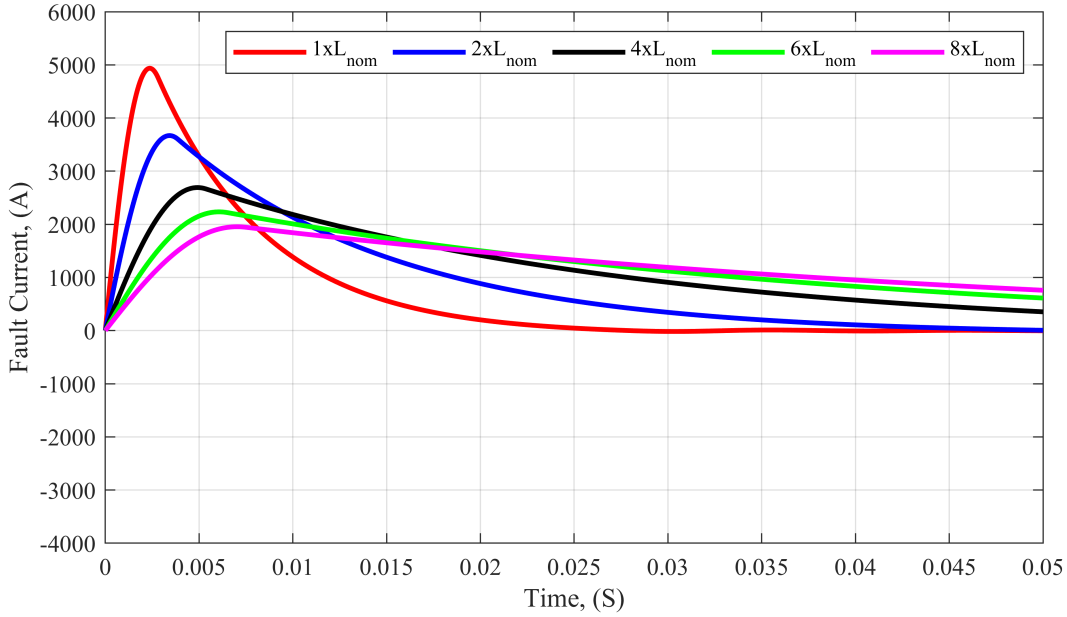

Figure 5.15: Relay Inductor effect on PP bolted faults (with freewheeling diodes)

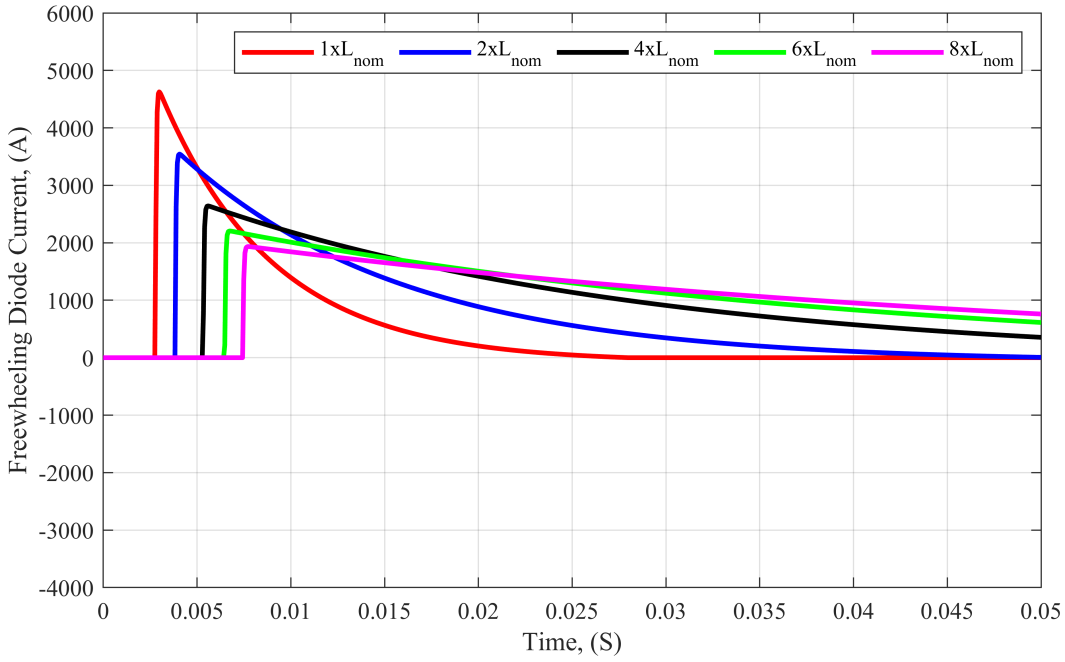

Figure 5.16: Freewheeling Diode Currents of PP bolted faults for different relay inductances

5.4.2 Signal Conditioning Circuit (SCC) Parameters

As mentioned in section 5.2.2, the SCC should be designed to provide a proper attenuation of the relay measurements during normal and fault conditions. The attenuated signals are then fed to the ADC channels of the processing unit to estimate the fault location. The system under study has a rated voltage level of 480V, and hence the DC link capacitor voltages are normally at 240V levels. On the other hand, there are no OP-AMP that can handle such high voltage, taking into consideration that the OP-AMP bias should be bipolar. As a result, the relay voltage quantities are attenuated through a voltage divider circuit consisting of R_a and R_b as shown in Fig. 5.19 and Fig. 5.20. The attenuation factor is 1:10 reducing the 240V to 24V which is suitable for the OP-AMP integrated circuit. An additional attenuation factor of at least 1:10 is used for signal attenuation for 5V or 3.3V ADC maximum voltage units. This can be achieved through selecting proper values of resistors R_{in}, R'_{in}, R_1, R_2, R_3, and R_4. The values of these resistors are shown in Table

5.1.

Table 5.1: SCC Voltage Sensing Units Parameters

R_{in}	R'_{in}	R_1	R_2	R_3	R_4	R_a	R_b
969kΩ	51kΩ	1kΩ	2kΩ	1kΩ	1kΩ	2MΩ	18MΩ

Each SCC voltage sensing circuit has three operational amplifiers. An ADA4099-1BUJZ-RL7 high bandwidth OP-AMP from Analog Devices Inc. has been used [269]. As mentioned in section 5.2.2, hall effect transducers cannot be used for measuring high-frequency damped voltages during fault conditions. Fig. 5.17 shows a compact Printed Circuit Board (PCB) that contains both voltage sensing circuits for the proposed SCC, while Fig. 5.18 shows an PCB of an industrial hall effect-based voltage transducer that capable of measuring up to 500V DC, AC, and pulsed voltages [270].

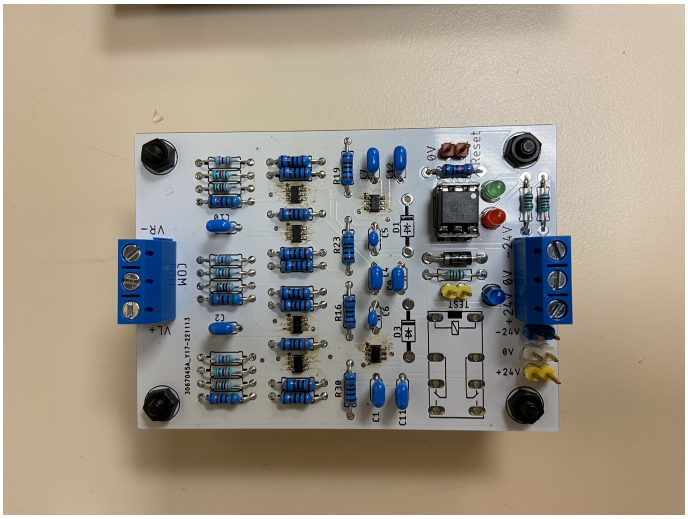

Figure 5.17: Signal Conditioning circuit

An experimental comparison between the proposed SCC voltage sensing circuit and the industrial transducer is established. A fault through resistance is forced for a reduced

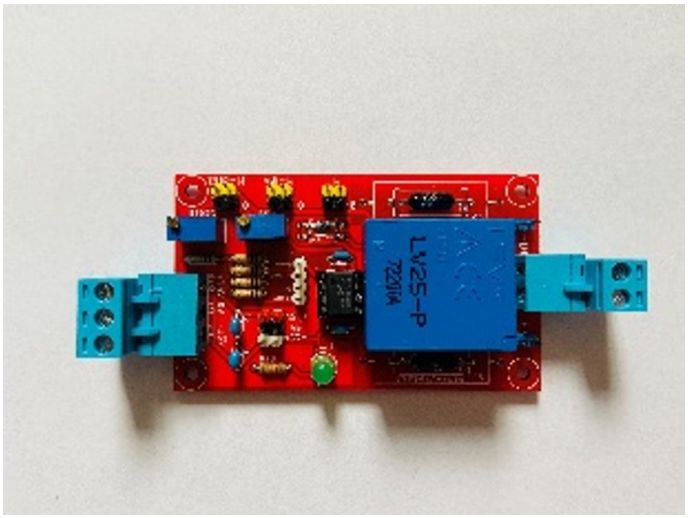

Figure 5.18: Voltage transducer circuit

voltage test system of a 24V DC system, and the sensed relay voltages are captured for each circuit using a Lab high bandwidth oscilloscope. Fig. 5.19 and 5.20 show the measurements of both circuits for the relay inductor voltage and the relay terminal voltage, respectively. It is clearly obvious that the industrial hall effect-based transducer cannot detect such high-frequency responses with $2\mu s$ rising time of the relay measurements. On the other hand, the proposed voltage sensing SCC is effectively able to detect high-frequency damped responses of the measured voltages.

For current sensing of SCC, there is no need to use a special high bandwidth current sensing circuit, as the fault current rate of change is very low compared to the voltage responses. As a result, an industrial hall effect-based current transducer is used for measuring the relay fault current. Fig. 5.21 shows an PCB of an LA55P industrial current transducer [260] that has been used for the proposed SCC.

For the SPC shown in Fig. 5.7 and 5.8, a low forward voltage, ultra-fast diode has been used for capturing the relay voltage measurements [271] for faults through resistance. For the SPC capacitor, a proper value should be selected to ensure a stable value of the sensed voltages until a trip signal is generated and sent to the bus Solid-State Circuit Breaker (SSCB). A 10pF capacitor is suitable for the system under study. It should be noted that

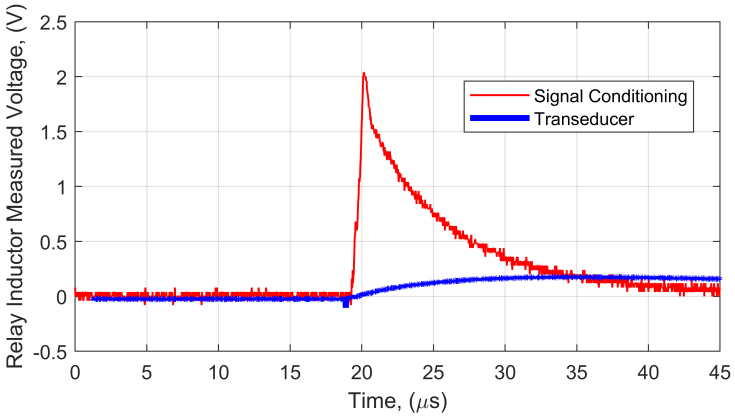

Figure 5.19: Relay inductor measured voltage

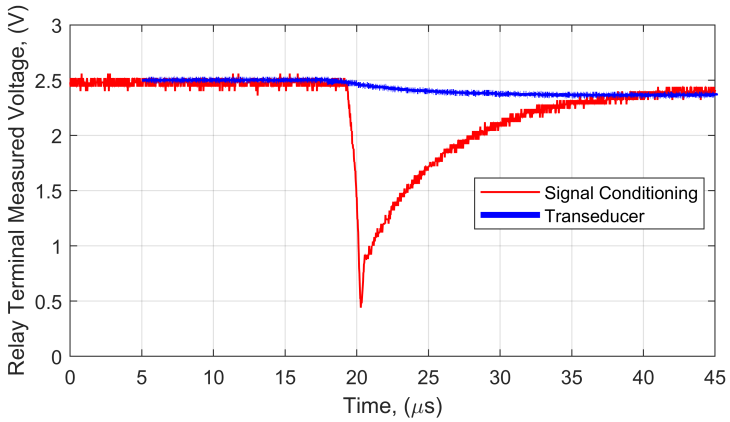

Figure 5.20: Relay terminal measured voltage

the fault location is determined based on the relay inductor current, inductor voltage, and relay terminal voltage. The measured current by the transducer is directly used for fault location estimating. For the voltage sensing, the input and the output of the SPC circuit are fed to the processing unit, and the fault location is determined in parallel for both of them and the more stable value represents the actual estimated fault location. This can be achieved by comparing the rate of change of both distance signals, and the signal with a lower rate of change is selected. For high resistance faults with overdamped response, the SPC output gives accurate fault distance estimation, while for underdamped responses the

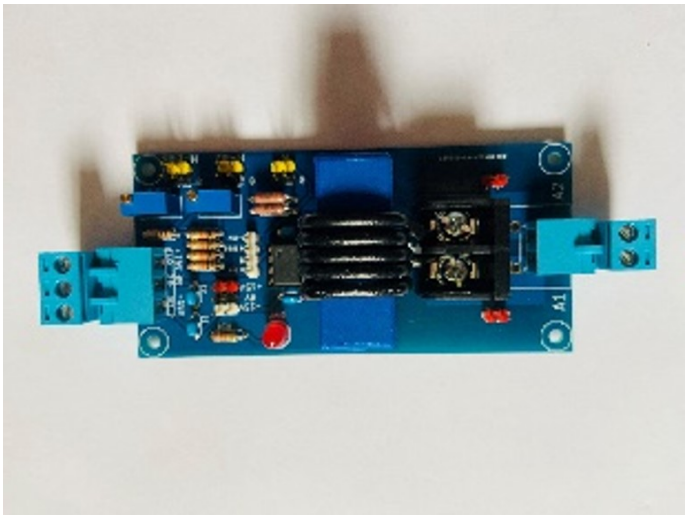

Figure 5.21: Current transducer circuit

output of the voltage sensing circuit-which is the input to the SPC unit- gives the accurate fault location. It should be noted that these processes of fault distance determination are done simultaneously in the processing unit to obtain an accurate estimation of the fault location.

5.4.3 Parameters of power system under study

A simple test power line of 1km length and 480 DC Voltage level ($\pm 240V$) is used to connect two buses. Each bus is connected to the local load and a DG unit. The parameters of the two buses, DG units capacity, initial load currents are illustrated in Table 4.1 for buses 2 and 3. For this study bus A refers to bus 2, while bus B refers to bus 3. The initial power line current from bus A to B is 17A as shown in Fig. 4.9 for power line b. Based on the analysis of relay inductor determination, an inductor of 66, while the DC link capacitor connected from both DC bus poles to the grounding point is $40mF$.

5.5 Numerical simulation results

5.5.1 Ideal testing of the protection system

In this case, the dynamic characteristics of the DC link capacitors connected at each bus in the power system are disregarded. This can simplify the transient response behavior during the fault condition. Disregarding the DC link capacitor dynamics can be achieved by simply replacing the DC link capacitors with independent voltage sources. This also disregards the dynamics of the DC-DC converter which connects the DG to the bus. Although this is not a practical case, it indicates the protection system performance through testing all the proposed protection system parts. To test the system under bolted faults, a bolted PP occurs at $t = 50\mu s$ at 200m away from bus A as shown in Fig. 5.22a, which illustrates the performance of the positive pole relay connected at bus A towards the power line AB. It can be seen that the measured fault current by the SCC unit is increased linearly as the fault circuit becomes purely inductive as the capacitors dynamics are disregarded. Moreover, the voltage measurements of the SCC (solid) and the SPC (dashed) units are identical for both the relay inductor and relay terminal voltages. As the relay measurements are accurately captured, the fault location is accurately estimated. It can be seen that the estimated fault location is accurately determined at 200m away from bus A. The results also show that the calculated fault distance before the fault instant has an extremely high value which indicates that there are no faults.

Similarly, Fig. 5.22b shows a high resistance fault at $t = 50\mu s$ at 200m away from bus A towards the power line AB through a 20Ω resistance. It can be seen that as the faulted circuit contains a resistance element, the system response starts damping after the fault instant. Hence, the SPC is extremely important in this case to capture the relay inductor and relay terminal voltages at the fault instant to accurately estimate the fault location. It can be seen that SPC unit maintains the peak value of the relay inductor voltage and the minimum value of the relay terminal voltage as shown by the red dashed lines. These two values as well as the measured current are collected by the processing unit and the fault location is accurately determined (xp). As mentioned before, the processing unit determines the fault distance based on the SCC (x) and the SPC (xp) units simultaneously. In this

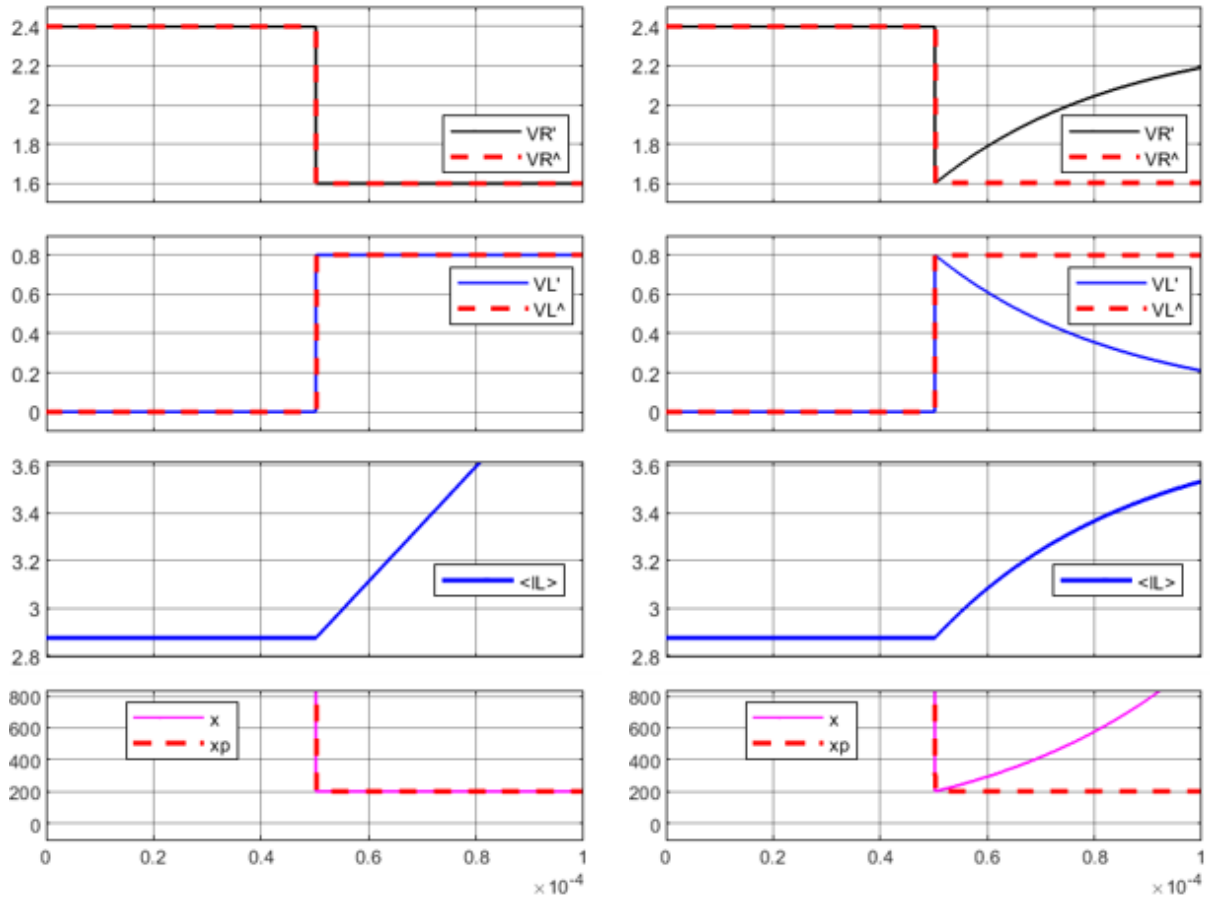

(a) Bolted PP Fault

(b) 20Ω resistance PP Fault

Figure 5.22: Protection system measurements for Ideal system without considering DC link capacitor dynamics

case, the calculated fault distance represents the actual fault location. It is clearly obvious that the estimated fault location is determined based on the SPC collected measurements.

5.5.2 Bolted Faults

In this case study, a bolted fault under a full dynamic power system is considered. The DC-DC converter and the DC link capacitors are included in the system, and a bolted PP

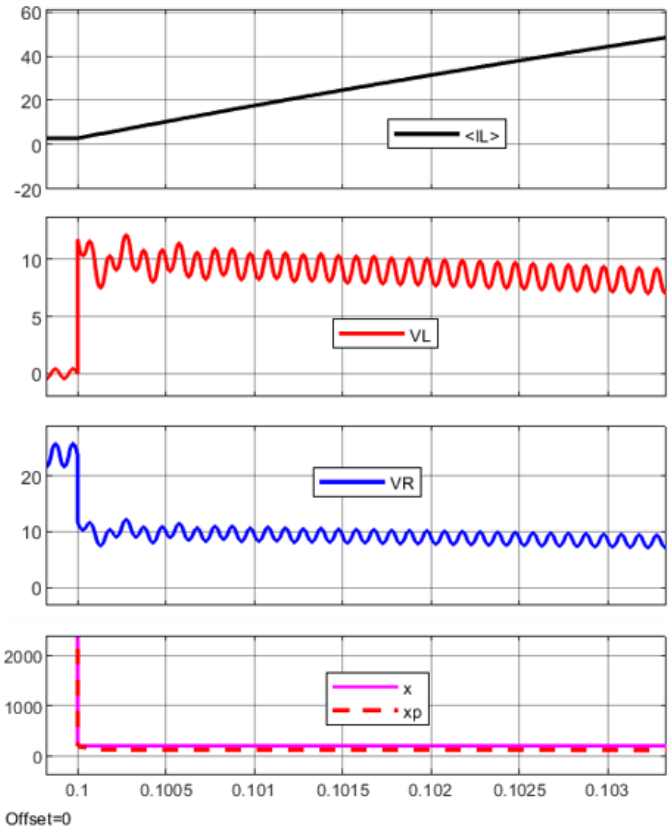

Figure 5.23: Relay states under bolted fault condition

fault occurs at $t = 0.1s$ as shown in Fig. 5.23. Similarly, the fault occurs at 200m distance away from bus A towards the power line AB. It can be seen clearly that the system responds in a completely different manner than the ideal case described in the previous subsection. There is an oscillatory response due to the interaction between the DC link capacitor the fault line and the integrated relay inductances. Although the DC-DC converter should be disabled by deactivating the converter power-electronic switch, the converter switch is kept active to investigate the proposed system's performance in estimating the fault location during fault conditions. It is shown in Fig. 5.23 that the proposed system can estimate the fault location accurately. On the other hand, the performance of the DC-DC buck converter that connects bus A to the corresponding DG is investigated as shown in Fig. 5.24.

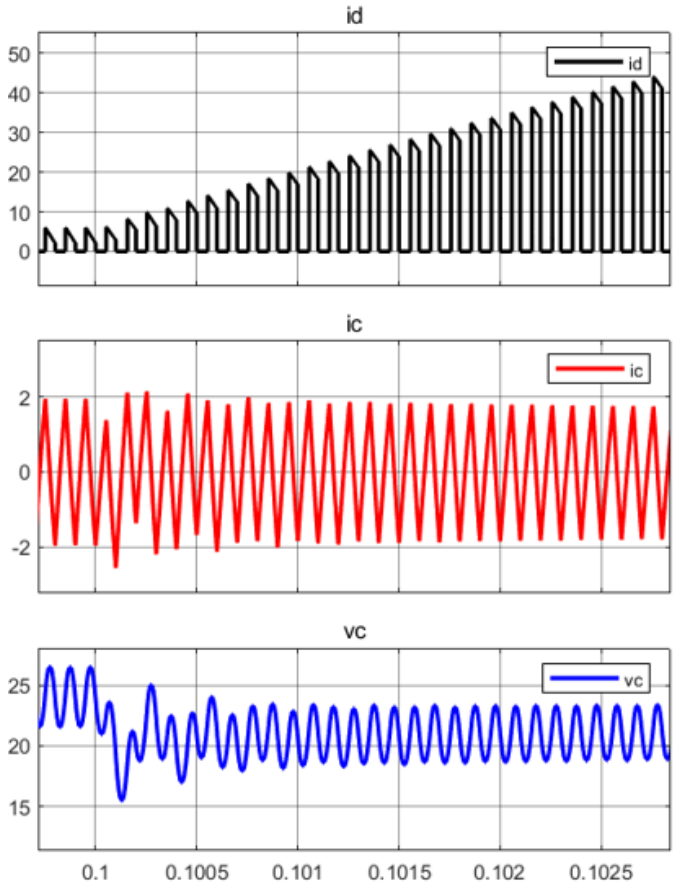

Figure 5.24: DC-DC converter states under bolted fault condition

It can be seen that there is an instantaneous voltage drop at the DC link capacitor at the fault instant then the DC-DC converter's controller restores the nominal DC link voltage while feeding the fault with rapidly increasing current. This current may destroy both the power-electronic switch and the freewheeling diode. Although the power switch can be deactivated in a few switching cycles, the freewheeling diode cannot be deactivated until all the energy stored in the system is released. So, it is necessary to clear the fault as fast as possible to protect the converter components. Fig. 5.25 and Fig. 5.26 illustrate the system performance under clearing the fault state.

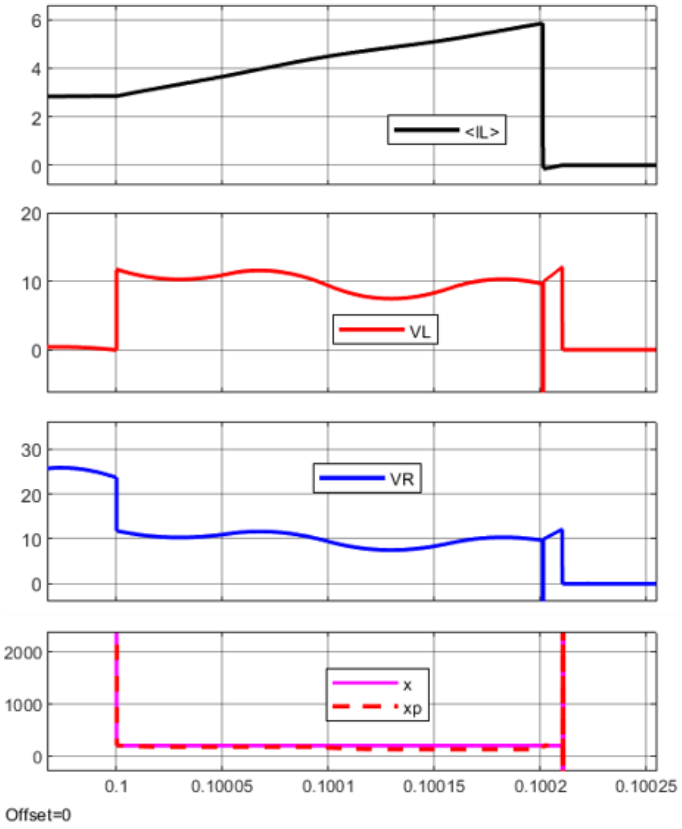

Figure 5.25: Relay states under clearing bolted fault condition

It can be seen from Fig. 5.25 that the fault location is estimated accurately at 200m distance from bus A, and once the power line is isolated, the estimated fault distance becomes a very high value indicating the fault clear state. It is also shown from the measured fault current, that the fault is cleared before one quarter cycle of the oscillating frequency of the fault current. The detection and the clear signals are illustrated in Fig. 5.26. The difference in time between these two signals is the actual fault-clearing time specified by the bus circuit breaker. This Fig. also shows the Dc-DC converter states before and after the fault instants. At the fault instant, there is a sudden voltage drop at the DC-link capacitors, a high peak discharge current, and the DC-DC converter starts feeding the fault.

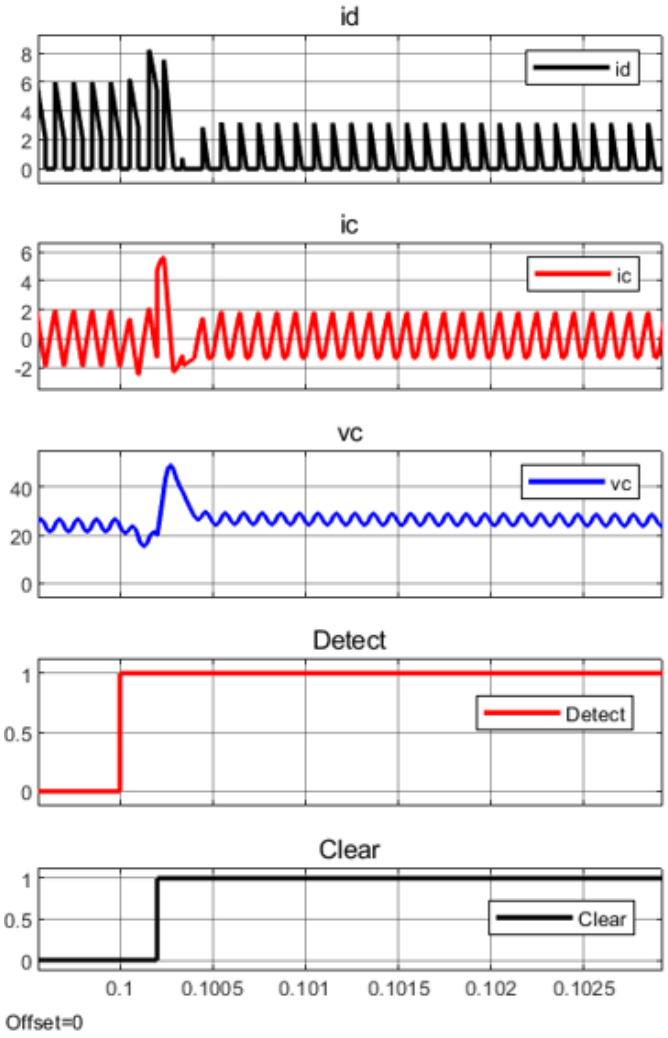

Figure 5.26: DC-DC converter states under clearing bolted fault condition

Once the fault is cleared by isolating the faulted power line, the DC link capacitor voltage increases suddenly due to faulted line disconnection and it is regulated again through the DC-DC converter controller. The converter diode current increases rapidly during the fault period then it is reduced once the fault is cleared. This reduced current corresponds to feeding the local load which proves that the faulted line is properly isolated.

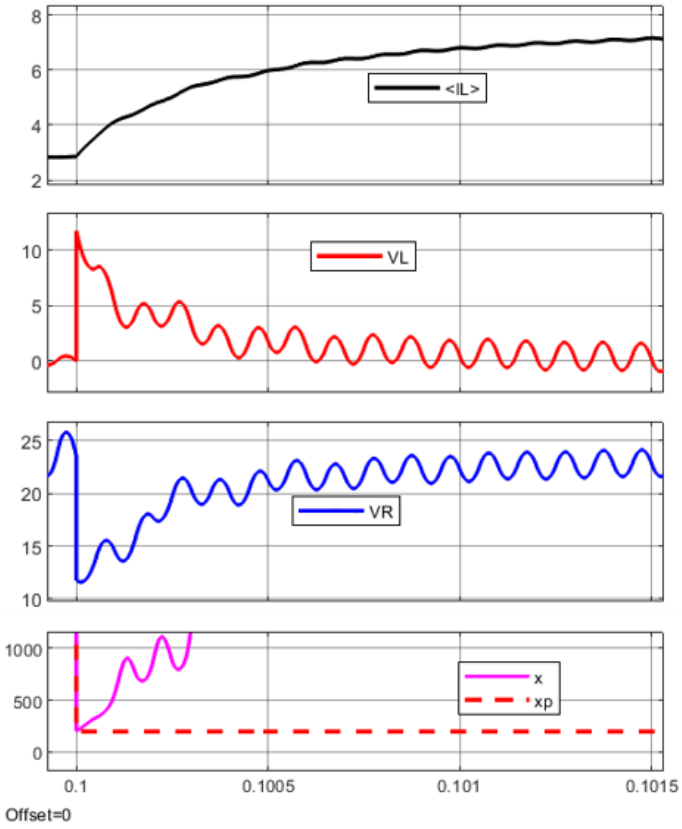

Figure 5.27: Relay states under resistance fault condition

5.5.3 Faults through resistance

Similarly, in this case, the same fault scenario is repeated but through a fault resistance. The effect of the fault resistance on the protection system and the DC-DC converter states is investigated. Fig. 5.27 shows the protection system states during resistance fault condition.

Similarly, the converter is forced to feed that fault to clearly illustrate the transient response of the system if the fault is not cleared. It is clearly seen that due to the presence of the fault resistance in the fault circuit, the relay measurements are damped quickly and hence the SPC captures the peak and minimum values of the relay inductor and terminal voltages to estimate the fault location accurately as shown in Fig. 5.27. Fig. 5.28 shows the transient response of the DC-DC converter states during fault conditions. It can be

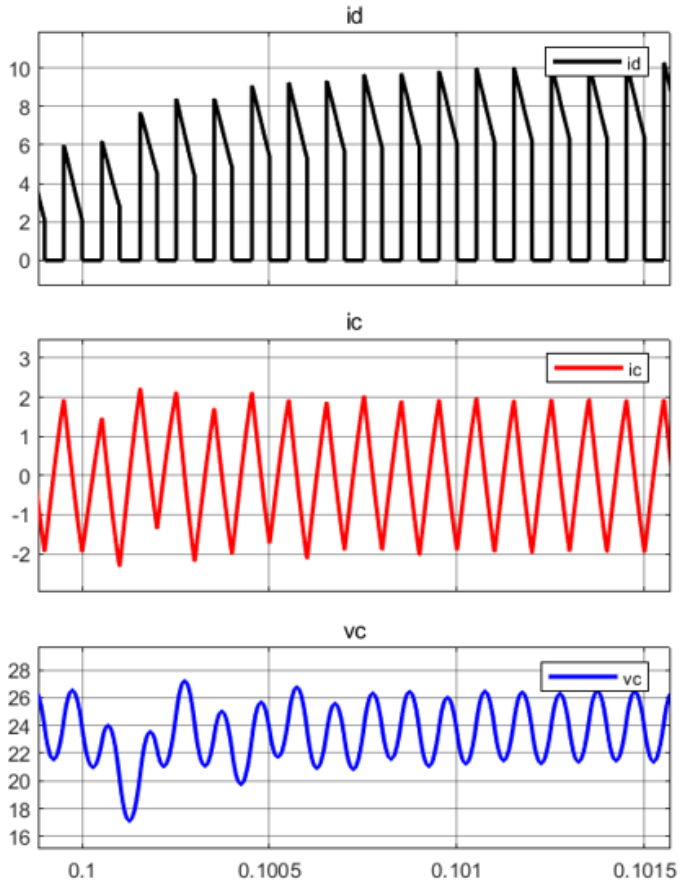

Figure 5.28: DC-DC converter states under resistance fault condition

seen from the diode current waveform that the fault current is relatively low as compared to the bolted fault in Fig. 5.24.

A detailed view of the fault clearance through isolating the power line is shown in Fig. 5.29 and Fig. 5.30. It is seen that the fault location is accurately estimated, the faulted power line is isolated, and the DC-DC converter restoring its operation through feeding the local loads.

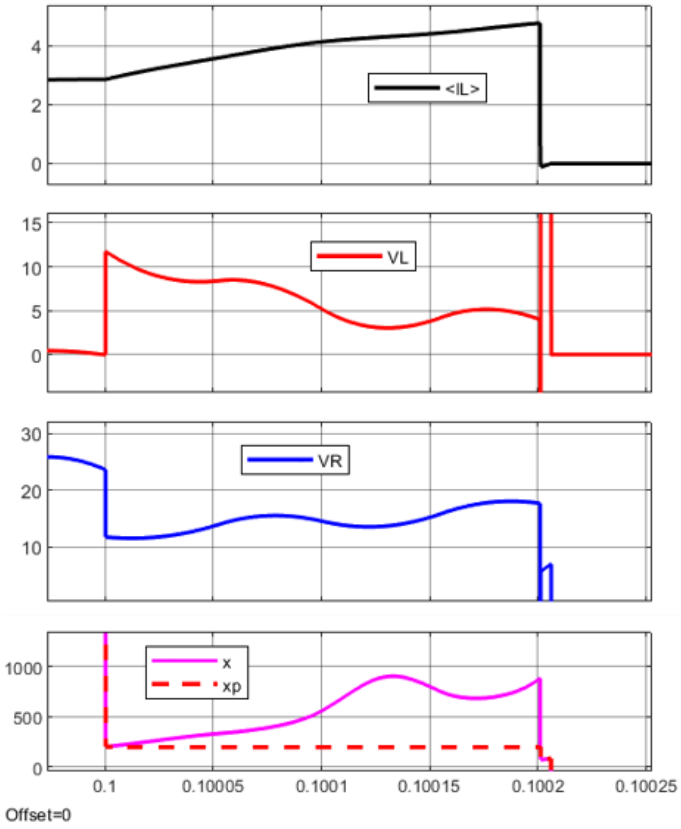

Figure 5.29: Relay states under clearing resistance fault condition

5.6 Conclusion

This chapter proposes a novel protection relay system that can detect, identify, locate, and isolate various fault conditions in DC microgrids. It consists of two elements: directional and distance elements for optimum identification and locating faults. Both elements are achieved by integrating a sensing inductor at both positive and negative poles of the power line connecting the network DC buses. By effectively capturing three local measurements: relay inductor voltage, relay terminal voltage, and the relay inductor current, the fault location is accurately determined. The design and consideration of the relay inductor are thoroughly described, while the effect of the fault types, fault resistance, grounding configuration, and grounding resistance are meticulously investigated. The proposed protection

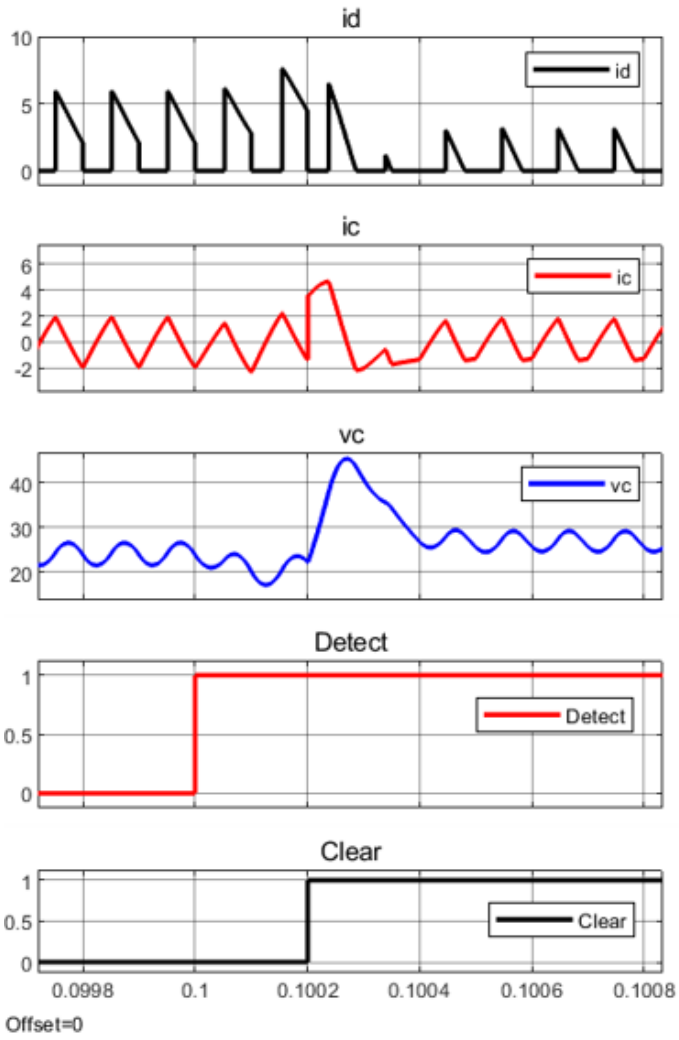

Figure 5.30: DC-DC converter states under clearing resistance fault condition

system incorporates SCC and SPC units for accurately capturing the relay measurements at the fault instance for both bolted faults and resistance faults. The proposed protection system has the ability to clear faults in a time frame of microseconds. The proposed relay system is tested and verified using MATLAB Simulink.

Chapter 6

Conclusion and Future Work

6.1 Summary and Conclusions

Although DC microgrids have garnered significant interest, several challenges persist in terms of control and protection, necessitating resolution to ensure their secure and reliable deployment on a large scale. The integration of diverse technologies, intermittent power profiles, and varying capacities in DGs, ESS, and loads makes maintaining load-generation equilibrium a complex task. Moreover, due to the inherent nature of DC power flow, DC microgrids face exceptionally high fault currents without zero crossings, highlighting the need for an efficient high-speed protection system capable of swiftly and safely managing these currents and promptly interrupting faulted sections. Simultaneously, the proliferation and complexity of microgrids have given rise to the concept of smart grids, wherein advanced digital automation and intelligent management become pivotal to operating small-scale grids (microgrids) efficiently and reliably. Modern microgrids, with the increased presence of DGs and ESS, have become intricate systems, but the advent of information technology and modern communication systems has facilitated opportunities for automated energy management. By integrating energy sources and connecting them to a cloud-based repository of real-time data, a smart system can optimize pricing, reliability, and the utilization of clean energy based on available parameters. However, the enhanced connectivity brought by communication networks in smart grids also brings heightened

security vulnerabilities and associated challenges. The critical nature and structure of a smart grid render it susceptible to cyber threats, underscoring its potential as a target.

Therefore, the main goal of this research work is to address the challenges of nowadays DC microgrid networks from the control and protection point of view. The main contributions of this thesis can be summarized in the following points:

- Developing a primary control layer that can effectively manage local transient loading and intermittent power profiles of renewable DGs while ensuring the secure and prolonged operation of integrated ESS. This will be achieved through real-time monitoring of charging/discharging rates and SoC levels. The proposed controller, named Improved Adaptive Model Predictive Controller (IAMPC), will serve as the primary controller in a hierarchical multi-layer smart control structure. Unlike conventional CCS-MPC, IAMPC is designed to exhibit enhanced convergence speed, handle nonlinear systems in real time, and account for dynamic equality and inequality constraints. It was rigorously evaluated using the CasADi online optimization platform and its robustness against parameter variations and system degradation was assessed.

- Creating a secondary control layer suitable for any network configuration, enabling data exchange among nodes through communication infrastructure. This secondary control layer ensures global voltage regulation across all network clusters and proportional power sharing among generating units, effectively preventing overloading of DGs. The proposed cooperative distributed consensus-based secondary control strategy functions as the second layer within the hierarchical control system structure. It is designed to operate effectively even with limited communication infrastructure and minimal available data. The controller is equipped with a state estimation layer based on the MHE algorithm, enhancing the control system's resilience against cyber threats and uncertainties in transducer measurements. Remarkably, the system operates without requiring knowledge of network line parameters, enabling plug-and-play functionality. A comprehensive assessment of the proposed controller's robustness and resiliency is conducted through diverse operational scenarios, including power line outages, communication line failures, measurement uncertainties, cyber threats, and the integration of generating units.

- Introducing a novel protection system for DC microgrids capable of detecting, identifying, locating, and isolating various faults. The proposed system incorporates multi-protection coordinated circuits to achieve optimum sensitivity and selectivity for a wide range of bolted faults and high-resistance faults. Unlike most existing literature on DC microgrid protection systems, this system considers the effects of fault resistance, DC link capacitor dynamics, grounding configuration, and grounding resistance. Moreover, the proposed system can detect both faults under high-frequency variable oscillations, particularly for bolted faults, and damped currents of high-resistance faults within a time frame of microseconds.

6.2 Directions for Future Work

Based on the results presented in this thesis, the following areas are suggested for future investigation:

- Investigation of the proposed system resiliency against various cyber attacks. Although the proposed system shows a great level of resiliency against general cyber threats and system uncertainties thanks to the integration of the MHE based state estimation layer, the performance of this estimation layer can be investigated for various high-level cyber attacks.

- Establishing an SoC global balancing strategy for all integrated ESS in different clusters. This can be achieved through the available consensus-based cyber network which is used for proportional load sharing and global voltage regulation objectives.

- Investigating the proposed protection system performance for special grounding configurations including grounding through power diodes and thyristors.

References

[1] Hui Hu, Nan Xie, Debin Fang, and Xiaoling Zhang. The role of renewable energy consumption and commercial services trade in carbon dioxide reduction: Evidence from 25 developing countries. *Applied energy*, 211:1229–1244, 2018.

[2] Akhtar Hussain, Van-Hai Bui, and Hak-Man Kim. Microgrids as a resilience resource and strategies used by microgrids for enhancing resilience. *Applied energy*, 240:56–72, 2019.

[3] Felix Garcia-Torres, Ascension Zafra-Cabeza, Carlos Silva, Stephane Grieu, Tejaswinee Darure, and Ana Estanqueiro. Model predictive control for microgrid functionalities: Review and future challenges. *Energies*, 14(5):1296, 2021.

[4] CERTS. Consortium for electric reliability technology solutions. https://certs.lbl.gov/research-areas/distributed-energy-resource-0.html, 2018. Accessed: (Use the date of access).

[5] Yael Parag and Malcolm Ainspan. Sustainable microgrids: Economic, environmental and social costs and benefits of microgrid deployment. *Energy for Sustainable Development*, 52:72–81, 2019.

[6] Vitor Fernão Pires, Armando Pires, and Armando Cordeiro. Dc microgrids: Benefits, architectures, perspectives and challenges. *Energies*, 16(3):1217, 2023.

[7] Luis Eduardo Zubieta. Are microgrids the future of energy: Dc microgrids from concept to demonstration to deployment. *IEEE Electrification Magazine*, 4(2):37–44, 2016.

[8] Vahidreza Nasirian, Seyedali Moayedi, Ali Davoudi, and Frank L Lewis. Distributed cooperative control of dc microgrids. *IEEE Transactions on Power Electronics*, 30(4):2288–2303, 2014.

[9] Jaysson Guerrero, Daniel Gebbran, Sleiman Mhanna, Archie C Chapman, and Gregor Verbič. Towards a transactive energy system for integration of distributed energy resources: Home energy management, distributed optimal power flow, and peer-to-peer energy trading. *Renewable and Sustainable Energy Reviews*, 132:110000, 2020.

[10] G Mutezo and J Mulopo. A review of africa's transition from fossil fuels to renewable energy using circular economy principles. *Renewable and Sustainable Energy Reviews*, 137:110609, 2021.

[11] David Klenert, Franziska Funke, Linus Mattauch, and Brian O'Callaghan. Five lessons from covid-19 for advancing climate change mitigation. *Environmental and Resource Economics*, 76:751–778, 2020.

[12] Anh Tuan Hoang, Sandro Nižetić, Aykut I Olcer, Hwai Chyuan Ong, Wei-Hsin Chen, Cheng Tung Chong, Sabu Thomas, Suhaib A Bandh, and Xuan Phuong Nguyen. Impacts of covid-19 pandemic on the global energy system and the shift progress to renewable energy: Opportunities, challenges, and policy implications. *Energy Policy*, 154:112322, 2021.

[13] Athanasios S Dagoumas and Nikolaos E Koltsaklis. Review of models for integrating renewable energy in the generation expansion planning. *Applied Energy*, 242:1573–1587, 2019.

[14] Yi Wang, Anastasios Oulis Rousis, and Goran Strbac. On microgrids and resilience: A comprehensive review on modeling and operational strategies. *Renewable and Sustainable Energy Reviews*, 134:110313, 2020.

[15] Walid El-Khattam and Magdy MA Salama. Distributed generation technologies, definitions and benefits. *Electric power systems research*, 71(2):119–128, 2004.

[16] Pathomthat Chiradeja and R Ramakumar. An approach to quantify the technical benefits of distributed generation. *IEEE Transactions on energy conversion*, 19(4):764–773, 2004.

[17] Hugo A Gil and Geza Joos. Models for quantifying the economic benefits of distributed generation. *IEEE Transactions on power systems*, 23(2):327–335, 2008.

[18] Guido Pepermans, Johan Driesen, Dries Haeseldonckx, Ronnie Belmans, and William D'haeseleer. Distributed generation: definition, benefits and issues. *Energy policy*, 33(6):787–798, 2005.

[19] Magdi Sadek Mahmoud, S Azher Hussain, and Mohammad A Abido. Modeling and control of microgrid: An overview. *Journal of the Franklin Institute*, 351(5):2822–2859, 2014.

[20] Ambarnath Banerji, Debasmita Sen, Ayan K Bera, Debtanu Ray, Debjyoti Paul, Anurag Bhakat, and Sujit K Biswas. Microgrid: A review. In *2013 IEEE Global Humanitarian Technology Conference: South Asia Satellite (GHTC-SAS)*, pages 27–35. IEEE, 2013.

[21] Lubna Mariam, Malabika Basu, Michael F Conlon, et al. A review of existing microgrid architectures. *Journal of engineering*, 2013, 2013.

[22] Sheetal Chandak and Pravat K Rout. The implementation framework of a microgrid: A review. *International Journal of Energy Research*, 45(3):3523–3547, 2021.

[23] KS Rajesh, SS Dash, Ragam Rajagopal, and R Sridhar. A review on control of ac microgrid. *Renewable and sustainable energy reviews*, 71:814–819, 2017.

[24] Amin Khodaei. Microgrid optimal scheduling with multi-period islanding constraints. *IEEE Transactions on Power Systems*, 29(3):1383–1392, 2013.

[25] Shay Bahramirad, Amin Khodaei, Joseph Svachula, and Julio Romero Aguero. Building resilient integrated grids: One neighborhood at a time. *IEEE Electrification Magazine*, 3(1):48–55, 2015.

[26] Marlon Huamani Bellido, Luiz Pinguelli Rosa, Amaro Olímpio Pereira, Djalma Mosqueira Falcao, and Suzana Kahn Ribeiro. Barriers, challenges and opportunities for microgrid implementation: The case of federal university of rio de janeiro. *Journal of cleaner production*, 188:203–216, 2018.

[27] Hossein Lotfi and Amin Khodaei. Ac versus dc microgrid planning. *IEEE Transactions on Smart Grid*, 8(1):296–304, 2015.

[28] Fahad Saleh Al-Ismail. Dc microgrid planning, operation, and control: A comprehensive review. *IEEE Access*, 9:36154–36172, 2021.

[29] Chitaranjan Phurailatpam, Bharat Singh Rajpurohit, and Lingfeng Wang. Planning and optimization of autonomous dc microgrids for rural and urban applications in india. *Renewable and Sustainable Energy Reviews*, 82:194–204, 2018.

[30] Mariana Resener, Steffen Rebennack, Panos M Pardalos, and Sérgio Haffner. *Handbook of optimization in electric power distribution systems*. Springer, 2020.

[31] Thomas Allen Short. *Electric power distribution handbook*. CRC press, 2014.

[32] Mahdi Zolfaghari, Gevork B Gharehpetian, Miadreza Shafie-khah, and João PS Catalão. Comprehensive review on the strategies for controlling the interconnection of ac and dc microgrids. *International Journal of Electrical Power & Energy Systems*, 136:107742, 2022.

[33] Hassan Bevrani, Bruno François, and Toshifumi Ise. *Microgrid dynamics and control*. John Wiley & Sons, 2017.

[34] Wenhua Wu, Yandong Chen, An Luo, Leming Zhou, Xiaoping Zhou, Ling Yang, Yanting Dong, and Josep M Guerrero. A virtual inertia control strategy for dc microgrids analogized with virtual synchronous machines. *IEEE Transactions on Industrial Electronics*, 64(7):6005–6016, 2016.

[35] Yunjie Gu, Xin Xiang, Wuhua Li, and Xiangning He. Mode-adaptive decentralized control for renewable dc microgrid with enhanced reliability and flexibility. *IEEE Transactions on Power Electronics*, 29(9):5072–5080, 2013.

[36] Mohammed Hijjo, Felix Felgner, and Georg Frey. Pv-battery-diesel microgrid layout design based on stochastic optimization. In *2017 6th International Conference on Clean Electrical Power (ICCEP)*, pages 30–35. IEEE, 2017.

[37] Changjie Yin, Hongwei Wu, Fabrice Locment, and Manuela Sechilariu. Energy management of dc microgrid based on photovoltaic combined with diesel generator and supercapacitor. *Energy conversion and management*, 132:14–27, 2017.

[38] Panbao Wang, Mohamed Zaery, Di Zhao, Wei Wang, and Dianguo Xu. Combined control strategy for proportional current sharing in dc microgrid clusters. *IEEE Transactions on Industrial Electronics*, 2022.

[39] Shivam Chaturvedi and Deepak Fulwani. Adaptive voltage tuning based load sharing in dc microgrid. *IEEE Transactions on Industry Applications*, 57(1):977–986, 2020.

[40] Tapan Shah and Zeeshan Ahmad Ansari. An overview of intelligent energy management system for dc microgrid: system and communication architecture and application in power distribution system. In *2018 IEEE 13th International Conference on Industrial and Information Systems (ICIIS)*, pages 1–4. IEEE, 2018.

[41] Ramachandra Rao Kolluri, Iven Mareels, and Julian de Hoog. Controlling dc microgrids in communities, buildings and data centers. *IET Smart Grid*, 3(3):376–384, 2020.

[42] Brian T Patterson. Dc, come home: Dc microgrids and the birth of the" enernet". *IEEE Power and Energy Magazine*, 10(6):60–69, 2012.

[43] Jiangkai Peng, Bo Fan, Jiajun Duan, Qinmin Yang, and Wenxin Liu. Adaptive decentralized output-constrained control of single-bus dc microgrids. *IEEE/CAA Journal of Automatica Sinica*, 6(2):424–432, 2019.

[44] Lantao Xing, Qianwen Xu, Fanghong Guo, Zheng-Guang Wu, and Meiqin Liu. Distributed secondary control for dc microgrid with event-triggered signal transmissions. *IEEE Transactions on Sustainable Energy*, 12(3):1801–1810, 2021.

[45] K Jithin, N Mayadevi, R Hari Kumar, et al. The effect of multiple pv and battery penetration on stability of dc microgrid with single bus topology. In *2021 9th IEEE International Conference on Power Systems (ICPS)*, pages 1–5. IEEE, 2021.

[46] Jiuping Pan Sandeep Bala and Magnus Callavik Peter Sandeberg. Dc connection of offshore wind power plants without platform. In *13th Wind Integration Workshop*, volume 11, page 13, 2014.

[47] Erdem Gümrükcü, Ferdinanda Ponci, Antonello Monti, Giuseppe Guidi, Salvatore D'Arco, and Jon Are Suul. Optimal load management strategy for large electric vehicle charging stations with undersized charger clusters. *IET Electrical Systems in Transportation*, 12(1):49–64, 2022.

[48] Sony Susan Varghese, Geza Joos, and Syed Qaseem Ali. Load management strategy for dc fast charging stations. In *2021 IEEE Energy Conversion Congress and Exposition (ECCE)*, pages 1620–1626. IEEE, 2021.

[49] D Ricchiuto, RA Mastromauro, Marco Liserre, Ionut Trintis, and Stig Munk-Nielsen. Overview of multi-dc-bus solutions for dc microgrids. In *2013 4th IEEE International Symposium on Power Electronics for Distributed Generation Systems (PEDG)*, pages 1–8. IEEE, 2013.

[50] Tomislav Dragičević, Xiaonan Lu, Juan C Vasquez, and Josep M Guerrero. Dc microgrids—part ii: A review of power architectures, applications, and standardization issues. *IEEE transactions on power electronics*, 31(5):3528–3549, 2015.

[51] Robert S Balog and Philip T Krein. Bus selection in multibus dc microgrids. *IEEE Transactions on Power Electronics*, 26(3):860–867, 2010.

[52] Nishantha C Ekneligoda and Wayne W Weaver. A game theoretic bus selection method for loads in multibus dc power systems. *IEEE Transactions on Industrial Electronics*, 61(4):1669–1678, 2013.

[53] Babangida Modu, Md Pauzi Abdullah, Mufutau Adewolu Sanusi, and Mukhtar Fatihu Hamza. Dc-based microgrid: Topologies, control schemes, and implementations. *Alexandria Engineering Journal*, 70:61–92, 2023.

[54] Minrui Leng, Guohua Zhou, Haoze Li, Guodong Xu, Frede Blaabjerg, and Tomislav Dragičević. Impedance-based stability evaluation for multibus dc microgrid without constraints on subsystems. *IEEE Transactions on Power Electronics*, 37(1):932–943, 2021.

[55] Qobad Shafiee, Tomislav Dragičević, Juan C Vasquez, and Josep M Guerrero. Hierarchical control for multiple dc-microgrids clusters. *IEEE transactions on energy conversion*, 29(4):922–933, 2014.

[56] Qobad Shafiee, Tomislav Dragicevic, Juan C Vasquez, and Josep M Guerrero. Modeling, stability analysis and active stabilization of multiple dc-microgrid clusters. In *2014 IEEE international energy conference (ENERGYCON)*, pages 1284–1290. IEEE, 2014.

[57] Robert Salas-Puente, Silvia Marzal, Raúl González-Medina, Emilio Figueres, and Gabriel Garcera. Experimental study of a centralized control strategy of a dc microgrid working in grid connected mode. *Energies*, 10(10):1627, 2017.

[58] Jae-Do Park, Jared Candelaria, Liuyan Ma, and Kyle Dunn. Dc ring-bus microgrid fault protection and identification of fault location. *IEEE transactions on Power delivery*, 28(4):2574–2584, 2013.

[59] Jaynendra Kumar, Anshul Agarwal, and Vineeta Agarwal. A review on overall control of dc microgrids. *Journal of energy storage*, 21:113–138, 2019.

[60] Junseok Song, Mohammad Chehreghani Bozchalui, Alexis Kwasinski, and Ratnesh Sharma. Microgrids availability evaluation using a markov chain energy storage model: a comparison study in system architectures. In *Pes T&d 2012*, pages 1–6. IEEE, 2012.

[61] Jafar Mohammadi, Firouz Badrkhani Ajaei, and Gary Stevens. Grounding the dc microgrid. *IEEE Transactions on Industry Applications*, 55(5):4490–4499, 2019.

[62] Fei Wang, Zhifang Lei, Xinwei Xu, and Xinyi Shu. Topology deduction and analysis of voltage balancers for dc microgrid. *IEEE Journal of Emerging and Selected Topics in Power Electronics*, 5(2):672–680, 2016.

[63] Henrique R Mamede, Walbermark M dos Santos, and Denizar C Martins. A new dc-dc power converter derived from the tab for bipolar dc microgrids. In *2015 IEEE Energy Conversion Congress and Exposition (ECCE)*, pages 6217–6222. IEEE, 2015.

[64] Chunsheng Guo, Jianquan Liao, and Yu Zhang. Adaptive droop control of unbalanced voltage in the multi-node bipolar dc microgrid based on fuzzy control. *International Journal of Electrical Power & Energy Systems*, 142:108300, 2022.

[65] K Raghavendra Naik, Bhooshan Rajpathak, Arghya Mitra, C Sadanala, and Mohan Lal Kolhe. Power management scheme of dc micro-grid integrated with photovoltaic-battery-micro hydro power plant. *Journal of Power Sources*, 525:230988, 2022.

[66] Ahmad Aziz Al Alahmadi, Youcef Belkhier, Nasim Ullah, Habti Abeida, Mohamed S Soliman, Yahya Salameh Hassan Khraisat, and Yasser Mohammed Alharbi. Hybrid wind/pv/battery energy management-based intelligent non-integer control for smart dc-microgrid of smart university. *IEEE Access*, 9:98948–98961, 2021.

[67] KR Bharath, Mithun M Krishnan, and P Kanakasabapathy. A review on dc microgrid control techniques, applications and trends. *International Journal of Renewable Energy Research (IJRER)*, 9(3):1328–1338, 2019.

[68] Zhangjie Liu, Mei Su, Yao Sun, Hua Han, Xiaochao Hou, and Josep M Guerrero. Stability analysis of dc microgrids with constant power load under distributed control methods. *Automatica*, 90:62–72, 2018.

[69] Mahmoud Saleh, Yusef Esa, and Ahmed Mohamed. Centralized control for dc microgrid using finite state machine. In *2017 IEEE Power & Energy Society Innovative Smart Grid Technologies Conference (ISGT)*, pages 1–5. IEEE, 2017.

[70] Mahmoud Saleh, Yusef Esa, and Ahmed A Mohamed. Communication-based control for dc microgrids. *IEEE Transactions on Smart Grid*, 10(2):2180–2195, 2018.

[71] Shweta Dahale, Aakriti Das, Naran M Pindoriya, and S Rajendran. An overview of dc-dc converter topologies and controls in dc microgrid. In *2017 7th International Conference on Power Systems (ICPS)*, pages 410–415. IEEE, 2017.

[72] Lihu Jia, Yongqiang Zhu, Shaofei Du, and Yinshun Wang. Analysis of the transition between multiple operational modes for hybrid ac/dc microgrids. *CSEE Journal of Power and Energy Systems*, 4(1):49–57, 2018.

[73] Byron Hernandez, Eduardo Giraldo, Steven Ospina, and Alejandro Garces. Master-slave operation of dc microgrids: An adaptive control approach with estimation. In *2019 IEEE 4th Colombian Conference on Automatic Control (CCAC)*, pages 1–6. IEEE, 2019.

[74] Li Guo, Yibin Feng, Xialin Li, Chengshan Wang, and Yunwei Li. Stability analysis of a dc microgrid with master-slave control structure. In *2014 IEEE Energy Conversion Congress and Exposition (ECCE)*, pages 5682–5689. IEEE, 2014.

[75] Amir Khorsandi, Mojtaba Ashourloo, and Hossein Mokhtari. A decentralized control method for a low-voltage dc microgrid. *IEEE Transactions on Energy Conversion*, 29(4):793–801, 2014.

[76] Ming-Hao Wang, Shuo Yan, Siew-Chong Tan, Zhao Xu, and Shu Yuen Hui. Decentralized control of dc electric springs for storage reduction in dc microgrids. *IEEE Transactions on Power Electronics*, 35(5):4634–4646, 2019.

[77] Sujan Adhikari, Qianwen Xu, Yi Tang, and Peng Wang. Decentralized control of dc microgrid clusters. In *2017 IEEE 3rd International Future Energy Electronics Conference and ECCE Asia (IFEEC 2017-ECCE Asia)*, pages 567–572. IEEE, 2017.

[78] Duy-Long Nguyen and Hong-Hee Lee. A survey on cooperative control strategies for dc microgrids. *Neurocomputing*, 486:225–236, 2022.

[79] Rekha P Nair and P Kanakasabapathy. Control of a dc microgrid under dynamic load condition. In *2017 International Conference on Technological Advancements in Power and Energy (TAP Energy)*, pages 1–6. IEEE, 2017.

[80] Sayli E Mhankale and AR Thorat. Droop control strategies of dc microgrid: A review. In *2018 International Conference on Current Trends towards Converging Technologies (ICCTCT)*, pages 372–376. IEEE, 2018.

[81] Tuyen V Vu, Dallas Perkins, Fernand Diaz, David Gonsoulin, Chris S Edrington, and Touria El-Mezyani. Robust adaptive droop control for dc microgrids. *Electric Power Systems Research*, 146:95–106, 2017.

[82] Jinxin Zhao and Florian Dörfler. Distributed control and optimization in dc microgrids. *Automatica*, 61:18–26, 2015.

[83] EG Shehata, Jean Thomas, RM Mostafa, and MA Ghalib. An improved droop control for a low voltage dc microgrid operation. In *2018 Twentieth International Middle East Power Systems Conference (MEPCON)*, pages 850–855. IEEE, 2018.

[84] Yuru Zhang and Yun Wei Li. Energy management strategy for supercapacitor in droop-controlled dc microgrid using virtual impedance. *IEEE Transactions on Power Electronics*, 32(4):2704–2716, 2016.

[85] Subham Sahoo, Sukumar Mishra, Shatakshi Jha, and Bhim Singh. A cooperative adaptive droop based energy management and optimal voltage regulation scheme for dc microgrids. *IEEE Transactions on Industrial Electronics*, 67(4):2894–2904, 2019.

[86] Eman K Belal, Doaa M Yehia, and Ahmed M Azmy. Adaptive droop control for balancing soc of distributed batteries in dc microgrids. *IET Generation, Transmission & Distribution*, 13(20):4667–4676, 2019.

[87] Sijo Augustine, Mahesh K Mishra, and N Lakshminarasamma. Adaptive droop control strategy for load sharing and circulating current minimization in low-voltage standalone dc microgrid. *IEEE Transactions on Sustainable Energy*, 6(1):132–141, 2014.

[88] Rohit Kumar and Mukesh K Pathak. Distributed droop control of dc microgrid for improved voltage regulation and current sharing. *IET Renewable Power Generation*, 14(13):2499–2506, 2020.

[89] Mohamed A Ghalib, EG Shehat, Jean Thomas, and RM Mostafa. Adaptive droop control for high-performance operation in low-voltage dc microgrids. *Electrical Engineering*, 101:1311–1322, 2019.

[90] Amir Khorsandi, Mojtaba Ashourloo, Hossein Mokhtari, and Reza Iravani. Automatic droop control for a low voltage dc microgrid. *IET Generation, Transmission & Distribution*, 10(1):41–47, 2016.

[91] Wei Xing, Hewu Wang, Languang Lu, Shuoqi Wang, and Minggao Ouyang. An adaptive droop control for distributed battery energy storage systems in microgrids with dab converters. *International Journal of Electrical Power & Energy Systems*, 130:106944, 2021.

[92] Seydali Ferahtia, Ali Djeroui, Hegazy Rezk, Aissa Chouder, Azeddine Houari, and Mohamed Machmoum. Adaptive droop based control strategy for dc microgrid including multiple batteries energy storage systems. *Journal of Energy Storage*, 48:103983, 2022.

[93] Ritu Kandari, Pankaj Gupta, and Ashwani Kumar. Battery state of charge based improved adaptive droop control for power management of a microgrid having large scale renewable generation. *Sustainable Energy Technologies and Assessments*, 57:103146, 2023.

[94] Duc Nguyen Huu. An innovative adaptive droop control based on available energy for dc micro distribution grids. *Energies*, 13(11):2983, 2020.

[95] Yasushi Eto, Yuichi Noge, Masahito Shoyama, and Tadatoshi Babasaki. An analysis of soc self-convergence for adaptive droop control systems of battery energy storage with different capacity. In *2022 IEEE Energy Conversion Congress and Exposition (ECCE)*, pages 1–6. IEEE, 2022.

[96] Nelson L Diaz, Tomislav Dragičević, Juan C Vasquez, and Josep M Guerrero. Intelligent distributed generation and storage units for dc microgrids—a new concept on cooperative control without communications beyond droop control. *IEEE Transactions on Smart Grid*, 5(5):2476–2485, 2014.

[97] Qiang Yang, Le Jiang, Hailin Zhao, and Hongmei Zeng. Autonomous voltage regulation and current sharing in islanded multi-inverter dc microgrid. *IEEE Transactions on Smart Grid*, 9(6):6429–6437, 2017.

[98] Mrutunjaya Panda, Vijaya Bhaskar Devara, and Tanmoy Maity. A novel dc bus-signaling based power management strategy for dc microgrid. *International Transactions on Electrical Energy Systems*, 31(2):e12758, 2021.

[99] Akansha Garg, Narsa Reddy Tummuru, and Ramesh Oruganti. Implementation of energy management scenarios in a dc microgrid using dc bus signaling. *IEEE Transactions on Industry Applications*, 57(5):5306–5317, 2021.

[100] Hongpeng Liu, Yongheng Yang, Poh Chiang Loh, Ferde Blaabjerg, Marko Angjelichinoski, Cedomir Stefanovic, and Petar Popovski. Power talk: A novel power line communication in dc microgrid. In *2016 IEEE 8th International Power Electronics and Motion Control Conference (IPEMC-ECCE Asia)*, pages 2870–2874. IEEE, 2016.

[101] Hyun-Jun Choi and Jee-Hoon Jung. Enhanced power line communication strategy for dc microgrids using switching frequency modulation of power converters. *IEEE Transactions on Power Electronics*, 32(6):4140–4144, 2017.

[102] Vasilis Kleftakis, Dimitris Lagos, Christina Papadimitriou, and Nikos D Hatziargyriou. Seamless transition between interconnected and islanded operation of dc microgrids. *IEEE Transactions on Smart Grid*, 10(1):248–256, 2017.

[103] Zhiyi Chen, Xinghuo Yu, Wenying Xu, and Guanghui Wen. Modeling and control of islanded dc microgrid clusters with hierarchical event-triggered consensus algorithm. *IEEE Transactions on Circuits and Systems I: Regular Papers*, 68(1):376–386, 2020.

[104] Zakaria El Mrabet, Naima Kaabouch, Hassan El Ghazi, and Hamid El Ghazi. Cyber-security in smart grid: Survey and challenges. *Computers & Electrical Engineering*, 67:469–482, 2018.

[105] Quan Zhou, Mohammad Shahidehpour, Ahmed Alabdulwahab, and Abdullah Abusorrah. A cyber-attack resilient distributed control strategy in islanded microgrids. *IEEE Transactions on Smart Grid*, 11(5):3690–3701, 2020.

[106] Weitao Yao, Yu Wang, Yan Xu, and Chao Deng. Cyber-resilient control of an islanded microgrid under latency attacks and random dos attacks. *IEEE Transactions on Industrial Informatics*, 19(4):5858–5869, 2022.

[107] Farzam Nejabatkhah, Yun Wei Li, Hao Liang, and Rouzbeh Reza Ahrabi. Cybersecurity of smart microgrids: A survey. *Energies*, 14(1):27, 2020.

[108] Hamidreza Shafei, Li Li, and Ricardo P Aguilera. A comprehensive review on cyberattack detection and control of microgrid systems. *Power Systems Cybersecurity: Methods, Concepts, and Best Practices*, pages 1–45, 2023.

[109] Yulin Chen, Donglian Qi, Hangning Dong, Chaoyong Li, Zhenming Li, and Jianliang Zhang. A fdi attack-resilient distributed secondary control strategy for islanded microgrids. *IEEE Transactions on Smart Grid*, 12(3):1929–1938, 2020.

[110] Dinesh Kumar, Firuz Zare, and Arindam Ghosh. Dc microgrid technology: system architectures, ac grid interfaces, grounding schemes, power quality, communication networks, applications, and standardizations aspects. *Ieee Access*, 5:12230–12256, 2017.

[111] Farzad Banihashemi, Mark Vygoder, Nick Hoeft, and Robert Cuzner. Earthing arrangements impacts on protection schemes for a commercial microgrid. In *2019 8th International Conference on Renewable Energy Research and Applications (ICRERA)*, pages 413–421. IEEE, 2019.

[112] Adil Ayub Sheikh, Sarvesh A Wakode, Rohit R Deshmukh, Makarand S Ballal, Hiralal M Suryawanshi, Mahesh K Mishra, and Shrawan Kumar. A brief review on dc microgrid protection. In *2020 IEEE First International Conference on Smart Technologies for Power, Energy and Control (STPEC)*, pages 1–6. IEEE, 2020.

[113] Kaloyan Mihaylov, Stanimir Valtchev, and Rumen Arnaudov. Smart microgrid sensorless load monitoring and management in tn-s and tn-cs electrical networks. In *2015 International Conference on Electrical Drives and Power Electronics (EDPE)*, pages 162–166. IEEE, 2015.

[114] Thiago R de Oliveira, Aécio S Bolzon, and Pedro Francisco Donoso-Garcia. Grounding and safety considerations for residential dc microgrids. In *IECON 2014-40th Annual Conference of the IEEE Industrial Electronics Society*, pages 5526–5532. IEEE, 2014.

[115] Ankan Chandra, Girish Kumar Singh, and Vinay Pant. Protection techniques for dc microgrid-a review. *Electric Power Systems Research*, 187:106439, 2020.

[116] Weiliang Zhang, Hui Zhang, and Na Zhi. A novel protection strategy for dc microgrid considering communication failure. *Energy Reports*, 9:2035–2044, 2023.

[117] Jin Yang, John E Fletcher, and John O'Reilly. Short-circuit and ground fault analyses and location in vsc-based dc network cables. *IEEE transactions on Industrial Electronics*, 59(10):3827–3837, 2011.

[118] Andre Kislovski. *Dynamic analysis of switching-mode DC/DC converters*. Springer Science & Business Media, 2012.

[119] Frede Blaabjerg, Mahajan Sagar Bhaskar, and Sanjeevikumar Padmanaban. Non-isolated dc-dc converters for renewable energy applications. 2021.

[120] Gade Kesava Rao and Premalata Jena. Unit protection of tapped line dc microgrid. *IEEE Journal of Emerging and Selected Topics in Power Electronics*, 10(4):4680–4689, 2022.

[121] Morteza Shamsoddini, Behrooz Vahidi, Ramin Razani, and Yasser Abdel-Rady I Mohamed. A novel protection scheme for low voltage dc microgrid using inductance estimation. *International Journal of Electrical Power & Energy Systems*, 120:105992, 2020.

[122] Steven DA Fletcher, Patrick J Norman, Stuart J Galloway, Paul Crolla, and Graeme M Burt. Optimizing the roles of unit and non-unit protection methods within dc microgrids. *IEEE transactions on Smart Grid*, 3(4):2079–2087, 2012.

[123] Gade Kesava Rao, Bhabani Kumari Choudhry, and Premalata Jena. Impedance based differential protection for zonal dc microgrid. In *2022 IEEE Global Conference on Computing, Power and Communication Technologies (GlobConPT)*, pages 1–6. IEEE, 2022.

[124] Jay Johnson, Birger Pahl, Charles Luebke, Tom Pier, Theodore Miller, Jason Strauch, Scott Kuszmaul, and Ward Bower. Photovoltaic dc arc fault detector testing

at sandia national laboratories. In *2011 37th IEEE Photovoltaic Specialists Conference*, pages 003614–003619, 2011.

[125] Manohar Mishra, Bhaskar Patnaik, Monalisa Biswal, Shazia Hasan, and Ramesh C Bansal. A systematic review on dc-microgrid protection and grounding techniques: Issues, challenges and future perspective. *Applied Energy*, 313:118810, 2022.

[126] Anju Meghwani, Saikat Chakrabarti, and S. C. Srivastava. A fast scheme for fault detection in dc microgrid based on voltage prediction. In *2016 National Power Systems Conference (NPSC)*, pages 1–6, 2016.

[127] Daniel Salomonsson, Lennart Soder, and Ambra Sannino. Protection of low-voltage dc microgrids. *IEEE Transactions on power delivery*, 24(3):1045–1053, 2009.

[128] Grace Madingou, Mahyar Zarghami, and Mohammad Vaziri. Fault detection and isolation in a dc microgrid using a central processing unit. In *2015 IEEE Power & Energy Society Innovative Smart Grid Technologies Conference (ISGT)*, pages 1–5. IEEE, 2015.

[129] SDA Fletcher, PJ Norman, SJ Galloway, and GM Burt. Analysis of the effectiveness of non-unit protection methods within dc microgrids. 2011.

[130] Chih-Wen Liu, Tzu-Chiao Lin, Chi-Shan Yu, and Jun-Zhe Yang. A fault location technique for two-terminal multisection compound transmission lines using synchronized phasor measurements. *IEEE Transactions on Smart Grid*, 3(1):113–121, 2011.

[131] Weilin Li, Antonello Monti, and Ferdinanda Ponci. Fault detection and classification in medium voltage dc shipboard power systems with wavelets and artificial neural networks. *IEEE Transactions on Instrumentation and Measurement*, 63(11):2651–2665, 2014.

[132] Xin Jin, Yang Shen, and Quan Zhou. A systematic review of robust control strategies in dc microgrids. *The Electricity Journal*, 35(5):107125, 2022.

[133] Chunpeng Li, Puran Rakhra, Patrick J Norman, Graeme M Burt, and Paul Clarkson. Multi-sample differential protection scheme in dc microgrids. *IEEE Journal of Emerging and Selected Topics in Power Electronics*, 9(3):2560–2573, 2020.

[134] Sadegh Azizi, Saeed Afsharnia, and Majid Sanaye-Pasand. Fault location on multiterminal dc systems using synchronized current measurements. *International Journal of Electrical Power & Energy Systems*, 63:779–786, 2014.

[135] Chenghan Zhou, Guibin Zou, Lindong Zang, and Xiaogong Du. Current differential protection for active distribution networks based on improved fault data self-synchronization method. *IEEE Transactions on Smart Grid*, 13(1):166–178, 2021.

[136] Khaled Saleh, Ali Hooshyar, and Ehab F El-Saadany. Fault detection and location in medium-voltage dc microgrids using travelling-wave reflections. *IET Renewable Power Generation*, 14(4):571–579, 2020.

[137] Sajay Krishnan Paruthiyil, Ali Bidram, and Matthew J Reno. A physics-informed learning technique for fault location of dc microgrids using traveling waves. *IET Generation, Transmission & Distribution*, 16(23):4791–4805, 2022.

[138] Rudy Montoya, Binod P Poudel, Ali Bidram, and Matthew J Reno. Dc microgrid fault detection using multiresolution analysis of traveling waves. *International Journal of Electrical Power & Energy Systems*, 135:107590, 2022.

[139] Zhen-Qiang Li and Yan-Ping Lv. A novel scheme of hvdc transmission line voltage traveling wave protection based on wavelet transform. In *2008 International Conference on High Voltage Engineering and Application*, pages 163–167. IEEE, 2008.

[140] Rui Li, Lie Xu, Derrick Holliday, Frederick Page, Stephen J Finney, and Barry W Williams. Continuous operation of radial multiterminal hvdc systems under dc fault. *IEEE Transactions on Power Delivery*, 31(1):351–361, 2015.

[141] Jeremy Sneath and Athula D Rajapakse. Fault detection and interruption in an earthed hvdc grid using rocov and hybrid dc breakers. *IEEE Transactions on Power Delivery*, 31(3):973–981, 2014.

[142] Rui Li, Lie Xu, and Liangzhong Yao. Dc fault detection and location in meshed multiterminal hvdc systems based on dc reactor voltage change rate. *IEEE Transactions on Power Delivery*, 32(3):1516–1526, 2016.

[143] Jian Liu, Nengling Tai, and Chunju Fan. Transient-voltage-based protection scheme for dc line faults in the multiterminal vsc-hvdc system. *IEEE Transactions on Power Delivery*, 32(3):1483–1494, 2016.

[144] Qiang Huang, Guibin Zou, Shuo Zhang, and Houlei Gao. A pilot protection scheme of dc lines for multi-terminal hvdc grid. *IEEE Transactions on Power Delivery*, 34(5):1957–1966, 2019.

[145] Mahmoud A Allam and Khaled A Saleh. A novel dc distance relay for mvdc microgrids. *IEEE Transactions on Smart Grid*, 13(2):962–974, 2021.

[146] Huiying Zheng, Shuhui Li, Chuanzhi Zang, and Weijian Zheng. Coordinated control for grid integration of pv array, battery storage, and supercapacitor. In *2013 IEEE Power & Energy Society General Meeting*, pages 1–5. IEEE, 2013.

[147] Victor Vega-Garita, Anindio Prabu Harsarapama, Laura Ramirez-Elizondo, and Pavol Bauer. Physical integration of pv-battery system: Advantages, challenges, and thermal model. In *2016 IEEE International Energy Conference (ENERGYCON)*, pages 1–6. IEEE, 2016.

[148] Sudip Bhattacharyya, S Puchalapalli, and Bhim Singh. Battery management and operation of a wind-pv based microgrid. In *2020 IEEE International Conference on Computing, Power and Communication Technologies (GUCON)*, pages 423–429. IEEE, 2020.

[149] Kamil Okay, Sermet Eray, and Aynur Eray. Development of prototype battery management system for pv system. *Renewable Energy*, 181:1294–1304, 2022.

[150] Hiroaki Kakigano, Yushi Miura, and Toshifumi Ise. Distribution voltage control for dc microgrids using fuzzy control and gain-scheduling technique. *IEEE transactions on power electronics*, 28(5):2246–2258, 2012.

[151] Enrique Espina, Jacqueline Llanos, Claudio Burgos-Mellado, Roberto Cardenas-Dobson, Manuel Martinez-Gomez, and Doris Saez. Distributed control strategies for microgrids: An overview. *IEEE Access*, 8:193412–193448, 2020.

[152] Dong Li and Carl Ngai Man Ho. A module-based plug-n-play dc microgrid with fully decentralized control for ieee empower a billion lives competition. *IEEE Transactions on Power Electronics*, 36(2):1764–1776, 2020.

[153] Qianwen Xu, Jianfang Xiao, Peng Wang, and Changyun Wen. A decentralized control strategy for economic operation of autonomous ac, dc, and hybrid ac/dc microgrids. *IEEE Transactions on Energy Conversion*, 32(4):1345–1355, 2017.

[154] NWA Lidula and AD Rajapakse. Microgrids research: A review of experimental microgrids and test systems. *Renewable and Sustainable Energy Reviews*, 15(1):186–202, 2011.

[155] Adam Hirsch, Yael Parag, and Josep Guerrero. Microgrids: A review of technologies, key drivers, and outstanding issues. *Renewable and sustainable Energy reviews*, 90:402–411, 2018.

[156] Sina Parhizi, Hossein Lotfi, Amin Khodaei, and Shay Bahramirad. State of the art in research on microgrids: A review. *IEEE access*, 3:890–925, 2015.

[157] Estefanía Planas, Jon Andreu, José Ignacio Gárate, Inigo Martinez De Alegria, and Edorta Ibarra. Ac and dc technology in microgrids: A review. *Renewable and Sustainable Energy Reviews*, 43:726–749, 2015.

[158] Ahmed T Elsayed, Ahmed A Mohamed, and Osama A Mohammed. Dc microgrids and distribution systems: An overview. *Electric power systems research*, 119:407–417, 2015.

[159] Reza Heydari and Mohammad Farrokhi. Robust model predictive control of biped robots with adaptive on-line gait generation. *International Journal of Control, Automation and Systems*, 15(1):329–344, 2017.

[160] Stefano Riverso, Marcello Farina, and Giancarlo Ferrari-Trecate. Plug-and-play decentralized model predictive control for linear systems. *IEEE Transactions on Automatic Control*, 58(10):2608–2614, 2013.

[161] Manfred Morari and Jay H Lee. Model predictive control: past, present and future. *Computers & Chemical Engineering*, 23(4-5):667–682, 1999.

[162] Carlos Bordons, Félix Garcia-Torres, Miguel A Ridao, Carlos Bordons, Félix Garcia-Torres, and Miguel A Ridao. Model predictive control fundamentals. *Model Predictive Control of Microgrids*, pages 25–44, 2020.

[163] Gianluca Serale, Massimo Fiorentini, Alfonso Capozzoli, Daniele Bernardini, and Alberto Bemporad. Model predictive control (mpc) for enhancing building and hvac system energy efficiency: Problem formulation, applications and opportunities. *Energies*, 11(3):631, 2018.

[164] Liuping Wang. *Model predictive control system design and implementation using MATLAB®*. Springer Science & Business Media, 2009.

[165] Marwa Turki, Nicolas Langlois, and Adnan Yassine. An analytical tuning of mpc control horizon using the hessian condition number. In *14th International Workshop on Advanced Control and Diagnosis*, 2017.

[166] Rolf Findeisen and Frank Allgöwer. An introduction to nonlinear model predictive control. In *21st Benelux meeting on systems and control*, volume 11, pages 119–141. Technische Universiteit Eindhoven Veldhoven Eindhoven, The Netherlands, 2002.

[167] Marco Forgione, Dario Piga, and Alberto Bemporad. Efficient calibration of embedded mpc. *IFAC-PapersOnLine*, 53(2):5189–5194, 2020.

[168] Jorge L Garriga and Masoud Soroush. Model predictive control tuning methods: A review. *Industrial & Engineering Chemistry Research*, 49(8):3505–3515, 2010.

[169] Sergio Vazquez, Eduardo Zafra, Ricardo P Aguilera, Tobias Geyer, Jose I Leon, and Leopoldo G Franquelo. Prediction model with harmonic load current components for

fcs-mpc of an uninterruptible power supply. *IEEE Transactions on Power Electronics*, 37(1):322–331, 2021.

[170] Matías Aguirre, Samir Kouro, Christian A Rojas, and Sergio Vazquez. Enhanced switching frequency control in fcs-mpc for power converters. *IEEE Transactions on Industrial Electronics*, 68(3):2470–2479, 2020.

[171] Petros Karamanakos, Eyke Liegmann, Tobias Geyer, and Ralph Kennel. Model predictive control of power electronic systems: Methods, results, and challenges. *IEEE Open Journal of Industry Applications*, 1:95–114, 2020.

[172] Sergio Vazquez, Jose Rodriguez, Marco Rivera, Leopoldo G Franquelo, and Margarita Norambuena. Model predictive control for power converters and drives: Advances and trends. *IEEE Transactions on Industrial Electronics*, 64(2):935–947, 2016.

[173] Tobias Geyer. A comparison of control and modulation schemes for medium-voltage drives: Emerging predictive control concepts versus pwm-based schemes. *IEEE Transactions on Industry Applications*, 47(3):1380–1389, 2011.

[174] Andrés Mora, Roberto Cárdenas-Dobson, Ricardo P Aguilera, Alejandro Angulo, Felipe Donoso, and Jose Rodriguez. Computationally efficient cascaded optimal switching sequence mpc for grid-connected three-level npc converters. *IEEE Transactions on Power Electronics*, 34(12):12464–12475, 2019.

[175] Ricardo P Aguilera and Daniel E Quevedo. Predictive control of power converters: Designs with guaranteed performance. *IEEE Transactions on Industrial Informatics*, 11(1):53–63, 2014.

[176] Milovan Majstorovic, Marco Rivera, Leposava Ristic, and Patrick Wheeler. Comparative study of classical and mpc control for single-phase mmc based on v-hil simulations. *Energies*, 14(11):3230, 2021.

[177] Bo Xu, Kaipei Liu, and Xiaohong Ran. Computationally efficient optimal switching sequence model predictive control for three-phase vienna rectifier under balanced and unbalanced dc links. *IEEE Transactions on Power Electronics*, 36(11):12268–12280, 2021.

[178] Xiongbo Wan, Fan Wei, Chuan-Ke Zhang, and Min Wu. Hybrid variables-dependent event-triggered model predictive control subject to polytopic uncertainties. *International Journal of Systems Science*, 53(14):3042–3055, 2022.

[179] WANG Benfei, Jingjing Huang, Jose Rodriguez, Cristian Garcia, and FENG Guodong. Event-triggered model predictive control for a three-phase inverter with output lc filter. In *2020 15th IEEE Conference on Industrial Electronics and Applications (ICIEA)*, pages 1259–1263. IEEE, 2020.

[180] Jose I Leon, Samir Kouro, Leopoldo G Franquelo, Jose Rodriguez, and Bin Wu. The essential role and the continuous evolution of modulation techniques for voltage-source inverters in the past, present, and future power electronics. *IEEE Transactions on Industrial Electronics*, 63(5):2688–2701, 2016.

[181] Matthias Preindl and Silverio Bolognani. Comparison of direct and pwm model predictive control for power electronic and drive systems. In *2013 Twenty-Eighth Annual IEEE Applied Power Electronics Conference and Exposition (APEC)*, pages 2526–2533. IEEE, 2013.

[182] Ali Alkasir, Seyed Ehsan Abdollahi, Seyed Reza Abdollahi, and Patrick Wheeler. A primary side ccs-mpc controller for constant current/voltage charging operation of series-series compensated wireless power transfer systems. In *2021 12th Power Electronics, Drive Systems, and Technologies Conference (PEDSTC)*, pages 1–5. IEEE, 2021.

[183] Mohammad Shadnam Zarbil, Masood Saeidi, Abolfazl Vahedi, and Hossein Azizi Moghaddam. Continuous control set model predictive control (ccs-mpc) of a three-phase rectifier. *ZANCO Journal of Pure and Applied Sciences*, 31(s3):342–350, 2019.

[184] Carlos Bordons and Carlos Montero. Basic principles of mpc for power converters: Bridging the gap between theory and practice. *IEEE Industrial Electronics Magazine*, 9(3):31–43, 2015.

[185] Cheng Xue, Li Ding, and YunweiRyan Li. Ccs-mpc with long predictive horizon for grid-connected current source converter. In *2020 IEEE Energy Conversion Congress and Exposition (ECCE)*, pages 4988–4993. IEEE, 2020.

[186] Mazen Alamir. *A Pragmatic Story of Model Predictive Control: Self Contained Algorithms and Case-studies*. CreateSpace Independent Publishing Platform, 2013.

[187] Wesam Rohouma, Morcos Metry, Robert S Balog, Aaqib Ahmad Peerzada, and Miroslav M Begovic. Adaptive mpc-based cost function for capacitorless var compensator in distribution networks. In *2020 IEEE 21st Workshop on Control and Modeling for Power Electronics (COMPEL)*, pages 1–6. IEEE, 2020.

[188] Amir Gholami, Alireza Sahab, Abdolreza Tavakoli, and Behnam Alizadeh. Dfig-based wind energy system robust optimal control by using of novel lmi-based adaptive mpc. *IETE Journal of Research*, pages 1–10, 2021.

[189] Miroslav Graf, Lukas Otava, and Ludek Buchta. Simple linearization approach for mpc design for small pmsm with field weakening performance. *IFAC-PapersOnLine*, 48(4):159–164, 2015.

[190] Sachidananda Sen and Vishal Kumar. Distributed adaptive-mpc type optimal pms for pv-battery based isolated microgrid. *IEEE Systems Journal*, 2022.

[191] Wenfei Ji, Ziwang Lu, and Guangyu Tian. An adaptive mpc slip controller for hub motor driven vehicles with a novel linearization method. In *2022 International Symposium on Electrical, Electronics and Information Engineering (ISEEIE)*, pages 272–277. IEEE, 2022.

[192] Rosana CB Rego. Lpv modeling of boost converter and gain scheduling mpc control. In *2019 IEEE 15th Brazilian Power Electronics Conference and 5th IEEE Southern Power Electronics Conference (COBEP/SPEC)*, pages 1–5. IEEE, 2019.

[193] Daud Sibtain, Muhammad Majid Gulzar, Ali F Murtaza, Sadia Murawwat, Muhammad Iqbal, Imran Rasool, Aamir Hayat, and Arslan Arif. Variable structure model predictive controller based gain scheduling for frequency regulation in renewable

based power system. *International Journal of Numerical Modelling: Electronic Networks, Devices and Fields*, 35(4):e2989, 2022.

[194] Min Jeong, Simon Fuchs, and Jürgen Biela. When fpgas meet regionless explicit mpc: An implementation of long-horizon linear mpc for power electronic systems. In *IECON 2020 the 46th annual conference of the ieee industrial electronics society*, pages 3085–3092. IEEE, 2020.

[195] Jing Chen, Yu Chen, Lupeng Tong, Li Peng, and Yong Kang. A backpropagation neural network-based explicit model predictive control for dc–dc converters with high switching frequency. *IEEE Journal of Emerging and Selected Topics in Power Electronics*, 8(3):2124–2142, 2020.

[196] Shumin Ruan, Yue Ma, Ningkang Yang, Changle Xiang, and Xunming Li. Real-time energy-saving control for hevs in car-following scenario with a double explicit mpc approach. *Energy*, 247:123265, 2022.

[197] Joel AE Andersson, Joris Gillis, Greg Horn, James B Rawlings, and Moritz Diehl. Casadi: a software framework for nonlinear optimization and optimal control. *Mathematical Programming Computation*, 11(1):1–36, 2019.

[198] Benjamin Stickan, Gianluca Frison, Bruno Burger, and Moritz Diehl. A nonlinear real-time pulse-pattern mpc scheme for power-electronics circuits operating in the microseconds range. In *2022 American Control Conference (ACC)*, pages 2070–2077. IEEE, 2022.

[199] Behnam Moradi and Mehran Mehrandezh. A non-linear mpc local planner for tractor-trailer vehicles in forward and backward maneuvering. *arXiv preprint arXiv:2212.11427*, 2022.

[200] Josip Vasilj, Damir Jakus, and Petar Sarajcev. Robust nonlinear economic mpc based management of a multi energy microgrid. *IEEE Transactions on Energy Conversion*, 36(2):1528–1536, 2020.

[201] Krzysztof Arendt and Christian T Veje. Mshoot: an open source framework for multiple shooting mpc in buildings. In *16th IBPSA International Conference and Exhibition Building Simulation 2019, Rome, 2-4 September*, 2019.

[202] T Guena and P Leblanc. How depth of discharge affects the cycle life of lithium-metal-polymer batteries. In *INTELEC 06-Twenty-Eighth International Telecommunications Energy Conference*, pages 1–8. IEEE, 2006.

[203] Gregory L Plett. *Battery management systems, Volume II: Equivalent-circuit methods*. Artech House, 2015.

[204] JR Dahn, JC Burns, and DA Stevens. Importance of coulombic efficiency measurements in r&d efforts to obtain long-lived li-ion batteries. *The Electrochemical Society Interface*, 25(3):75, 2016.

[205] Gregory L Plett. *Battery management systems, Volume I: Battery modeling*. Artech House, 2015.

[206] Yingzhi Cui, Chunyu Du, Geping Yin, Yunzhi Gao, Lingling Zhang, Ting Guan, Lijie Yang, and Fuping Wang. Multi-stress factor model for cycle lifetime prediction of lithium ion batteries with shallow-depth discharge. *Journal of Power Sources*, 279:123–132, 2015.

[207] Fuqiang An, Hongliang Zhao, and Ping Li. Self-discharge rates in cells have a critical effect on the cycle life of parallel lithium-ion batteries. *RSC advances*, 8(54):30802–30812, 2018.

[208] A123 SYSTEMS. Nanophosphate® high power lithium ion cellanr26650m1-b. https://datasheetspdf.com/pdf/1424845/A123Systems/ANR26650M1-B/1.

[209] Kathleen Cavanagh, Julia A Belk, and Konstantin Turitsyn. Transient stability guarantees for ad hoc dc microgrids. *IEEE Control Systems Letters*, 2(1):139–144, 2017.

[210] Michele Cucuzzella, Riccardo Lazzari, Sebastian Trip, Simone Rosti, Carlo Sandroni, and Antonella Ferrara. Sliding mode voltage control of boost converters in dc microgrids. *Control Engineering Practice*, 73:161–170, 2018.

[211] CN Papadimitriou, EI Zountouridou, and ND Hatziargyriou. Review of hierarchical control in dc microgrids. *Electric Power Systems Research*, 122:159–167, 2015.

[212] Anand Abhishek, Aashish Ranjan, Sachin Devassy, Brijendra Kumar Verma, Subhash Kumar Ram, and Ajeet Kr Dhakar. Review of hierarchical control strategies for dc microgrid. *IET Renewable Power Generation*, 14(10):1631–1640, 2020.

[213] Bo Fan, Shilin Guo, Jiangkai Peng, Qinmin Yang, Wenxin Liu, and Liming Liu. A consensus-based algorithm for power sharing and voltage regulation in dc microgrids. *IEEE Transactions on Industrial Informatics*, 16(6):3987–3996, 2019.

[214] Sebastian Trip, Michele Cucuzzella, Xiaodong Cheng, and Jacquelien Scherpen. Distributed averaging control for voltage regulation and current sharing in dc microgrids. *IEEE Control Systems Letters*, 3(1):174–179, 2018.

[215] Mahdieh S Sadabadi and Azwirman Gusrialdi. Resilient average consensus on general directed graphs in presence of cyber-attacks. *European Journal of Control*, 68:100669, 2022.

[216] Shankar Abhinav, Hamidreza Modares, Frank L Lewis, and Ali Davoudi. Resilient cooperative control of dc microgrids. *IEEE Transactions on Smart Grid*, 10(1):1083–1085, 2018.

[217] Mi Dong, Li Li, Yuwen Nie, Dongran Song, and Jian Yang. Stability analysis of a novel distributed secondary control considering communication delay in dc microgrids. *IEEE Transactions on Smart Grid*, 10(6):6690–6700, 2019.

[218] Mehdi Doostinia, Mohammad TH Beheshti, Seyed A Alavi, and Josep M Guerrero. Distributed control strategy for dc microgrids based on average consensus and fractional-order local controllers. *IET Smart Grid*, 4(6):549–560, 2021.

[219] Mahdieh S Sadabadi, Subham Sahoo, and Frede Blaabjerg. Stability-oriented design of cyberattack-resilient controllers for cooperative dc microgrids. *IEEE Transactions on Power Electronics*, 37(2):1310–1321, 2021.

[220] Andreu Cecilia, Subham Sahoo, Tomislav Dragičević, Ramon Costa-Castelló, and Frede Blaabjerg. On addressing the security and stability issues due to false data injection attacks in dc microgrids—an adaptive observer approach. *IEEE Transactions on Power Electronics*, 37(3):2801–2814, 2021.

[221] Oscar Danilo Montoya, Federico Martin Serra, and Alexander Molina-Cabrera. Hierarchical control for dc microgrids using an exact feedback controller with integral action. *Computers*, 11(2):22, 2022.

[222] Kaushik Gajula, Vu Le, Xiu Yao, Shaofeng Zou, and Luis Herrera. Quickest detection of series arc faults on dc microgrids. In *2021 IEEE Energy Conversion Congress and Exposition (ECCE)*, pages 796–801. IEEE, 2021.

[223] Subham Sahoo, Sukumar Mishra, Jimmy Chih-Hsien Peng, and Tomislav Dragičević. A stealth cyber-attack detection strategy for dc microgrids. *IEEE Transactions on Power Electronics*, 34(8):8162–8174, 2018.

[224] Subham Sahoo and Sukumar Mishra. A distributed finite-time secondary average voltage regulation and current sharing controller for dc microgrids. *IEEE Transactions on Smart Grid*, 10(1):282–292, 2017.

[225] Ali Bidram, Vahidreza Nasirian, Ali Davoudi, and Frank L Lewis. *Cooperative synchronization in distributed microgrid control*. Springer, 2017.

[226] Vo-Van Thanh and Wencong Su. Improving current sharing and voltage regulation for dc microgrids: A decentralized demand response approach. *IEEE Transactions on Smart Grid*, 2022.

[227] Yangming Dou, Ming Chi, Zhi-Wei Liu, Guanghui Wen, and Qihai Sun. Distributed secondary control for voltage regulation and optimal power sharing in dc microgrids. *IEEE Transactions on Control Systems Technology*, 30(6):2561–2572, 2022.

[228] Michele Tucci, Lexuan Meng, Josep M Guerrero, and Giancarlo Ferrari-Trecate. Stable current sharing and voltage balancing in dc microgrids: A consensus-based secondary control layer. *Automatica*, 95:1–13, 2018.

[229] Michele Cucuzzella, Sebastian Trip, Claudio De Persis, Xiaodong Cheng, Antonella Ferrara, and Arjan van der Schaft. A robust consensus algorithm for current sharing and voltage regulation in dc microgrids. *IEEE Transactions on Control Systems Technology*, 27(4):1583–1595, 2019.

[230] Amirreza Silani, Michele Cucuzzella, Jacquelien MA Scherpen, and Mohammad Javad Yazdanpanah. Robust output regulation for voltage control in dc networks with time-varying loads. *Automatica*, 135:109997, 2022.

[231] Yunpeng Li, Wenchao Meng, Bo Fan, Shiyi Zhao, and Qinmin Yang. Distributed aperiodic control of multibus dc microgrids with dos-attack resilience. *IEEE Transactions on Smart Grid*, 13(6):4815–4827, 2022.

[232] Mahdieh S Sadabadi, Nenad Mijatovic, and Tomislav Dragičević. A robust cooperative distributed secondary control strategy for dc microgrids with fewer communication requirements. *IEEE Transactions on Power Electronics*, 38(1):271–282, 2022.

[233] Fei Gao, Ren Kang, Jun Cao, and Tao Yang. Primary and secondary control in dc microgrids: a review. *Journal of Modern Power Systems and Clean Energy*, 7(2):227–242, 2019.

[234] KM Bhargavi, NS Jayalakshmi, DN Gaonkar, Ashish Shrivastava, and Vinay Kumar Jadoun. A comprehensive review on control techniques for power management of isolated dc microgrid system operation. *IEEE Access*, 9:32196–32228, 2021.

[235] R Dadi, K Meenakshy, and SK Damodaran. A review on secondary control methods in dc microgrid. *Journal of Operation and Automation in Power Engineering*, 11(2):105–112, 2023.

[236] Chao Deng, Fanghong Guo, Changyun Wen, Dong Yue, and Yu Wang. Distributed resilient secondary control for dc microgrids against heterogeneous communication

delays and dos attacks. *IEEE Transactions on Industrial Electronics*, 69(11):11560–11568, 2021.

[237] A Ashok Kumar and N Amutha Prabha. A comprehensive review of dc microgrid in market segments and control technique. *Heliyon*, page e11694, 2022.

[238] Nataraj Pragallapati, Satish J Ranade, and Olga Lavrova. Cyber physical implementation of improved distributed secondary control of dc microgrid. In *2021 1st international conference on power electronics and energy (ICPEE)*, pages 1–5. IEEE, 2021.

[239] Hyeong-Jun Yoo, Thai-Thanh Nguyen, and Hak-Man Kim. Consensus-based distributed coordination control of hybrid ac/dc microgrids. *IEEE Transactions on Sustainable Energy*, 11(2):629–639, 2019.

[240] Anuoluwapo Aluko, Andrew Swanson, Leigh Jarvis, and David Dorrell. Modeling and stability analysis of distributed secondary control scheme for stand-alone dc microgrid applications. *Energies*, 15(15):5411, 2022.

[241] Anuoluwapo Aluko, Elutunji Buraimoh, Oluwafemi Emmanuel Oni, and Innocent Ewean Davidson. Advanced distributed cooperative secondary control of islanded dc microgrids. *Energies*, 15(11):3988, 2022.

[242] Subham Sahoo and Sukumar Mishra. An adaptive event-triggered communication-based distributed secondary control for dc microgrids. *IEEE Transactions on Smart Grid*, 9(6):6674–6683, 2017.

[243] Pouya Shafiee, Babak Abdolmaleki, Mojtaba Ahmadi, and Qobad Shafiee. Need-based communication in fully-distributed secondary control of dc microgrids. In *2019 Smart Grid Conference (SGC)*, pages 1–7. IEEE, 2019.

[244] Vahidreza Nasirian, Ali Davoudi, Frank L. Lewis, and Josep M. Guerrero. Distributed adaptive droop control for dc distribution systems. *IEEE Transactions on Energy Conversion*, 29(4):944–956, 2014.

[245] Vahidreza Nasirian, Ali Davoudi, and Frank L Lewis. System and method for distributed control of an electrical network, October 20 2020. US Patent 10,809,678.

[246] Mehrdad Yazdanian and Ali Mehrizi-Sani. Distributed control techniques in microgrids. *IEEE Transactions on Smart Grid*, 5(6):2901–2909, 2014.

[247] Shan Zuo, Tuncay Altun, Frank L Lewis, and Ali Davoudi. Distributed resilient secondary control of dc microgrids against unbounded attacks. *IEEE Transactions on Smart Grid*, 11(5):3850–3859, 2020.

[248] Subham Sahoo, Tomislav Dragičević, and Frede Blaabjerg. Multilayer resilience paradigm against cyber attacks in dc microgrids. *IEEE Transactions on Power Electronics*, 36(3):2522–2532, 2020.

[249] Subham Sahoo, Jimmy Chih-Hsien Peng, Sukumar Mishra, and Tomislav Dragičević. Distributed screening of hijacking attacks in dc microgrids. *IEEE Transactions on Power Electronics*, 35(7):7574–7582, 2019.

[250] Alexander Julian Gallo, Mustafa Sahin Turan, Francesca Boem, Thomas Parisini, and Giancarlo Ferrari-Trecate. A distributed cyber-attack detection scheme with application to dc microgrids. *IEEE Transactions on Automatic Control*, 65(9):3800–3815, 2020.

[251] Subham Sahoo, Jimmy Chih-Hsien Peng, Annavaram Devakumar, Sukumar Mishra, and Tomislav Dragičević. On detection of false data in cooperative dc microgrids—a discordant element approach. *IEEE Transactions on Industrial Electronics*, 67(8):6562–6571, 2019.

[252] Sebastian Trip, Renke Han, Michele Cucuzzella, Xiaodong Cheng, Jacquelien Scherpen, and Josep Guerrero. Distributed averaging control for voltage regulation and current sharing in dc microgrids: Modelling and experimental validation. *IFAC-PapersOnLine*, 51(23):242–247, 2018.

[253] Douglas A Allan and James B Rawlings. Moving horizon estimation. *Handbook of model predictive control*, pages 99–124, 2019.

[254] Mahshad Valipour and Luis A Ricardez-Sandoval. A robust moving horizon estimation under unknown distributions of process or measurement noises. *Computers & Chemical Engineering*, 157:107620, 2022.

[255] Mohamed W Mehrez, George KI Mann, and Raymond G Gosine. Nonlinear moving horizon state estimation for multi-robot relative localization. In *2014 IEEE 27th Canadian Conference on Electrical and Computer Engineering (CCECE)*, pages 1–5. IEEE, 2014.

[256] Moritz Diehl, Hans Joachim Ferreau, and Niels Haverbeke. Efficient numerical methods for nonlinear mpc and moving horizon estimation. *Nonlinear model predictive control: towards new challenging applications*, pages 391–417, 2009.

[257] S Augustine, JE Quiroz, MJ Reno, and S Brahma. Dc microgrid protection: Review and challenges; sandia national lab. *SNL-NM): Albuquerque, NM, USA*, 2018.

[258] Kamal Kant and Om Hari Gupta. Dc microgrid: A comprehensive review on protection challenges and schemes. *IETE Technical Review*, pages 1–17, 2022.

[259] Shrikrishna Yawale and Sangita Yawale. *Operational Amplifier*. Springer, 2022.

[260] LEM Transeducers. *LA55P Current Transducer*, 2018. Version 17.

[261] Texas Instruments Incorporated. *Non-inverting op amp with non-inverting positive reference voltage circuit*, 2019. SBOA263A.

[262] Qing Mu, Jun Liang, Yalou Li, and Xiaoxin Zhou. Power flow control devices in dc grids. In *2012 IEEE Power and Energy Society General Meeting*, pages 1–7. IEEE, 2012.

[263] DKJS Jayamaha, NWA Lidula, and AD Rajapakse. Protection and grounding methods in dc microgrids: Comprehensive review and analysis. *Renewable and Sustainable Energy Reviews*, 120:109631, 2020.

[264] Mohammed H Ibrahim, Ebrahim A Badran, and Mansour H Abdel-Rahman. On the dc microgrids protection challenges, schemes, and devices-a review. *DC Microgrids: Advances, Challenges, and Applications*, pages 1–62, 2022.

[265] Mesut E Baran and Nikhil R Mahajan. Dc distribution for industrial systems: opportunities and challenges. *IEEE transactions on industry applications*, 39(6):1596–1601, 2003.

[266] Boris Jacobson and John Walker. Grounding considerations for dc and mixed dc and ac power systems. *Naval Engineers Journal*, 119(2):49–62, 2007.

[267] Michael F Singer. Solving homogeneous linear differential equations in terms of second order linear differential equations. *American Journal of Mathematics*, 107(3):663–696, 1985.

[268] Abhishek Das. A novel method to solve cubic and quartic equations. *Preprint*, 2014.

[269] Analog Devices Inc. *ADA4099-1BUJZ-RL7*, 2018. IC OPAMP GP 1 CIRCUIT TSOT6.

[270] LEM Transeducers. *LV 25-P, 500V Voltage Transducer*, 2018. Version 20.

[271] ON semiconductors. *Ultra fast recovery diode*, 2022. Version 20.